PYLON EFFECTS ON A SCRAMJET CAVITY FLAMEHOLDER FLOWFIELD

DISSERTATION

Andrew B. Freeborn, Lt Col, USAF

AFIT/DS/ENY/08-04

DEPARTMENT OF THE AIR FORCE
AIR UNIVERSITY

AIR FORCE INSTITUTE OF TECHNOLOGY

Wright-Patterson Air Force Base, Ohio

APPROVED FOR PUBLIC RELEASE; DISTRIBUTION IS UNLIMITED

The views expressed in this thesis are those of the author and do not reflect the official policy or position of the United States Air Force, Department of Defense, or the United States Government.

AFIT/DS/ENY/08-04

PYLON EFFECTS ON A SCRAMJET CAVITY FLAMEHOLDER FLOWFIELD

DISSERTATION

Presented to the Faculty

Graduate School of Engineering and Management

Air Force Institute of Technology

Air University

Air Education and Training Command

in Partial Fulfillment of the Requirements for the

Degree of Doctor of Philosophy

Andrew B. Freeborn, BS, MAE

Lt Col, USAF

September 2008

APPROVED FOR PUBLIC RELEASE; DISTRIBUTION UNLIMITED

AFIT/DS/ENY/08-04

PYLON EFFECTS ON A SCRAMJET CAVITY FLAMEHOLDER FLOWFIELD

Andrew B. Freeborn, BS, MAE
Lt Col, USAF

Approved:

Dr. Paul I. King (Chairman)	12 Sept 08 Date
Dr. Mark R. Gruber (Member)	12 Sep 2008 Date
Dr. Glen P. Perram (Member)	12 Sept 08 Date
Dr. Mark F. Reeder (Member)	12 Sept. 08 Date

Accepted:

Marlin U. Thomas Dean, Graduate School of Engineering and Management	17 Sep 08 Date

Abstract

Cavity flameholders in supersonic combustion ramjet (scramjet) combustors, while effective, fail to take advantage of the full combustor volume. Adding a pylon to the leading edge of a cavity flameholder generates a flowfield increasing mass exchange between the cavity and main combustor flow, increasing the mixing interface between flameholder products and main combustor flow, and exhibiting minimal Reynolds number effects. To demonstrate this modified flowfield driven by supersonic expansion behind the pylon, pylon-cavity flameholder flowfield data were obtained through a combination of wind tunnel experimentation and steady-state computational fluid dynamics (CFD). Flowfield effects of the pylon-cavity were examined at a Mach number of two and Reynolds numbers from approximately 32 million m^{-1} to 55 million m^{-1}. Addition of the pylon resulted in approximately three times the mass exchange between the cavity and overlying flow. Both CFD and particle image velocimetry data showed strong upward flow behind the pylon, increasing exposure and exchange of cavity fluid with the main combustor flow. Reynolds number effects were weak within the range of test conditions. Assuming a suitably reacting fuel-air mixture, the addition of a pylon offers the scramjet designer an attractive option to take advantage of a greater proportion of combustor volume and improve combustor performance.

Acknowledgments

There are many people who deserve my heartfelt appreciation for their assistance in completing this work. First among these for his guidance and encouragement is my advisor, Dr. Paul King. He was usually ready with helpful advice and insights whenever I would drop by unexpectedly with the crisis of the day. Our sponsor, Dr. Mark Gruber with the AFRL Propulsion Directorate has been a valuable resource in preparing the study and answering questions when results didn't make sense.

I'd like to also thank Dr. Mark Reeder for being willing to sit down almost anytime and discuss PIV and wind tunnel operations, as well as Dr. Ray Maple for always having an open door to talk about preparing my CFD models. Their assistance went a long way towards minimizing the potential frustration associated with my chosen data collection techniques.

None of the experimental work would have been possible without the support of the laboratory personnel, especially Mr. John Hixenbaugh for always having the fix for whatever problem had cropped up and for showing me how to get the machines to work. Thanks to Mr. Jay Anderson for his management support in the laboratory. Thanks also to fellow students Maj. Jason Doster and Maj. Bartt Greene, for their role in resurrecting the 6" x 6" wind tunnel and preparing it for data collection.

Finally, I want to thank my family for their encouragement and support, but especially my wife, Lynn Gawell. Over the years of long nights, short weekends, and the occasional frustrated rants, her help, patience and love have made this possible.

Table of Contents

Page

Abstract iv

Acknowledgments v

Table of Contents vi

List of Figures viii

List of Tables xv

List of Symbols xvi

I. Introduction 1

1.1 Scope of Research 6
1.1.1 Thesis Statement 7
1.1.2 Research Approach 7
1.2 Document Organization 8

II. Background 9

2.1 Scramjet Overview 9
2.2 Cavity Flameholders 15
2.3 Cavity-Pylon Flameholder 26

III. Experimental Approach 32

3.1 Wind Tunnel and Test Section 32
3.2 Instrumentation 40

IV. Computational Approach 49

4.1 Computational Domains 49
4.2 Computational Method 52

V. Results and Discussion 56

5.1 Flow Visualization 56
5.2 Pressure Data 62
5.3 Flowfield Data 70
5.4 Frequency Data 93

Page

5.5 Cavity Mass Exchange/Residence Time 97

VI. Summary and Conclusions 102

6.1 Summary 102
6.2 Conclusions 102
6.3 Recommendations for Future Research 106

Appendix A: Wind Tunnel Operations 109

A1. Test Section Design and Construction 109
A2. Wind Tunnel Procedures 124
A3. Data Collection and Reduction 135
A4. Tunnel Nozzle Contours 141
A5. Detailed Wind Tunnel Test Conditions ($M \approx 2$) 147
A6. PIV Images 148
A7. Comparison of PIV and CFD Turbulence Intensity 151

Appendix B: CFD Details 156

B1. Grid Convergence 156
B2. Computational Method 159
B3. Detailed CFD Test Conditions ($M \approx 2$) 165

Appendix C: Additional Surface Pressure Data 166

Bibliography 177

Vita 184

List of Figures

Page

Figure 1. Approximate Mach number regimes 2

Figure 2. Air-breathing propulsion specific impulse trends [based on Ref. 3] 3

Figure 3. Illustration of pylon-cavity flow 7

Figure 4. Scramjet engine reference stations 14

Figure 5. Step flameholder 16

Figure 6. Rectangular cavity flameholder 17

Figure 7. Cavity classifications 18

Figure 8. Inclined cavity flameholder 21

Figure 9. Computational streamlines for $M = 3$, Re = 51 x 10^6 m^{-1} flow over an $L/D = 3$, 30° inclined cavity flameholder [38] 23

Figure 10. Flame spread geometry 25

Figure 11. Cavity flameholder with inclined downstream ramp and leading edge pylon (on centerline) 27

Figure 12. Two-dimensional pylon shock/expansion system 28

Figure 13. Comparison of cavity shear layer and cavity shear layer plus pylon wake 30

Figure 14. AFIT 6" x 6" Supersonic Wind Tunnel 33

Figure 15. Stagnation tank pressure and temperature traces (stagnation pressure setting = 241 kPa, peak stagnation pressure = 258 kPa) 34

Figure 16. AFIT 6" x 6" Supersonic Wind Tunnel add-on test section with pylon installed and configured for PIV (near-side window and probe plate removed) 36

Figure 17. Mach number profile across the test section entrance (x = -22 cm, y = 3.7 cm; Re ≈ 32 x 10^6 m^{-1}) 37

Figure 18. Test article geometry 38

Figure 19. Coordinate system and pressure tap placement 39

Page

Figure 20. Static and pitot probes 41

Figure 21. Refraction of parallel light beams passing through the test section used in Shadowgraph/Schlieren photography [56] 42

Figure 22. Two-dimensional PIV component relationships 43

Figure 23. PIV data reduction flow (flow from right; details in App. A) 44

Figure 24. Cavity CO_2 injector 46

Figure 25. Boundary layer entering the test section ($x \approx$ -12 cm, $z \approx$ 2.5 cm; Re $\approx$ 32 x 10^6 m^{-1}; probe data at x = -22 cm; surface pressure data at x = -10.8 cm; velocity corrected for temperature variation) 48

Figure 26. Computational domains 50

Figure 27. Close-up of mesh on centerline (z = 0 cm) 51

Figure 28. Cross-stream mesh from cavity floor to tunnel ceiling (x = 5 cm) 51

Figure 29. Computational process 53

Figure 30. Test section convergence history a) without pylon and b) with pylon {plot of $\left|\dot{m}_{in} - \dot{m}_{out}\right| / \left|\dot{m}_{in} - \dot{m}_{out}\right|_{n=1}$ } 55

Figure 31. Shadowgraph image of significant features (Re# $\approx$ 42 x 10^6 m^{-1}, M = 2; hatched area unusable) 57

Figure 32. CFD density gradient (data from z = 0, 2, 4, 6 cm; grey scale of $d\rho/dx$; Re# $\approx$ 42 x 10^6 m^{-1}, M = 2) 57

Figure 33. Flowfield behind the top of the pylon in the plane x = 1 cm (contours of vertical velocity; dashed line represents the pylon) 58

Figure 34. Instantaneous Schlieren photographs of near-pylon flow (1/64000 sec exposure time) 60

Figure 35. Instantaneous Schlieren photograph of flow over the downstream ramp (Re# $\approx$ 42 x 10^6 m^{-1}; 1/64000 sec exposure time) 61

Page

Figure 36. CFD cavity surface pressure coefficient a) cavity-only, Re ≈ 32 x 10^6 m^{-1}; b) cavity-only, Re ≈ 55 x 10^6 m^{-1}; c) pylon-cavity, Re ≈ 32 x 10^6 m^{-1}; and d) pylon-cavity, Re ≈ 55 x 10^6 m^{-1} 64

Figure 37. Wind tunnel and CFD centerline surface pressure coefficients at Re ≈ 32 x 10^6 m^{-1} and Re ≈ 55 x 10^6 m^{-1}, a) without pylon and b) with pylon..... 67

Figure 38. Cross ramp pressures near shear layer impingement: a) pressure coefficient and b) absolute pressure (x = 10.8 cm, y = -0.94 cm) 68

Figure 39. Streamwise velocities measured above the cavity ramp (probe data, x = 8.8 cm, y = 3.7 cm, Re ≈ 32 x 10^6 m^{-1}) 69

Figure 40. Cross ramp surface pressure coefficients with pylon installed..... 69

Figure 41. CFD centerline pressure coefficient with streamlines (Re ≈ 32 x 10^6 m^{-1}) 70

Figure 42. CFD off-centerline pressure coefficient with streamlines (Re ≈ 32 x 10^6 m^{-1}): a) z = 0.5 cm; and b) z = 2 cm 72

Figure 43. Vertical velocity on centerline a) PIV data (Re ≈ 32 x 10^6 m^{-1}); b) CFD data (Re ≈ 32 x 10^6 m^{-1}); and c) CFD data (Re ≈ 55 x 10^6 m^{-1}) 73

Figure 44. Centerline vertical velocities behind pylon pressure tap (y = 1.9 cm)..... 74

Figure 45. CFD vertical velocity contours a) Re ≈ 32 x 10^6 m^{-1}; and b) Re ≈ 55 x 10^6 m^{-1} 81

Figure 46. Velocity magnitude behind pylon 3.7 cm above the cavity a) PIV data (Re ≈ 32 x 10^6 m^{-1}); b) CFD data (Re ≈ 32 x 10^6 m^{-1} and T_t = 273 K); c) CFD data (Re ≈ 55 x 10^6 m^{-1} and T_t = 287 K) (flow from right; hatched area unusable due to low particle density and surface reflections) 82

Figure 47. Number of usable PIV image pairs in wake flow 3.7 cm above the cavity (corresponds to Figure 46a; Re ≈ 32 x 10^6 m^{-1}) 83

Figure 48. Profile of velocity magnitude on either side of wake (y = 3.7 cm, z = +/- 3 cm; CFD velocities corrected for temperature differences) 83

Figure 49. Spanwise velocities at z = +/- 3 cm 84

Figure 50. PIV and CFD velocity magnitude across test section with pylon (x = 8.8 cm, y = 3.7 cm, CFD velocities corrected for temperature differences) 84

Page

Figure 51. Streamwise velocity behind pylon (y = 3.7 cm, z = 0 cm, Re ≈ 32 x 10^6 m^{-1}) 85

Figure 52. Velocity vectors in y-z plane at x = 1 cm across full span of test section (contours of x velocity; Re ≈ 32 x 10^6 m^{-1}) 86

Figure 53. Velocity vectors in y-z plane at x = 5 cm across full span of test section (contours of x velocity; Re ≈ 32 x 10^6 m^{-1}) 87

Figure 54. Velocity vectors in y-z plane at x = 10 cm across full span of test section (contours of x velocity; Re ≈ 32 x 10^6 m^{-1}) 88

Figure 55. Velocity vectors in y-z plane at x = 15 cm across full span of test section (contours of x velocity; Re ≈ 32 x 10^6 m^{-1}) 89

Figure 56. CFD streamlines off cavity centerline 90

Figure 57. Velocity magnitude and streamlines in cavity mid-plane 91

Figure 58. Diagram of mass exchange between the main flow and cavity vortices a) rectangular cavity (M = 3, Ref. [38]); b) no pylon (Re = 32 x 10^6 m^{-1}); and c) with pylon (Re = 32 x 10^6 m^{-1}) 92

Figure 59. Pressure fluctuation power spectrum at ambient conditions (baseline cavity) 93

Figure 60. Pressure fluctuation power spectrum at ambient conditions (pylon-cavity) 94

Figure 61. High-speed Schlieren frames of flow separating at the leading edge of the cavity showing structures propagating downstream (baseline cavity, Re# ≈ 42 x 10^6 m^{-1}) 96

Figure 62. Vertical velocity contours at the top cavity boundary (y = 0 cm) for Re# ≈ 32 x 10^6 m^{-1} (pylon installed; black line indicates zero vertical velocity) 100

Figure 63. Vertical velocity contours at the top cavity boundary (y = 0 cm) for Re# ≈ 32 x 10^6 m^{-1} (baseline cavity; black line indicates zero vertical velocity) 101

Figure 64. Notional cavity fuel-air injection scheme 108

Figure 65. AFIT 6" x 6" Supersonic Wind Tunnel: a) original test section; b) new Test section inserted behind old test section; c) closeup of new test section with baseline cavity test article installed 111

Figure 66. Test section side plate 112

Page

Figure 67. Test section bottom plate 113

Figure 68. Test section top plate (6 7/8 in or 4 in long) 114

Figure 69. Test section side window frame 115

Figure 70. Test section top window frame 116

Figure 71. Test section side window 117

Figure 72. Test section top window 118

Figure 73. Test article cavity section 119

Figure 74. Pylon insert 120

Figure 75. Plain insert 121

Figure 76. Location of surface pressure taps 122

Figure 77. Representation of the new test section junction (not to scale) 123

Figure 78. Wind tunnel operations checklist 129

Figure 79. Supply valves configured for operation without the backpressure regulator 130

Figure 80. Supply valves configured for operation with the backpressure regulator 131

Figure 81. Main and pressure control valves 132

Figure 82. Regulator controller 132

Figure 83. Wind tunnel stagnation tank pressure calibration chart and selected test condition settings 133

Figure 84. Screenshot of LabView monitoring program during a typical wind tunnel data run 134

Figure 85. Derived wind tunnel nozzle contours ($M \approx 2$) 141

Page

Figure 86. Average quality PIV wake image (pylon on center-right of frame, image plane at y = 3.7 cm)..... 148

Figure 87. Good quality PIV wake image (pylon on center-right of frame, image plane at y = 3.7 cm)..... 149

Figure 88. Comparison of good quality image pair (pylon on center-right of frame, image plane at y = 3.7 cm)..... 149

Figure 89. Average quality image of pylon wake on centerline (pylon on right edge of frame)..... 150

Figure 90. Turbulence intensity behind pylon 3.7 cm above the cavity (CFD; Re ≈ 32 x 10^6 m^{-1}; corresponds to Figure 46)..... 154

Figure 91. Turbulence intensity behind pylon 3.7 cm above the cavity (PIV; Re ≈ 32 x 10^6 m^{-1}; corresponds to Figure 46)..... 154

Figure 92. Turbulence intensity profile across test section (x = 8.8 cm, y = 3.7 cm)..... 155

Figure 93. Grid convergence (cross ramp pressure coefficient)..... 157

Figure 94. Grid convergence (centerline pressure coefficient)..... 158

Figure 95. Grid convergence (average downstream ramp pressure coefficient)..... 158

Figure 96. Surface pressure coefficients with and without a pylon installed (x = -10.8 cm)..... 166

Figure 97. Surface pressure coefficients with and without a pylon installed (x = -2.3 cm, y = 0 cm)..... 167

Figure 98. Cavity step pressure (with and without pylon installed) and pylon base pressure..... 168

Figure 99. Surface pressure coefficients with and without a pylon installed (x = 1.2 cm, y = -2.54 cm)..... 169

Figure 100. Surface pressure coefficients with and without a pylon installed (x = 3.4 cm, y = -2.54 cm)..... 170

Figure 101. Surface pressure coefficients with and without a pylon installed (x = 5.5 cm, y = -2.54 cm)..... 171

Page

Figure 102. Surface pressure coefficients with and without a pylon installed (x = 7.6 cm, y = -2.2 cm) 172

Figure 103. Surface pressure coefficients with and without a pylon installed (x = 9.2 cm, y = -1.6 cm) 173

Figure 104. Surface pressure coefficients with and without a pylon installed (x = 10.9 cm, y = -0.95 cm) 174

Figure 105. Surface pressure coefficients with and without a pylon installed (x = 12.4 cm, y = -0.32 cm) 175

Figure 106. Surface pressure coefficients with and without a pylon installed (x = 14.0 cm, y = 0 cm)..... 176

List of Tables

Page

Table 1. Rectangular cavity oscillation frequencies..... 20

Table 2. Wind tunnel test conditions (M ≈ 2)..... 35

Table 3. Pressure transducer list 40

Table 4. Average cavity pressures..... 63

Table 5. Mass averaged test section total pressure ratios..... 66

Table 6. Pressure coefficients and upward velocity on centerline behind the pylon 71

Table 7. Approximate cavity reverse-flow velocities (CFD, x = 8 cm, y = -2 cm, z = 4 cm) 78

Table 8. 6" x 6" Supersonic Wind Tunnel nozzle contours (M ≈ 2) 142

List of Symbols

a_1	Sound speed above cavity (high speed side) (m/s)
a_2	Sound speed in cavity (low speed side) (m/s)
A	Area (m^3)
C_p	Pressure coefficient
D	Cavity depth (m)
D_H	Hydraulic diameter (m)
f	Pressure oscillation frequency (Hz)
I	Turbulent intensity
k	Turbulent kinetic energy (m^2/s^2)
K	Ratio of convective to freestream/duct velocity (U_c/U)
l	Turbulent length scale (m)
L	Cavity length (m)
m	Mode number
$\dot{m}_{cav}$	Cavity mass flow (kg/s)
$\dot{m}_{freestream}$	Freestream/duct mass flow (kg/s)
MFR	Mass flow ratio ($\dot{m}_{cav} / \dot{m}_{freestream}$)
M_∞	Free-stream Mach number
M_{c1}	Convective Mach number on high speed side of shear layer
M_{probe}	Probe Mach number
$M_{combustor}$	Combustor entrance Mach number

M_{flight}	Flight Mach number
p_{ref}	Reference pressure (Pa)
P_t	Total pressure (Pa)
P_{floor}	Tunnel floor static pressure (Pa)
P_{pitot}	Pitot probe pressure (Pa)
P_{cone}	Static cone probe pressure (Pa)
P	Static pressure (Pa)
q	Dynamic pressure (Pa)
R	Gas constant (J/kg-K)
Re	Reynolds number
t	Time (s)
T_t	Total temperature (K)
T	Static temperature (K)
U	Streamwise velocity (m/s)
u_f	Turbulent flame speed (m/s)
u_{y+}	Positive component of vertical velocity passing the top of the cavity (m/s)
u'	Turbulent velocity fluctuation (m/s)
U	Duct velocity (m/s)
U_1	Velocity above shear layer (high speed side) (m/s)
U_2	Velocity below shear layer (low speed side) (m/s)
U_c	Convective velocity (m/s)
v	Vertical velocity (m/s)

x	Streamwise coordinate (cm, m)
y	Vertical coordinate (cm, m)
z	Lateral coordinate (cm, m)
α	Cavity oscillation phase constant
γ	Ratio of specific heats
δ	Boundary layer thickness (m)
ε	Turbulent dissipation rate (m^2/s^3)
μ	Dynamic viscosity (kg/m-s)
ρ	Density (kg/m^3)
ω	Specific turbulent dissipation rate (s^{-1})
∞	Free stream conditions

PYLON EFFECTS ON A SCRAMJET CAVITY FLAMEHOLDER FLOWFIELD

I. Introduction

The desire for faster response times or cheap access to space drives both government program requirements and industry driven innovation in propulsion. Applications such as rapid transportation, ballistic missile defense, long range strike, or airbreathing access to space continue to push the envelope in terms of altitude and airspeed. Today, turbine engines power most high speed aircraft, but they can no longer be expected to provide the primary source of air-breathing propulsion as speed and altitude requirements increase. Supersonic combustion ramjet (scramjet) propulsion provides a method of achieving this higher performance. Unlike their low-speed counterparts, scramjet designers must contend with supersonic velocities through the entire engine which results in minimal time to burn fuel before the flow exits the engine.

Aerospace propulsion varies over an enormously wide range of speeds from zero velocity before takeoff all the way to escape velocity for space access. Considering only air-breathing propulsion, one potential path through this airspeed spectrum, as shown in Figure 1, starts with the familiar turbine engine for flight Mach numbers less than three, moving to the ramjet for Mach numbers up to approximately five, and ending with the supersonic combustion ramjet. Nothing special defines these Mach number boundaries. Turbine engine designs could operate above a Mach number of three; they

would just do so less efficiently. Turbine engines compress air using a rotating compressor to take low pressure, high-speed air and convert it into a high pressure, slow moving flow favorable for combustion. The hot products of this combustion expand through a turbine and out a nozzle to produce thrust. Eventually, as speed increases, the ram effect of the incoming flow suffices to compress the air for combustion eliminating the need for mechanical compressors. This compression provides the basis for ramjet engines. The air in a ramjet engine still decelerates to subsonic speed and to a higher pressure suitable for combustion. The flow then accelerates through a nozzle to provide thrust, but without the inefficiencies and mechanical complexity associated with rotating machinery. At even faster speeds, the high static pressures and temperatures that result from decelerating air above Mach numbers of approximately five to subsonic speeds for combustion may lead to molecular dissociation of the incoming flow and unacceptable material stresses. Scramjets provide one approach to achieving these higher speeds, where air decelerates for combustion yet remains supersonic through the entire engine. Refs. [1-2] provide an excellent overview of the mechanics and evolution of scramjet propulsion outlined above.

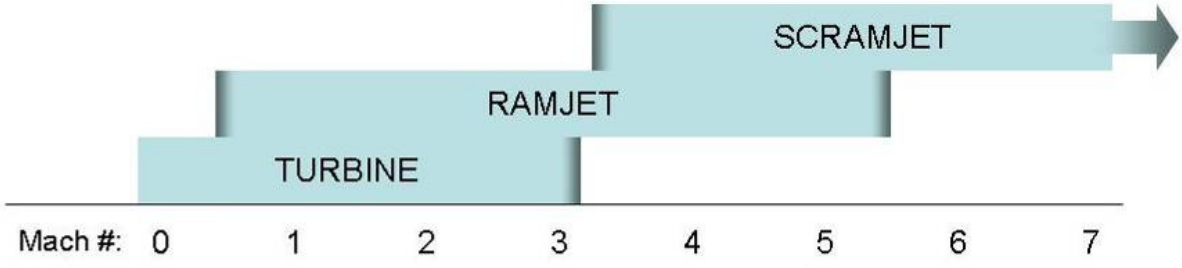

Figure 1. Approximate Mach number regimes

The idea of the supersonic combustion ramjet, or scramjet, has been studied for about 50 years [1]. Its predecessor, the ramjet was conceived in 1913 even before the turbojet [2:3]. With this much history, one wonders why the skies are not crowded with ramjets and scramjets. Ramjets cannot operate at low speeds which presents the problem of getting a ramjet-powered vehicle up to a sustainable speed. As speed increases, turbine engine performance decreases such that ramjet performance becomes superior, driving the desire for improved ramjet and scramjet designs. As speed increases further, ramjet performance gives way to the scramjet. Decreases in specific impulse as shown in Figure 2 clearly show these performance trends as well as the significant performance advantage of hydrogen fuel over typical hydrocarbon fuels.

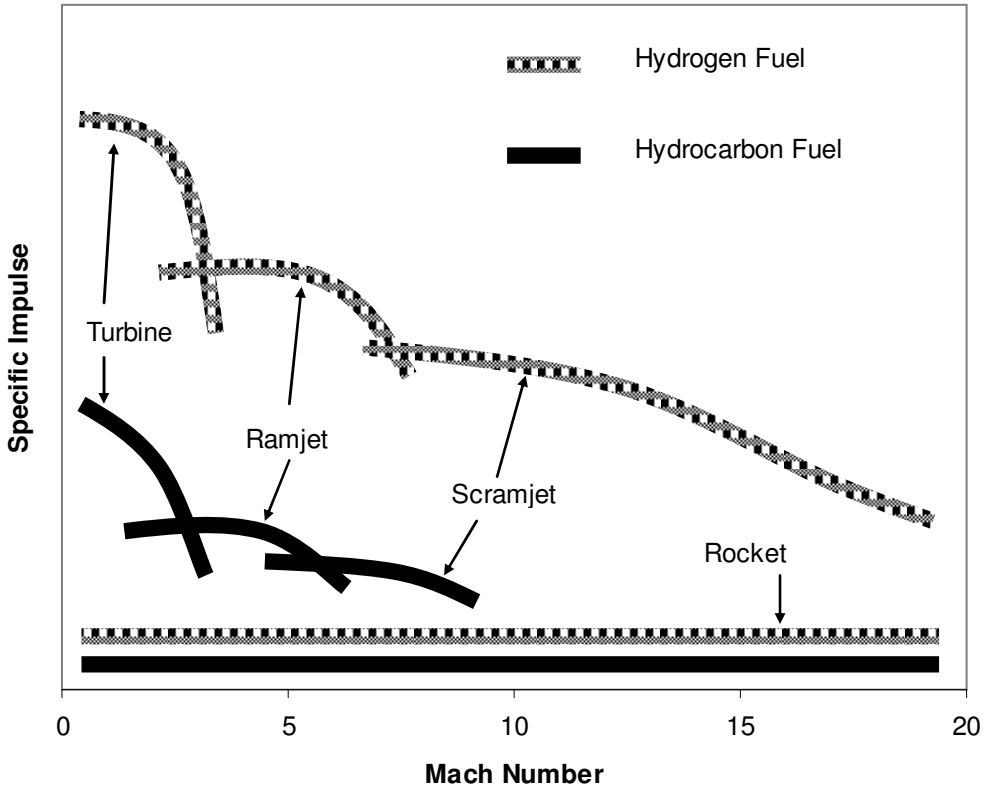

Figure 2. Air-breathing propulsion specific impulse trends [based on Ref. 3]

A variety of past and current programs in the United States and other countries around the world show the continuing interest in scramjet technology as a potential propulsion source in the hypersonic flight regime [4; 5; 6; 7; 8; 9; 10]. In order to provide propulsion at these high speeds, a scramjet must ignite and burn the fuel as quickly as possible, since residence time of the flow inside the engine is very short—on the order of a millisecond. Hydrogen fuel has very fast ignition, beneficial cooling properties, and a high heating value resulting in higher engine performance compared to hydrocarbon fuels. Unfortunately, the logistics of handling large amounts of cryogenic liquid hydrogen are formidable and the vehicle structure requires a larger vehicle volume for fuel storage contributing to aerodynamic limitations. Denser than hydrogen, hydrocarbon fuels allow for smaller vehicles and less drag for a given mass of fuel. The well established transportation and storage infrastructure for handling hydrocarbon fuel (e.g., JP-8), greatly simplifies logistics and vehicle storage problems. Unfortunately, hydrocarbon fuels have significantly longer ignition delay times, have a heating value less than half that of hydrogen, and lower flame speeds requiring longer engines. For example, at one atmosphere, stoichiometric hydrogen has an ignition delay time of about 0.01 ms compared to a typical hydrocarbon value of about 0.1 ms. The laminar flame speed for hydrogen is about 220 cm/s and for a typical hydrocarbon it is about 45 cm/s with the turbulent flame speed being about an order of magnitude higher for both [11:124, 140, 201]. Considering just the ignition delay for a one dimensional 500 m/s flow, the hydrogen will travel about 5 mm downstream before it ignites. The hydrocarbon fuel in the same flow will travel about 50 mm.

Flameholders can aid ignition and flame-spreading within the engine by providing distributed, stable energy sources. The US Air Force Research Laboratory Propulsion Directorate (AFRL/RZ) and Air Force Institute of Technology Department of Aeronautics and Astronautics (AFIT/ENY) have been studying the use of wall cavities as one potential flame holding solution. Flameholding is important regardless of the chosen fuel. However, the less robust combustion characteristics of hydrocarbon fuels compared to hydrogen drive a need for additional mechanisms to provide effective hypersonic propulsion. In addition to wall cavities, the use of pylons, struts or ramps either as injectors or simply as passive devices upstream of the cavity, such as vortex generators or spoilers, may improve combustor performance sufficiently for practical use of hydrocarbon fuels. Several studies have explored such devices in order to improve flameholding and flame spreading characteristics in scramjet engines [12; 13; 14; 15; 16; 17].

The addition of a pylon to the leading edge of a cavity flameholder should increase penetration of flameholder products into the main flow and improve flame-spreading, increasing use of available combustor volume [15; 16; 17]. Two significant problems arise with the installation of a pylon. First, the increased mass exchange between the cavity and main combustor flow will tend to drive the mean residence time in the cavity down which could eventually lead to a flameout [18]. Second, pylon-induced shocks and three-dimensional cavity flow will create hot-spots in areas of high static temperature and pressure, and have the potential to cause pockets of excessively lean or rich fuel-air mixture resulting in overall cavity combustion characteristics different than

those encountered in cavity-only research [15; 17]. Overly lean or rich regions in pylon-cavity flameholders may require direct fuel and/or air injection of the cavity [13; 15]. By characterizing the flowfield of the pylon-cavity flameholder, this study will provide the scramjet designer with data to maximize the potential increase in flameholder effectiveness while minimizing the problems inherent in the use of a pylon.

The literature contains significant data regarding cavity flows that form the basis for cavity flameholder design. However, the limited quantitative data of combined pylon-cavity flows generally focus on combustion and flow visualization, not overall flowfield characteristics of the pylon-cavity flameholder itself.

The terms *pylon* and *strut* have been used somewhat interchangeably in the literature. This paper will use the term *pylon* for a structure that does not span the combustor and will reserve the term *strut* for a device that spans the diameter of the combustor. SI or non-dimensional units are used in this study with two exceptions. First, documentation refers to the wind tunnel as the *6" x 6" Supersonic Wind Tunnel* and references to the *6" x 6"* wind tunnel are maintained as a naming convention. Second, dimensions for the test section and test article design and construction were specified in English units and engineering drawings remain in English units.

1.1 Scope of Research

This study contributes to the literature by characterizing the flowfield effects of locating a pylon ahead of a scramjet cavity flameholder. Figure 3 illustrates the upward flow of cavity fluid behind the pylon that will give scramjet designers a means of carrying reacting flameholder products into the main combustor flow. Effectiveness of the overall

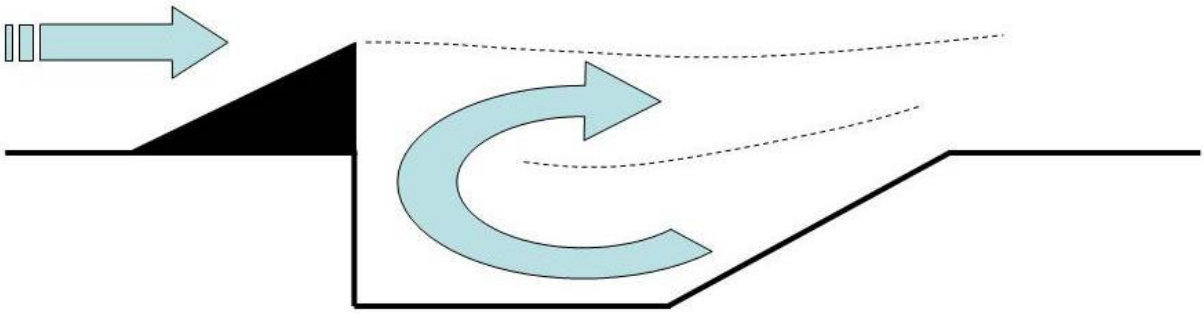

Figure 3. Illustration of pylon-cavity flow

concept depends on penetration of combustion products from inside the cavity out into the core flow improving flame spreading, mixing, and overcoming performance losses due to addition of the pylon. In fact, the flow structures and flameholder behavior observed in this non-reacting flow study were consistent with increased mass flow through the cavity with strong upward flow behind the pylon up into the core flow. Further contributions include exploration of Reynolds number effects on the pylon-cavity geometry as well as the design, construction and commissioning of an upgraded wind tunnel facility suited to wall-based wind tunnel research.

1.1.1 Thesis Statement *The addition of a pylon to the leading edge of a cavity flameholder will generate a flowfield that increases mass exchange between the cavity and main combustor flow, increases the mixing interface between flameholder products and main combustor flow, and exhibits minimal Reynolds number effects.*

1.1.2 Research Approach Both computational and experimental methods in parallel provided the data for this research. A simple computational fluid dynamics

model assisted in wind tunnel test section design and construction. Once wind tunnel commissioning was accomplished, a detailed computational model of the wind tunnel nozzle and test section was constructed. This detailed model complemented experimental results and provided a means of examining flow features that were difficult or impractical to acquire experimentally.

Wind tunnel data collection used a variety of tools, including surface pressure measurements, static and total pressure probe measurements, high-speed Schlieren/shadowgraph video flow visualization, and particle image velocimetry (PIV). These wind tunnel data combined with computational results form a comprehensive picture of the cavity-pylon flameholder flowfield.

1.2 Document Organization

The following sections of this dissertation are organized as follows:

Section II: Provides background on scramjets, cavity flow/flameholders and previous work on pylon-cavity flameholder behavior.

Section III: Describes the wind tunnel facilities, instrumentation and method used in acquiring the experimental data.

Section IV: Describes the computational fluid dynamics (CFD) method and computational domains used in calculating CFD results.

Section V: Presents the combined computational/experimental results in terms of flow structures, cavity behavior and Reynolds number effects.

Section VI: Summarizes the results of the current research and directions for future research.

II. Background

2.1 Scramjet Overview

This section will present a brief overview of supersonic combustion ramjet propulsion. It will address two general questions, i.e., what flight conditions drive the need for scramjet propulsion, and what components make up a scramjet engine?

Scramjets provide an airbreathing source of propulsion for hypersonic vehicles and typically operate at high altitudes with correspondingly high Mach numbers. Assume a typical, low hypersonic flight condition of $M = 5$ at 24.4 km (80,000 feet) above mean sea level. The ambient temperature and pressure are approximately 220 K (400 °R) and 2,800 Pa (0.41 psia). Considering the static pressure and temperatures that result from slowing a hypersonic flow down to subsonic speed, the need for supersonic combustion becomes clear. Applying a simple isentropic deceleration from $M = 5$ to a typical combustor inlet speed of $M \approx 0.3$ [19:395] gives some notable results.

By applying the isentropic relations to calorically perfect air at $M = 5$ at 24.4 km (80,000 feet) above mean sea level:

$$T_t = T_\infty \left(1 + \frac{\gamma - 1}{2} M_\infty^2 \right) \tag{1}$$

$$P_t = P_\infty \left(1 + \frac{\gamma - 1}{2} M_\infty^2 \right)^{\gamma/\gamma - 1} \tag{2}$$

the total temperature and pressure are determined to be 1300 K and 1480 kPa. At $M = 0.3$, the resulting static conditions rise to 1280 K and 1390 kPa. These temperatures are at or above the melting point of some common aerospace materials (aluminum melts at

approximately 930 K [20:4-133]). Even if suitable materials are used, the fuel will be severely limited in the amount of heat it can release due to thermal choking, molecular dissociation, or diminishing performance [2:68, 157, 435]. Faster flow through the engine, and therefore supersonic combustion, becomes necessary. If the flow in this idealized example slowed to $M = 2$, the resulting static conditions would be a much more benign 720 K and 190 kPa. The lower temperatures and pressures encountered using supersonic flow through the engine greatly ease the materials design problem. It also turns out that the pressure environment of a typical scramjet flow is well suited for hydrocarbon fuel combustion [21:12]. In addition, a limited range of dynamic pressure for practical hypersonic vehicle operations bounds the pressure loads on the engine.

Hypersonic vehicles operate over a limited range of dynamic pressure, and as noted in Ref. [2] tend toward a value of 47,880 Pa (1000 lb_f/ft^2). Below dynamic pressures of approximately 23,940 Pa (500 lb_f/ft^2) the wing area required for flight may become excessive, and above dynamic pressures of approximately 95,760 Pa (2000 lb_f/ft^2) drag and structural forces grow too high [2:38-39]. These approximate vehicle limits bound the environment that scramjet engines need to operate in.

The upper speed limit on scramjet engines results from the choice of fuel, internal fluid dynamics and external aerodynamics. The heating value of the fuel will limit the total available chemical energy to the engine, as well as the ignition and burning characteristics. Hydrogen enjoys a significant performance advantage over hydrocarbon fuels, as seen in Figure 2, and has a significantly higher heating value per mass (approximately 120,000 kJ/kg for hydrogen and 45,000 kJ/kg for typical hydrocarbon

fuels) [2:113]. However, the heating value per volume favors hydrocarbon fuels and allows for smaller, more aerodynamic flight vehicles (approximately 8,000 kJ/m^3 for hydrogen and 35,000-40,000 kJ/ m^3 for typical hydrocarbon fuels) [3]. This trade off in heating value between hydrogen and hydrocarbon fuel suggests that to take advantage of the higher density of hydrocarbon fuels, some means of enhancing the performance of hydrocarbon fuel in the scramjet engine requires consideration, such as more effective use of combustor volume. The cooling capacity of the fuel, in fuel-cooled engines, may drive the selection of materials or limit allowable flight Mach number to maintain acceptable engine temperatures [22]. Furthermore, in a hydrocarbon-fueled engine, fouling of fuel lines and cooling channels becomes a significant concern. Hydrocarbon fuel can leave deposits in lines through chemical reactions or through the thermal reactions that can provide additional heat sink capability and performance [3; 22]. In general the rate of deposition is proportional to temperature [3]. Different fuels also drive different storage mechanisms. For instance, liquid hydrogen fuel requires cryogenic storage with relatively large and heavy storage tanks which will adversely affect vehicle performance aerodynamically. Hydrocarbon fuels, on the other hand, are denser and storable at ambient temperatures allowing for smaller vehicles [2:507; 3; 22]. All of these fuel characteristics have significant effects on engine performance. Additionally, the internal fluid dynamics generated by engine components such as isolators, flameholders, injectors, etc., may lead to insurmountable overall losses or lead to local extremes of temperature and pressure at Mach numbers significantly different than the design Mach number of the engine.

Since the vehicle body will likely form part of the compression and expansion system of the engine, external aerodynamic and operational design choices may also limit the ability of the engine to produce thrust off-design. Complicating the design situation, the choice of fuel can greatly influence the external aerodynamics since the different densities and storage requirements of the fuel may impose severe volume and weight requirements. Lastly, as flight Mach number increases, total temperature and pressure of the decelerating air entering the engine rise exponentially, ultimately resulting in molecular dissociation, structural limitations, and limited available heat addition from the fuel before thermal choking [2]. For instance, at approximately 2000 K, the oxygen in the atmosphere begins to dissociate into atomic oxygen. This endothermic reaction is slower than the typical characteristic time of the flow through the engine and robs the overall flow of energy that might otherwise be available for thrust [2:49-50]. At a typical hypersonic cruising altitude, the total temperature of the oncoming flow reaches 2000 K at approximately $M = 6.4$, which indicates that dissociation becomes a consideration even at low hypersonic velocities.

The lower speed limit on scramjet engines largely results from the actual engine design, since as speed decreases other forms of airbreathing propulsion become more attractive. As Mach number decreases, static temperature and pressure of the air entering the scramjet engine combustor decrease which leads to increased ignition delay times and less robust combustion [2:325-326]. This study focuses on the lower end of hypersonic flight which presents a more difficult ignition environment for the scramjet designer.

This study focused on a combustor inlet Mach number of two which approximates a flight Mach number of about five. Ref. [2] presents this relationship as a design rule of thumb correlating flight and combustor inlet Mach numbers [2:159]:

$$M_{combustor} \approx 0.4 M_{flight} \tag{3}$$

Knowing the flight Mach number (M = 5), and accepting a middle range dynamic pressure of 47,880 Pa (1000 lb_f/ft^2), the ambient pressure, and therefore mean altitude may be determined using [2:37-39]

$$q_\infty = \frac{\gamma}{2} P_\infty M_\infty^2 \tag{4}$$

In this example, the resulting ambient pressure is 2740 Pa, which occurs near 24.4 km (80,000 feet) above mean sea level. The preceding argument provides the basis of the flight condition used in this study: M = 5 at 24.4 km (80,000 feet). Higher flight Mach numbers require less robust flameholding since the temperature and pressure within the engine can cause the fuel to auto-ignite [2:326; 18].

Scramjet engines produces thrust in much the same manner as other air-breathing engines. The basic functions (compression, combustion, expansion) of other air breathing engines still exist, but are implemented differently than in slower speed propulsion systems, such as the turbojet or turbofan. In fact, to achieve a positive net thrust a scramjet engine will likely integrate more closely with the airframe than lower speed propulsion systems such that the airframe itself will form part of the compression and expansion systems. The remainder of this section explores the various scramjet

component and system functions. Four major sections of the scramjet engine designated by the numbering shown in Figure 4 are the inlet, isolator, combustor, and nozzle [2:151].

As in other air-breathing propulsion systems, the oncoming air requires compression for efficient combustion. In the case of the scramjet, the compression can occur in two different phases. First, the shock wave generated from the motion of the vehicle through the air will provide some degree of external compression. Second, a converging inlet will serve to provide the remaining required compression internally. The use of the internal and external compressions highlights the need for a tightly integrated engine and airframe.

A constant area duct ahead of the scramjet combustor section called an isolator contains the shock-train that results as the inlet static pressure increases to the combustor static pressure. An isolator too short for the amount of static pressure rise due to combustion leads to the leading edge of the shock train in the isolator moving upstream until an approximately normal shock forms ahead of the inlet. The resulting unstart, with

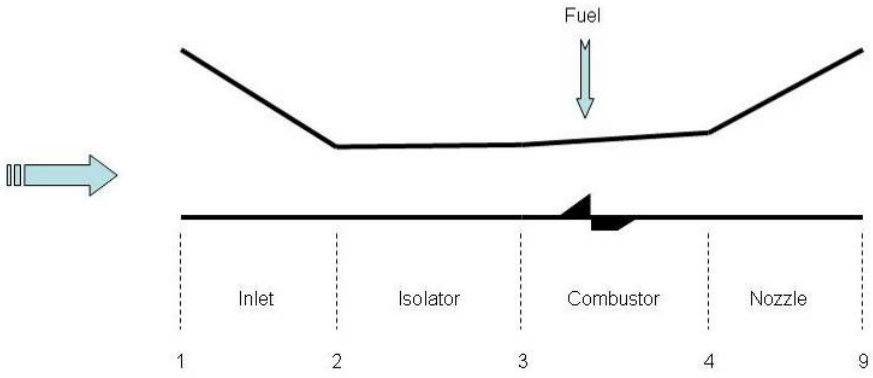

Figure 4. Scramjet engine reference stations

associated loss of mass flow and increased pressure losses, will result in loss of thrust and may cause significant transient structural loads [2:250-254].

The combustor itself contains the fuel injectors and flameholders and designates the region where combustion begins. This section of the engine contains the focus of this study in the hope that by improving the flameholding within the engine, a shorter combustor with improved performance results. A more detailed discussion on flameholders follows in the next section.

The nozzle in a scramjet engine provides the surface for the expanding flow to act against and produce thrust just like rocket or turbine engines. Unlike turbine engines there may be a significant amount of external compression or expansion where the vehicle body acts as part of the propulsion system similar to the two regions of compression discussed earlier. Also, with the very short residence time in a scramjet, burning will likely continue out of the combustor and through the nozzle.

2.2 Cavity Flameholders

The ignition of fuel within the engine requires appropriate temperature, pressure, equivalence ratio, and sufficient residence time for the combustion reaction to occur. The flameholder minimizes the ignition delay time, and therefore combustor length, required for initiating and sustaining combustion within the engine [18]. Any component that provides a zone with a flow velocity small enough for effective mixing and for the flame to stabilize can work as a flameholder. Common flameholders include the v-gutter commonly found in turbine afterburners or a simple step, found on some scramjet designs and represented in Figure 5. Flameholders provide a turbulent recirculation region where

combustion can take place with fuel and air entrained from the main flow. If the recirculation region entrains an appropriate fuel-air mixture a stable flame should burn and provide a constant ignition source. The incorporation of the flameholder in the combustor design must thoroughly minimize drag [23:258-259].

Cavity flameholders, similar to the simple rectangular cavity shown in Figure 6, present a potential low-drag flameholding solution. Both step and cavity flameholders rely on recirculation behind a discontinuous step in the combustor surface. However, the step design suffers from higher drag and stagnation pressure losses than the cavity design [18]. Both faces of a cavity experience similar static pressures greatly reducing, or eliminating, the pressure drag of the step flameholder [21:18]. Also, the total temperature within the cavity can approach the freestream total temperature allowing the cavity flameholder to take better advantage of the energy in the oncoming flow [13].

Cavity flameholders alone provide a relatively low drag recirculation region where fuel and air can react and provide a stable flame source. Without a flameholder,

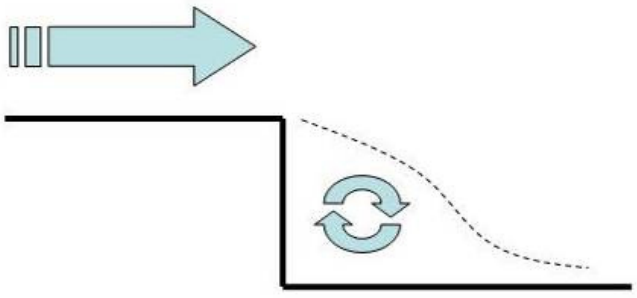

Figure 5. Step flameholder

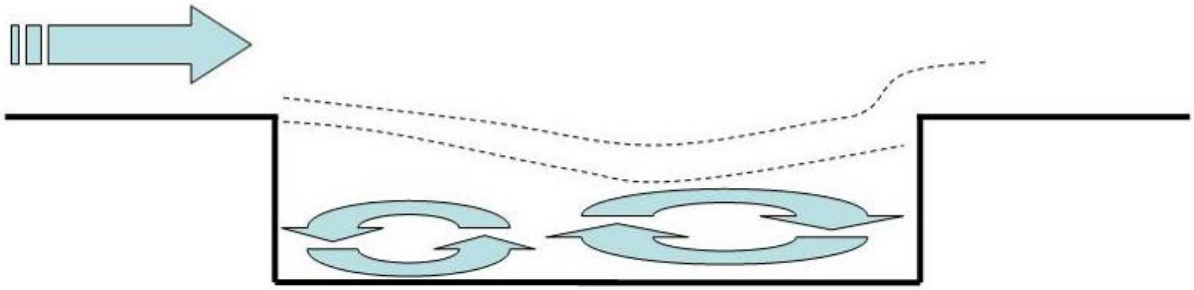

Figure 6. Rectangular cavity flameholder

the length of the combustor would need to account for the ignition delay time of the fuel. The ignition of hydrocarbon fuel in a supersonic combustor may take a significant distance since the ignition delay of hydrocarbon fuels is on the order of 1 millisecond [11]. Thrust-to-drag ratio is roughly proportional to the ratio of combustor diameter and combustor length making shorter engines highly desirable [24]. If the cavity residence time is equal to or greater than the ignition delay, a stable flame can exist within the flameholder enabling a shorter combustor.

Cavity flows can be classified as either open or closed based primarily on their length-to-depth ratio (L/D). A shear layer forming at the leading edge of the cavity and then reattaching on the downstream wall of the cavity characterizes open cavity flow as seen in Figure 7. The shear layer over a closed cavity, on the other hand, reattaches to the floor of the cavity. Significantly higher drag results from the flow encountering the downstream wall in closed cavities, which favors the use of open cavities as flameholders. The actual transition from open cavity to closed cavity depends on the overall flow, but typically occurs as the L/D increases past ten [18]. Some of the factors

influencing the cavity flow include geometry and freestream Mach number [25]. The incoming boundary layer will greatly influence the shear layer that forms above the cavity, but otherwise Reynolds number has a minimal effect on cavity-only flows.

The shape of the cavity has probably the strongest effect on cavity flow characteristics. Open cavities with L/D greater than about 2-3 have two large counter-rotating vortices similar to Figure 6 dominating the cavity flow [18]. Reverse flow velocities along the floor of the cavity may be very high. For example, Ref. [26] noted reverse flow velocities along the floor of the cavity up to about 40% of the free-stream velocity magnitude for a Mach 2 free-stream flow. Rectangular cavities are prone to unsteady flow due to acoustic disturbances caused by the shear layer impinging on the downstream wall and by periodic mass exchange with the main flow as the disturbed shear layer moves up and down [27; 28].

When the shear layer impinges on the downstream wall of the cavity, a pressure wave may form, travel upstream at the local speed of sound, and reflect off the leading edge of the cavity. As the pressure wave reflects off the leading edge, it produces a

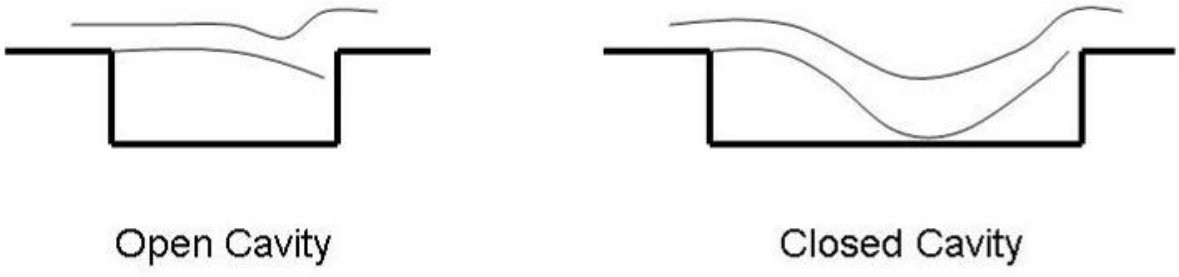

Figure 7. Cavity classifications

vortex structure within the shear layer that travels downstream at the convective velocity. The convective velocity, U_c, is the velocity at which large-scale structures within the shear layer travel downstream and is discussed in more detail later. When this vortex reaches the downstream wall it creates another pressure wave closing the loop [25; 29]. This oscillating structure causes the shear layer above the cavity to lift up resulting in unsteadiness in the overlying flow [29]. The shear layer moving up at the downstream edge allows mass to exit the cavity, and immediately followed by mass entering the cavity when the shear layer moves down below the downstream edge. This flapping of the shear layer results in the periodic mass exchange at the downstream edge of the cavity [27; 28]. Traveling disturbances of the shear layer can be quite large as demonstrated in Ref. [26] where the shear layer oscillated upward a distance equal to about 40% of the cavity depth. An empirical relation for estimating the frequencies of pressure oscillations in a rectangular cavity flow [28] and subsequently modified to account for compressible flow [30] is

$$f = \frac{U}{L}\frac{(m-\alpha)}{\left(\frac{1}{K}+M\left(1+\frac{\gamma-1}{2}M^2\right)^{1/2}\right)} \tag{5}$$

where U is the *duct velocity*, L is the *cavity length*, m is the *mode number*, α and K are empirical constants and M is the *tunnel Mach number*. Ref. [28] concluded $\alpha = 0.25$ and $K = 0.57$ for an $L/D = 4$ cavity, although research in Ref. [31] found that $\alpha = 0.1$ fit the data better for a slightly longer cavity. Ref. [28] further explained that K is the ratio of the speed at which the shear layer disturbances move downstream to the free stream velocity,

i.e., $K = U_c/U$. The first three mode frequencies for $\alpha = 0.25$ and $\alpha = 0.1$ are presented in Table 1. Equation 5 only estimates the frequencies for each mode and does not include any prediction on the amplitude of each mode. Experimental data show that as free-stream Mach number increases, the size of the large-scale structures within the shear layer decreases [29].

Table 1. Rectangular cavity oscillation frequencies

(U = 500 m/s, L = 10 cm, M = 2, K = 0.57)

mode	f (Hz) $\alpha = 0.25$	f (Hz) $\alpha = 0.1$
m = 1	861	1198
m = 2	2330	2530
m = 3	3158	3862

High convective Mach numbers significantly inhibit the growth of turbulent shear layers and the effectiveness of the turbulent mixing within them [32; 33]. The convective Mach number is defined as the Mach number in a frame of reference that moves within the shear layer at the speed of the dominant structures or waves, i.e., the convective velocity, U_c. The convective velocity may be approximated by the speed of sound weighted average, assuming $\gamma_1 = \gamma_2$ [33]:

$$U_c = \frac{a_2 U_1 + a_1 U_2}{a_1 + a_2} \tag{6}$$

where U_1 and a_1 are the *velocity* and *sound speed* above the shear layer (high-speed side), and U_2 and a_2 represent the flow below the shear layer (low-speed side). The convective Mach number on the high speed side of the shear layer is defined as:

$$M_{c1} \equiv \frac{U_1 - U_c}{a_1} \tag{7}$$

Convective Mach numbers may also be calculated below the shear layer. Shear layer growth decreases asymptotically to about 20% of the incompressible value as the convective Mach number approaches one [33; 34]. Since the convective Mach number associated with a scramjet flameholder is likely high, additional mixing mechanisms such as pylons become desirable.

Inclining the rear wall downstream, as seen in Figure 8, allows the shear layer to smoothly reattach thereby reducing the magnitude of the unsteady effects associated with rectangular cavities [18; 27]. However, even with an inclined downstream wall, oscillations of the shear layer remain possible [21:134-136; 35]. Other effects within the flameholder may even further reduce unsteady fluctuations. For instance, fuel injection upstream of the cavity has been shown to reduce cavity instability [36]. Additionally, the heat addition due to combustion may suppress cavity instabilities seen under cold flow conditions [37].

In addition to reducing pressure fluctuations, inclining the downstream wall results in slightly increased drag and mass exchange rate [38; 39]. Inclining the downstream wall also exposes more of the downstream wall to the oncoming flow increasing drag. Ref. [39] presented data in a $M = 2.9$ flow showing cavity drag

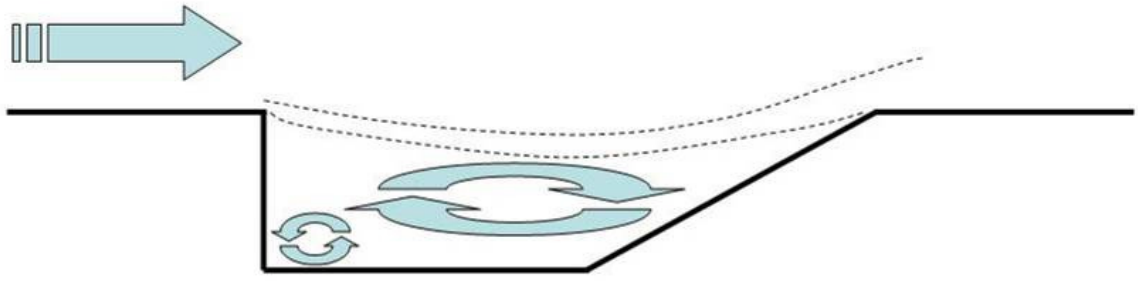

Figure 8. Inclined cavity flameholder

coefficient increasing approximately 13% (0.0028 to 0.0032) when decreasing the downstream wall angle from 90 degrees to 30 degrees. Combusting flow would at least partially offset this added drag since the top of the shear layer has been shown to rise up in combusting flow [40]. A large vortex oriented span-wise across the cavity dominates the inclined cavity flow. This large span-wise vortex governs the mass exchange between the cavity and main flow. A smaller counter rotating vortex may form along the bottom of the upstream cavity wall [21:119; 38; 39]. These vortices provide a zone for the fuel-air mixture to ignite and form a stable flame. Ongoing research has examined these vortices in an attempt to improve flameholding and ensure sufficient cavity residence time to counter the increased mass exchange driven by inclining the downstream wall of the cavity [13; 38; 39]. The overall flow in the cavity may appear dominated by two-dimensional effects, but the flow remains three-dimensional. Stream-wise vortex structures form off the side wall and produce a non-uniform pressure distribution along the downstream wall. This effect was computationally presented in Ref. [27] and also noted in an experimental injection study in Ref. [13].

References [38-39] present computational and experimental results for various cavity configurations supporting the above cavity flow characteristics. Computational results shown in Figure 9 for an $M = 3$, Re = 51 x 10^6 m^{-1} flow over an $L/D = 3$, 30 degree inclined cavity [38] clearly show the dominant spanwise vortex and the smaller upstream corner vortex. The computational model in Ref. [39] solved the two-dimensional, Reynolds-averaged Navier-Stokes equations using the same k-ω shear stress transport (SST) turbulence model used in the present study. At approximately $M = 2.9$ and Re = 66

Figure 9. Computational streamlines for M = 3, Re = 51 x 10^6 m^{-1} flow over an L/D = 3, 30° inclined cavity flameholder [38]

x 10^6 m^{-1}, the flow conditions were slightly different, but with results consistent with Ref. [38]. In addition to the overall flow characteristics, such as the spanwise vortex, Refs. [38-39] also presented an inverse relationship between cavity mass exchange and cavity residence time. In order for the flameholder to function effectively, the residence time must remain high enough for a stable flame to burn in the flameholder, yet sustain sufficient mass exchange to provide a steady source of fresh air and/or fuel. Cavity flameholders tend to become fuel-rich, or at least contain significant fuel-rich regions [38; 41], highlighting the importance of balancing sufficient mass exchange with the main combustor flow and the increased residence time required for hydrocarbon combustion.

The goal of a cavity flameholder is to increase the residence time of the fuel-air mixture and reduce engine length and drag. Open cavities such as the one under study tend to have less mass exchange with the main flow compared to closed cavities [38]. Cavity shape alone appears to have little effect on residence time or mass entrainment [39]. Residence time is primarily driven by cavity depth since a deeper cavity has a larger volume and therefore contains more mass for a given density. Longer cavities also have increased volume which increases residence time, but higher mass exchange due to the

larger area exposed to the free-stream flow decreases residence time. As a result, length has little effect on residence time. The inclined cavity has a lower residence time when compared to the rectangular cavity of the same L/D ratio due to the higher entrainment caused by the shear layer moving lower into the cavity [38; 39].

Shock and expansion waves caused by the cavity flow correspond to three primary cavity flow characteristics: flow changes at the leading edge of the cavity, flow impinging on the downstream wall or ramp, and shear layer structures caused by unsteady flow within the cavity. When the flow encounters the leading edge of the cavity and separates, it may cause a compression or an expansion wave depending on the angle the shear layer makes with the incoming duct [34; 38]. In general, a longer cavity is more likely to have a leading edge expansion than a shorter cavity due to the flow deflecting deeper into the cavity. In contrast, when the supersonic flow encounters the downstream wall of the cavity a compression wave will always result. Waves outside the cavity are a prominent visual feature of unsteady flow within the cavity and are caused by disturbances within the shear layer. Shocks may form off large scale structures in the shear layer directly or may also form as a result of the displaced shear layer due to unsteady pressure in the cavity [26; 29]. Waves caused by an oscillating shear layer may be characterized by curved waves originating at the shear layer. Several research teams have captured these curved waves in shadowgraph images [26; 29; 38].

Though cavity flameholders provide a steady source of ignition, cavity combustion products generally remain near the floor of the combustor. Assuming a

uniform and suitable equivalence ratio and a main flow parallel to the cavity, the flame spread in natural flame convection can be estimated by (see Figure 10):

$$\text{spread angle} = \sin^{-1}\left(\frac{u_f}{U}\right) \tag{8}$$

where u_f is the *turbulent flame speed* and U is the *flow speed*. For example, a typical hydrocarbon turbulent flame speed is about 4.5 m/s (about an order of magnitude above the laminar flame speed) [11]. In a 500 m/s flow, the spread angle is about a half degree. Thus, even with effective flameholding the flame will remain near the combustor wall as seen in previous research [42]. The spread angle of hydrogen under similar circumstances is approximately 2.6 degrees.

Assuming a cavity flameholder successfully ignites an oncoming fuel-air mixture in the main combustor flow parallel to the cavity, a hydrogen flame growing from the leading edge of the cavity will grow at four times the rate of a hydrocarbon flame. In order for a hydrocarbon fueled engine to take advantage of more of the combustor volume, some mechanism, such as a pylon at the flameholder leading edge, must be

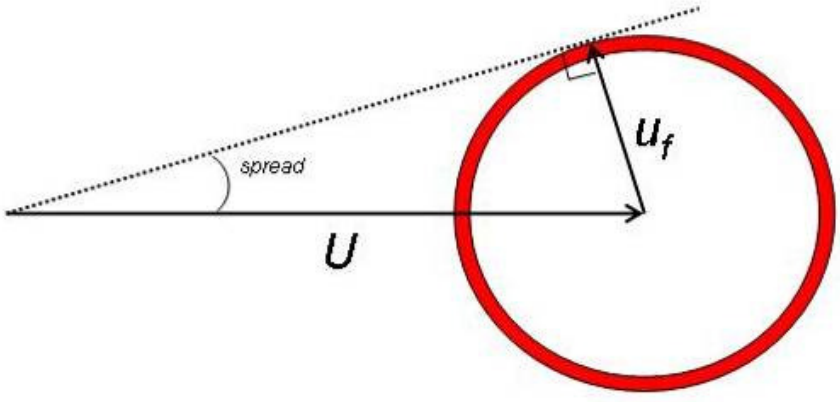

Figure 10. Flame spread geometry

installed. For example, a 5 cm high, 1 cm wide pylon upstream of a 10 cm wide cavity will approximately double the area growth rate of the hydrocarbon flame within the engine (not including the area directly in the pylon wake) enabling a significantly shorter engine than the cavity-only, hydrocarbon fueled engine. Considering the inverse proportion of engine thrust-to-drag and engine length, the addition of a leading edge pylon in this idealized example should provide a nearly 100% improvement in engine thrust-to-drag ratio. Thus, while hydrocarbon fuels cannot match the combustion characteristics of hydrogen, the use of a pylon in combination with a cavity flameholder should provide a means of significantly enhancing the use of available combustor volume, providing for a shorter engine and improving performance.

2.3 Cavity-Pylon Flameholder

Intrusive devices can enhance the interaction between a cavity-based flameholder and a fuel-air mixture in the core flow [14; 43; 44]. A pylon placed at the leading edge of the cavity provides such a mechanism by increasing the mass exchange between the cavity and freestream [16] and improving mixing due to pylon vortex/shock interactions [44]. Low pressure behind the pylon draws fluid out of the higher pressure cavity and into the main flow which leads to increased mass exchange between the cavity and main flow compared to a cavity-only case [15; 16] (see Figure 11). Supersonic expansion at the pylon edges, as represented in the two-dimensional example in Figure 12, results in low pressure behind the pylon [45:174-183]. The pressure differential between the cavity and pylon base should result in a flow of cavity fluid upward behind the pylon. This upward flow will lie between a pair of streamwise counter-rotating vortices that form as

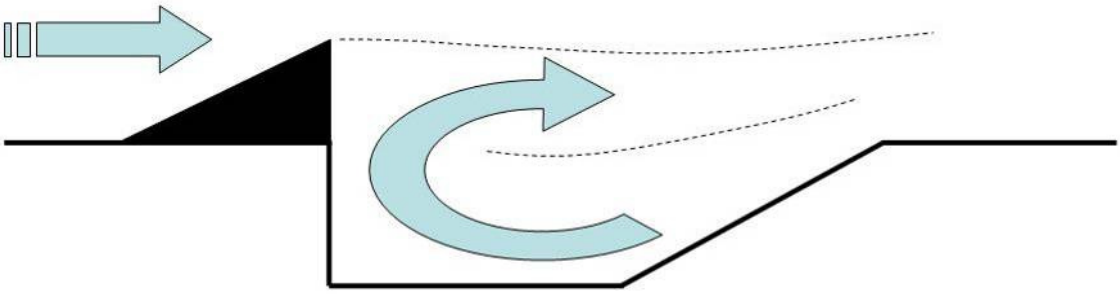

Figure 11. Cavity flameholder with inclined downstream ramp and leading edge pylon (on centerline)

the flow over the top of the pylon spills over each side. The vortices generated by a ramp fuel injector produce a similar effect. This additional streamwise vorticity should enhance mixing of the fluid behind the pylon and the main flow [2:309; 46].

While the use of pylons to specifically induce flow out of a cavity flameholder has only recently been explored [15; 16; 17], pylons, ramps and struts as combustor enhancements have been the focus of several research efforts [14; 43; 44; 47; 48; 49]. More specifically, Refs. [14; 47; 48] demonstrated improved fuel penetration and mixing of wall-injected fuel into the low-pressure region behind small pylons upstream of the fuel injectors. In addition to the improved penetration of fuel into the main combustor flow, these studies noted improved mixing due to axial vorticity shed off the pylons. In addition to the improved penetration and mixing behind the pylons, Ref. [48] presented data showing no significant total pressure losses from the addition of small pylons (approximately 1 cm high) with sharp leading edges ahead of the fuel injectors. Pylon fuel injection ahead of step flameholders has been shown to sustain methane combustion [50]. Ref. [51] explored the use of wedge fuel injectors alone or ahead of a cavity and

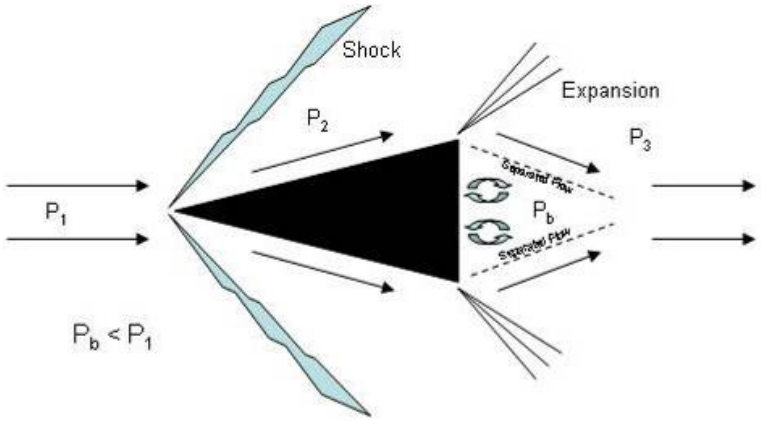

Figure 12. Two-dimensional pylon shock/expansion system

showed improved combustion characteristics of ethylene fuel with the cavity placed behind the wedge fuel injector.

Increased mass exchange will tend to reduce the overall residence time in the cavity resulting in a design limitation for the engine designer since it may drive the operating and ignition envelope [15]. The increased mass exchange due to the pylon has an effect similar to increasing the length of an open inclined cavity [39], but probably more pronounced due to the intrusive interaction of the pylon with the main flow. The improved penetration of flameholder products into the main flow will enable the use of a larger volume of the main flow for combustion, although the reduced residence time must be accounted for. Drag is a concern; however, static pressure rise due to combustion behind the pylon should at least partially offset the pressure drag increase from adding the pylon to the cavity flameholder [44].

Experimental data in Ref. [52] showed adding a strut ahead of a cavity flameholder resulted in more stable combustion. The increased mass exchange due to the pylon induced flow should contribute to steadier flow since mass can leave the cavity

behind the pylon at a more or less constant rate instead of through the shear layer oscillating up and down at the rear of the cavity. Even relatively small rectangular spoilers placed spanwise ahead of a cavity disturbed the flow ahead of a cavity resulting in significantly reduced pressure fluctuations in a rectangular cavity, although oscillation frequencies were unaffected [28]. Ref. [12] noted possible oscillations of the shear layer near the ramps of a ramp mixer ahead of a step flameholder. Therefore, it seems reasonable that fluctuations may remain after the addition of a pylon to the cavity flameholder, although at a greatly reduced magnitude.

The pylon wake and the cavity shear layer will interact. The shear layer should progressively grow out of the cavity in the vicinity of the wake due to the lower velocity of the pylon wake flow. The cavity shear layer should grow nearly linearly and the wake should grow proportional to the square root of the downstream distance [53:485]. The combined mixing layer/wake should eventually present a raised shear layer to the oncoming flow such as shown in Figure 13. This combined pylon wake and cavity shear layer will present a larger interface between the oncoming flow and flameholder products than a cavity flameholder without the pylon. Since the growth rates differ and the flow will interact with the side walls, the proportions of the profile will likely change as the flow progresses downstream.

Extrapolating from Ref. [14], by transporting fuel-rich combustion products from within the cavity, there may be a larger region above the cavity with suitable conditions for combustion. Ref. [14] also noted the pylon ahead of the cavity configuration may also

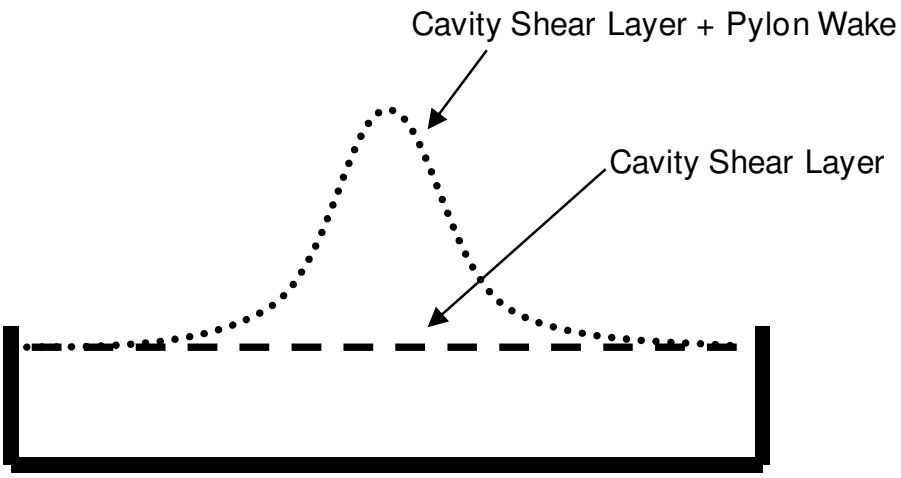

Figure 13. Comparison of cavity shear layer and cavity shear layer plus pylon wake

lift the shear layer. Additionally, the shocks off the pylon may further enhance mixing in the shear layer as they reflect off the duct walls and over the cavity [46].

Adding a pylon to a cavity flameholder will create strong shocks within the combustor section of the engine. An oblique or bow shock will form off the leading edge of the pylon reflecting off the duct ceiling and wall. Expansion waves will form at the back of the pylon. The reduced pressure behind the pylon due to the expansion should draw higher pressure cavity fluid up the rear of the pylon and into the pylon wake which should significantly increase the volume of reacting products within the main flow. The pylon waves and reflections will interact with the waves due to the cavity and will result in a complex three-dimensional flow field downstream of the pylon. Since shocks are an inevitable result of using a pylon with the cavity flameholder, the shock system in a final design should be *tuned* to enhance mixing in the flameholder and throughout the combustor section.

Addition of a pylon to a cavity-based flameholder should enhance the interaction of the flameholder and fuel-air mixture in the main combustor flow. The effects just discussed should provide a mechanism by which hydrocarbon fuels can provide sufficient performance for useful scramjet operations without the burden of the complex fuel logistics and airframe design issues associated with hydrogen fuel. Knowledge of the characteristics of the overall pylon-cavity flow will provide a previously unavailable tool for the scramjet researcher to enhance the effectiveness of scramjet combustor designs.

III. Experimental Approach

This section presents the facilities and procedures used in the experimental portion of the study. Data with and without the pylon installed were collected for comparison purposes. A range of Reynolds numbers provided an initial look at any scale effects that might exist affecting the pylon-cavity flowfield. The limited wind tunnel data combined with the computational fluid dynamics (CFD) data (discussed in the next section) allowed a more complete picture of the flow features of the pylon-cavity flameholder in a non-reacting flow. Wind tunnel operations techniques, lab procedures and detailed hardware drawings are provided in Appendix A.

3.1 Wind Tunnel and Test Section

Testing was accomplished in the AFIT 6" x 6" Supersonic Wind Tunnel, shown in Figure 14. The tunnel is a blow-down type tunnel built by Aerolab, capable of Mach numbers from 1.4 to 4.0. A lower sliding block nozzle with contours based on Ref. [54] provides the ability to adjust Mach number. Air for the tunnel is stored in a 22.7 kiloliter (800 cubic foot) tank at up to 1380 kPa (200 psi) and provided by two 37.3 kW (50 hp) compressors (Ingersoll-Rand UP6-50PE-200) with two desiccant-type dryers (Donaldson AHLD-350). Dew point measured downstream of the dryers is below -40 °C. A perforated steel disc inside the upstream end of the stagnation tank evenly distributes the supply flow across the stagnation tank. Additionally, three stainless steel screens installed in the stagnation tank enhance flow uniformity [55]. A pressure regulator installed immediately upstream of the stagnation tank held mean tank pressures to within approximately 3% of the target pressure. In order to have a statistically significant

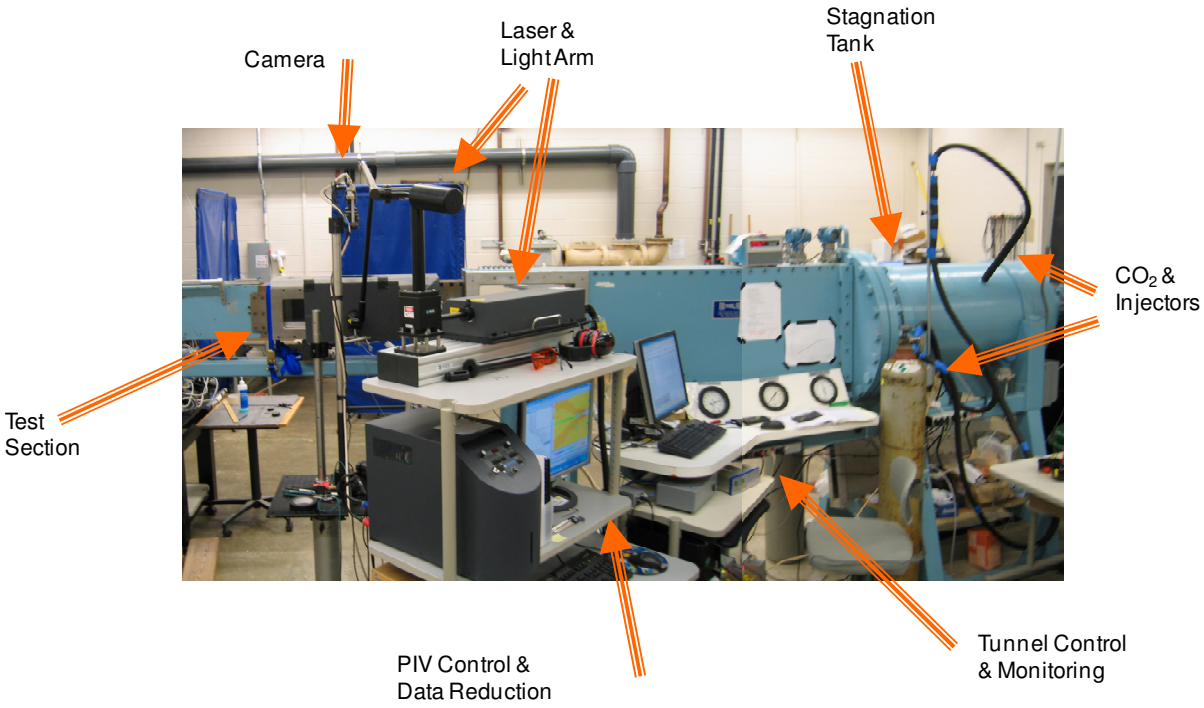

Figure 14. AFIT 6" x 6" Supersonic Wind Tunnel

number of samples, conditions were considered stable for data collection when stagnation pressure (P_t) was within 10% of peak pressure for each run. Stable run times varied with stagnation pressure from approximately 15 seconds at P_t = 248.2 kPa (36 psia) to approximately 8 seconds at P_t = 427.5 kPa (62 psia) with M = 2. Supply temperature was not controllable and varied between approximately 260 K and 300 K over the course of the study. Stagnation temperature varied approximately +/- 3% during data runs and, therefore, Reynolds number also varied by approximately +/- 3% for a given stagnation pressure setting. Figure 15 presents a typical run stagnation tank temperature and pressure time history.

Two effects limited the range of stagnation pressures, and therefore Reynolds numbers, during wind tunnel operations. First, excessive vibration of the entire tunnel

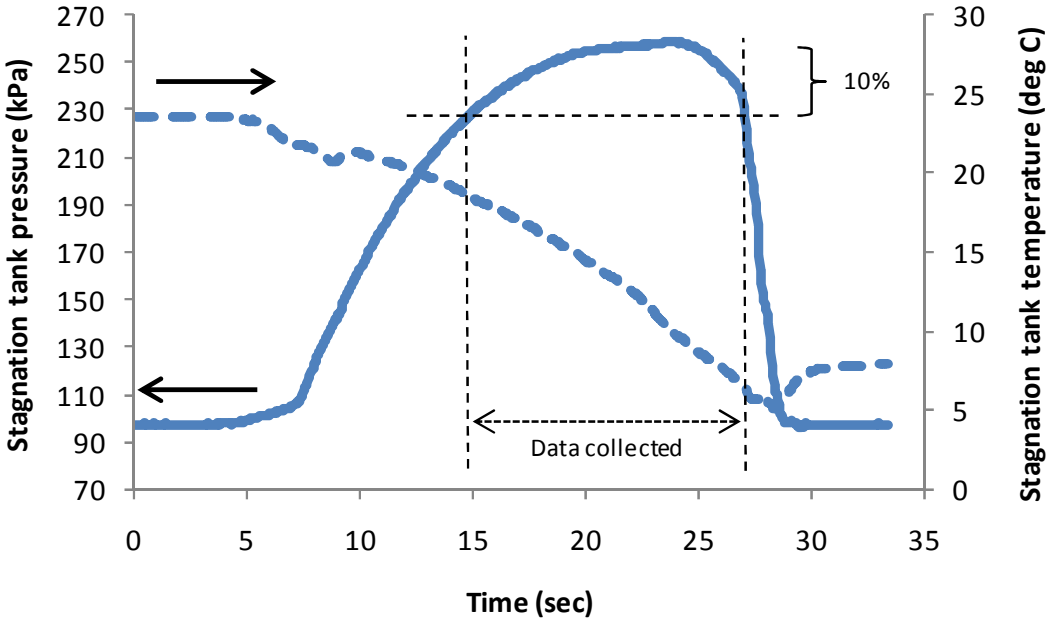

Figure 15. Stagnation tank pressure and temperature traces (stagnation pressure setting = 241 kPa, peak stagnation pressure = 258 kPa)

began to develop above stagnation pressure settings of approximately 517.1 kPa (75 psia). These vibrations intermittently disrupted writing data to hard drives in the laboratory computers. Second, the pressure regulator could not respond fast enough to achieve stagnation pressures significantly above 448.2 kPa (65 psia). As a result of the pressure regulator characteristics, the pressure achieved in the stagnation tank did not equal the pressure setting. The four test conditions chosen for this study are listed in Table 2 along with the associated variability in stagnation pressure and Reynolds number. The variability in conditions from run to run was attributed to the inability to control temperature. The regulator calibration, detailed test conditions and additional details are presented in Appendix A.

The range of stagnation tank pressure in the wind tunnel testing was limited from approximately 241.3 kPa to 448.2 kPa (35 psia to 65 psia). As previously discussed in

Table 2. Wind tunnel test conditions (M ≈ 2)

Condition	Stagnation pressure setting (kPa / psia)	Mean stagnation pressure (kPa / psia)	Standard deviation of stagnation pressure (kPa / psia)	Mean Reynolds number (m^{-1})	Standard deviation of Reynolds number (m^{-1})
1	241.3 / 35	248.2 / 36	6.1 / 0.89	3.2×10^7	1.2×10^6
2	379.2 / 55	324.1 / 47	9.0 / 1.30	4.2×10^7	1.3×10^6
3	517.1 / 75	372.3 / 54	5.9 / 0.85	4.9×10^7	1.5×10^6
4	655.0 / 95	427.5 / 62	7.6 / 1.10	5.5×10^7	2.5×10^6

Section II, the approximate flight condition represented in this study is $M = 5$ at 24.4 km (80,000 feet) above mean sea level. Temperature for this study didn't represent a realistic flight condition due to wind tunnel limitations. A representative static temperature entering the combustor section would exceed 700K, but typical wind tunnel temperatures approached 280 K. The resulting unit Reynolds numbers were approximately three times higher than a flight representative condition.

The original wind tunnel was modified by inserting a new, more accessible test section, seen in Figure 16, downstream of the original test section. The test section provided a 86.4 cm (34 in) long, constant area duct with internal dimensions of 15.2 cm by 16.5 cm (6 in by 6.5 in) and had optical access through the top and both sides. Although the internal duct dimensions do not match precisely, documentation refers to the *6" x 6" Supersonic Wind Tunnel* [55]. A removable side window allowed the insertion of a mounting plate for probe measurements. The test section floor accommodated access to the test article for surface pressure tap tubing, pressure transducer wiring and PIV seeding.

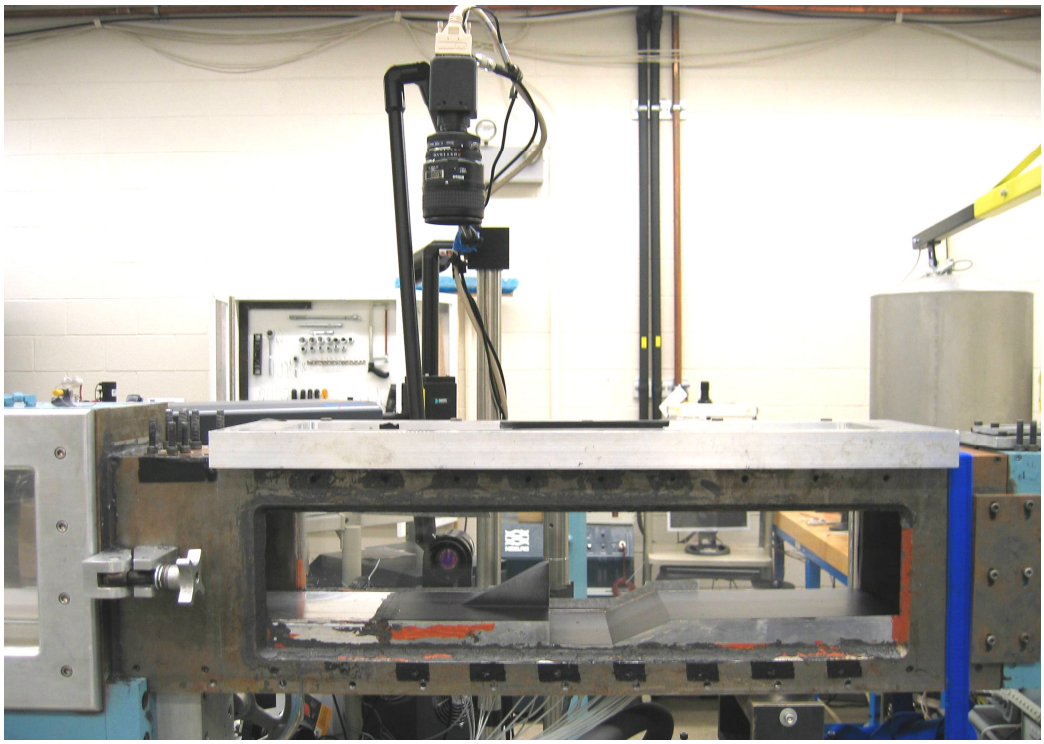

Figure 16. AFIT 6" x 6" Supersonic Wind Tunnel add-on test section with pylon installed and configured for PIV (near-side window and probe plate removed)

Limited probe data across the entrance of the test section (x = -22 cm, y = 3.7 cm) shown in Figure 17 show non-uniform flow, but generally good agreement between the CFD and probe measurements. The boundary layer on the $-z$ side of the test section appears slightly thicker resulting in a small velocity gradient from one side to the other ($dM/dz \approx 0.008\,\text{cm}^{-1}$). Also, a slight velocity deficit on centerline led to a higher centerline pressure measured on the downstream ramp of the baseline cavity.

The test article geometry was based on previous work at AFIT and AFRL [13; 14; 38; 40; 42; 43] and selected to clearly show the various flow features, but not optimally designed to minimize drag losses. The downstream face of the pylon is flush with the cavity step and rectangular in shape, resulting in a flat, triangular top face as shown in

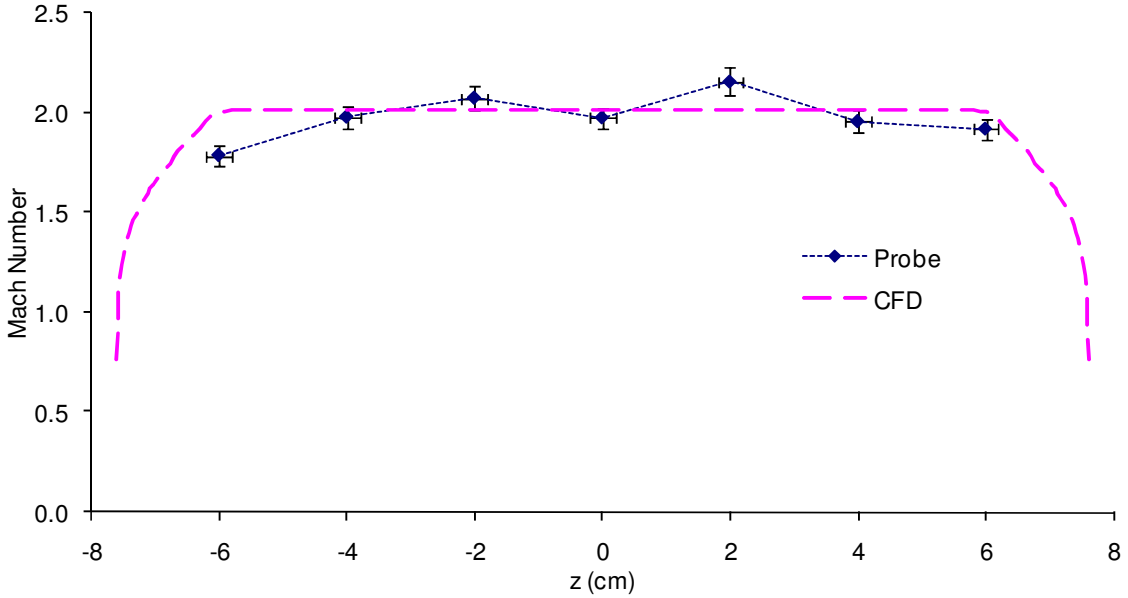

Figure 17. Mach number profile across the test section entrance (x = -22 cm, y = 3.7 cm; Re ≈ 32 x 10^6 m^{-1})

Figure 18. This design provides a simple geometry to study flow traveling from the cavity into the core flow. The cavity depth (D) is 2.54 cm (1 inch) and the length (L) is 10.16 cm (4 inches). The test section duct is 15.24 cm (6 inches) wide and 16.51 cm high (6.5 inches). The pylon, when installed, is 5.08 cm high (2 inches) and 10.16 cm (4 inches) long and 1.016 cm (0.4 inches) wide. Cavity length to depth (L/D) ratio is 4.0, pylon height to cavity depth (h/D) ratio is 2.0, and pylon width to depth (w/D) ratio is 0.4. The downstream ramp is inclined 22 degrees from the horizontal and the pylon is swept back 29 degrees from horizontal. The distance from the cavity leading edge to the mid-point of the downstream ramp defines the cavity length. Ongoing combustion research at AFRL uses a similar pylon-cavity flameholder with h/D = 1.5 and w/D = 0.6 [15]. Forty 0.03 inch diameter pressure taps, located at several locations, provided for surface pressure measurements in and around the flameholder. Figure 19 illustrates the locations of the

pressure taps as well as the port used for a flush-mounted pressure transducer or cavity PIV injector. Figure 19 also depicts the coordinate system. The coordinate system associated with the test article centers on the leading edge of the cavity at the base of the pylon. The positive *x*-direction is downstream of the cavity leading edge, positive *y*-direction is vertically upward from the cavity leading edge, and the positive *z*-direction is oriented across the cavity to complete a right hand system.

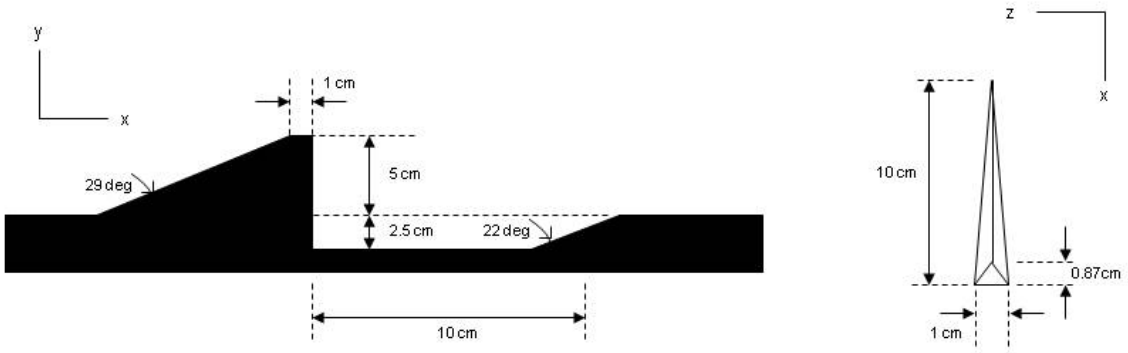

Figure 18. Test article geometry

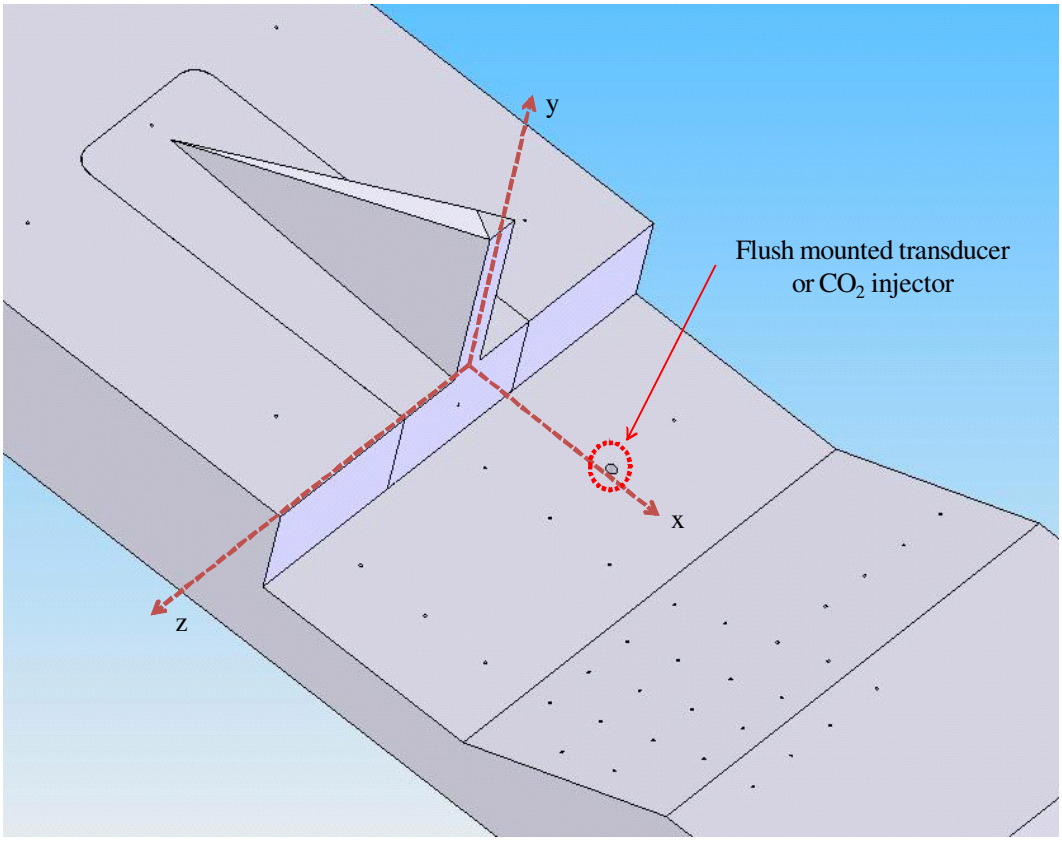

Figure 19. Coordinate system and pressure tap placement

3.2 Instrumentation

Wind tunnel monitoring used a locally developed LabView program. Pressure monitoring used Endevco piezo-electric pressure transducers shown in Table 3. The pressure transducers were calibrated to local atmospheric pressure one, or more, times every day using a Druck Inc. DPI-141 Resonant Sensor Barometer accurate to +/- 0.0075 in Hg (25.5 Pa / 0.0037 psi). All pressure transducers were calibrated to +/- 68.9 Pa (0.01 psi). Watlow, exposed, beaded tip, K-type thermocouples (P/N: ACEF00Q060EK000) placed in the supply channel and stagnation chamber provided temperature data accurate to +/- 2.2 deg C. A National Instruments data acquisition system collected data at 20 Hz (SCXI-1000 chassis, SCXI-1600 USB Data Acquisition and Control Module, SCXI-1112 Thermocouple Input Module, and two SCXI-1121 Isolation Amplifier Modules).

Pitot or static probe pressures routed into an Endevco pressure transducer through the probe and a short rubber tube provided probe data. Individual static and pitot pressure probes allowed for a limited survey of mean pressure measurements across the test section. The diamond-shaped supersonic probes were restricted to y = 3.7 cm and discrete streamwise stations ahead of and behind the pylon (x = 8.8 cm and x = -12 cm

Table 3. Pressure transducer list

Location	Part number	Full-scale pressure (kPa / psi)	Gauge / Absolute
Supply duct	8510B	3447.4 / 500	Gauge
Stagnation tank	8530C	689.5 / 100	Absolute
Tunnel ceiling	8530C	689.5 / 100	Absolute
Tunnel floor	8530C	344.7 / 50	Absolute
Cavity floor	8530C	103.4 / 15	Absolute
Probe	8530C	344.7 / 50	Absolute

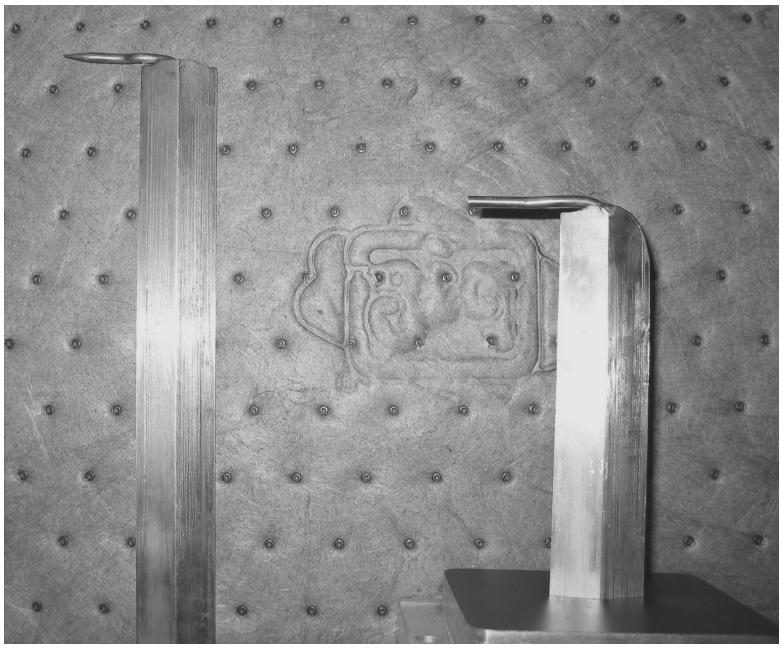

Figure 20. Static and pitot probes

were used). However, the probes were unrestricted across the test section (z-axis). Figure 20 shows the static and pitot probes used for testing.

Average surface pressure data were collected using an Esterline Pressure Systems DTC Initium pressure scanning system with a 206.8 kPa (30 psi) differential pressure scanner (P/N: 64HD-0803001000) and supporting hardware, controlled independently of other lab systems on a personal computer. The pressure scanner accuracy of 0.1% of full scale equated to +/- 206.8 Pa (0.03 psi). The scanner operated at approximately 8.5 Hz over 41 channels. Surface pressure taps were connected to the pressure scanner using 1.6 mm (0.063 inch) metal tubing mounted beneath each tap and approximately 60 cm of 1.5 mm (0.06 inch) (ID) plastic tubing and associated fittings.

Frequency data were collected using a 103.4 kPa (15 psia) Endevco pressure transducer flush-mounted on the cavity floor (Figure 19). The pressure transducer

received 10 V excitation power from an Agilent E3631A DC Power Supply. Electrical signals from the transducer were fed directly into an Agilent 35670A Digital Signal Analyzer. The signal analyzer produced a power spectral density data set saved to an ASCII file for further processing.

Shadowgraph photography relies on the relationship between density and refractive index of air allowing visualization of density variations, such as shock waves, as a function of $d^2\rho/dx^2$. Schlieren photography provides similar data, but through the use of a knife edge at the focal point to block out the refracted light rays, allows the visualization of density gradient directly, i.e., $d\rho/dx$ [56]. Both methods rely on parallel light beams passing through the test section. Figure 21 depicts the light beam refraction through the test section for both shadowgraph and Schlieren photography.

Shadowgraph and Schlieren data were collected using a Photron Fastcam-X color, high-speed camera system with a Tokina 80-200 mm lens at an f-stop of 4. All captured

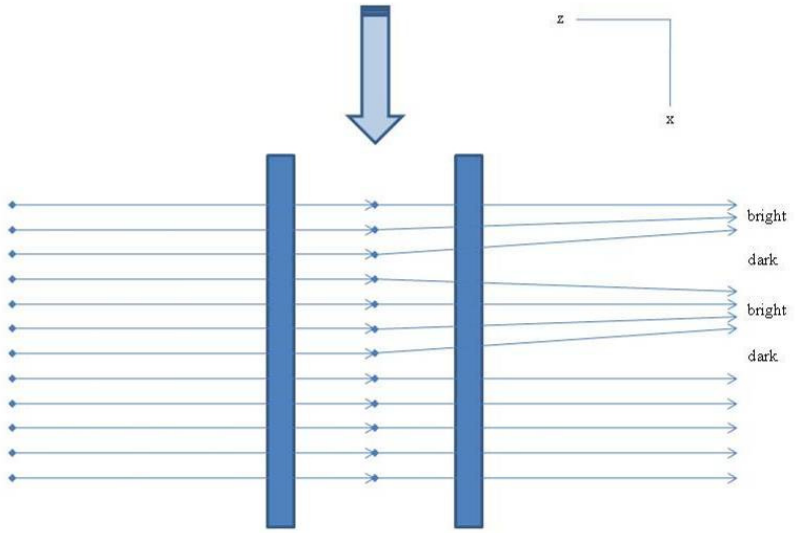

Figure 21. Refraction of parallel light beams passing through the test section used in Shadowgraph/Schlieren photography [56]

images used an exposure time of 1.5625 x 10^{-5} sec (1/64000 sec). The system was independently controlled from a stand-alone personal computer. The Fastcam system supports video capture at up to 16,000 frames per second. Full-frame video (1280x1024 pixels) was available at up to 500 frames per second and used for imaging the overall flow. Frame size became increasingly limited at the higher frame rates used to examine the shear layer immediately downstream of the baseline cavity lip (320x32 pixels at 16,000 frames per second).

Particle image velocimetry (PIV) measures the displacement of seed particles within the flow. The displacement of seed particles in two different images at different times provides a velocity vector. For large numbers of particles, statistical methods are used in post-processing to return vectors within the illuminated plane. Laser light formed into a planar sheet and projected into the flow provides illumination of seed particles in the flow. Figure 22 represents the relationship between the PIV laser sheet, camera, and flow. Figure 23 diagrams the PIV data reduction process. Further details on PIV may be found in Refs. 57, 58, 59, or 60.

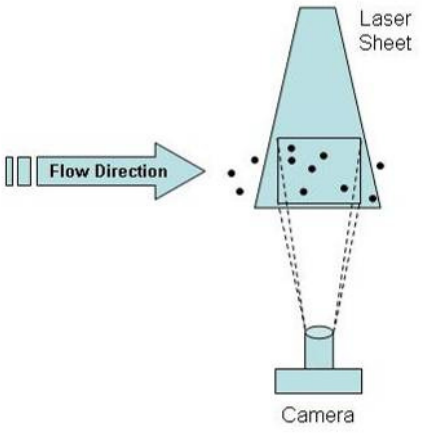

Figure 22. Two-dimensional PIV component relationships

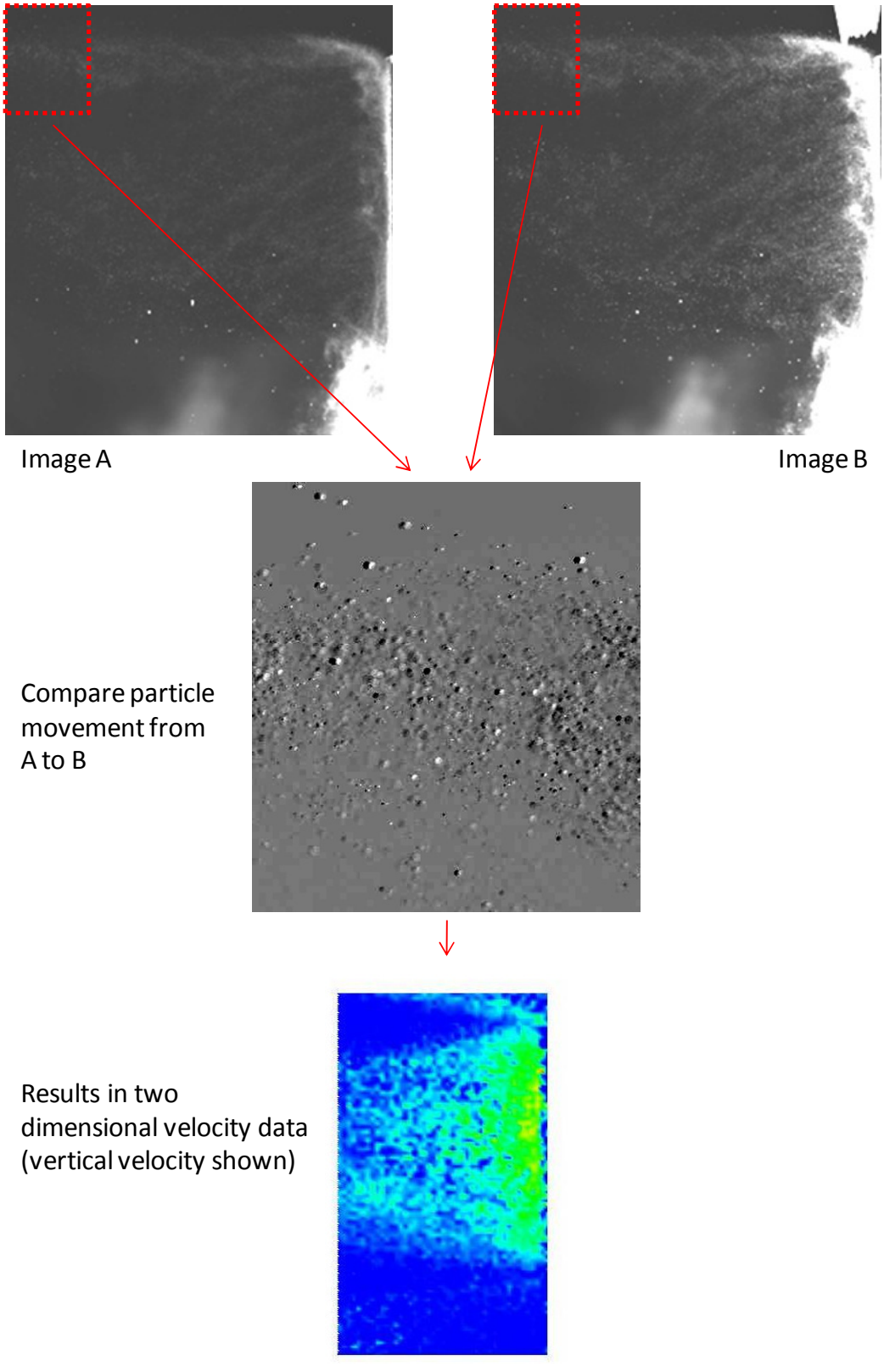

Figure 23. PIV data reduction flow (flow from right; details in App. A)

A Dantec Dynamics DC PIV system provided Particle Image Velocimetry (PIV) data. The light sheet was created using a New Wave Research SOLO200XT dual flash lamp-pumped Nd:YAG laser emitting a 532 nm beam. Dantec Dynamics Model 80x70 light sheet optics mounted to a Model 80x39 Mirror Arm formed the laser sheet in the test section. The camera was a Dantec FlowSense 4M, using an AF Micro Nikkor 60mm lens at an f-stop of 2.8. PIV system control and data reduction were accomplished on an independent personal computer running Dantec Dynamic Studio version 2.0. Details on the PIV data reduction may be found in Appendix A. Flow seeding was accomplished using a CO_2/dry ice clean seeding method under development at AFIT [61; 62; 63; 64].

This study used two different particle seeding configurations. Two injector ports installed in the stagnation tank upstream of the tunnel nozzle provided seeding without disturbing the overall flow. The stagnation tank injectors and high pressure liquid CO_2 bottle are visible in Figure 14. The second injector was added due to the very sparse seeding in the 6" x 6" wind tunnel noted in Ref. [64] which documented boundary layer data in the same tunnel using only one injector. Even with the second injector, useable PIV data required approximately 700-1100 image pairs. Typical PIV images showing the sparse nature of the seeding can be seen in Appendix A. The low seeding density contributed to a bias toward low velocities in some interrogation regions and manifested as a grainy or noisy appearance in the PIV data. This bias towards lower velocities could result in velocity errors of up to 15% to 40%. [60]. Since a single data run could only capture 70 image pairs and the conditions of the wind tunnel varied slightly from run to run, the resulting images average the results of 10-15 runs. The other injector

configuration used a single stagnation tank injector and an injector mounted to the cavity floor oriented toward the +z wall of the cavity as seen in Figure 24. Mounting an injector within the cavity obviously disturbs the flow within the cavity, but provided the ability to seed the pylon wake for qualitative analysis.

The stagnation tank injectors used a 2.0 mm / 3.2 mm (0.08 in / 0.125 in) (ID/OD) feed tube and an approximately 25 cm long 6.4 mm / 9.5 mm (0.25 in / 0.375 in) (ID/OD) shroud tube. Ref. [64] used the same shroud tube for the 6" x 6" tunnel stagnation tank injector, but used a 0.8 mm / 1.6 mm (0.03 in / 0.0625 in) (ID/OD) feed tube. The cavity injector used a 0.8 mm / 1.6 mm (0.03 in / 0.0625 in) (ID/OD) feed tube and an approximately 5 cm long 2 mm / 3.2 mm (0.08 in / 0.125 in) (ID/OD) shroud tube bent 90 degrees to sit against the cavity floor. All lines from the CO_2 source to the tunnel were

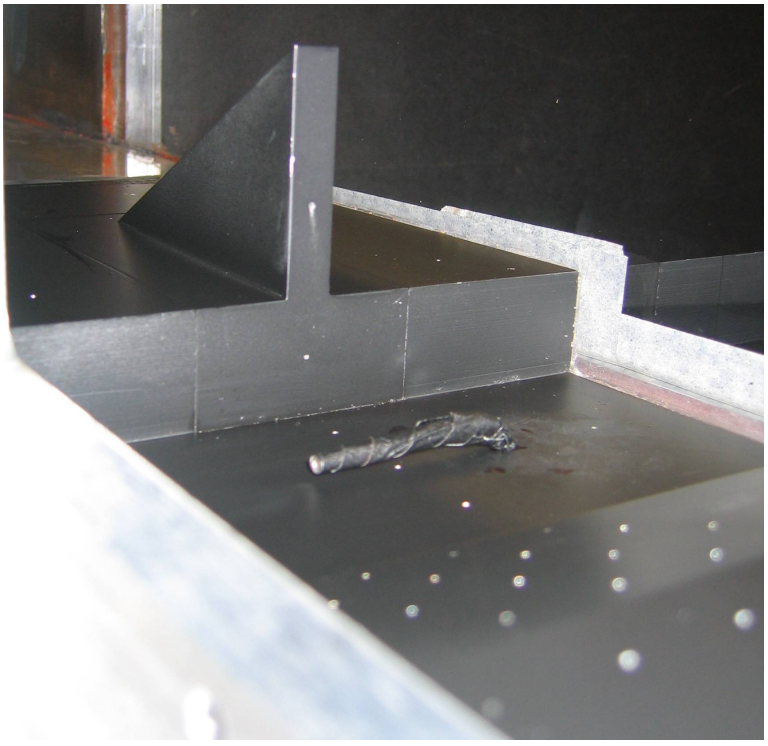

Figure 24. Cavity CO_2 injector

insulated to maximize the particle size leaving the injectors (the solid CO_2 sublimates as it progresses downstream). Ref. [62] measured a CO_2 mass flow of 0.0064 kg/s using the 0.8 mm (0.03 in) feed tube from a high pressure CO_2 bottle and should loosely approximate the mass flow through the cavity injector. Mass flow through the stagnation tank injectors was not measured. A single high pressure bottle of liquid CO_2 could only seed 10-15 wind tunnel runs. Additionally, the high-pressure bottle CO_2 was initially pressurized to approximately 11.4 MPa (1650 psia) and had a constantly decreasing pressure as the bottle emptied. A higher capacity, constant pressure, dewar substituted for the high pressure bottle resulted in qualitatively similar or slightly better seeding. Particle sizes have not been characterized in the 6" x 6" tunnel, however bench results venting to atmosphere in Ref. [64] found a CO_2 particle diameter of approximately 2 μm when using a configuration similar to the cavity injector.

PIV provided a boundary layer profile off the floor as the flow approached the test section at $x \approx 12$ cm, validating the computationally modeled conditions approaching the test article. Agreement between CFD, PIV and an analytical curve fit was excellent as seen in Figure 25. A probe data point at x = -22 cm and y = 3.7 cm, as well as surface pressure data at x = -10.8 cm used to monitor wind tunnel operations, further verified the mean free stream velocity of approximately 500 m/s. The analytical boundary layer velocity profile was based on a 1/7th power law [65:192]:

$$u = U\left(\frac{y}{\delta}\right)^{1/7} \tag{9}$$

The boundary layer approximately 2.5 cm off-centerline on the floor of the tunnel measured approximately 2 cm thick (based on both PIV and CFD results). The boundary layer measured in this work was about 8 mm thicker than the results presented in Ref. [64] for the same tunnel, but used about 3.5 times as many image pairs which should result in better resolution. A disturbance between y = 2 cm and y = 2.5 cm evident in the PIV data was consistent with either a data drop out due to sparse PIV seeding or flow disturbances from small discrepancies in the test section construction (see Appendix A). The agreement between three different experimental data methods, computational and analytical results provide good validation of the techniques themselves as well as the mean velocity magnitude entering the test section.

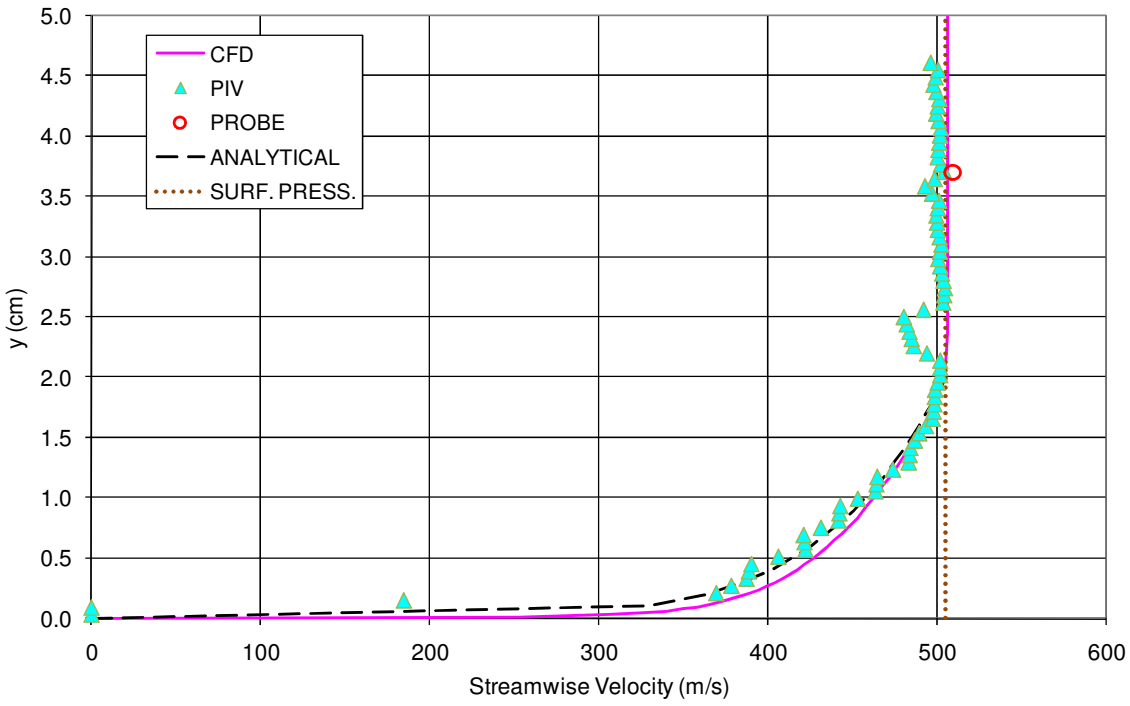

Figure 25. Boundary layer entering the test section ($x \approx$ -12 cm, $z \approx$ 2.5 cm; Re $\approx$ 32 x 10^6 m^{-1}; probe data at x = -22 cm; surface pressure data at x = -10.8 cm; velocity corrected for temperature variation)

IV. Computational Approach

This section presents the computational fluid dynamics (CFD) domains and method. Steady-state computational data were obtained using Fluent version 6.3.21 and the mesh generation used GridGen version 15.11. A Linux cluster at AFIT, using up to 24 processors, provided a parallel computing environment for flow solutions. Direct comparison to wind tunnel results provided validation and will be discussed in tandem with experimental results in Section V. More detailed descriptions of the software, grid convergence study and solution techniques are presented in Appendix B.

4.1 Computational Domains

The computational domain shown in Figure 26, consisted of several different meshes. The tunnel nozzle mesh consisted of a structured grid of approximately 4.4 million cells. The cavity was an independent mesh and merged with the duct mesh within Fluent. Using an independent cavity mesh helped ensure as much commonality between the pylon and no-pylon models as possible. The cavity mesh consisted of approximately 2.1 million cells. This study used two different test section duct meshes. The no-pylon duct consisted of approximately 3.9 million structured cells. The pylon duct used a hybrid mesh consisting of approximately 3.6 million structured cells in three blocks surrounding approximately 550,000 unstructured cells in the vicinity of the pylon. The cavity-pylon and cavity-only meshes used identical wall spacing and spacing above/below the cavity shear layer. The height of the first cell center above the test section floor upstream of the cavity was 7.5×10^{-5} m. The resulting y+ values of the first cell center

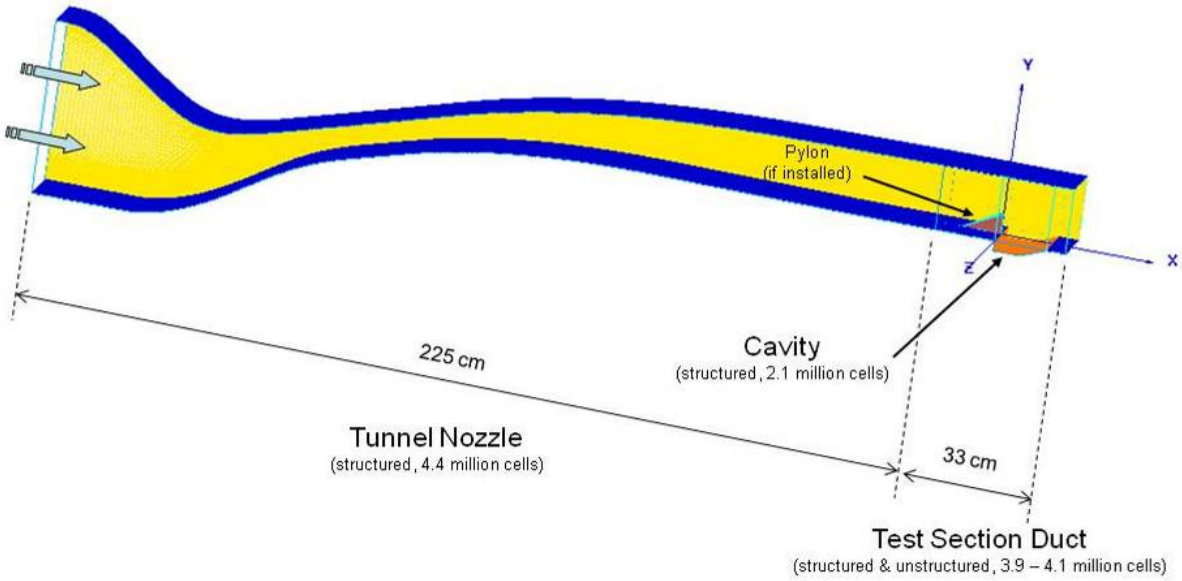

Figure 26. Computational domains

averaged approximately 35 to 57 depending on Reynolds number necessitating the use of wall functions to more accurately model the bottom of the boundary layer. This spacing resulted in approximately 32 cells in the boundary layer depicted in Figure 25 at $x \approx -12$ cm. Course spacing along the tunnel ceiling conserved computational expense (y+ ≈ 600-1000).

Figure 27 presents a close-up of the mesh on centerline ($z = 0$ cm) including the cavity and rear of the pylon, showing the clustering in the shear layer and along the surface of the pylon. The unstructured cells surrounding the pylon upstream of the cavity edge are clearly seen above the pylon. Figure 28 presents the mesh spanning the test section from the tunnel ceiling to the cavity floor at $x = 5$ cm showing cell clustering near the shear layer and pylon wake as well as the finer spacing along the tunnel walls to more accurately capture boundary layer behavior. The dense mesh within the cavity is evident in both figures, with very close spacing along the cavity floor and ramp (y+ < 10).

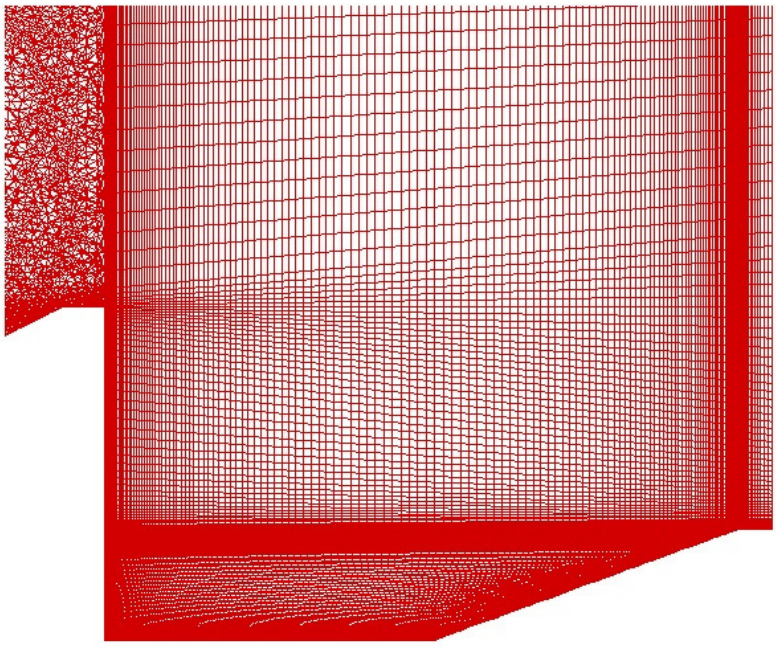

Figure 27. Close-up of mesh on centerline (z = 0 cm)

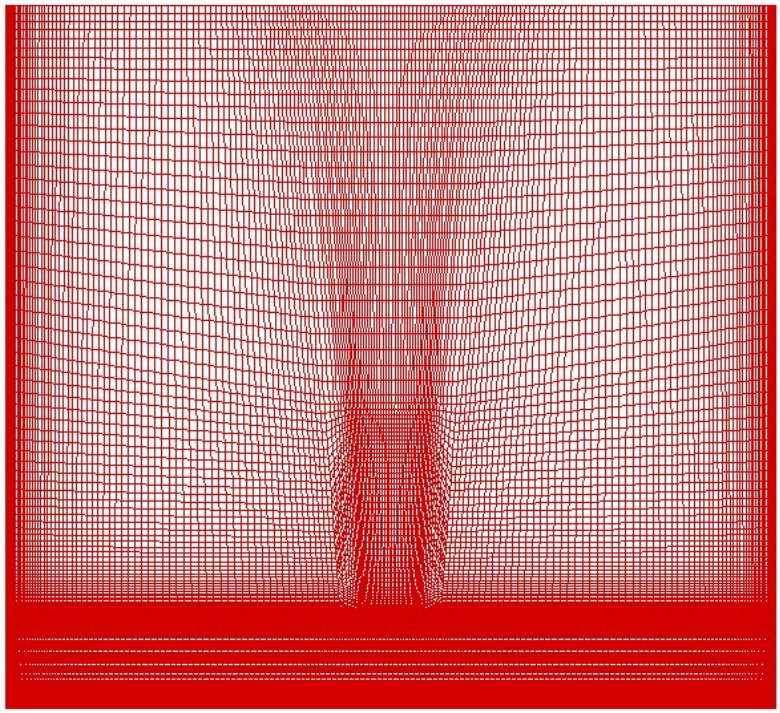

Figure 28. Cross-stream mesh from cavity floor to tunnel ceiling (x = 5 cm)

4.2 Computational Method

The three-dimensional Favre-averaged Navier-Stokes equations were solved using a coupled, implicit, second-order upwind solver. Cell fluxes were computed using a Roe scheme and the viscosity was determined using Sutherland's law. The working fluid was air treated as an ideal gas with no reactions modeled, corresponding to the wind tunnel test conditions. The CFL number in all cases was five.

The k-ω shear stress transport (SST) model [66] was used for turbulence modeling. The SST model combines the advantages of the k-ω model near solid surfaces with the k-ε model which has good free shear flow characteristics making it well suited for this flow. The SST model also has improved performance in adverse pressure gradient flows over either the k- ω or k- ε models.

Figure 29 diagrams the two-stage process used to arrive at computational solutions. First, the wind tunnel nozzle was modeled up to the entrance of the test section duct, shown in Figure 26, and only needed solving once, unlike the test section. Actual wind tunnel stagnation tank conditions populated the pressure inlet boundary condition at the nozzle inlet. Estimated average conditions for the nozzle exit based on wind tunnel test section measurements provided the initial conditions at the outlet boundary. The converged tunnel nozzle outlet conditions were then stored and used for the test section inlet conditions with and without the pylon installed. Supersonic flow at the entrance and exit allowed the use of test section inlet boundary conditions for the initialization of the test section outlet. All wall boundaries were modeled as smooth, no-slip, adiabatic surfaces.

The computational study began before the conclusion of the wind tunnel work. The inability to control wind tunnel temperature and scatter in the stagnation tank pressure resulted in initial conditions (stagnation tank temperature and pressure) for CFD slightly different from the mean values used in wind tunnel data reduction (detailed CFD flow conditions are tabulated in Appendix B).

Convergence monitoring compared the difference between inlet and outlet mass flow rates. As convergence was approached this difference approached zero. As a secondary measure of convergence the same check was made at the junction between the cavity and test section duct. The solution was considered converged when the average error in mass flow for the duct decreased by approximately three orders of magnitude. Figure 30 shows acceptable convergence for all cases required less than 20,000 iterations

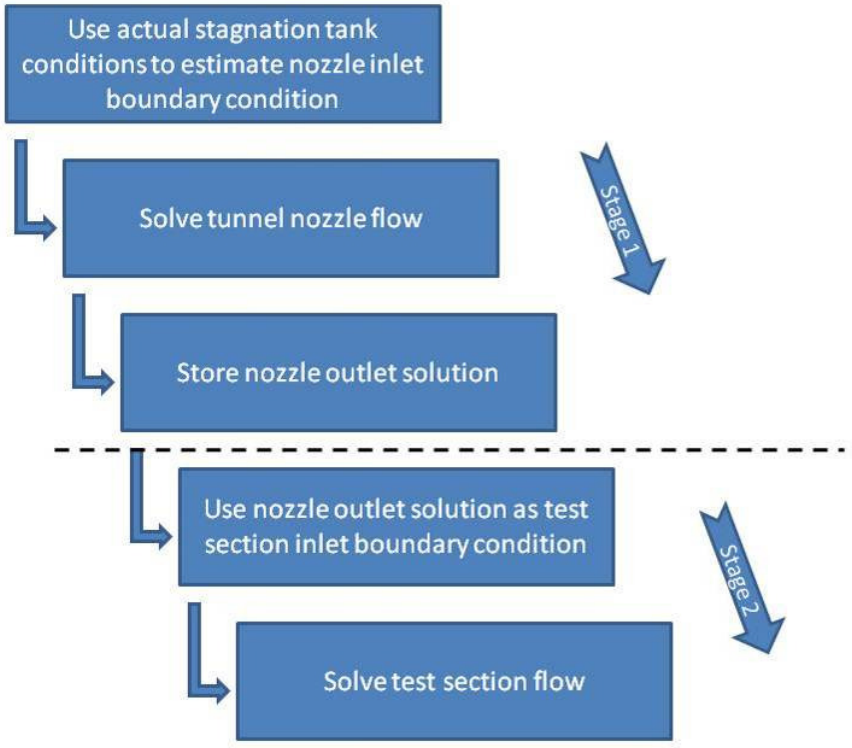

Figure 29. Computational process

which corresponded to approximately 110 hours per case. In absolute terms, the difference in mass flow was small from the first iteration. After the first iteration in the Re ≈ 32 x 10^6 m^{-1} case (pylon installed), the difference in inlet and outlet mass flows was 0.11 kg/s, compared with an overall mass flow through the duct of 7.85 kg/s. After 20,000 iterations, the error had reduced to 1.4 x 10^{-5} kg/s or about 0.0002% of the overall freestream mass flow (although this value fluctuated approaching convergence as seen in Figure 30b). The percentage error increased to approximately 0.0004% for the Re ≈ 55 x 10^6 m^{-1} case (pylon installed), although this remained acceptable. The percentage errors in the no-pylon cases were of the same order of magnitude as the pylon installed cases.

a)

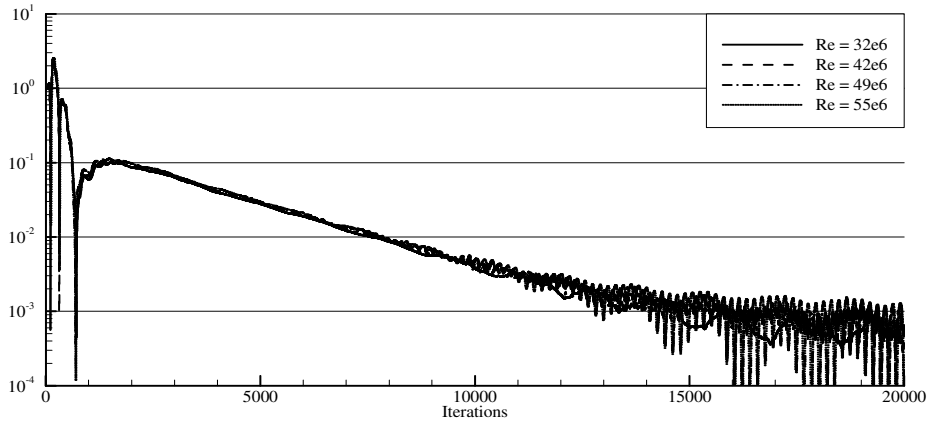

b)

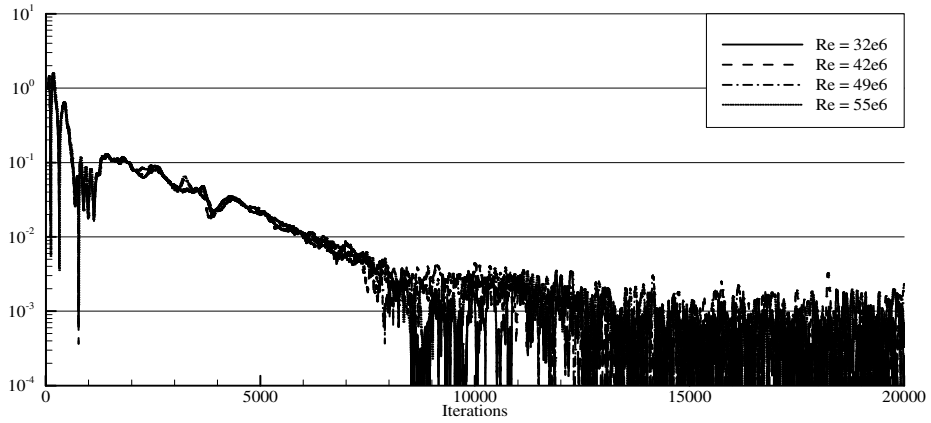

Figure 30. Test section convergence history a) without pylon and b) with pylon {plot of $\left|\dot{m}_{in}-\dot{m}_{out}\right| / \left|\dot{m}_{in}-\dot{m}_{out}\right|_{n=1}$ }

V. Results and Discussion

This section presents the combined computational/experimental test results. Flow visualization, surface pressures, probe pressures, and particle image velocimetry were all combined with CFD results to obtain a comprehensive picture of the pylon-cavity flowfield. The combined methods provided more confidence in the results than either technique standing alone. The wind tunnel data validated the CFD models, which in turn provided a more complete picture of the flow.

5.1 Flow Visualization

Flow visualization using shadowgraph video provided a quick assessment of prominent flameholder structures as well as validation of the CFD model's ability to capture the prominent flow features. Figure 32 presents a shadowgraph image of the pylon-cavity flameholder model at Re $\approx 42 \times 10^6$ m^{-1} and was created by joining two images at the same stagnation pressure setting. The two circular fields of view overlapped and created the unusable region identified by the hatched region in Figure 31. The flow is from the left and the prominent flow features closely match the predicted CFD results shown in Figure 32 created by overlapping density gradient contours from four *z*-planes (light shading corresponds to decreasing density and dark shading to increasing density). Prominent features visible in Figure 31 include a shock off the leading edge of the pylon, a recompression shock forming off the downstream cavity ramp, and an expansion at the cavity leading edge. The cavity shear layer and pylon wake also appear in the image. The flow off the top of the pylon is more complex. The pylon

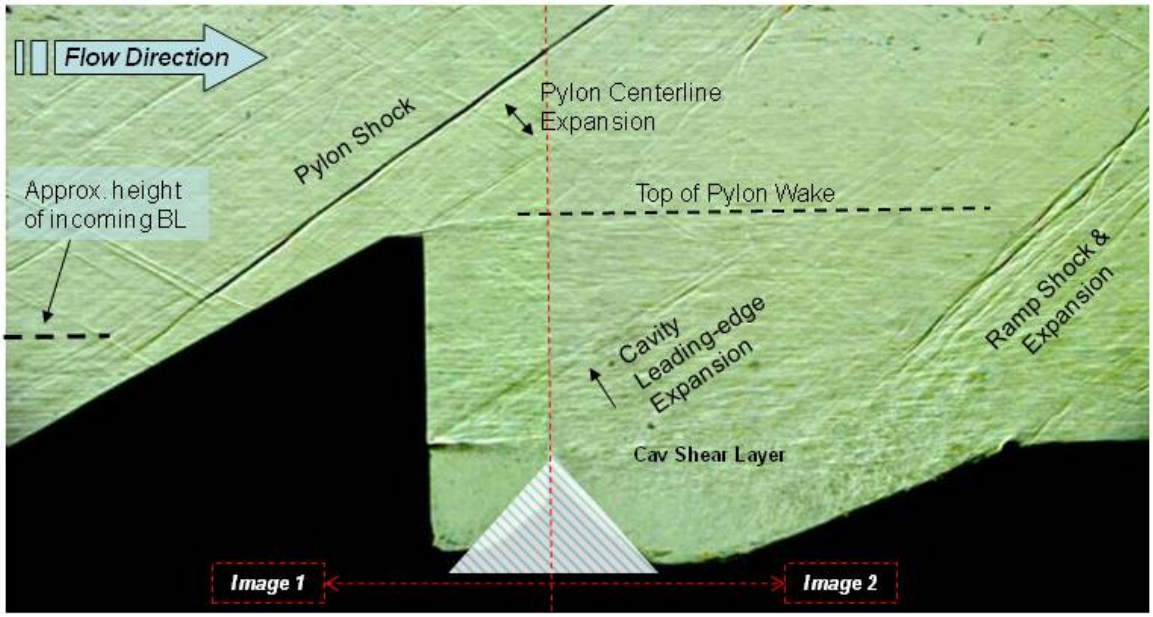

Figure 31. Shadowgraph image of significant features (Re# ≈ 42 x 10^6 m^{-1}, M = 2; hatched area unusable)

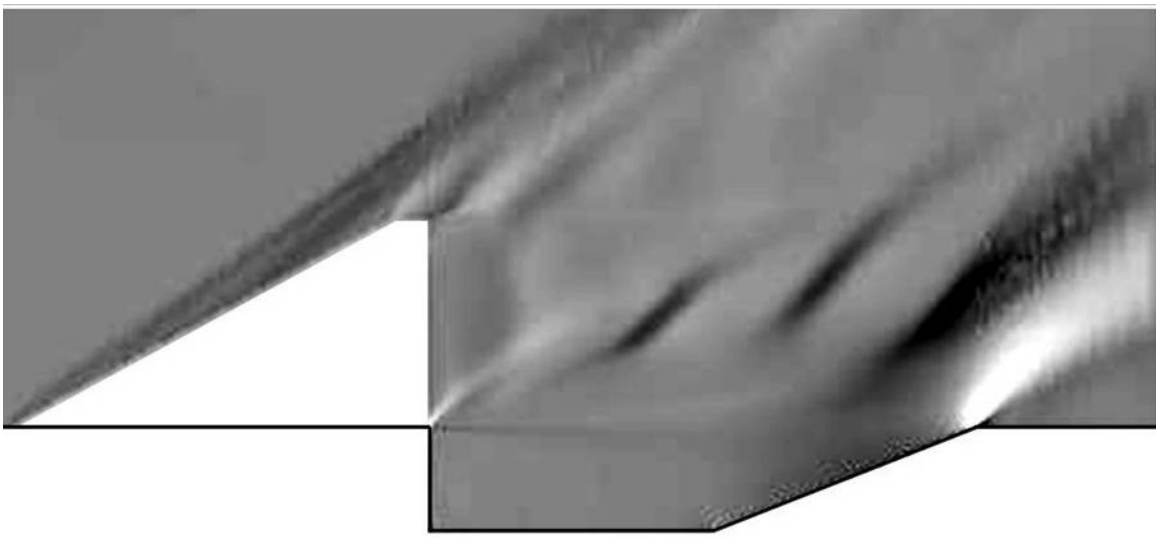

Figure 32. CFD density gradient (data from z = 0, 2, 4, 6 cm; grey scale of dρ/dx; Re# ≈ 42 x 10^6 m^{-1}, M = 2)

wake in Figure 31 appears to extend up above the top of the pylon. Considering the CFD results of Figure 33, the wake only extends above the pylon on the outside edges of the pylon base ($z \approx$ +/- 0.5 cm) where the flow travels away from the wake at about a 45 degree angle between two sets of counter-rotating vortices. The wave feature angling upward off the top, rear edge of the pylon in Figure 31 corresponds to an expansion as seen in the density gradient data in Figure 32. These wave and shear structures also compare qualitatively well to results presented in Ref. [15] for a similar test condition, although they used a different pylon and slightly divergent duct.

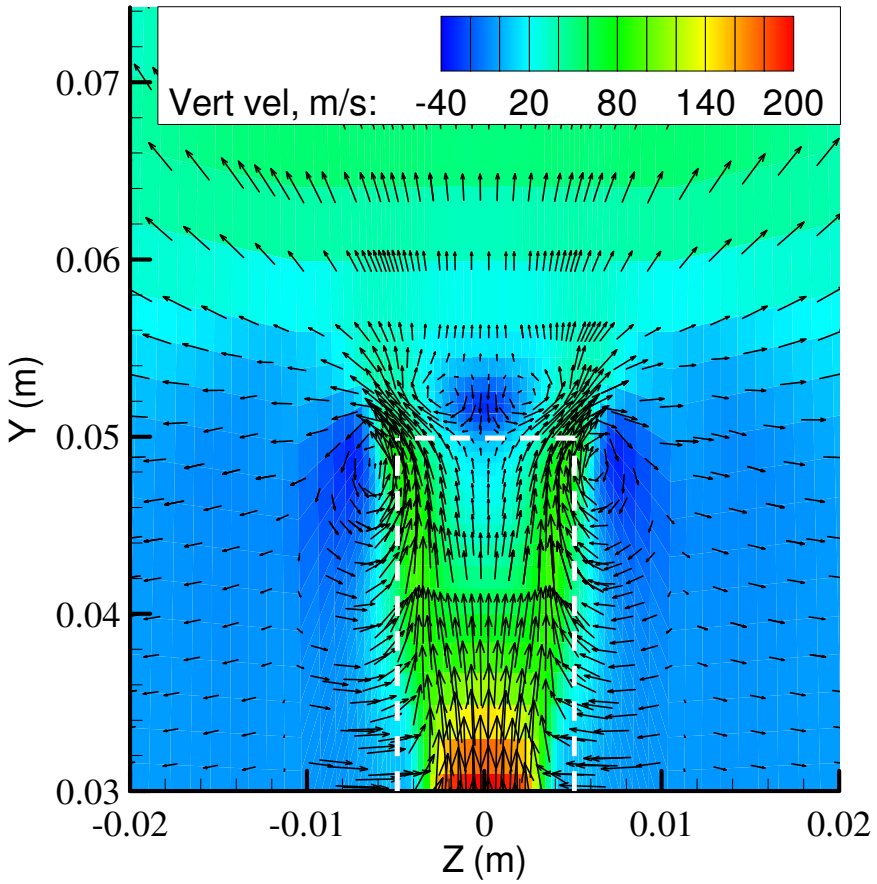

Figure 33. Flowfield behind the top of the pylon in the plane x = 1 cm (contours of vertical velocity; dashed line represents the pylon)

Schlieren photography did not reveal any significant Reynolds number effects near the pylon. Figure 34 shows Schlieren photographs of the four cases. The pylon shock closely resembles the CFD prediction of Figure 31. Note that due to equipment limitations only the portions immediately around the pylon and slightly upstream were affected by the Schlieren effect. This necessitated choosing which feature in the field of view to examine, in this case the pylon shock. Other features in the field of view returned shadowgraph imagery. Note the flow disturbances from upstream in Figure 34. The most significant disturbance appeared to emanate from a very small expansion at the top window/frame junction (< 1 mm) due to construction errors. Efforts to reduce these disturbances were unsuccessful. These disturbances obviously influence the flow, however the effect of the disturbances seen in Figure 34 should be small since the angle of the features shows them to approach Mach waves. Fortunately, the underlying flow is robust enough that it still approaches CFD predictions. The construction errors affecting the wind tunnel results are discussed in Appendix A.

Flow disturbances and vibration in the test section significantly affected the Schlieren images over the downstream ramp, and manifested as highly variable structures when viewed over several frames. However, on average, the flow resembled the CFD prediction of Figure 32. Figure 35 shows a typical Schlieren image taken of the ramp shock at Re $\approx 42 \times 10^6$ m^{-1} and shows the compression wave resulting from the flow turning upward over ramp. The apparent branch in the compression wave over the cavity was attributed to slightly different conditions on each side of the pylon resulting from

upstream flow disturbances. Since the image captures the flow through the entire test section, waves on each side of the pylon wake could manifest as a branched wave.

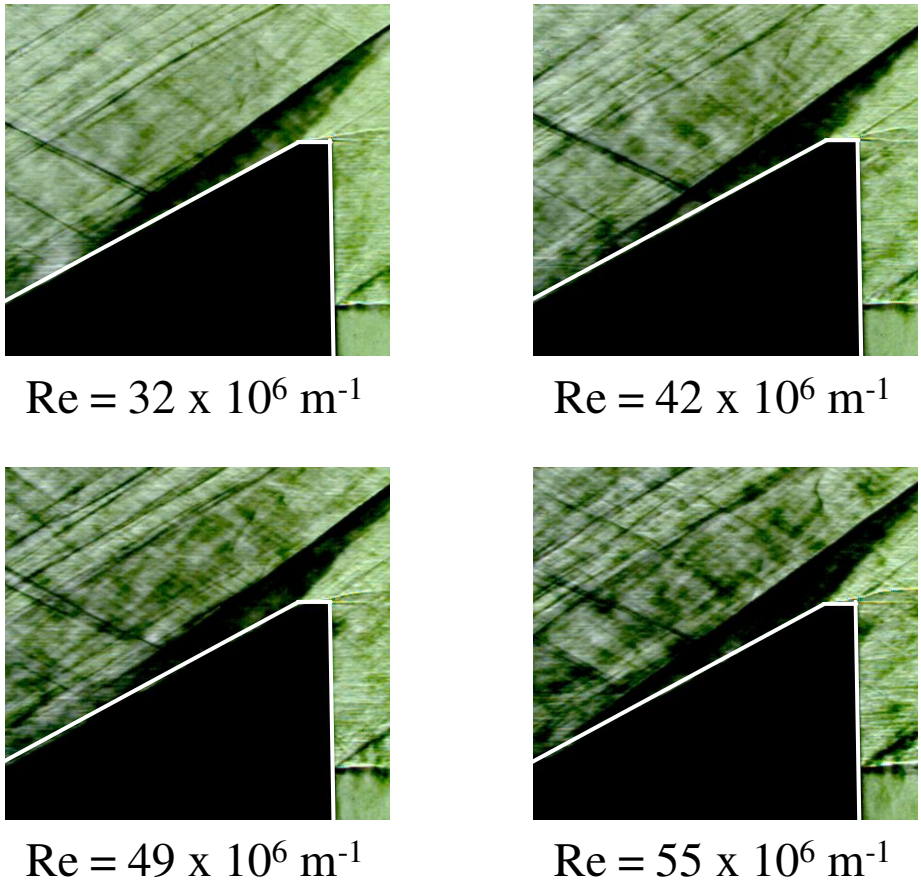

Figure 34. Instantaneous Schlieren photographs of near-pylon flow (1/64000 sec exposure time)

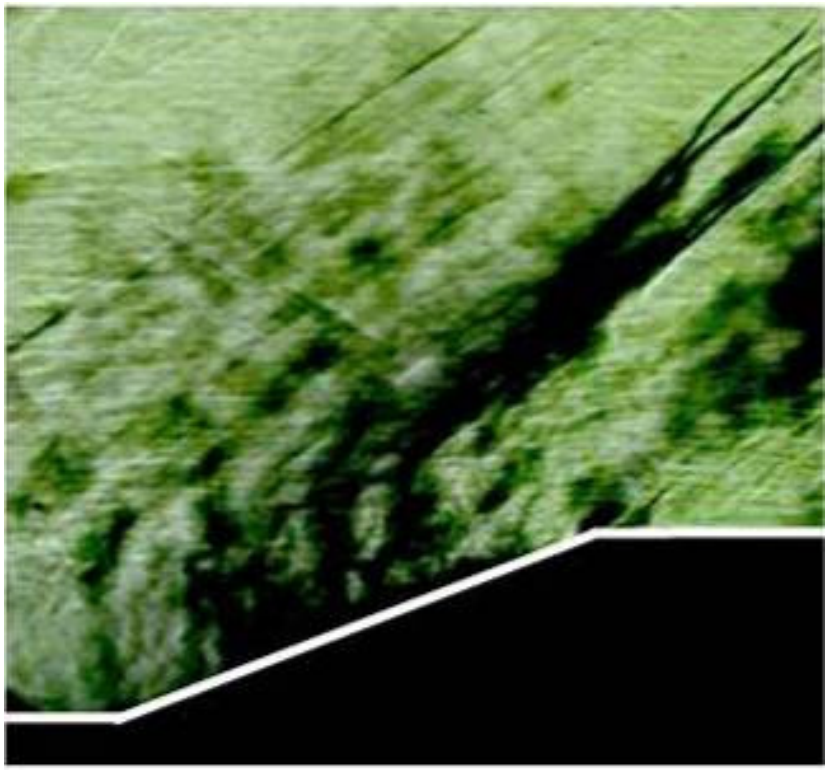

Figure 35. Instantaneous Schlieren photograph of flow over the downstream ramp (Re# ≈ 42 x 10^6 m^{-1}; 1/64000 sec exposure time)

5.2 Pressure Data

Surface pressures provide a means of estimating the shape and characteristics of the cavity shear layer impinging on the downstream ramp. The static pressure within the flameholder directly affects reactions within the flameholder and surface pressure data within the cavity provide a means of estimating the regions favorable or unfavorable for combustion, assuming an appropriate fuel-air mixture. Additionally, the use of CFD allowed for the estimation of overall average pressure effects. The measured pressure coefficient results were computed using a reference surface pressure (p_{ref}) from a pressure tap approximately 1 cm ahead of the pylon (x = -11 cm) and estimated dynamic pressure (q) entering the test section. Since wind tunnel conditions varied from run-to-run, pressure coefficient was usually used for comparative analysis. Pressure coefficient was computed as

$$C_p = \frac{p - p_{ref}}{q} \tag{10}$$

Table 4 presents the CFD mass-averaged static pressures within the entire cavity (y < 0 cm) showing a very small pressure rise with the addition of the pylon (< 2% at all Reynolds numbers). This pressure rise equated to an approximately 3% increase in average cavity pressure over the incoming duct static pressure. Higher average static pressure should contribute to better overall ignition and flameholding. However, just as important as average pressure within the flameholder are local pressures at various points within the cavity as they can represent hot spots or regions unsuitable for combustion. The pressure environment along the floor and upstream edge of the cavity where the flow

Table 4. Average cavity pressures

Mean Reynolds Number (m^{-1})	Mass-averaged duct pressure[1] (kPa)	Mass-averaged cavity static pressure (pylon, kPa)	Mass-averaged cavity static pressure (no-pylon, kPa)
3.2×10^7	30.0	30.9	30.5
4.2×10^7	38.5	39.7	39.0
4.9×10^7	48.6	50.0	49.2
5.5×10^7	52.5	54.0	53.1

[1] Calculated ahead of pylon/cavity at x = -12 cm

is subsonic was relatively unchanged with the addition of the pylon as seen in the surface pressure results in Figure 36.

On the downstream ramp, surface pressure data for the cavity-only case show relatively uniform pressures along the lower half of the cavity ramp with a gradual increase toward the top of the ramp (Figure 36a and b). However, with the pylon installed, the surface pressure takes on a more complicated appearance with pressure rising along the downstream ramp, but with relatively low pressure near the wake of the pylon and increasing pressure toward the walls where the cavity shear layer impinges on the ramp (Figure 36c and d). No significant Reynolds number effects on the surface pressure coefficients were noted. Figure 37 shows measured and predicted centerline surface pressure data and show generally good agreement between computational and wind tunnel results. However, at lower Reynolds numbers the centerline pressure without the pylon in Figure 37a rises higher on the downstream ramp than the CFD predicted and is associated with a small centerline velocity deficit in the incoming test section flow. With the pylon installed (Figure 37b), the measured centerline pressures along the downstream ramp appear slightly lower than predicted by CFD. Figure 37b suggests that

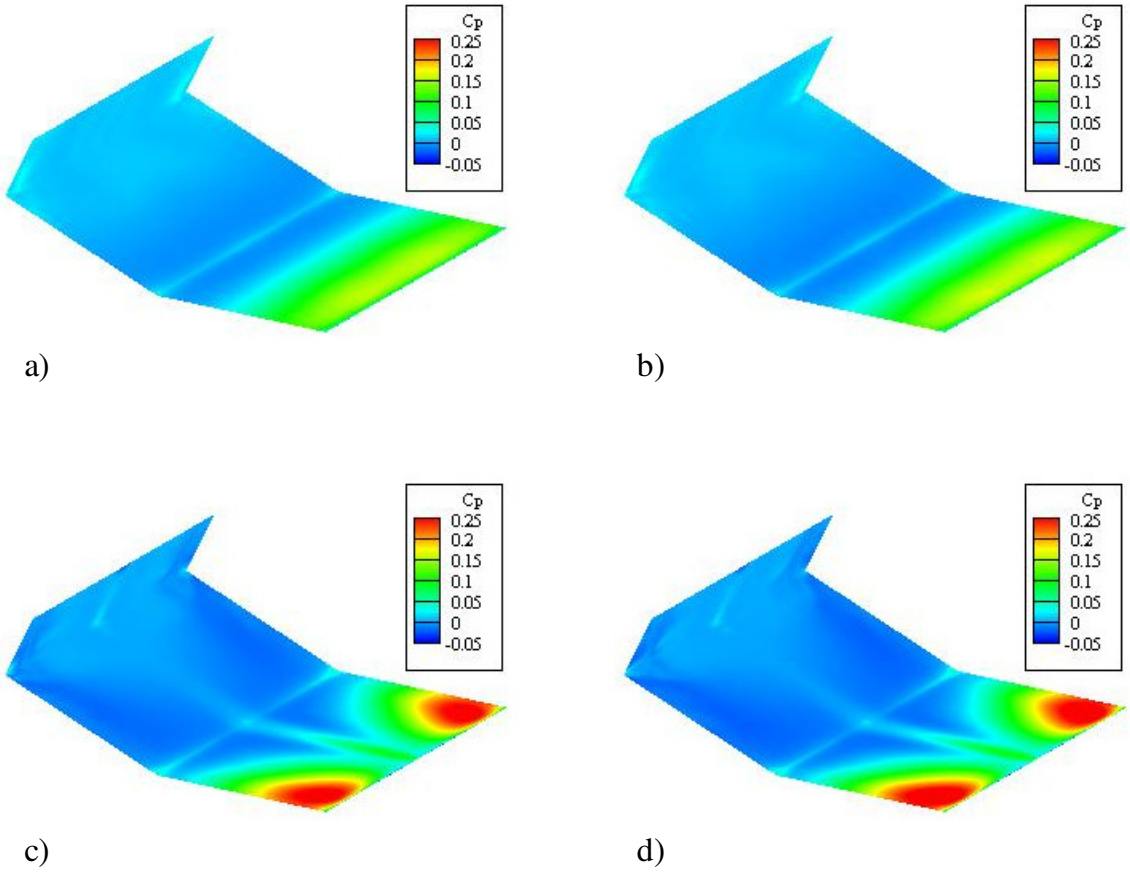

Figure 36. CFD cavity surface pressure coefficient a) cavity-only, Re ≈ 32 x 10^6 m^{-1}; b) cavity-only, Re ≈ 55 x 10^6 m^{-1}; c) pylon-cavity, Re ≈ 32 x 10^6 m^{-1}; and d) pylon-cavity, Re ≈ 55 x 10^6 m^{-1}

the shear layer with the pylon installed may sit lower on the ramp than predicted in the low Reynolds number case as indicated by the peak pressure occurring lower on the ramp (smaller *x* coordinate).

Two significant effects likely explain the high pressures on the top, outboard corners of the cavity ramp. First, the extra mass drawn up behind the pylon draws a portion of the duct flow lower into the cavity leading to a deeper impingement of the shear layer. Second, the recompression shock off the pylon wake interacts with the ramp shock that develops above the outboard edges of the cavity ramp seen in Figure 32. The

pressure on the ramp in these regions reaches approximately 20% of the stagnation pressure value and signifies potential hot spots in a reacting flow. In a reacting flow, however, the shear layer will rise up [40] relieving these high-pressure zones somewhat and spreading the effects across the ramp, reducing their potential local severity. Surface pressure data from the wind tunnel near the shear layer impingement validate the pressure rise on either side of the cavity ramp as seen in Figure 38. The skewness in the pressure data across the ramp in Figure 38 is likely due to small imperfections in the test section construction on the $-z$ side of the test section as described in Appendix A and suggests a thicker boundary layer and lower velocity flow on the $-z$ side of the tunnel as indicated by probe data in Figure 39. Figure 38 presents both pressure coefficient and absolute pressure data to compare the high and low Reynolds number cases. Because the pressure coefficient data amplifies the errors, the absolute data are included for comparison purposes. Wind tunnel pressure coefficient data collapse well on each other, except near the centerline. On centerline the pressure coefficient of the low Reynolds number case is substantially higher than the high Reynolds number case. Although the difference is within the 95% confidence bounds shown in Figure 38, when the other two cases are included there is a smooth decrease in the centerline pressure with Reynolds number as seen in Figure 40. It is likely that this decrease in centerline pressure towards the CFD result as Reynolds number increase is associated with flow irregularities from upstream in the wind tunnel, i.e., centerline velocity deficit or upstream shock waves.

CFD allowed the exploration of overall total pressure effects that would be difficult to measure in the 6" x 6" wind tunnel. The compressible effects resulting from the addition of the pylon led to a larger total pressure loss as expected and seen in Table 5. The mass-averaged total pressure ratio for the baseline case was approximately 97.9%. The addition of the pylon decreased the ratio to approximately 96.5%, although designing the pylon for minimum losses should regain some of the lost total pressure. The slight increase in pressure ratio with increasing Reynolds number seen in Table 5 is most likely attributed to using the same mesh for the different cases, rather than an actual effect of the flow. In any case, changing Reynolds number had essentially no effect on total pressure loss. In terms of total pressure loss, the improved overall performance of the combustor with the addition of the pylon to the cavity flameholder must be sufficient to counter the 1.4% loss attributed to the pylon.

Table 5. Mass averaged test section total pressure ratios

Mean Reynolds Number (m^{-1})	P_{t_out}/P_{t_in} (no-pylon, kPa)	P_{t_out}/P_{t_in} (pylon, kPa)
3.2×10^7	0.978	0.964
4.2×10^7	0.979	0.964
4.9×10^7	0.979	0.965
5.5×10^7	0.979	0.965

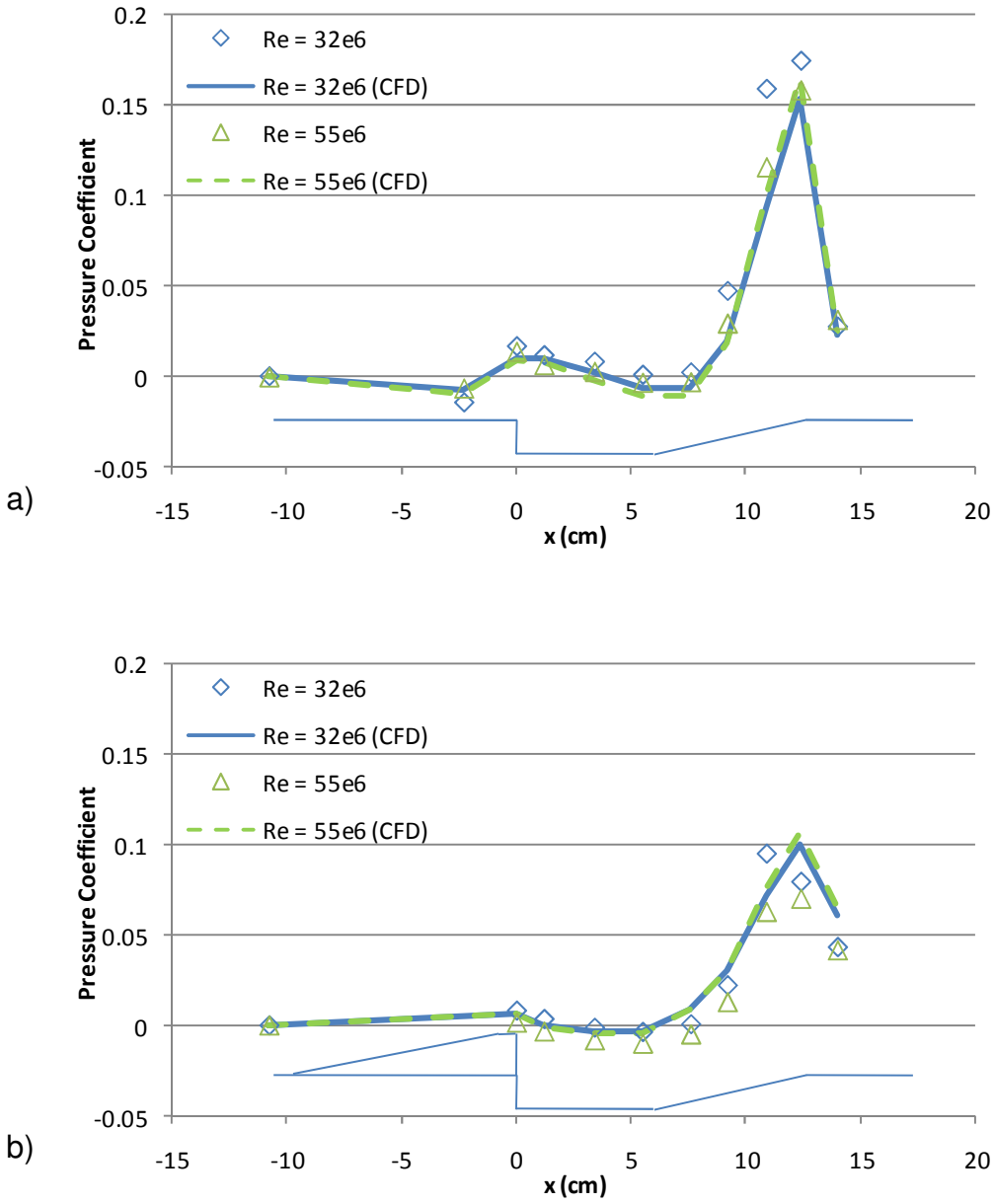

Figure 37. Wind tunnel and CFD centerline surface pressure coefficients at Re ≈ 32 x 10^6 m^{-1} and Re ≈ 55 x 10^6 m^{-1}, a) without pylon and b) with pylon

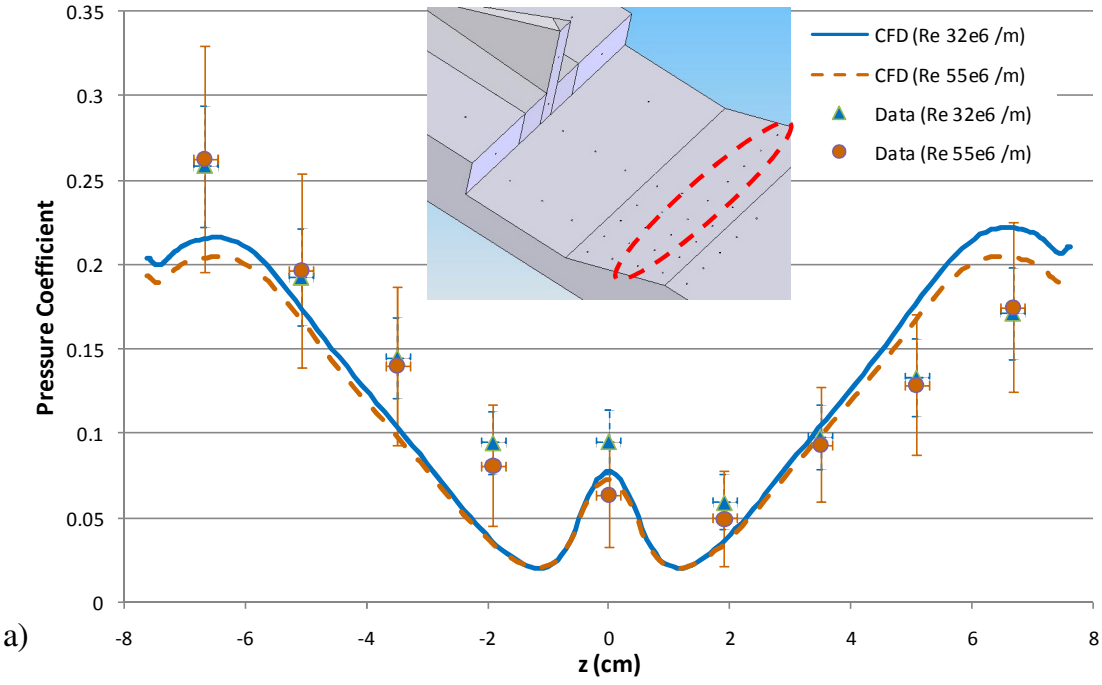

a)

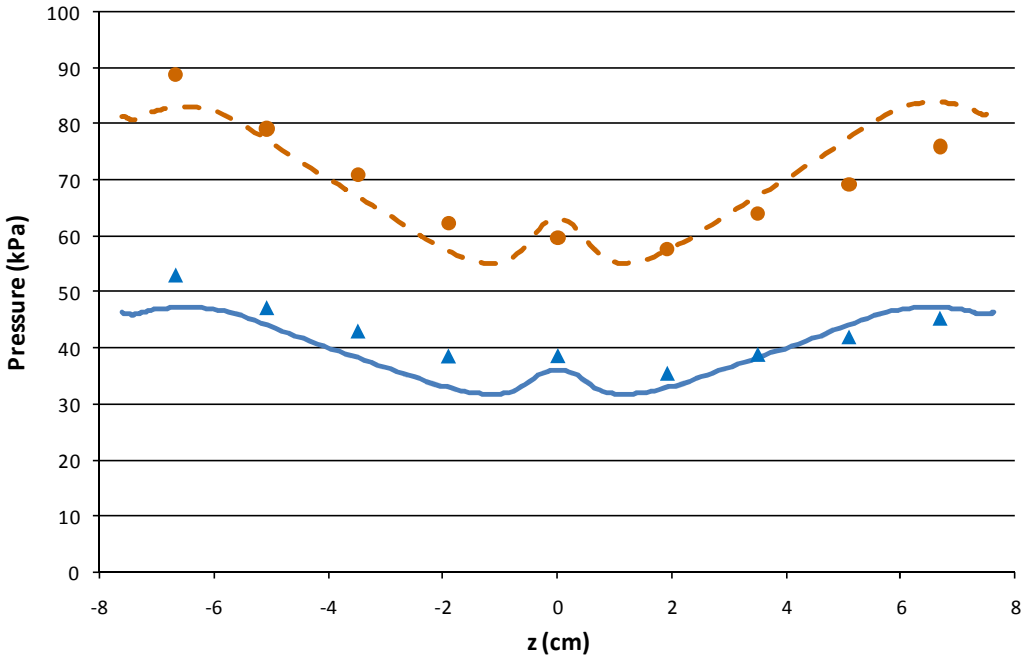

b)

Figure 38. Cross ramp pressures near shear layer impingement: a) pressure coefficient and b) absolute pressure (x = 10.8 cm, y = -0.94 cm)

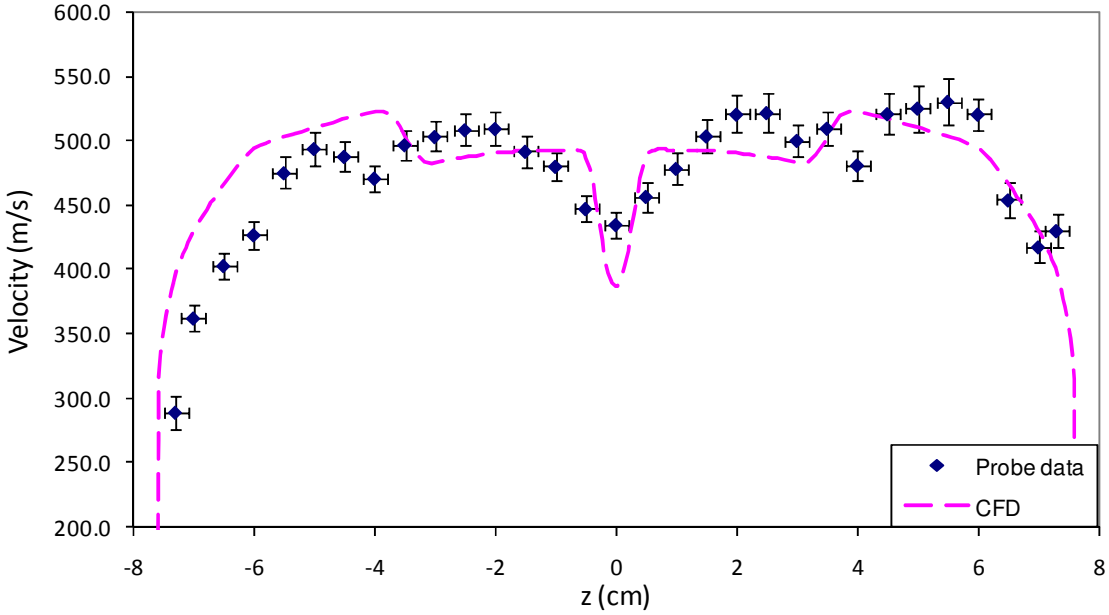

Figure 39. Streamwise velocities measured above the cavity ramp (probe data, x = 8.8 cm, y = 3.7 cm, Re ≈ 32 x 10^6 m^{-1})

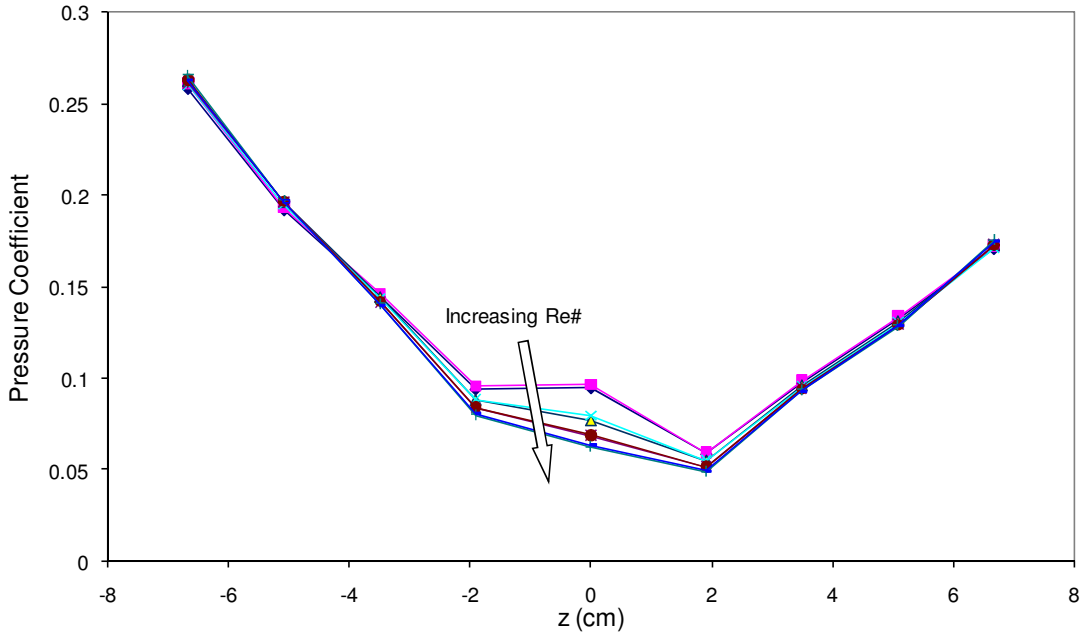

Figure 40. Cross ramp surface pressure coefficients with pylon installed

5.3 Flowfield Data

The primary flowfield characteristic of interest is the flow of cavity fluid behind the pylon and into the main flow. The computational results shown in Figure 41 clearly show a strong flow through the low pressure region behind the pylon from the cavity and into the main flow (approx. $M = 1$ at 1 cm behind the downstream face of the pylon at $y = 1.9$ cm). Supersonic expansion behind the pylon and the resulting low static pressure induce the upward flow. The pressure coefficient measured behind the pylon pressure tap at $y = 1.9$ cm was approximately -0.16 at all Reynolds numbers which supported the computational results (Table 6). The computational pressure coefficient and upward

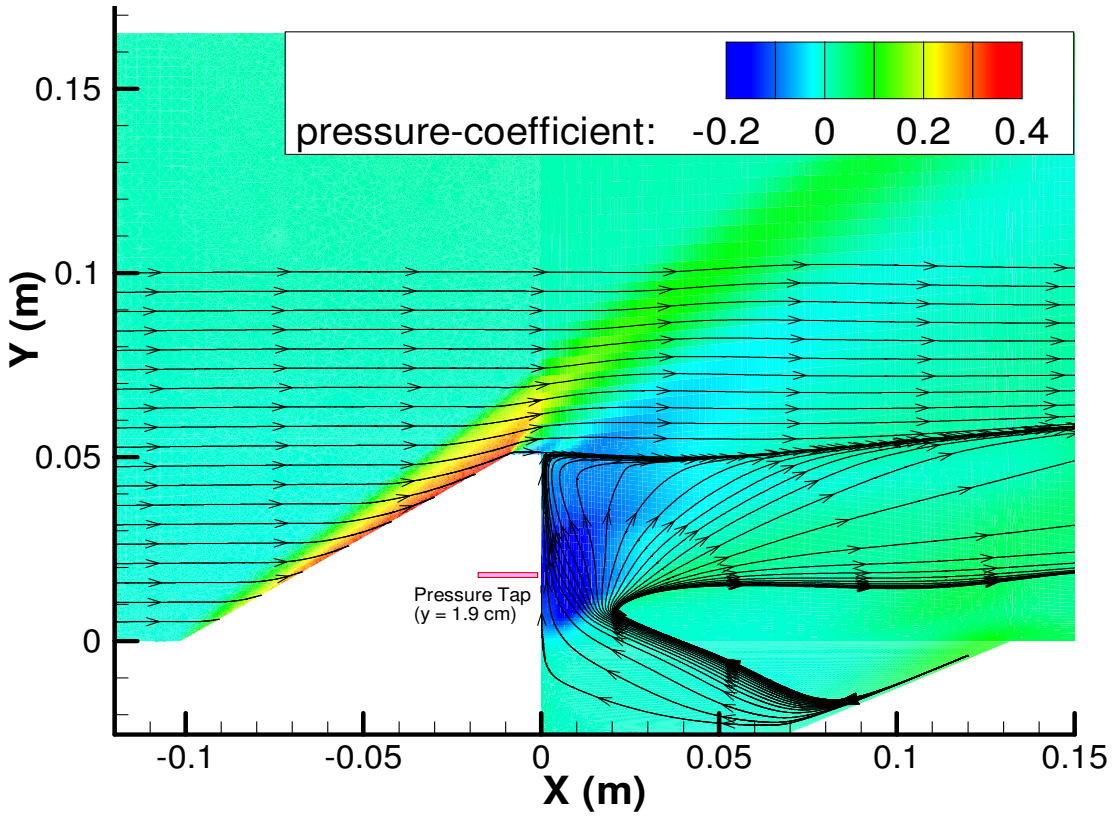

Figure 41. CFD centerline pressure coefficient with streamlines (Re ≈ 32 x 10^6 m^{-1})

Table 6. Pressure coefficients and upward velocity on centerline behind the pylon

Mean Reynolds Number (m^{-1})	Pressure Coefficient (CFD)	Pressure Coefficient (Wind Tunnel)	Upward velocity[1] (m/s)
3.2×10^7	-0.156	-0.159	254
4.2×10^7	-0.158	-0.160	253
4.9×10^7	-0.159	-0.159	256
5.5×10^7	-0.160	-0.159	261

[1] Computed 1 cm behind the pressure tap (x = 1cm, y = 1.9 cm, z = 0 cm)

velocity behind the pylon varied only slightly over the Reynolds number range used in this study (Table 6). The upward flow out of the cavity associated with the pylon wake was mostly confined to the base region immediately behind the pylon on-centerline ranging from the tunnel floor to the top of the pylon (y = 5 cm) and downstream approximately 2 cm (or about twice the pylon width). Figure 42b illustrates how the height of the upward flow out of the cavity drops off with distance off-centerline. At z = 0.5 cm (aligned with the edge of the pylon), the upward flow extends approximately 1.5 cm above the cavity. At z = 2 cm (Figure 42c), the cavity traps the flow near the floor of the duct. This off-centerline flow into the cavity provides the mass flow supporting the upward flow in the pylon wake.

PIV results for vertical velocity, shown in Figure 43a, show the upward flow behind the pylon. These results are qualitative since in order to seed the cavity for PIV an injector was placed along the cavity floor (Figure 24) disrupting the normal flow within the cavity. The injector mounted across the cavity floor disrupted cavity flow as did the added mass of CO_2 into the cavity. Assuming a cavity injection mass flow of CO_2 of approximately 0.0064 kg/s, the mass flow of CO_2 approached 12% to 21% of the mass

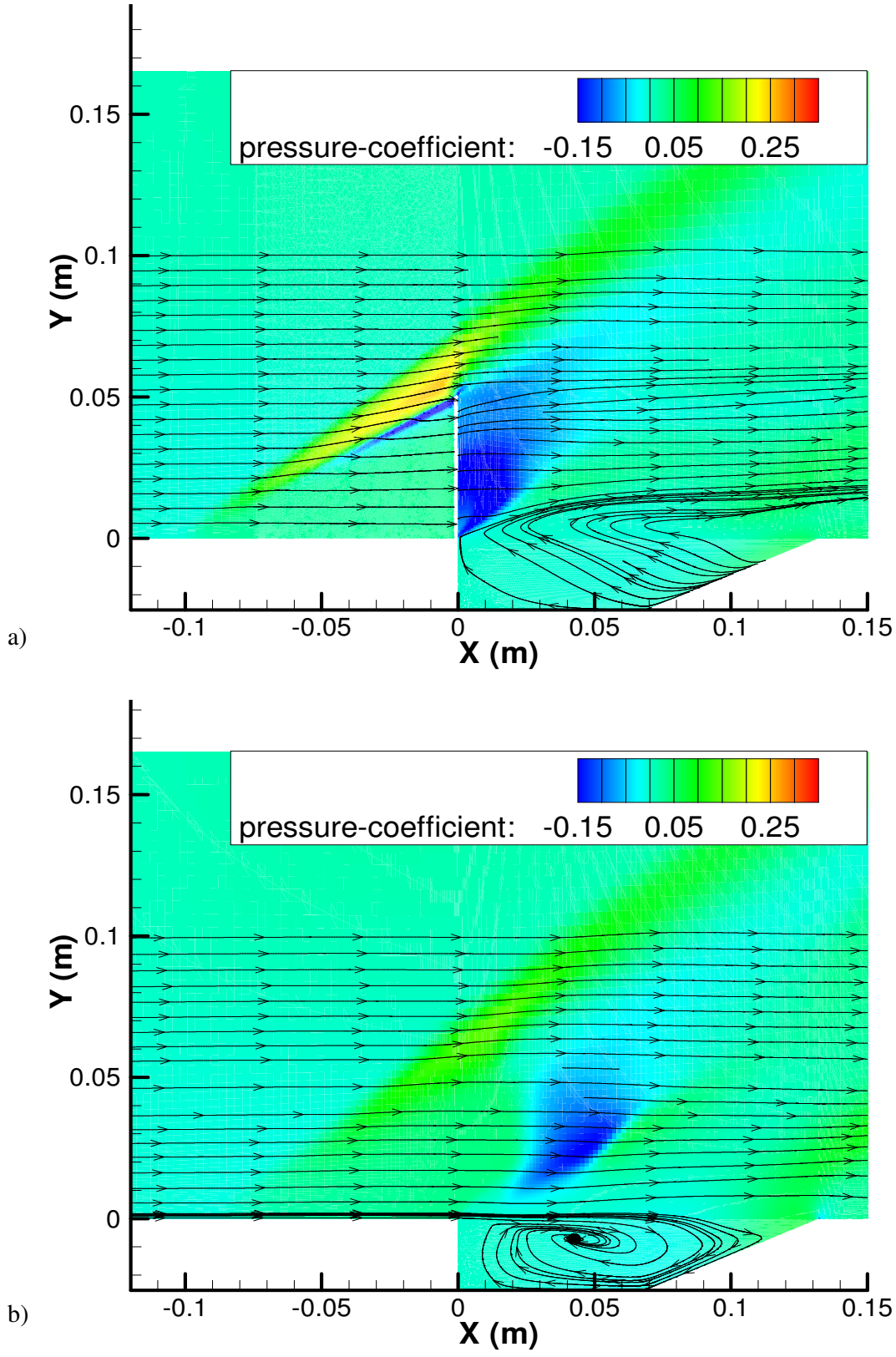

Figure 42. CFD off-centerline pressure coefficient with streamlines (Re ≈ 32 x 10^6 m^{-1}): a) z = 0.5 cm; and b) z = 2 cm

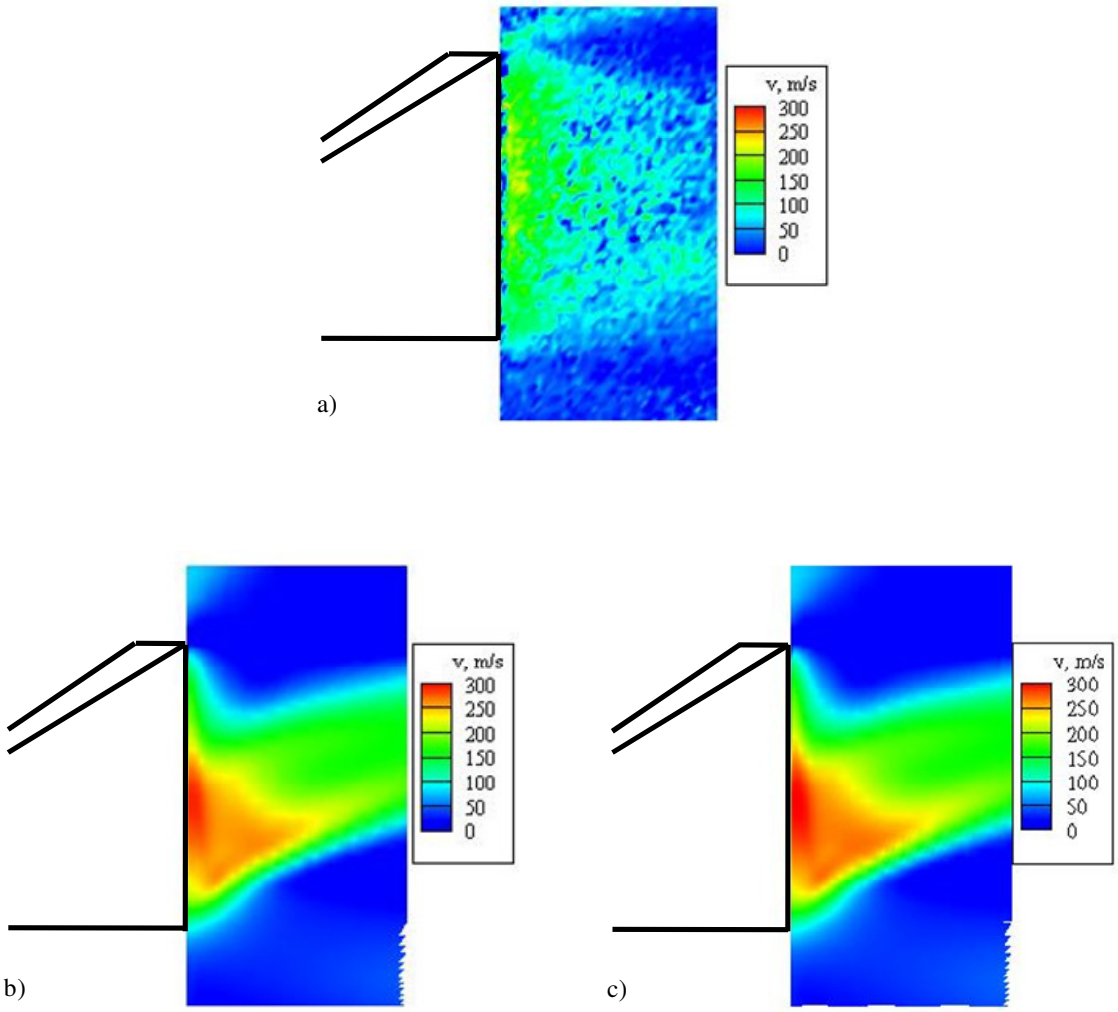

Figure 43. Vertical velocity on centerline a) PIV data (Re ≈ 32 x 10^6 m^{-1}); b) CFD data (Re ≈ 32 x 10^6 m^{-1}); and c) CFD data (Re ≈ 55 x 10^6 m^{-1})

flow of air passing through an undisturbed cavity, depending on Reynolds number. These PIV results demonstrate that upward flow behind the pylon does not strictly depend on undisturbed flow within the cavity. Figure 43b and c show the computed upward velocity behind the pylon for the undisturbed flow and demonstrate negligible Reynolds number effect on the upward flow behind the pylon on centerline. The computed vertical velocity along centerline behind the pylon pressure tap at y = 1.9 cm in Figure 44 indicated that the vertical velocity drops off relatively quickly approximately 2.5 cm behind the pylon. The PIV results in Figure 44 show the vertical velocity dropping off within approximately 1 cm from the back of the pylon then remaining fairly constant. Comparing the PIV vertical velocity with the computed vertical velocity 2 mm off centerline in Figure 44 shows a similar drop-off in vertical velocity along the streamwise coordinate and suggest the possibility of a slight misalignment of the laser sheet in the z-axis. Figure 45 shows the computed vertical velocity along the centerline of the flameholder as well as in four x-

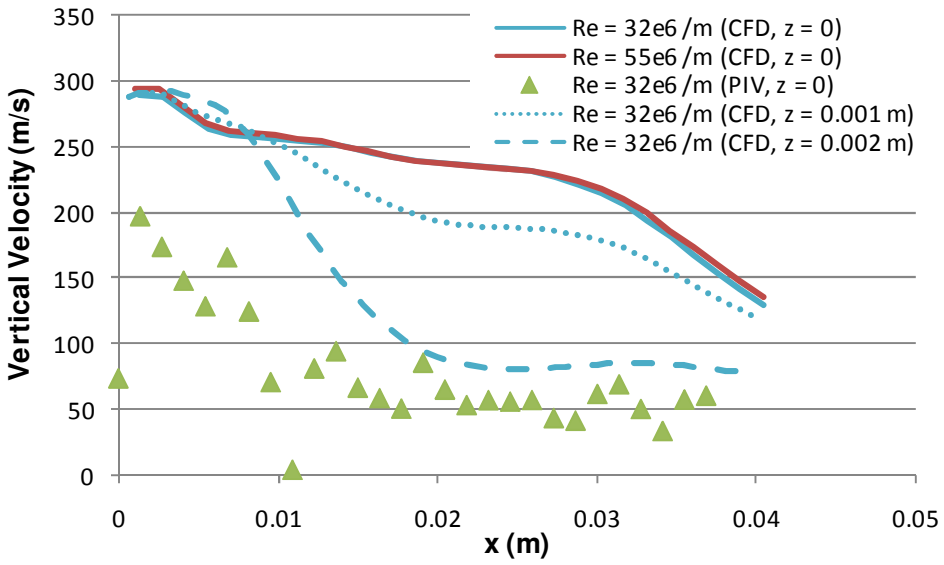

Figure 44. Centerline vertical velocities behind pylon pressure tap (y = 1.9 cm)

planes spaced along the flameholder. The upward velocity within the pylon wake is clearly visible. Also, seen in Figure 45 are the changes in flow direction due to the pylon and ramp shocks. The upward flow out of the cavity is largely confined to the pylon wake directly behind the pylon itself. However, a region over the middle of the cavity (seen in the x = 5 cm plane in Figure 45) indicates a slightly wider region of upward flow out of the cavity. The off-centerline upward flow out of the cavity drops off quickly as previously discussed and seen in Figure 42. Figure 45 also shows negligible variation in upward velocity due to Reynolds number changes.

Figure 46 shows that the pylon wake induces an expansion and recompression shock behind the pylon that could further improve mixing with the main flow as described in Ref. [2:309-310]. The small differences in overall velocity passing the pylon in the CFD cases resulted from the different stagnation tank temperatures used to initialize the simulations (T_t = 273 K for 32 x 10^6 m^{-1} and T_t = 287 for Re = 55 x 10^6 m^{-1}). Also, the PIV velocity data in the pylon wake may have been biased lower due to very few available image pairs as seen in Figure 47. Input from particles on the outward edges of each 1.2 mm x 1.2 mm interrogation region may have led to higher PIV wake velocities. A contributing possibility, discussed in more detail later, is that CFD results in base flows are susceptible to error. However, as seen in Figure 46, the CFD and PIV data agree on the overall shock and expansion structure behind the pylon. Recompression shock angles agree very well at 32.7 degrees for CFD and 33.1 degrees for PIV, although estimating the edge of the shock for the PIV is difficult due to the grainy data. The computational results indicate the recompression shocks beginning to curve outward as

the flow approaches the ramp shocks at the rear of the cavity. Both CFD and PIV have difficulty capturing large velocity gradients as seen in Figure 48 and Figure 49 near the recompression shock at approximately x = 7.5 cm. In both cases the change in velocity near the shock should be virtually instantaneous on the scale of these figures, however limitations of the 2nd order CFD scheme and particle lag in the PIV lead to a smoothed velocity gradients at the shock. The lag error in the PIV appears worse than the diffusion error in the CFD results. Another aspect to note in Figure 48 and Figure 49 is the asymmetry in the shock locations. In both figures, the shock on the +z side of the flow is about 5mm closer to the cavity leading edge at x = 0 cm. This asymmetry may derive from flow gradients introduced from upstream of the test section and can be seen in both probe and PIV velocity data spanning the test section above the downstream ramp, although the PIV data present a gentler gradient (Figure 39 and Figure 50). Figure 51 compares PIV and CFD streamwise velocities on centerline behind the pylon in the plane of the probe. PIV data sets using both stagnation tank seeding as well as cavity seeding were used to build a single PIV streamwise velocity profile. The two sets of PIV data are consistent with each other and measure a higher than computationally derived streamwise velocity. It is possible that the CFD results over-estimated the reverse flow velocity seen in Figure 51 since that is a common problem with base flow calculations (see Appendix B for further discussion).

Figures 52-55 present contours of streamwise velocity with velocity vectors in the normal (y-z) plane. The dashed white lines in each figure represent the outline of the pylon and the top of cavity leading edge at y = 0 cm. Figure 52 shows that the vortices

immediately behind the top of the pylon are still very small. However, the vortices grow and descend rapidly as the flow moves downstream (Figures 53-55). These vortices will draw fluid from the flow alongside the wake into contact with the cavity products being carried by the pylon wake. Figure 53 and Figure 54 show cavity flow exiting the base of the pylon wake up to about 2 cm above the top of the cavity and providing a larger volume of flameholder products to interact with the oncoming main flow. This outward flow at the base of the pylon wake appears to result from the interaction of streamwise vortices within the cavity interacting with the pylon wake. These vortices span the cavity from the leading edge and continue downstream out of the cavity as seen bracketing the base of the pylon wake in Figure 55. These vortex pairs should provide an avenue for igniting the oncoming fuel-air mixture above the flameholder assuming a suitable and reacting fuel-air mixture in and around the pylon wake. The raised shear layer seen in Figure 53 through Figure 55 will also provide an increased mixing area to the oncoming flow. The downward flow behind the cavity caused by the expansion behind the ramp shock seen below $y = 2$ cm in Figure 55 would tend to keep cavity products near the floor of the downstream duct. However, with the addition of the pylon, cavity products have been carried above the expansion and the ramp shock seen at $y = 4.5$ cm in Figure 55.

Both the baseline cavity and the pylon-cavity had a large vortex oriented across the cavity (z-axis) shown in Figure 56 for $z = 4$ cm. However, unlike the cavity-only case, the cavity flow was split into two regions by the pylon flow effects as shown in Figure 57b and d. In the pylon-cavity case, the flow below the pylon wake inside the cavity was generally upstream (negative x-direction) and upward (positive y-direction) as seen in

Table 7. Approximate cavity reverse-flow velocities (CFD, x = 8 cm, y = -2 cm, z = 4 cm)

Mean Reynolds Number (m^{-1})	Velocity (no-pylon) (m/s)	Velocity (pylon) (m/s)
3.2×10^7	130	155
4.2×10^7	130	155
4.9×10^7	135	155
5.5×10^7	135	160

Figure 41. The off-centerline flow behavior of the pylon-cavity model (Figure 56b and d) appears to be similar to the cavity-only model (Figure 56a and c) and previous cavity-only studies [13, 38, 39, 40, 42], i.e., the cavity flow was dominated by a large vortex oriented across the cavity (oriented in the z-direction). However, the addition of the pylon led to the vortex filling most of the cavity. Without the pylon, the off-centerline vortex was confined to the downstream 75% of the cavity with lower speed flow dominating the upstream portion. The only appreciable Reynolds number effect on the spanwise vortices was the more pronounced secondary vortex at the base of the cavity leading edge for the high Reynolds number, no-pylon case (Figure 56b). The reverse flow velocity across the bottom of the downstream ramp with the pylon installed (Figure 56b and d) was approximately 155-160 m/s or about 32% of freestream velocity. Without the pylon (Figure 56a), the velocity was about 130-135 m/s or about 26% of freestream velocity. The velocity magnitude down the ramp was a weak function of Reynolds number as seen in Table 7.

In the cavity mid-plane (y = -1.27 cm) seen in Figure 57, large counter-rotating vortices oriented with the y-axis dominate the flow on either side of the pylon wake (Figure 57b and d). These regions promote the flow moving forward and upward beneath

the pylon wake, and streamwise and downward along the tunnel walls. This pair of vortices defines a region of relatively slow moving flow. In the cavity-only case (Figure 57a and c), the vortices are confined to the upstream wall of the cavity. Changing Reynolds number had only small effect on these vortices. The outward vortices along the cavity leading edge appeared larger without the pylon (Figure 57c) and the streamlines with the pylon case (Figure 57d) passed closer to the side walls for the high Reynolds number case. The local residence time within these vortices should be relatively high, and, assuming a suitable fuel-air mixture is entrained into them, may provide a relatively still environment for stable flameholding. The interaction of these low velocity regions with the fast moving flow upstream beneath the pylon wake may provide the pool of reacting flameholder products to be carried upwards behind the pylon and into the main combustor flow.

According to Ref. [38], the dominant (downstream) vortex in a rectangular flow controls the mass exchange between the cavity and main flow. In turn, the smaller counter-rotating vortex against the upstream wall of the cavity exchange mass primarily with the downstream vortex. The end result is that there was little mass exchange between the smaller upstream vortex and the main flow. Assuming a combustible mixture in the dominant vortex, these regions of little mass exchange could potentially become too fuel rich for combustion. Figure 58 compares the upstream and downstream vortices within the cavity from this study as well as Ref. [38]. The arrows in Figure 58 signify the paths over which the mass exchange occurs. While the conditions are not identical, the overall behavior is consistent. Also notable is the shrinking of the upstream

vortex when the downstream wall is inclined and the even smaller upstream vortex when the pylon is installed.

In summary, the flow features associated with adding a pylon to a cavity flameholder have both positive and negative aspects. The flow is much more dynamic than the cavity-only case, as exemplified by the mass drawn up behind the pylon. Additionally, while the vortices in the cavity will increase the mass exchanged between different areas of the flameholder and the main flow, some vortices in the cavity, such as at the bottom of the front cavity wall or either side of the pylon wake, may entrap fuel and be too rich for combustion. These effects may define the limits on flameholder effectiveness, although direct air injection may expand the envelope [38, 40, 42]. The interaction of the vortices may improve the residence time within or near the vortices.

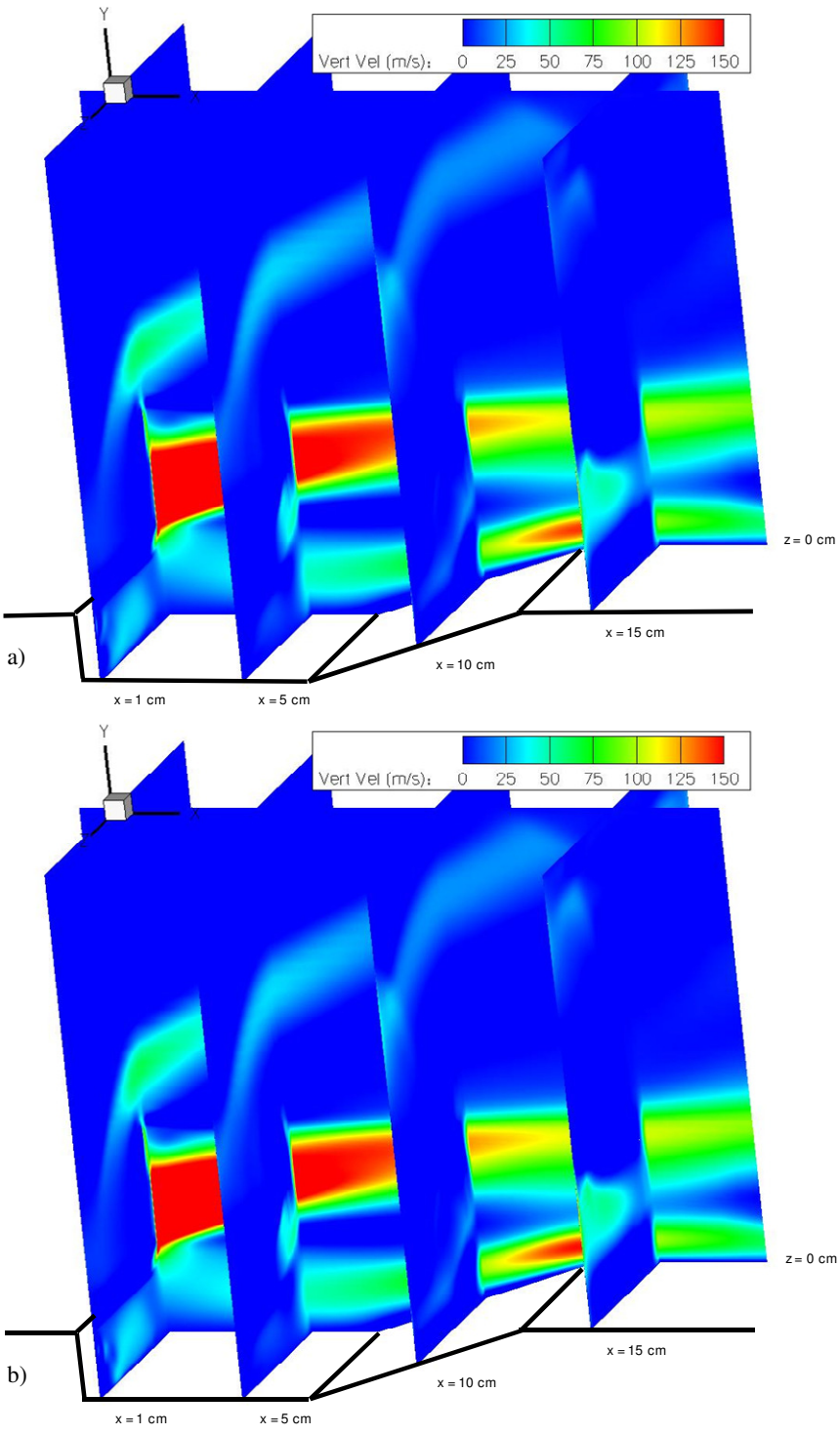

Figure 45. CFD vertical velocity contours
a) Re ≈ 32 x 10^6 m^{-1}; and b) Re ≈ 55 x 10^6 m^{-1}

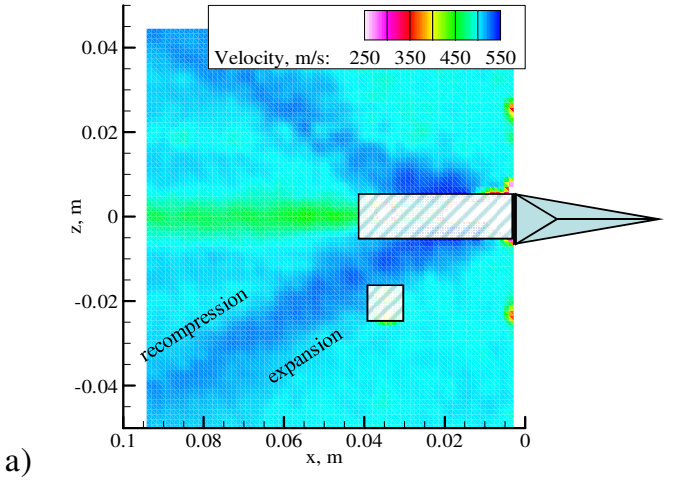

a)

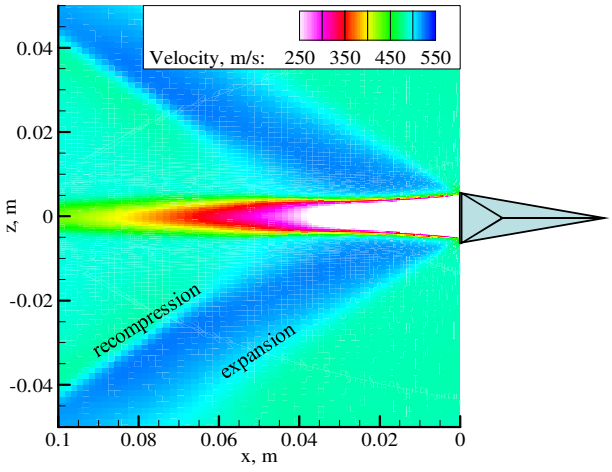

b)

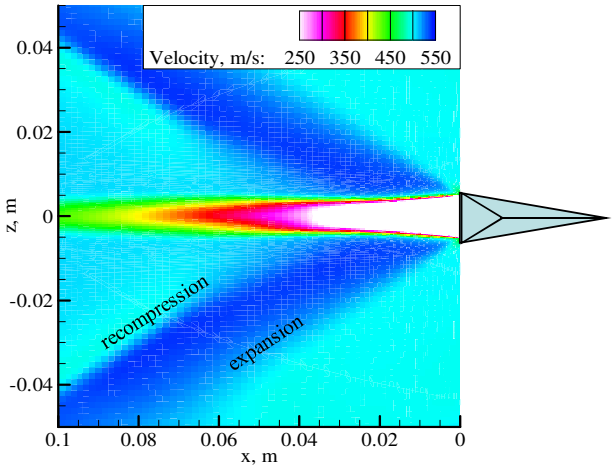

c)

Figure 46. Velocity magnitude behind pylon 3.7 cm above the cavity a) PIV data ($Re \approx 32 \times 10^6$ m^{-1}); b) CFD data ($Re \approx 32 \times 10^6$ m^{-1} and $T_t = 273$ K); c) CFD data ($Re \approx 55 \times 10^6$ m^{-1} and $T_t = 287$ K) (flow from right; hatched area unusable due to low particle density and surface reflections)

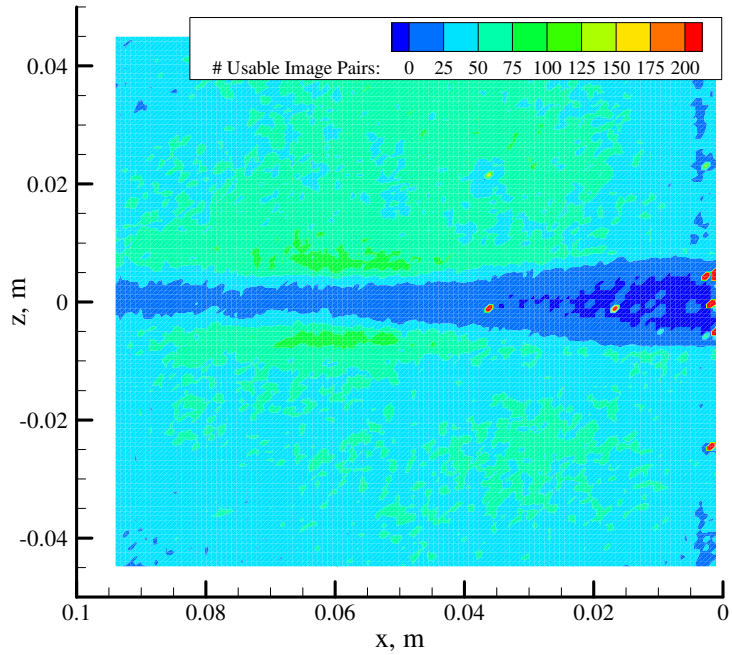

Figure 47. Number of usable PIV image pairs in wake flow 3.7 cm above the cavity (corresponds to Figure 46a; Re ≈ 32 x 10^6 m^{-1})

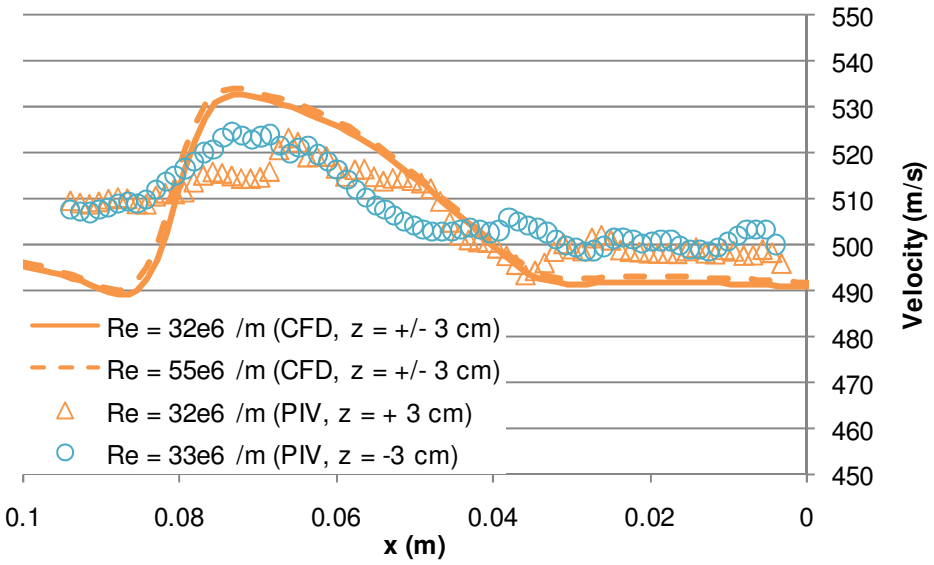

Figure 48. Profile of velocity magnitude on either side of wake (y = 3.7 cm, z = +/- 3 cm; CFD velocities corrected for temperature differences)

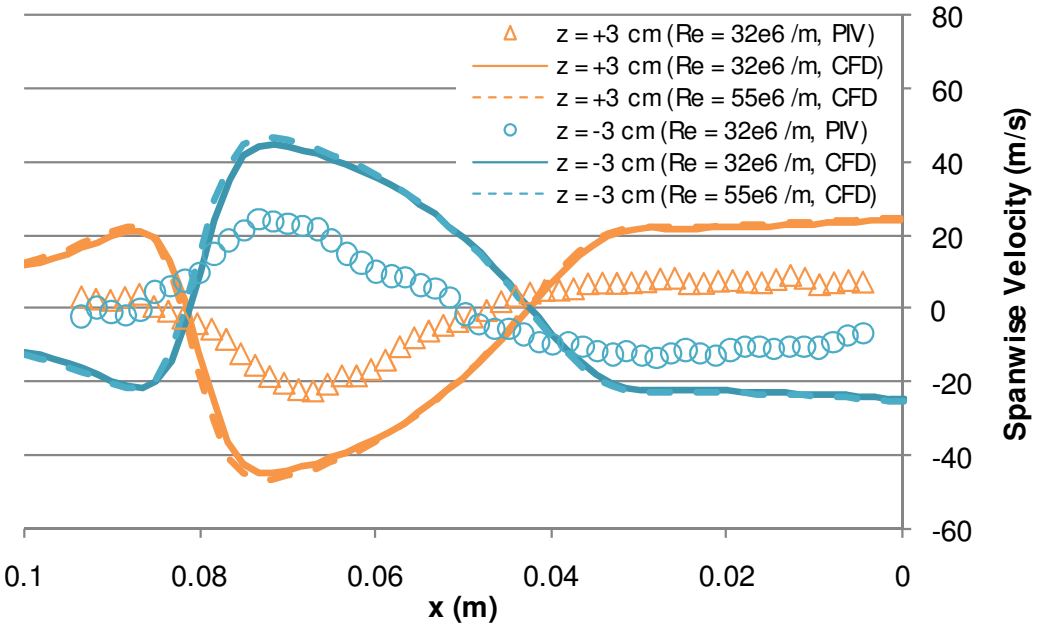

Figure 49. Spanwise velocities at z = +/- 3 cm

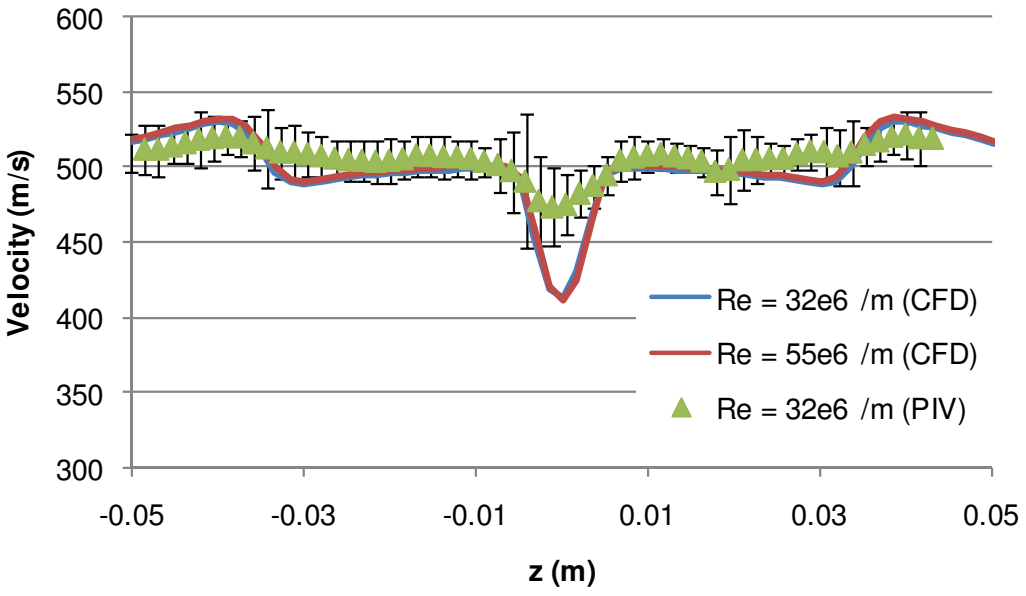

Figure 50. PIV and CFD velocity magnitude across test section with pylon (x = 8.8 cm, y = 3.7 cm, CFD velocities corrected for temperature differences)

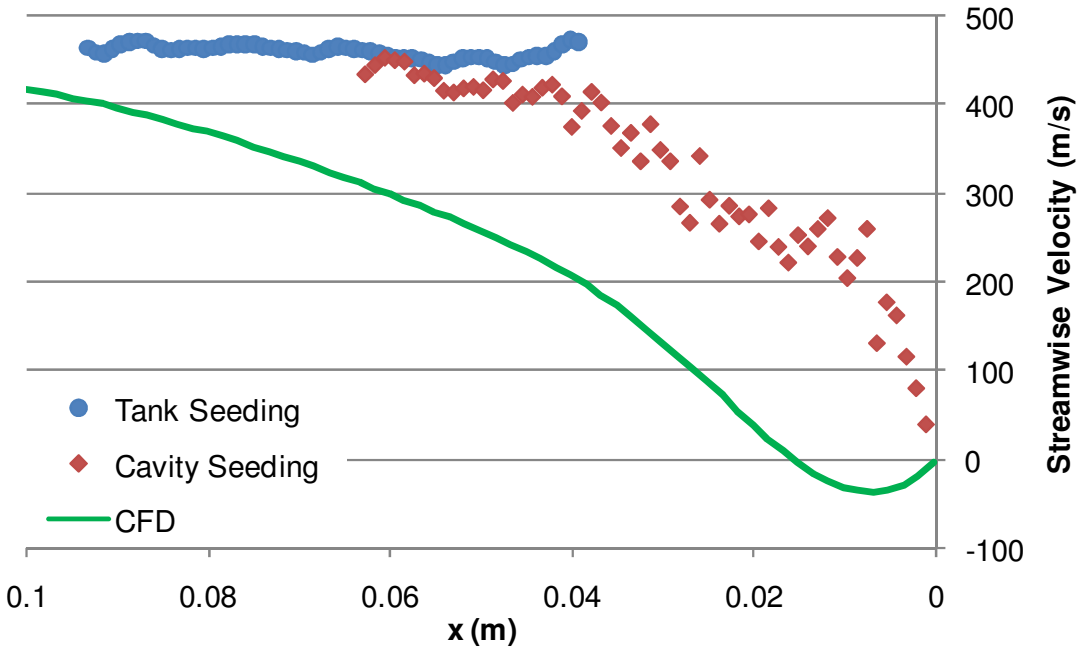

Figure 51. Streamwise velocity behind pylon
(y = 3.7 cm, z = 0 cm, Re ≈ 32 x 10^6 m^{-1})

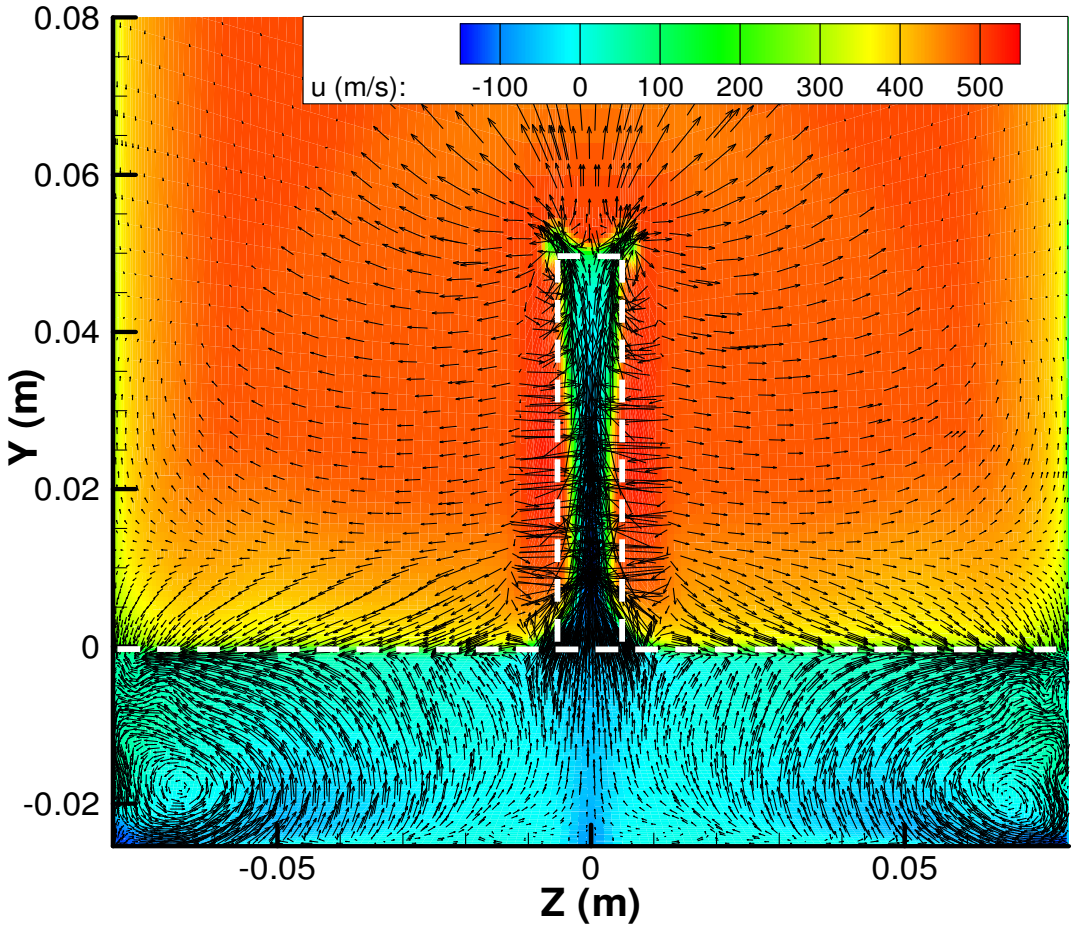

Figure 52. Velocity vectors in *y*-*z* plane at *x* = 1 cm across full span of test section (contours of *x* velocity; Re ≈ 32 x 10^6 m^{-1})

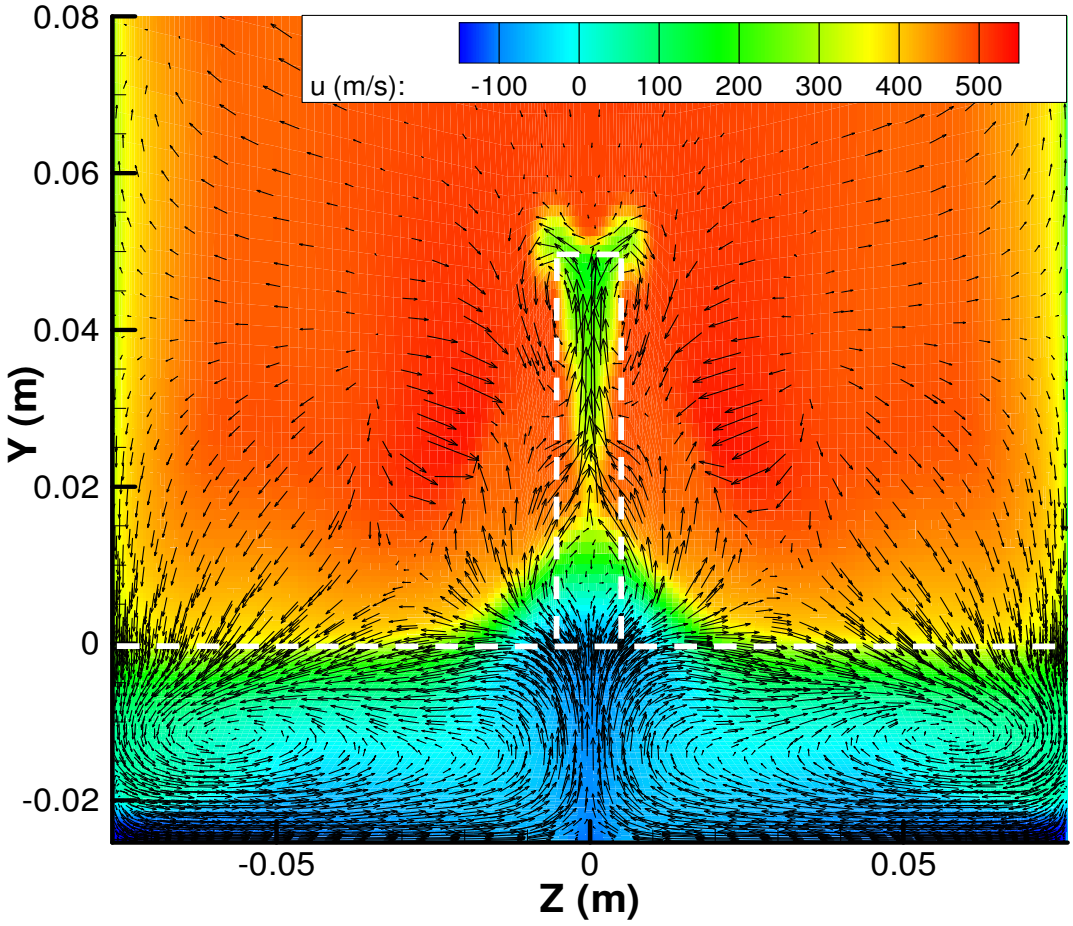

Figure 53. Velocity vectors in *y-z* plane at *x* = 5 cm across full span of test section (contours of *x* velocity; Re ≈ 32 x 10^6 m^{-1})

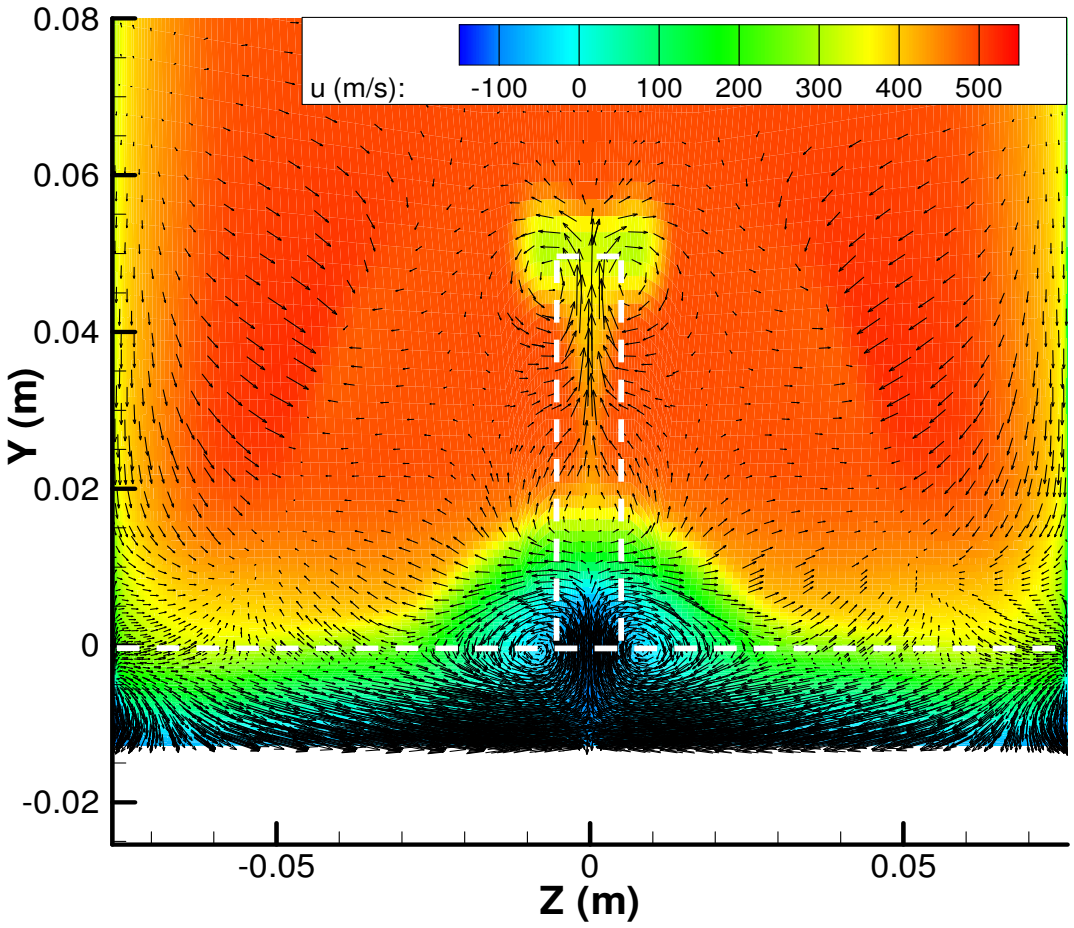

Figure 54. Velocity vectors in *y*-*z* plane at *x* = 10 cm across full span of test section (contours of *x* velocity; Re ≈ 32 x 10^6 m^{-1})

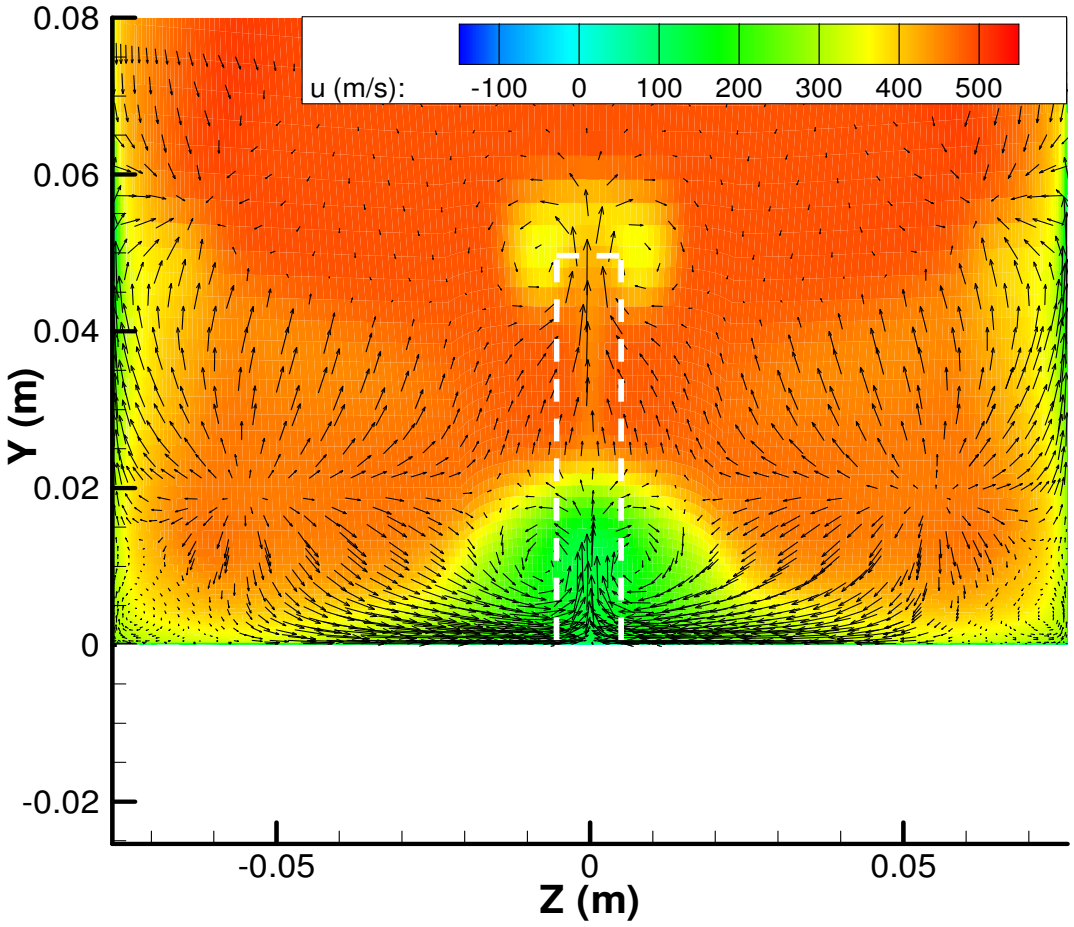

Figure 55. Velocity vectors in *y*-*z* plane at *x* = 15 cm across full span of test section (contours of *x* velocity; Re ≈ 32 x 10^6 m^{-1})

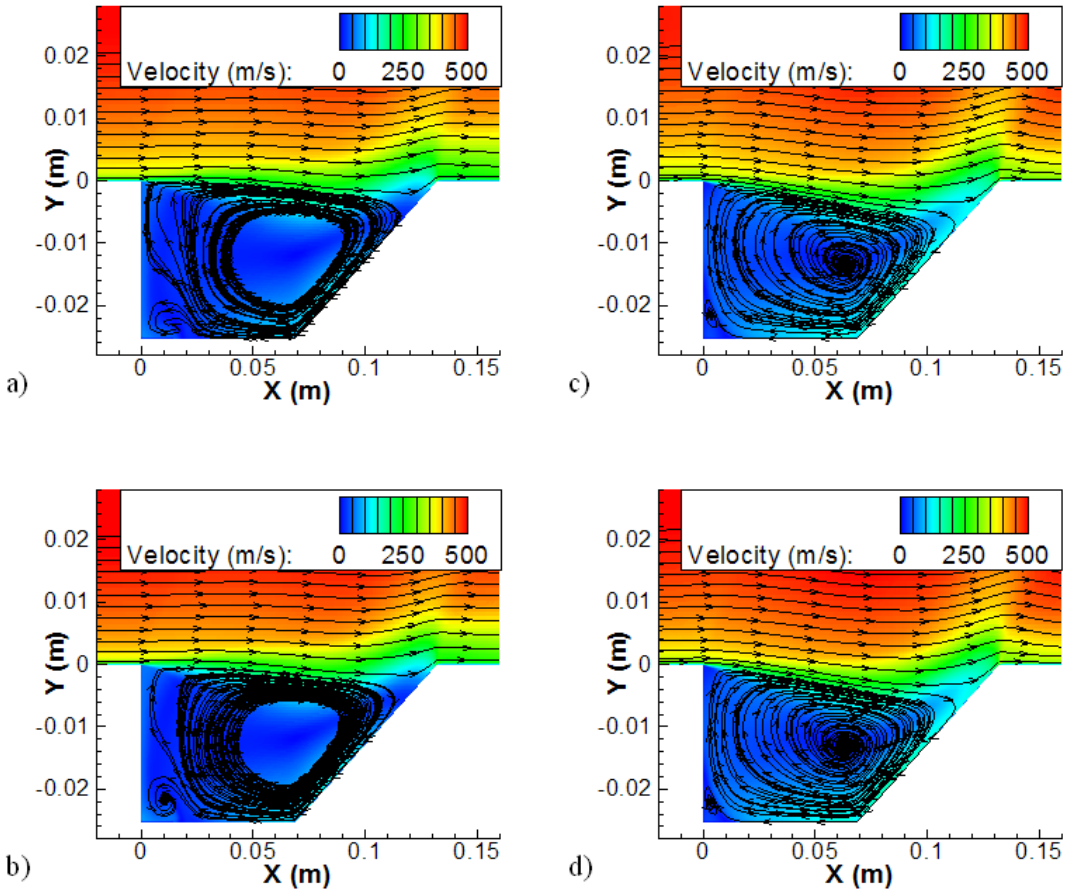

Figure 56. CFD streamlines off cavity centerline (z = 4 cm): a) without pylon (Re ≈ 32 x 10^6 m^{-1}); b) with pylon (Re ≈ 32 x 10^6 m^{-1}); c) without pylon (Re ≈ 55 x 10^6 m^{-1}); and with pylon (Re ≈ 55 x 10^6 m^{-1})

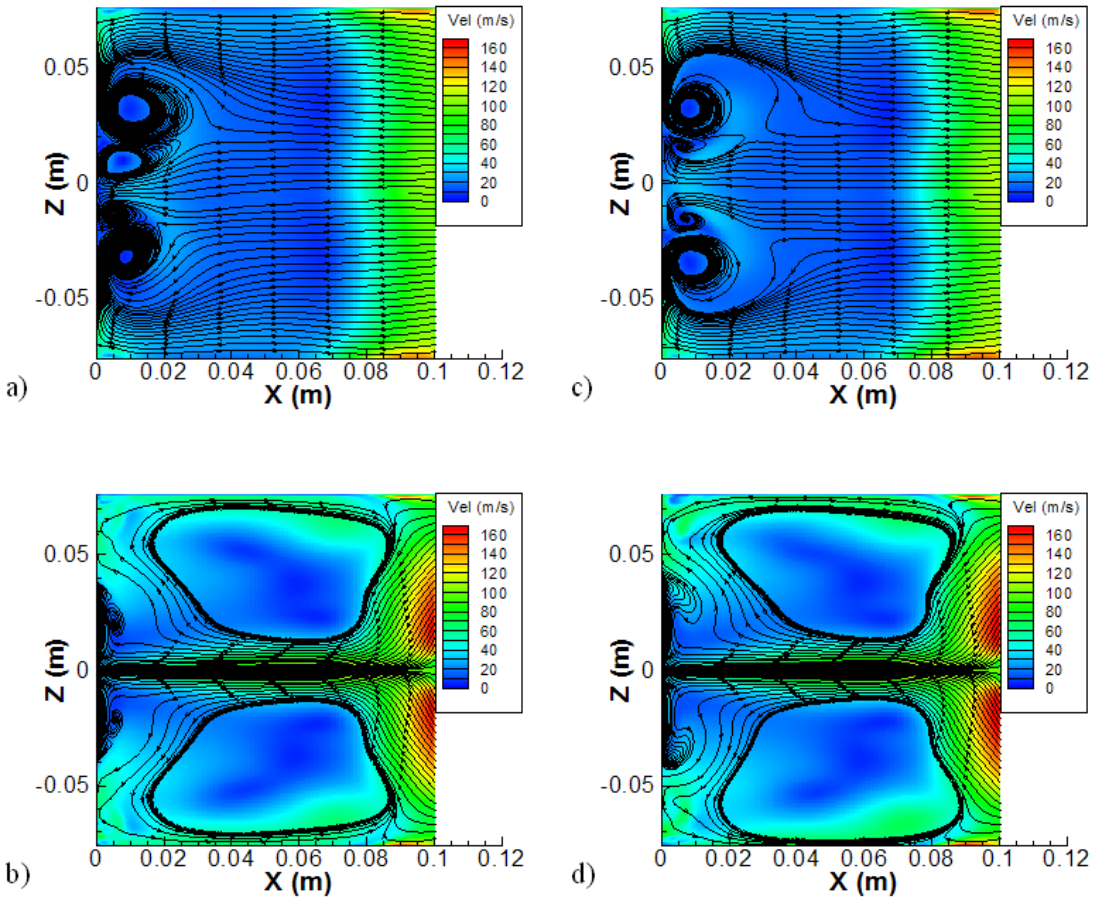

Figure 57. Velocity magnitude and streamlines in cavity mid-plane (y = -1.27 cm): a) without pylon (Re ≈ 32 x 10^6 m^{-1}); b) with pylon (Re ≈ 32 x 10^6 m^{-1}); c) without pylon (Re ≈ 55 x 10^6 m^{-1}); and d) with pylon (Re ≈ 55 x 10^6 m^{-1})

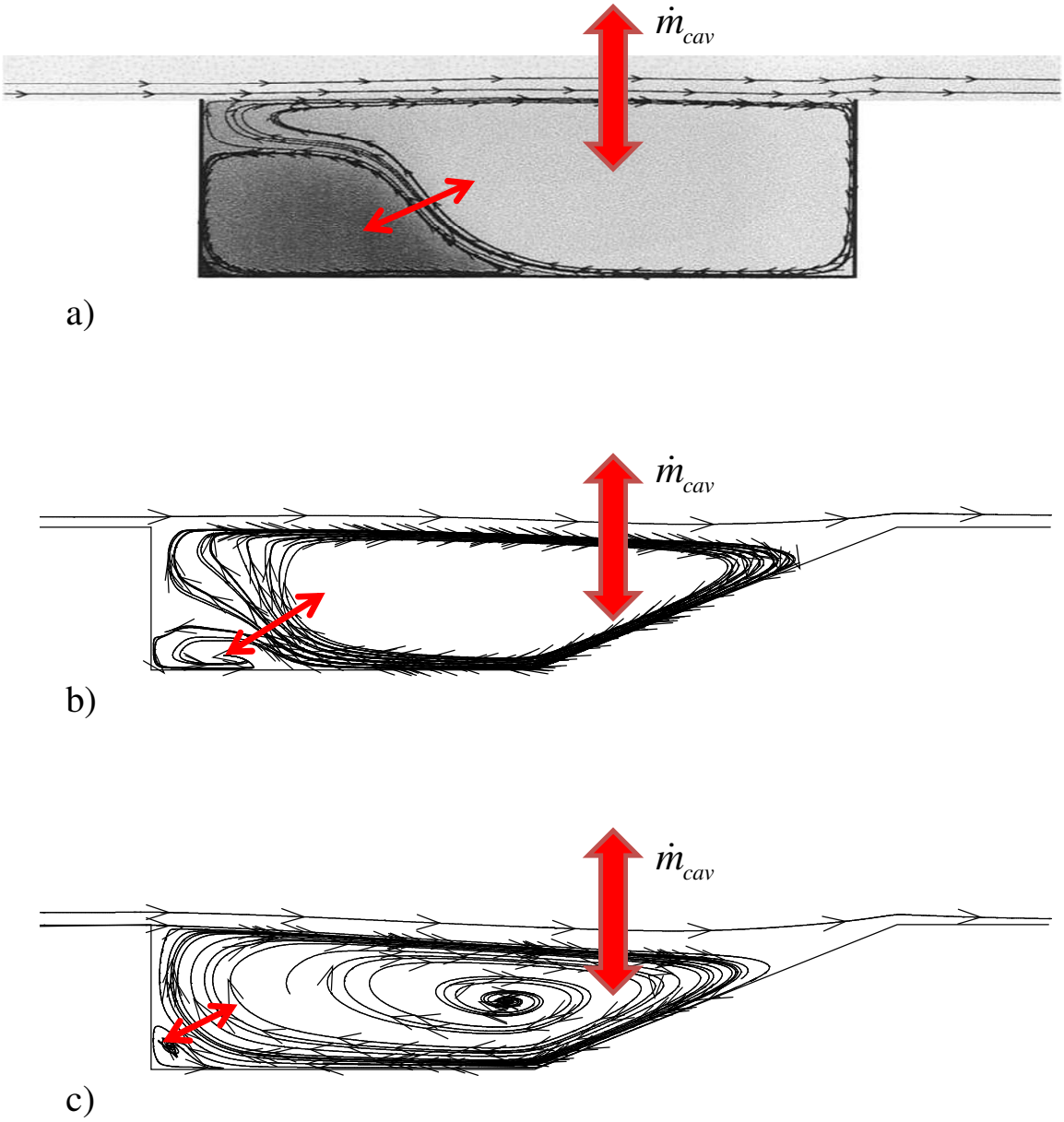

Figure 58. Diagram of mass exchange between the main flow and cavity vortices a) rectangular cavity (*M* = 3, Ref. [38]); b) no pylon (Re = 32 x 10^6 m^{-1}); and c) with pylon (Re = 32 x 10^6 m^{-1})

5.4 Frequency Data

Direct pressure measurements and high-speed Schlieren video enabled the exploration of unsteady flow within the cavity. The small magnitude of any pressure fluctuations on the cavity floor prevented the flush mounted transducer from detecting any significant fluctuations over the noise of the wind tunnel. Figure 59 shows the power spectrum for two wind tunnel runs with the baseline cavity as well as the ambient environment before starting the wind tunnel. As seen in Figure 59, no significant frequencies were detected above the noise except at approximately 6500 Hz which was determined to be a mechanical frequency associated with tunnel vibrations (determined by taping over the pressure transducer during a run and still getting the spike near 6500 Hz). The low magnitude of any pressure fluctuations further highlights the expected steadying effect of inclining the downstream wall in a cavity flameholder. Figure 60

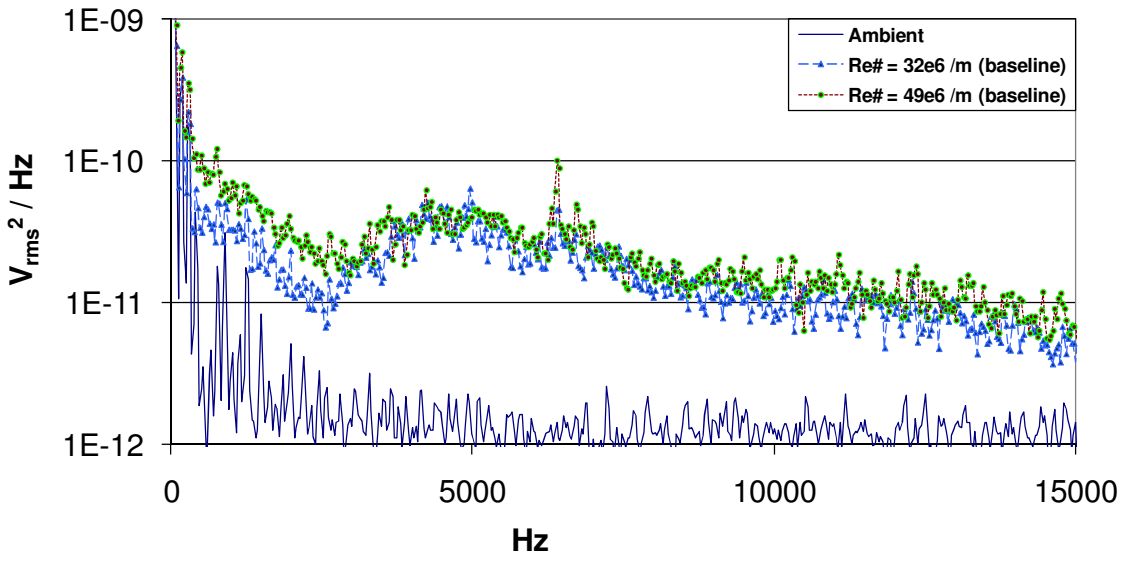

Figure 59. Pressure fluctuation power spectrum at ambient conditions (baseline cavity)

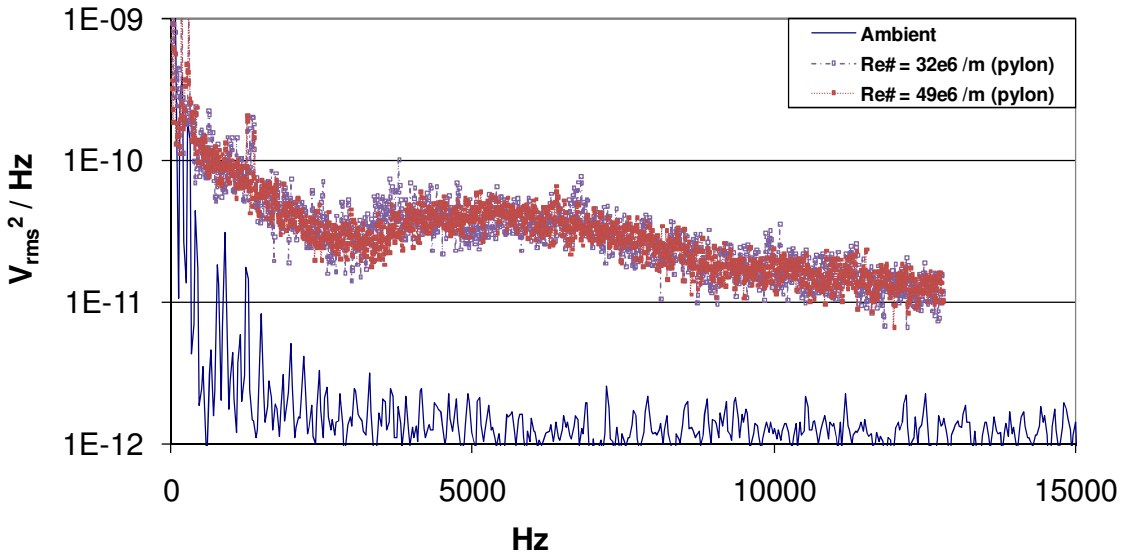

Figure 60. Pressure fluctuation power spectrum at ambient conditions (pylon-cavity)

presents the same data with the pylon installed. The overall noise level with the pylon is slightly higher at the low frequencies. The pylon data identify possible pressure fluctuations near 1300Hz. The cause of the 1300 Hz data is not certain, but doesn't correspond to a Rossiter mode in an open cavity flow as determined below for the baseline cavity. The frequency data in Figure 59 and Figure 60 indicate that the magnitude of any pressure fluctuations at the transducer must be less than approximately 5 Pa (0.0007 psia) [67].

The other means of collecting frequency data took advantage of the high-speed video system used for Schlieren photography. Only the baseline cavity produced observable structures for the high-speed video. Attempts to video unsteady flow with the pylon installed were unsuccessful. The high-speed video provided a means to determine convective velocity, U_c, of the baseline cavity shear layer. As previously described, the

convective velocity is the speed at which large structures within the shear layer travel downstream. Using 16,000 fps video of the shear layer developing between the baseline cavity leading edge and 7 cm downstream the convective velocity at Re ≈ 42 x 10^6 m^{-1} and $M = 2$ was estimated at 200 m/s. Figure 61 shows some of these structures propagating downstream. Structures within the shear layer are thought to be a trigger of cavity unsteadiness. Disturbances generated by the shear layer structures impinging on the downstream wall of the cavity will propagate upstream in the cavity and create more disturbances in the shear layer. Knowing the convective velocity and length of the shear layer allowed the estimation of the cycle frequency. Since the shear layer impinges on the ramp at approximately $x = 12$ cm and the measured convective velocity was approximately 200 m/s, the resulting frequency is approximately 1670 Hz, which corresponds to the second Rossiter mode. Since the main flow was approximately 500 m/s, $K = U_c/U \approx 0.4$. The phase lag term, α, in equation 5 varies with cavity length as tabulated in Ref. [28]. Using the impingement length for the inclined ramp instead of the previously defined cavity length results in $\alpha \approx 0.32$ [28:7]. Applying equation 5 with $K = 0.4$, $\alpha = 0.32$, $L = 0.12$ and $M = 2$, results in a second mode frequency estimate of approximately 1750 Hz, which is well within the 10% margin of accuracy claimed in Ref. [28]. The frequency estimate approaches 1670 Hz when $\alpha = 0.4$. The constants K and α, are frequently adjusted in the literature to better fit empirical observations [25; 26; 36], so the wind tunnel derived $K = 0.4$ and $\alpha = 0.4$ are not unreasonable values. Using $K = 0.4$ and $\alpha = 0.4$ with equation 5 the first three Rossiter modes for the non-reacting baseline cavity flameholder should be: 630 Hz, 1670 Hz and 2700 Hz. A more sensitive pressure

transducer would be required to detect fluctuation modes, if present. Locating the flush-mounted pressure transducer on the ramp may also improve the possibility of detecting pressure fluctuation modes since the fluctuation magnitude should be higher near the shear layer impingement [28; 68].

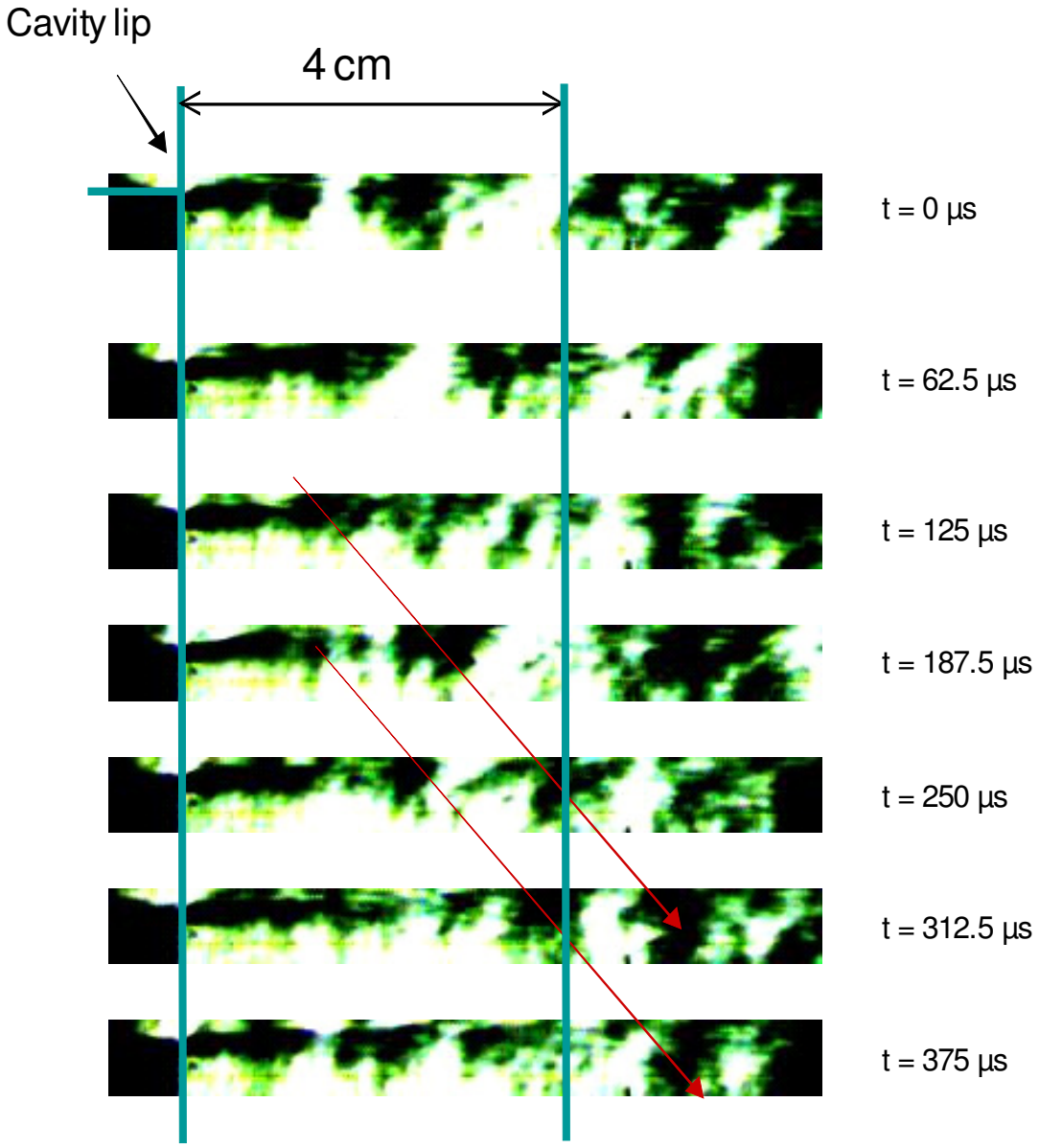

Figure 61. High-speed Schlieren frames of flow separating at the leading edge of the cavity showing structures propagating downstream (baseline cavity, Re# ≈ 42 x 10^6 m^{-1})

5.5 Cavity Mass Exchange/Residence Time

Addition of the pylon to the leading edge of the cavity should enable a greater exchange of mass between the free stream flow and the flameholder. This additional mass will be available to react within the flameholder and return to the main flow through the pylon wake or edge of the cavity and improve the flameholder performance. The average mass flow passing from the main flow through the cavity and back to the main flow was estimated by integrating the positive mass flow per unit area determined using CFD across the top of the cavity:

$$\dot{m}_{cav} = \left[\int_A \rho u_{y_+} dA \right]_{y=0} \tag{11}$$

where ρ is the local cell density and u_{y+} is the positive component of vertical velocity. Only the positive component is needed since the mean mass flow into the cavity and out of the cavity are equal (the difference between positive and negative mass flow CFD solutions through the top of the cavity is less than 1%). Figure 62 and Figure 63 show the vertical velocity components across the top of the cavity (y = 0 cm). The flow exiting the cavity in Figure 62 is concentrated beneath the pylon wake and above the downstream ramp. The bulk of the flow entering the cavity occurs about halfway across the cavity (x ≈ 5 cm). This flow pattern suggests that upstream fuel injection near the sides of the duct would enable the flameholder to capture fuel from upstream. The flow in Figure 63 exhibits more two-dimensional behavior with the only significant upward flow restricted to the vicinity of the trailing edges of the cavity. Unlike the situation with pylon installed the entire span of the baseline cavity captures some of the oncoming flow.

The previously discussed flow structures mechanically drive much of the mass exchange in the very three-dimensional pylon-cavity flow. In contrast, the cavity-only case has significantly less interaction between the cavity flow and free stream. Since a steady-state CFD calculation cannot reliably predict cavity residence time, the mass flow ratio (*MFR*) provides a better comparison between pylon and no-pylon cases, i.e., the proportion of free stream mass flow that passes through the cavity:

$$MFR = \dot{m}_{cav} \Big/ \dot{m}_{freestream} \tag{12}$$

The mass flow ratio of the pylon-cavity case was approximately 0.012 for all Reynolds numbers, i.e., slightly over 1% of the mass flow transits the cavity. Without the pylon, the mass flow fraction was 0.004 for all Reynolds numbers, or about one-third the cavity mass flow of the pylon-cavity. Assuming fuel injection upstream of the flameholder, three times more fuel-air mixture passes through the flameholder and back into the freestream per unit time with the pylon added to the leading edge. As described in Ref. 38, increasing cavity length also increases the mass exchange with the free stream. However, the addition of a pylon significantly alters the cavity flowfield and produces more dynamic three-dimensional effects than only lengthening the cavity. Cavity mass flows approximated using Ref. [38] data showed a modest increase (~ 15%) when increasing cavity L/D from three to five as opposed to the approximately 300% increase from the addition of the pylon used in this study. Note that these characteristics would obviously change in the case of direct cavity injection of fuel and/or air. Also, the *MFR* presents only the mean mass flow through the top of the cavity and fails to account for significant local differences. For instance, in the middle of the relatively still flow on

either side of the cavity, as seen in Figure 57b and d, the local residence time will be relatively high.

In general, increased mass exchange can be beneficial in terms of exposing more reacting flameholder products to the main flow. However, the inverse relationship between mass exchange and residence time, requires care to ensure that mass exchange isn't increased beyond the capability of the flameholder to sustain combustion. If necessary, increasing the cavity depth, and therefore volume, should increase overall residence time. As described in Ref. 38, the flameholder mass exchange will decrease in a reacting flow with the resulting increased residence time. Therefore, the cold-flow relationships noted in this study are conservative with regards to mean residence time.

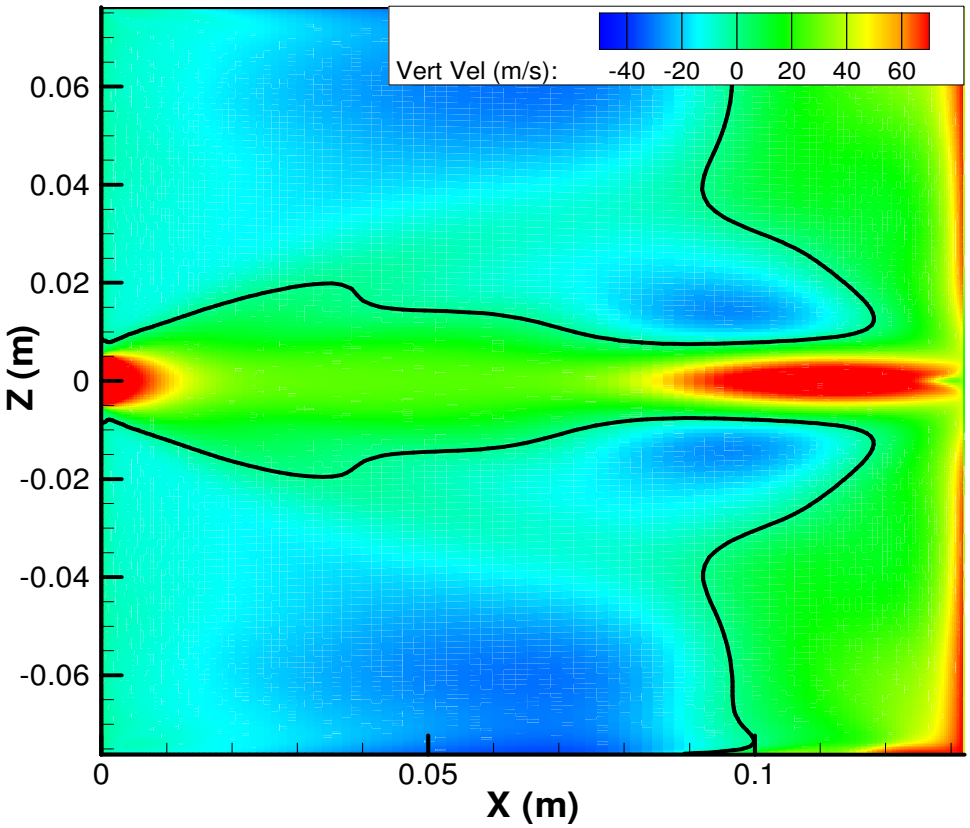

Figure 62. Vertical velocity contours at the top cavity boundary (y = 0 cm) for Re# ≈ 32 x 10^6 m^{-1} (pylon installed; black line indicates zero vertical velocity)

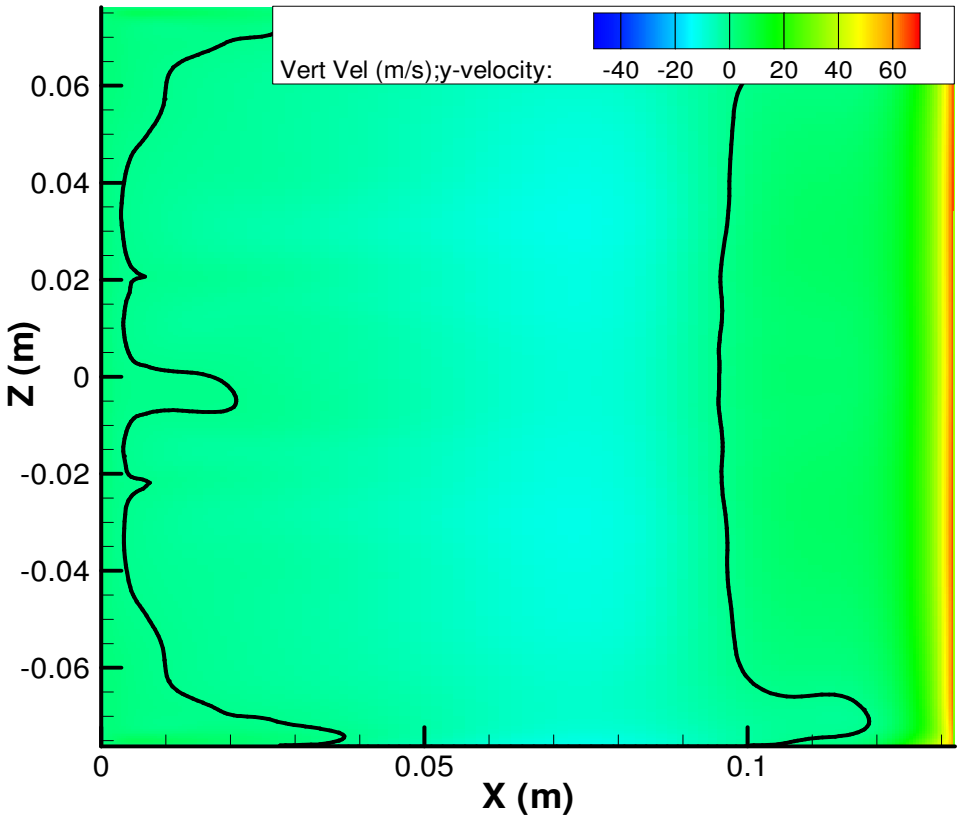

Figure 63. Vertical velocity contours at the top cavity boundary (y = 0 cm) for Re# ≈ 32 x 10^6 m^{-1} (baseline cavity; black line indicates zero vertical velocity)

VI. Summary and Conclusions

6.1 Summary

Results of the combined experimental/computational study of an inclined cavity flameholder with a leading edge pylon will fill a gap in the literature and help bound part of the design problem facing a scramjet engine designer opting to use a pylon-cavity flameholder. The addition of a pylon to a cavity flameholder may provide a necessary performance boost for effective use of hydrocarbon fuels. Hydrocarbon fuels are preferred over hydrogen at low hypersonic Mach numbers due to the simpler logistics and smaller resulting flight vehicles. The test conditions were Mach number of two and unit Reynolds numbers between approximately 32 million m^{-1} and 55 million m^{-1}. Computational solutions were steady-state and non-reacting.

PIV, pressure measurements, and CFD provided evidence of strong upward flow of cavity fluid in the low pressure region behind the pylon. The low pressure behind the pylon resulted from supersonic expansion around the pylon edges. Both CFD and surface pressure measurements showed the pressure coefficient on the downstream face of the pylon (3.7 cm above the tunnel floor on centerline) equaled approximately -0.16 at all Reynolds numbers. Shadowgraph flow visualization in combination with CFD showed the pylon wake extending up to the height of the pylon and even slightly higher on the outboard edges, providing a means of carrying flameholder products into the main flow. Computational velocity profiles showed the cavity shear layer rising up near the pylon wake with cavity products carried up above the tunnel floor. The combined pylon wake

and cavity shear layer present an increased mixing area to the oncoming flow compared to the cavity-only shear layer which remained nearly level with the tunnel floor.

Adding the pylon resulted in a pair of large counter-rotating vortices within each half of the cavity. These vortices contained relatively large, low-velocity regions surrounded by fast moving flow upstream along the cavity floor on centerline. These regions were beneath the main source of mass flow into the cavity that eventually makes its way into the pylon wake. Spanwise vortices, such as found dominating cavity-only flows were present on either side of the cavity wake and tended to fill more of the cavity volume than identical L/D cavities with no pylon.

Computational studies of the mass flow transiting the plane separating the cavity and duct indicated substantially increased cavity mass flow. Calculated as a percentage of the total flow to pass through the cavity, installing the pylon increased the cavity mass flow from approximately 0.4% to approximately 1.2% at all Reynolds numbers. Increased mass flow comes at the cost of decreased residence time and requires care to ensure residence time does not decrease below that required for stable combustion in the flameholder.

Variations in Reynolds number provided a means to explore any significant effects from changing design point or change in scale. The primary flow features of interest, i.e., flow upward behind the pylon, location of the shear layer/wake, and mass exchange appeared unaffected by changing Reynolds number. The only significant Reynolds number effects noted were small changes in the size of the spanwise and vertically oriented cavity vortices.

This study required a new, more accessible test section than the original 6" x 6" wind tunnel test section. Design, construction and commissioning of a new test section, inserted downstream of the original test section, provides AFIT with an upgraded wind tunnel facility suited to wall-based wind tunnel research. The test section had optical access through the top and both sides. Alternatively, a side window could be replaced with a mounting plate for probe measurements. The test section floor accommodated access to the test article for surface pressure tap tubing, pressure transducer wiring and PIV seeding. Schlieren/shadowgraph flow visualization, surface pressure measurements, probe measurements, and PIV were all used successfully in the new test section for this study. Flow seeding was accomplished using a CO_2/dry ice clean seeding method under development at AFIT.

6.2 Conclusions

- The flowfield resulting from installation of a pylon to the leading edge of a cavity flameholder in a $M = 2$ cold flow resulted in a strong upward flow from the cavity reaching approximately sonic velocity in the low pressure pylon base region extending approximately 2 cm downstream of the pylon. This upward flow persisted to approximately the top of the pylon and provides a mechanism for improved transport of reacting flameholder products into the main combustor flow when compared to cavity-only flameholder configurations.
- The combined pylon wake and cavity shear layer provided a larger interface to the oncoming fuel-air mixture. This larger interface provides more area for hot flameholder products to interact and ignite the oncoming fuel-air mixture. Better

flame-spreading may reduce the required combustor length for complete combustion in the supersonic flow, thus increasing engine thrust to drag ratio.

- Mass exchange for the pylon-cavity flameholder increased approximately three times over the mass exchange of the baseline cavity flameholder. The increased mass exchange means more availability of reacting flameholder products to aid ignition of an oncoming fuel-air mixture in the main flow as well as more oncoming fuel-air mixture passing through the cavity to reduce the fuel-rich tendency of cavity-only flameholders.
- Flow features unique to the pylon-cavity combination can provide an effective mechanism for improved flameholding. Large, vertically-oriented, counter-rotating vortices inside the cavity on either side of the pylon wake contain significant low-velocity regions while passing flow upstream between them toward the base of the pylon at approximately 20% of the free stream velocity magnitude. These regions reside within spanwise vortices inside the cavity which draw mass from the oncoming fuel-air mixture and provide the primary source of mass flow passing through the cavity. With a flammable oncoming flow, these vortices, taken together, bring together critical elements needed in an effective flameholder: slow moving flow (i.e., long residence time), and a replenishing, suitable fuel-air mixture.
- Flight operations do not happen at a single altitude and vehicle designs may be larger or smaller than research test articles. Negligible Reynolds number effects over the range tested provide confidence that the pylon-cavity combination will maintain stable operations over changing design points or physical scaling in size. The lack of

any appreciable Reynolds number effects suggests that limited extrapolation of the flowfield described in this study towards lower, more flight representative Reynolds numbers is reasonable.

- The new test section provides AFIT with an upgraded facility to study wall-based phenomena in supersonic flows using a variety of instrumentation. This new capability is well suited for future scramjet combustor-related research simulating flight vehicle Mach numbers up to approximately ten. The use of particle image velocimetry for flameholder research had not been previously accomplished in this wind tunnel and, together with the supporting data collected through other methods, contributes valuable data to developers seeking to perfect the new CO_2 clean seeding method at AFIT.

6.3 Recommendations for Future Research

Future research into pylon-cavity flameholders can proceed in a number of directions. While future studies could proceed purely computationally, the use of combined experimental/computational studies lends more weight to the results obtained and should be considered whenever practical. Some recommendations include:

1. Characterize the flow parameters and structures, such as cavity mass exchange/residence time, pylon base pressure, ramp surface pressures, or pylon wake up-flow velocity with differing pylon/cavity geometries. For instance, the test article in this study was not designed for minimum losses or maximum mass exchange and determining these limiting cases would help define the envelope of pylon-cavity flow.

2. Characterize the flow parameters as a function of both Mach number and Reynolds number instead of Reynolds number alone. The current flameholder test condition, $M = 2$, corresponds to a low hypersonic flight condition and testing higher Mach numbers would expand knowledge of the operating envelope.
3. Quantify mean residence time in the cavity using a time-accurate cold-flow or reacting flow CFD simulation. Mean residence time results for different flow conditions will enable a first estimate on the overall ability of the cavity to sustain combustion using various fuels.
4. Examine the large, vertically-oriented cavity vortices in order to determine under what conditions they will provide a ready pool of hot flameholder products for the upward flow behind the pylon. Quantifying local residence time and mass exchange behavior within these vortices will provide insight on exploiting the low-velocity regions within the cavity even if mean residence time of the cavity becomes too small for effective combustion.
5. Define the effect of reacting flow on the cavity-pylon flow structures. Stable burning in pylon-cavity flameholders has already been demonstrated, but combustion effects on the areas described in this study present a logical next step in this line of research.
6. Explore direct fuel and/or air injection in the cavity supporting the natural flow structures of the pylon-cavity flameholder. For example, injecting fuel downward and inward along the downstream ramp and injecting air forward from the edges of the cavity step, as illustrated in Figure 64, could strengthen the already existing

flow structures, hopefully alleviating some of the losses associated with injection and providing a better fuel-air mixture to interact with the main combustor flow.

7. Study the influence of high back-pressure induced shock trains on the pylon-cavity flowfield. Shock trains can result from boundary layer separation due to the adverse pressure gradient encountered as the flow passes from the inlet through the supersonic combustor or from slowing a supersonic inlet flow to subsonic speeds in a ramjet mode [2]. Both reacting and non-reacting studies would provide insight on the flow structures and flameholder environment with a shock-train passing over or upstream of a pylon-cavity flameholder.

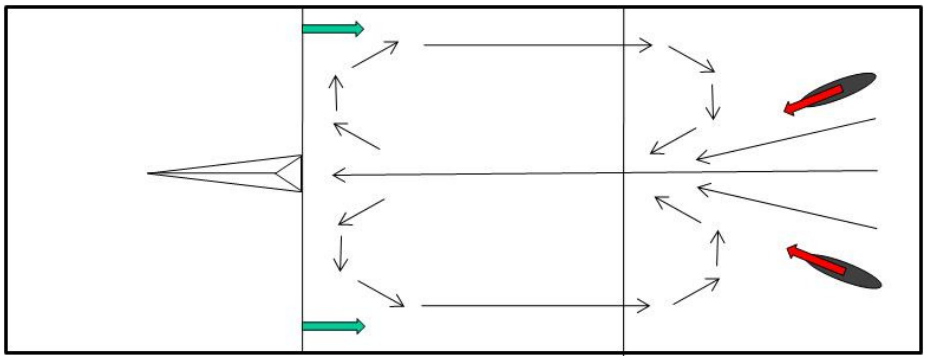

Figure 64. Notional cavity fuel-air injection scheme

Appendix A: Wind Tunnel Operations

This appendix details the design of the add-on test section for the 6" x 6" wind tunnel. Lab procedures and data reduction techniques will also be reviewed. This appendix can loosely serve as an operations manual for the 6" x 6" tunnel since the modifications and new instrumentation make the very small amount of previous documentation obsolete.

A1. Test Section Design and Construction

The existing 6" x 6" supersonic wind tunnel test section was unsuited for wall-based testing. An add-on test section, designed and built in-house, was inserted behind the existing test section and upstream of a sliding diffuser section. Figure 65 pictures the wind tunnel before and after the new test section was inserted. Figure 65c shows a close up view of the new test section with the baseline cavity test article installed. Figure 66 through Figure 72 present the three-view drawings of the new test section. Figure 73 through Figure 75 present the cavity test article, plain and pylon inserts. Figure 76 provides the location of the surface pressure taps. The test section was constructed of steel, except for the window frames which were made of aluminum. The test article was fashioned of aluminum. Both glass and plastic windows were manufactured. RTV silicon rubber was used to seal the junctions.

There were several small errors in the wind tunnel construction. The most prominent were at the junction between the old and new test section and the window mounting on the $-z$ side plate (see Figure 77). The side walls at the junction lined up poorly which resulted in a sudden expansion on the $+z$ side on the order of 1 mm and a contraction on the opposite side on the order of 1 mm. The contraction was smoothed out

to minimize flow disruption without measurable success. A CFD model including a similar expansion and contraction on the tunnel side walls failed to fully model the skewed flow. While the CFD results failed to match the tunnel data the pressure gradient direction was correctly modeled as increasing toward the $-z$ side of the downstream ramp. Interaction with other identified and unidentified flow disturbances, such as the small expansion at the top window frame resulted in a complex flowfield that wasn't successfully modeled. However, CFD does support the construction errors as the cause of the flow gradients in the test section. The window mount errors resulted from milling the steel plate incorrectly and required significant silicon filler to cover the gaps which led to a relatively rough surface on the inside leading edge of the window.

This first attempt at a new test section design should be considered a prototype. Numerous problems had to be overcome in order to get usable data. The errors at the test section junction and top window frame have already been discussed. Other problems included the method of sealing the test section. Anytime the configuration was changed, e.g. from side window to probe, the frame had to be re-sealed which required 24 hours curing time. Additionally, leaking from underneath the test section required excessive sealant, to the point that the lower sliding block of the wind tunnel could not be adjusted and restricting testing to a single Mach number. The next version of the test section should include dry gaskets or o-rings for sealing gaps to prevent down time and ease operator workload. A provision for an *easy-on/off* top window frame would greatly simplify changes to the test article, such as installing or removing the pylon.

a)

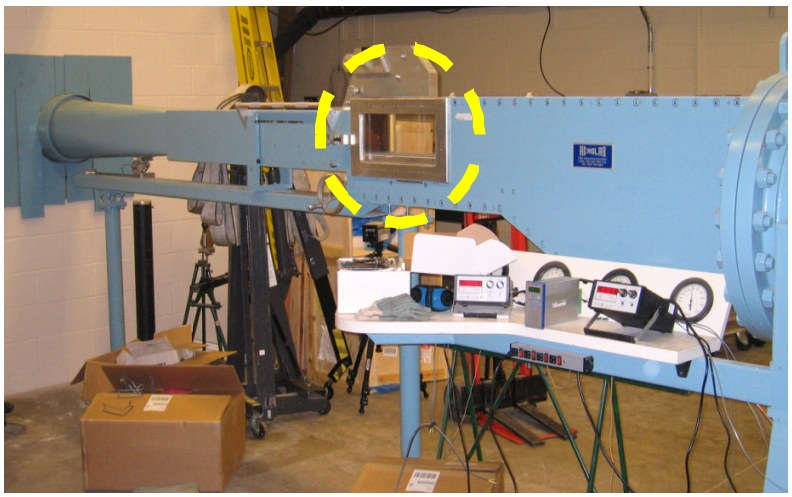

b)

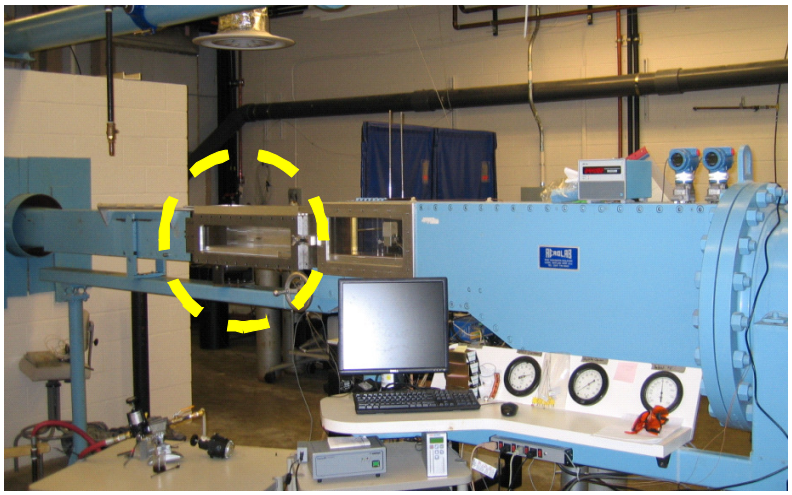

c)

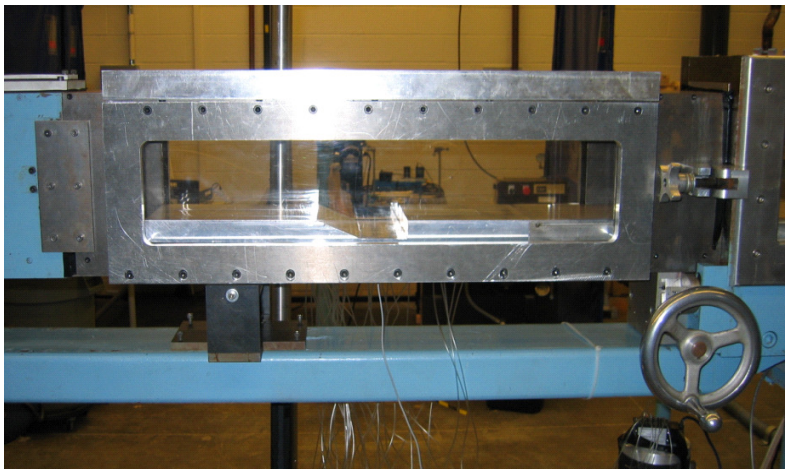

Figure 65. AFIT 6" x 6" Supersonic Wind Tunnel: a) original test section; b) new Test section inserted behind old test section; c) closeup of new test section with baseline cavity test article installed

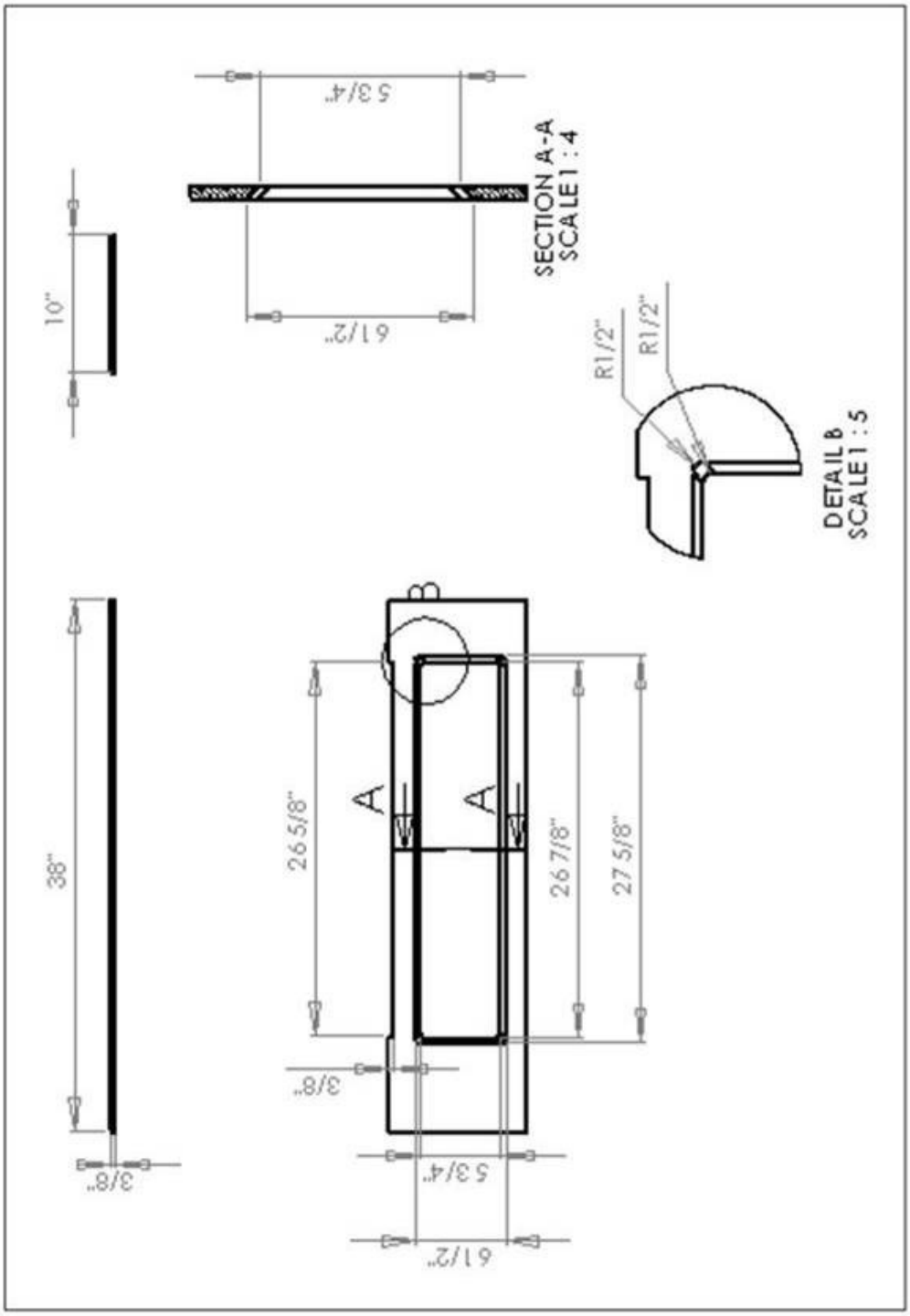

Figure 66. Test section side plate

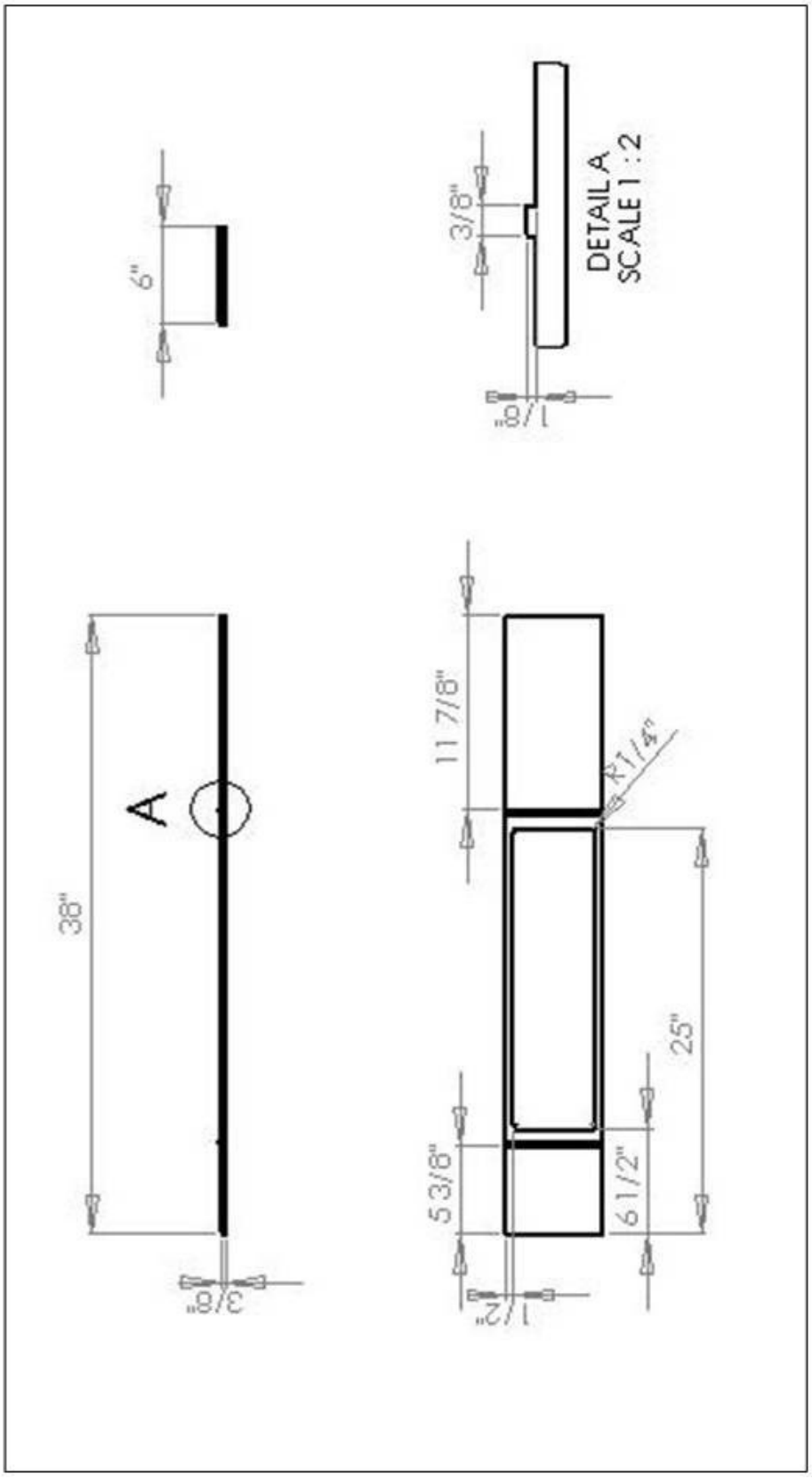

Figure 67. Test section bottom plate

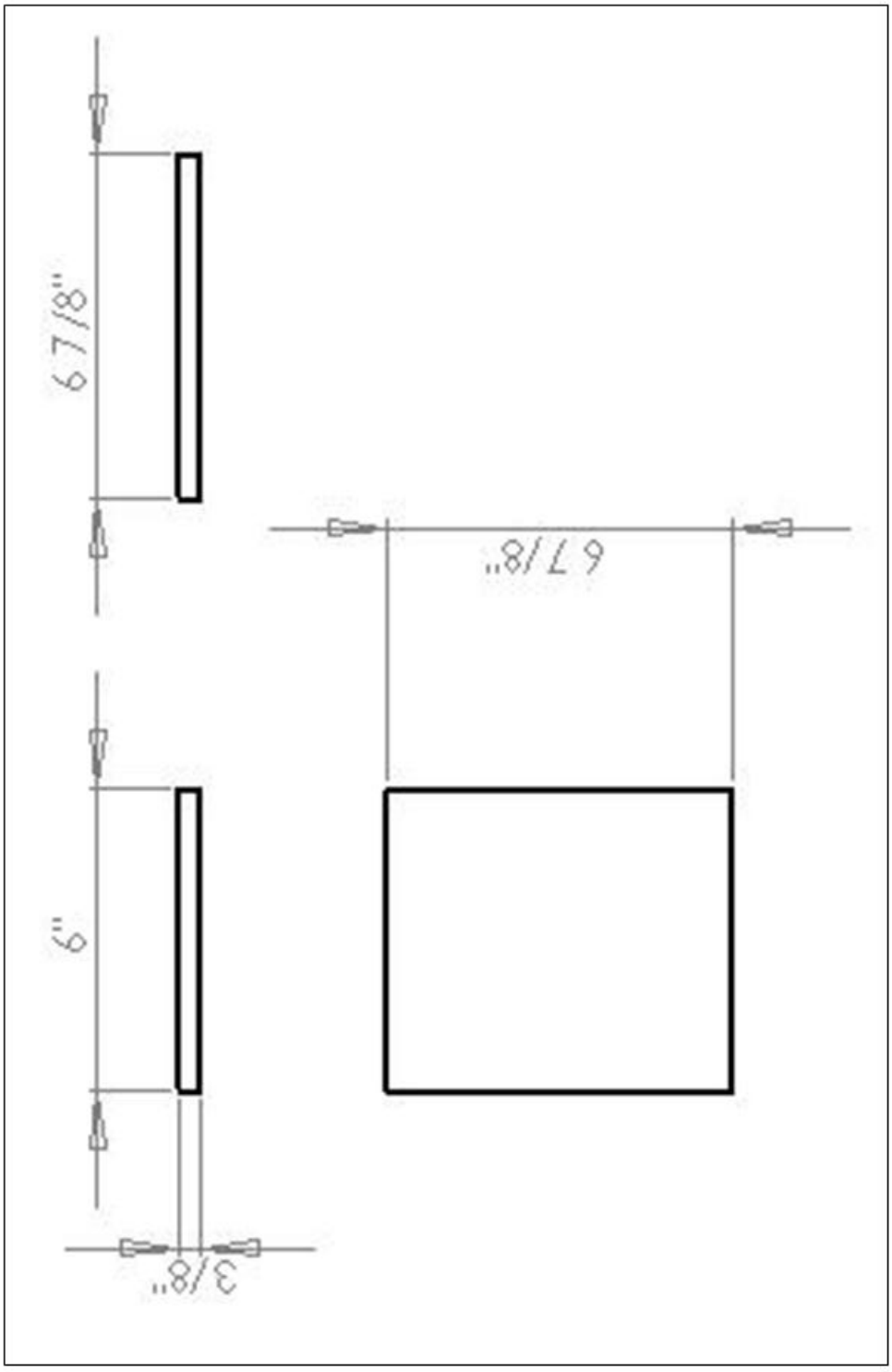

Figure 68. Test section top plate (6 7/8 in or 4 in long)

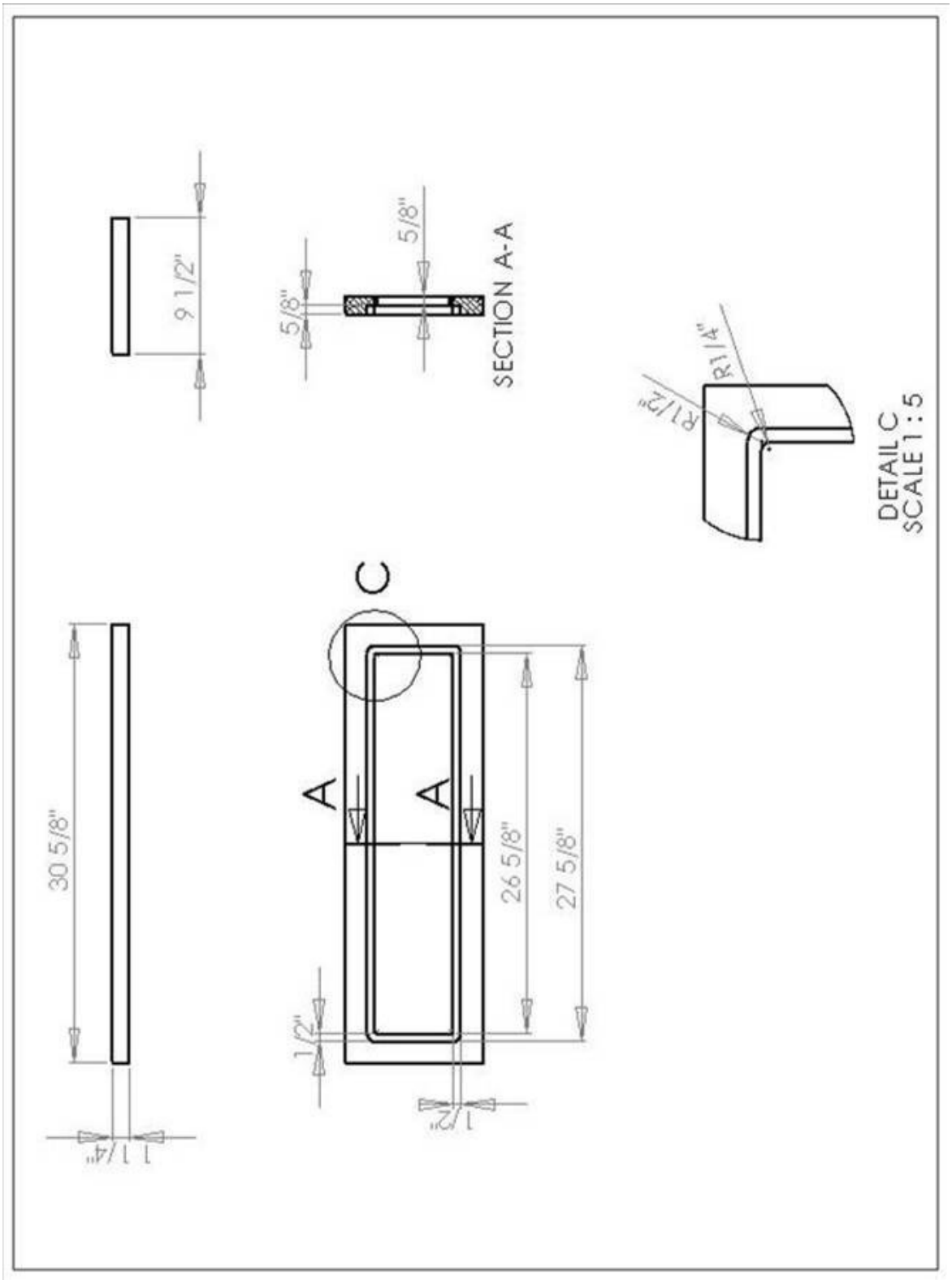

Figure 69. Test section side window frame

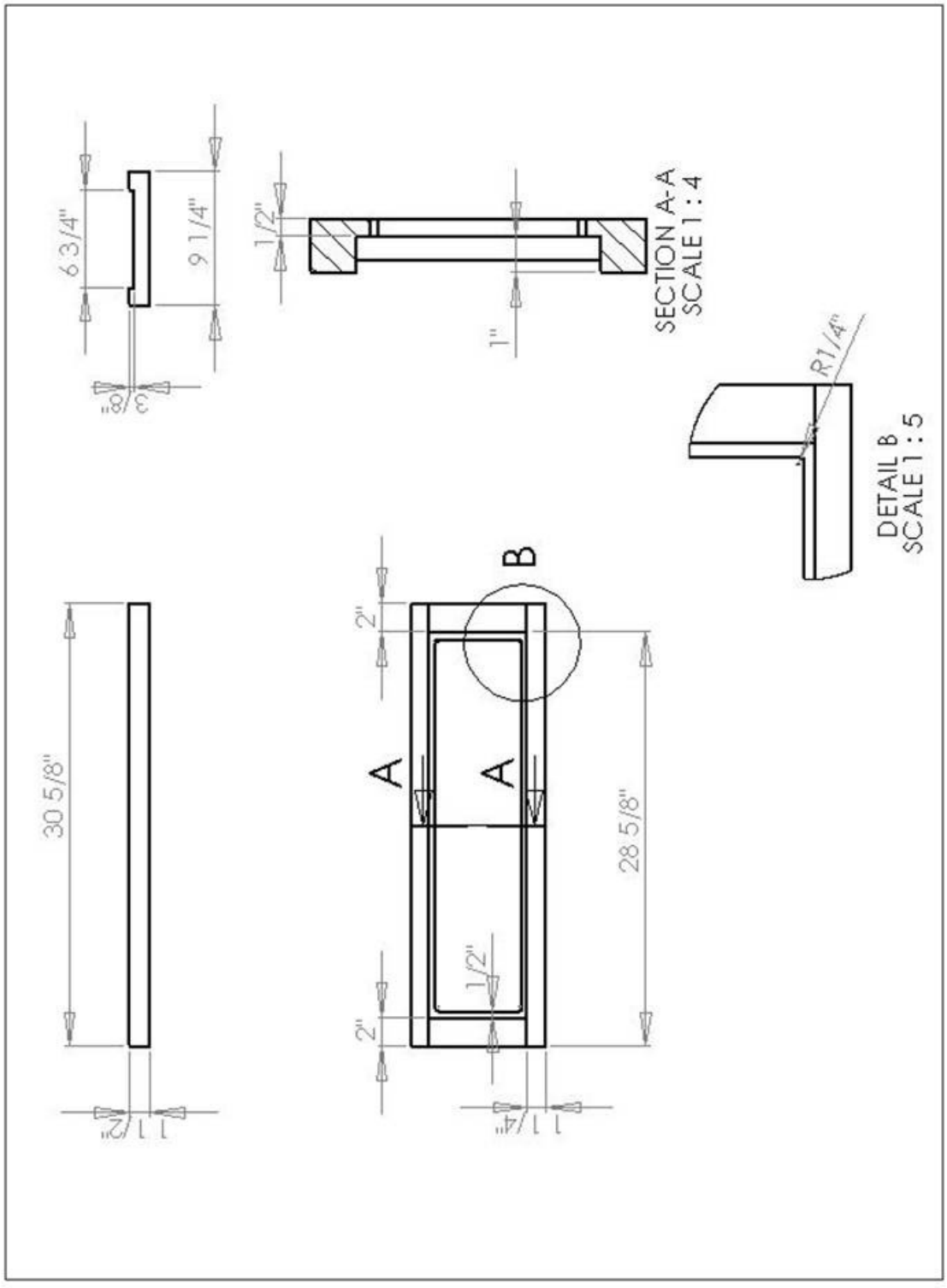

Figure 70. Test section top window frame

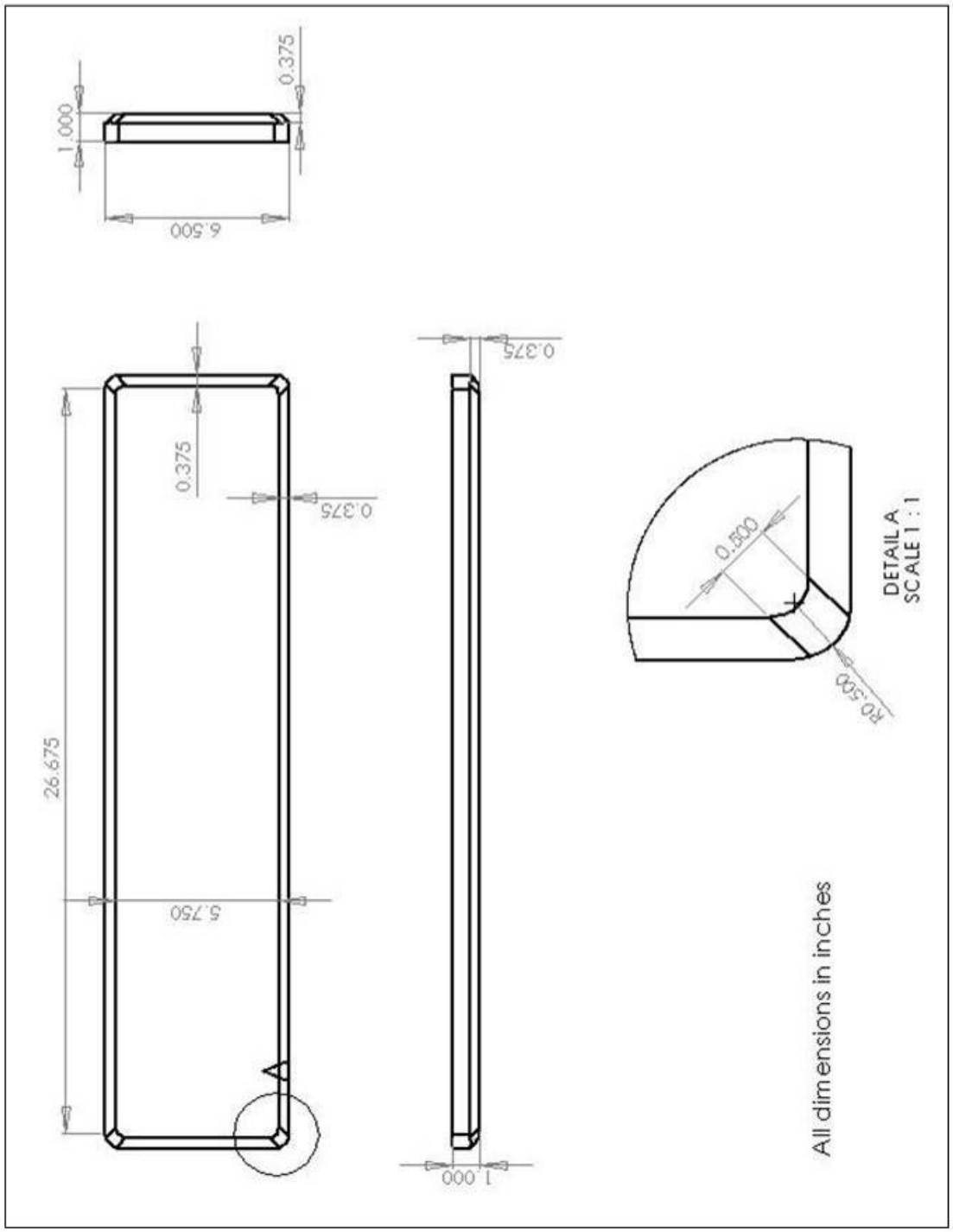

Figure 71. Test section side window

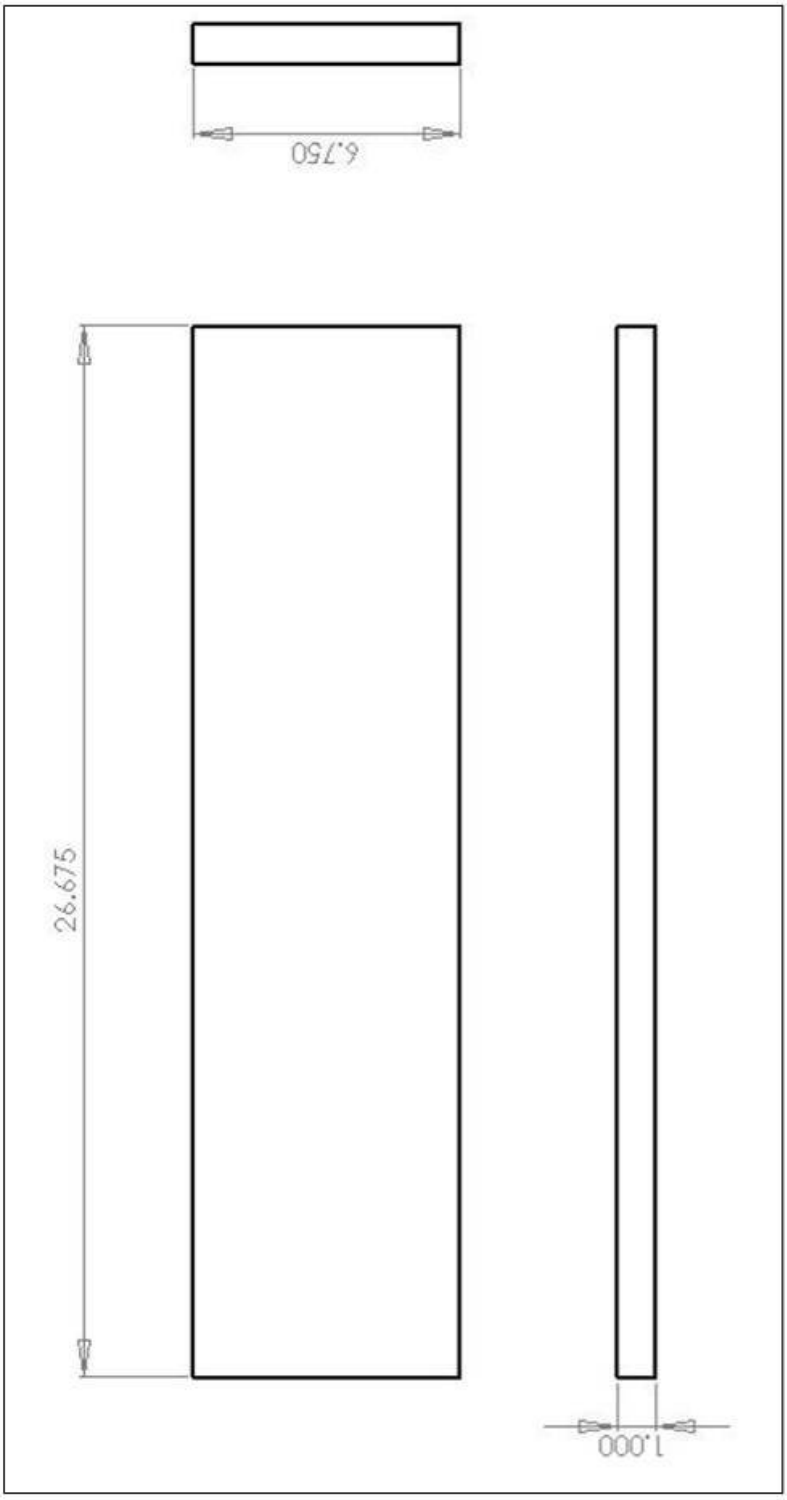

Figure 72. Test section top window

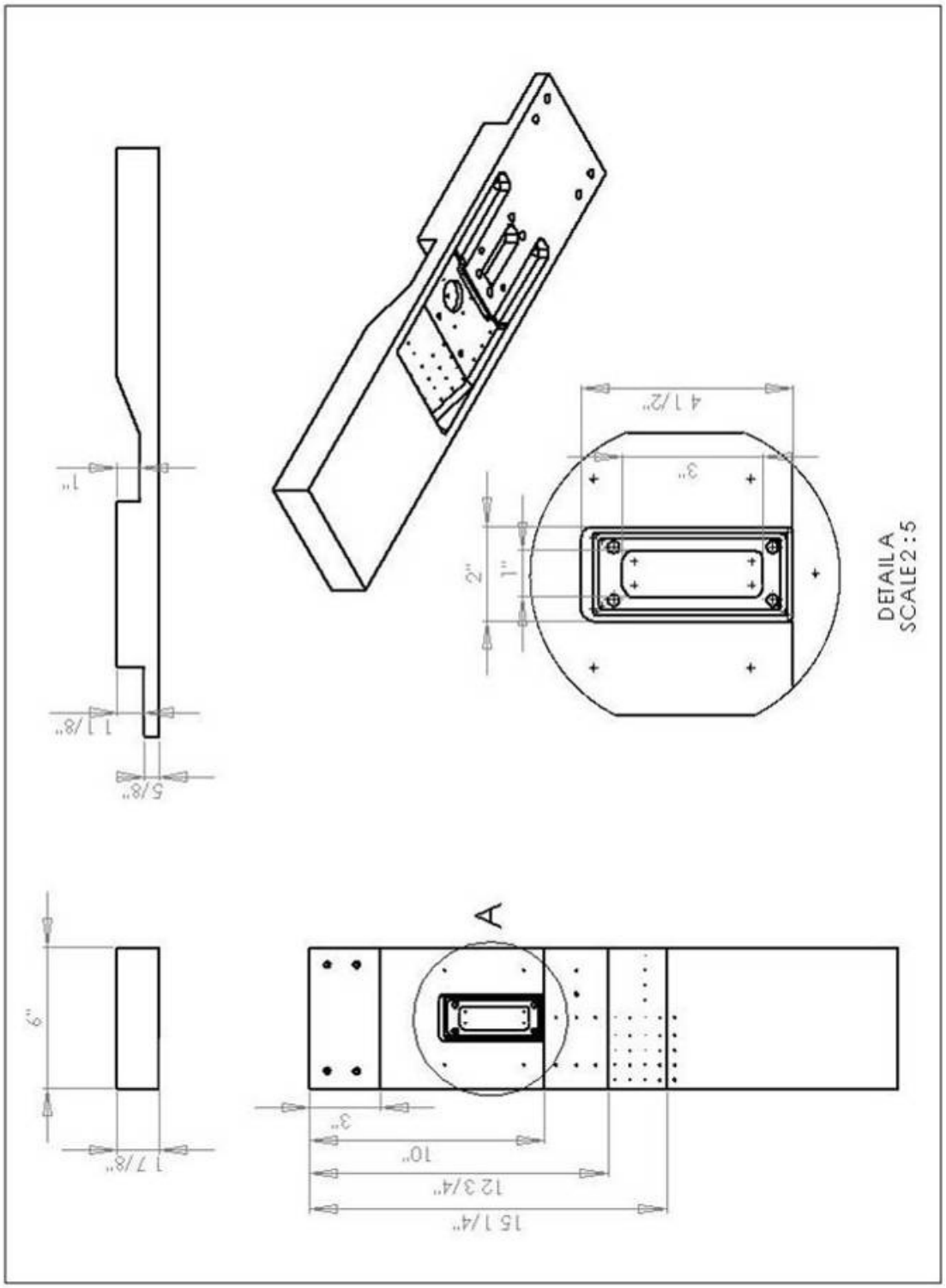

Figure 73. Test article cavity section

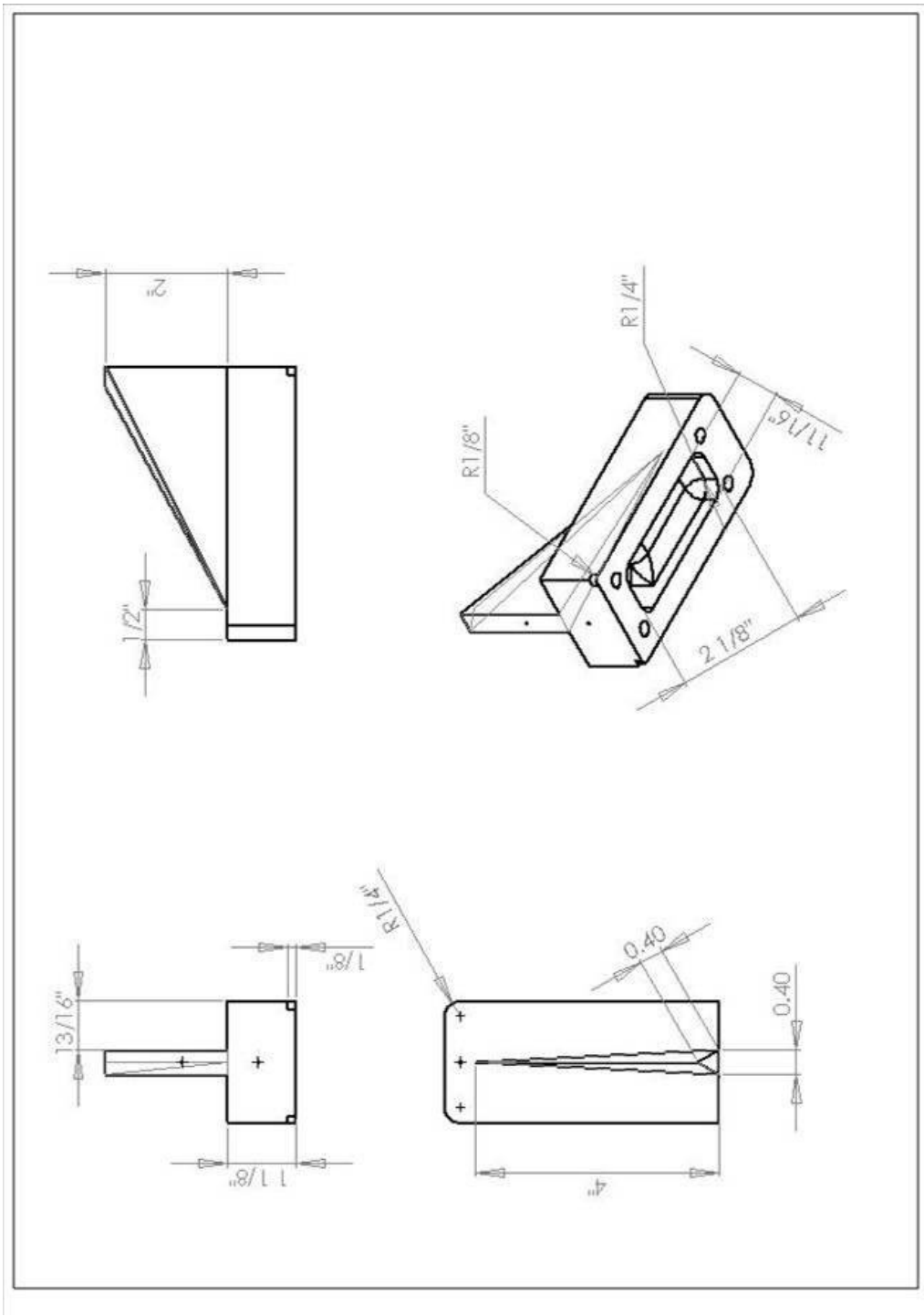

Figure 74. Pylon insert

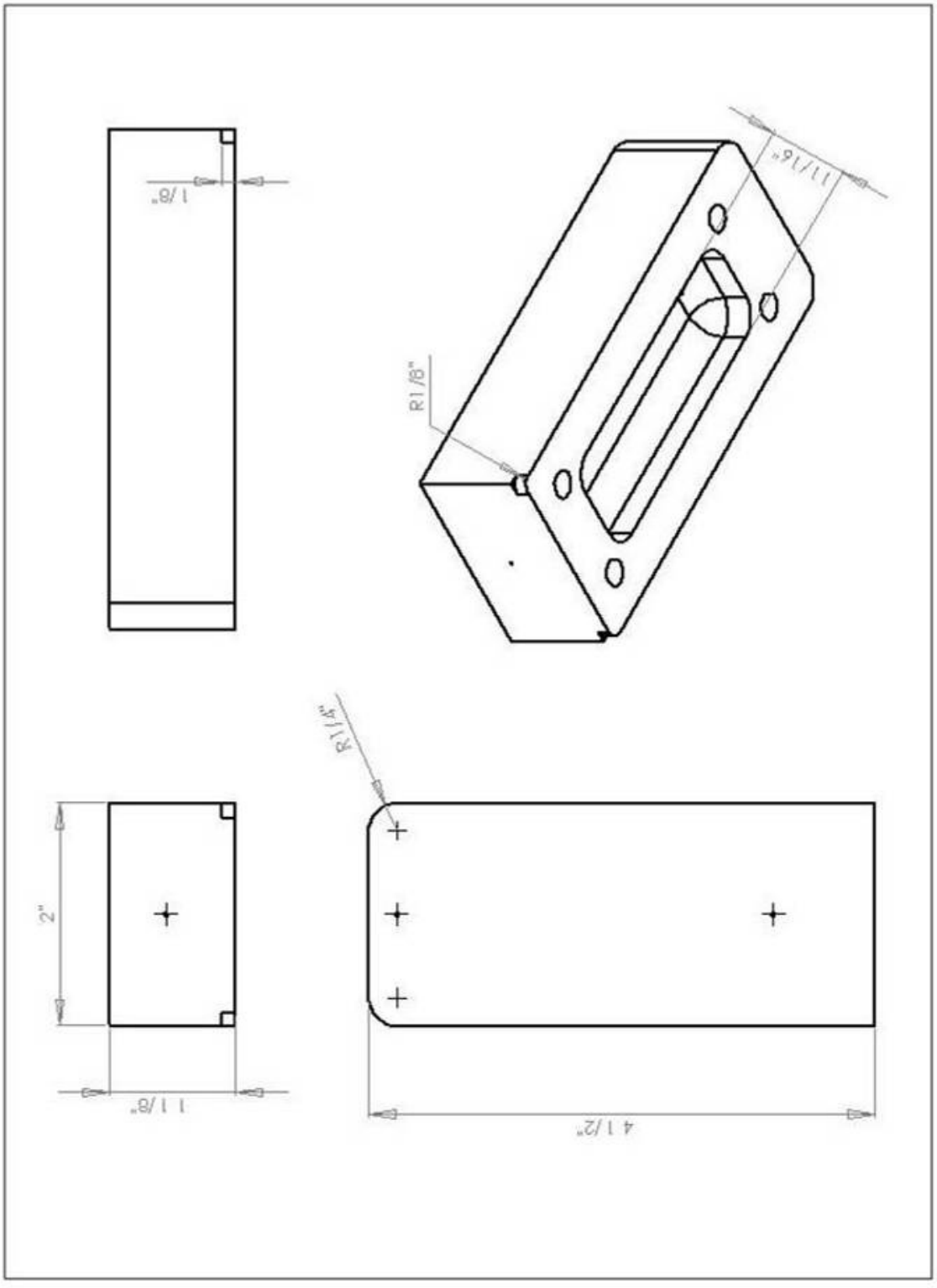

Figure 75. Plain insert

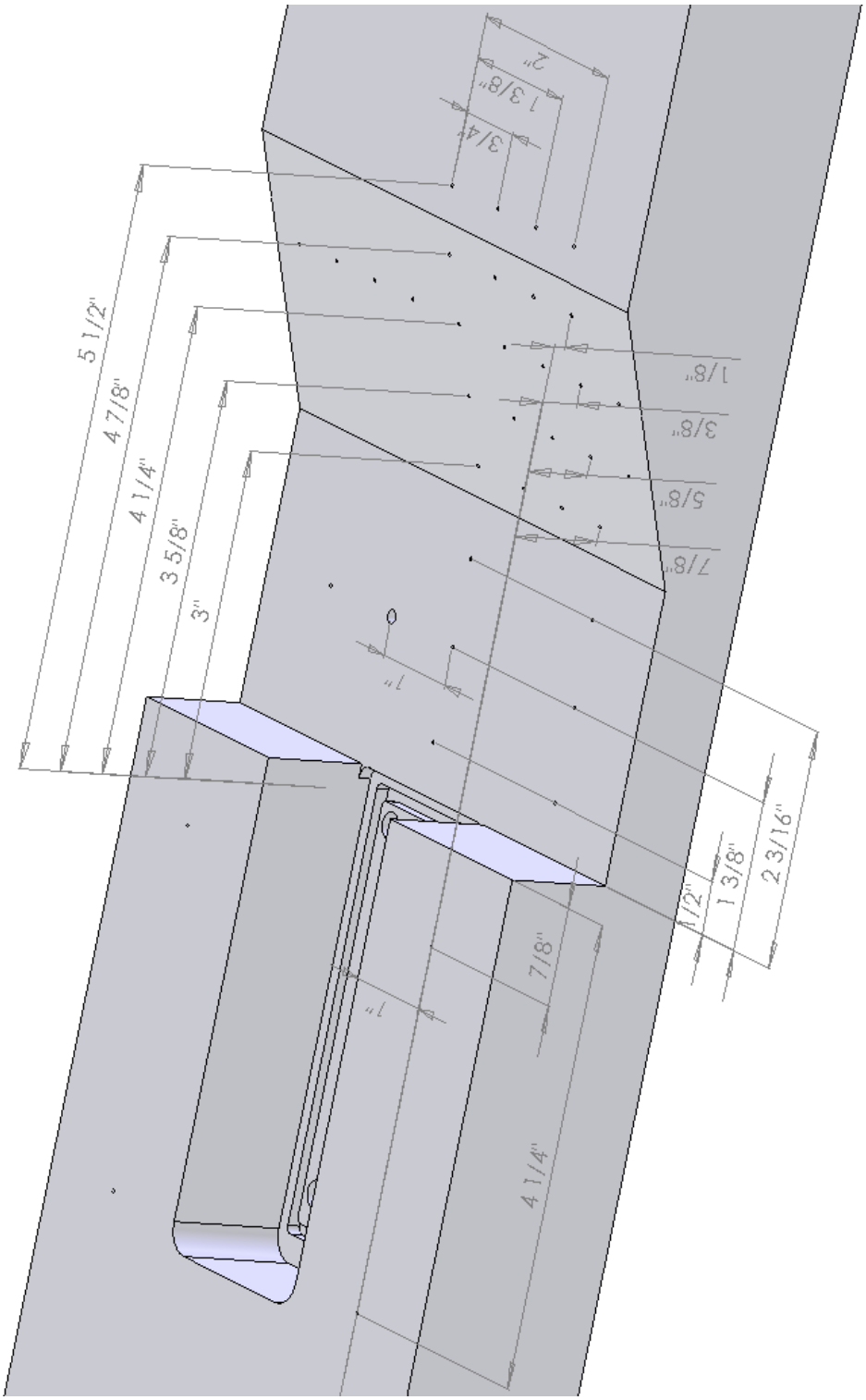

Figure 76. Location of surface pressure taps

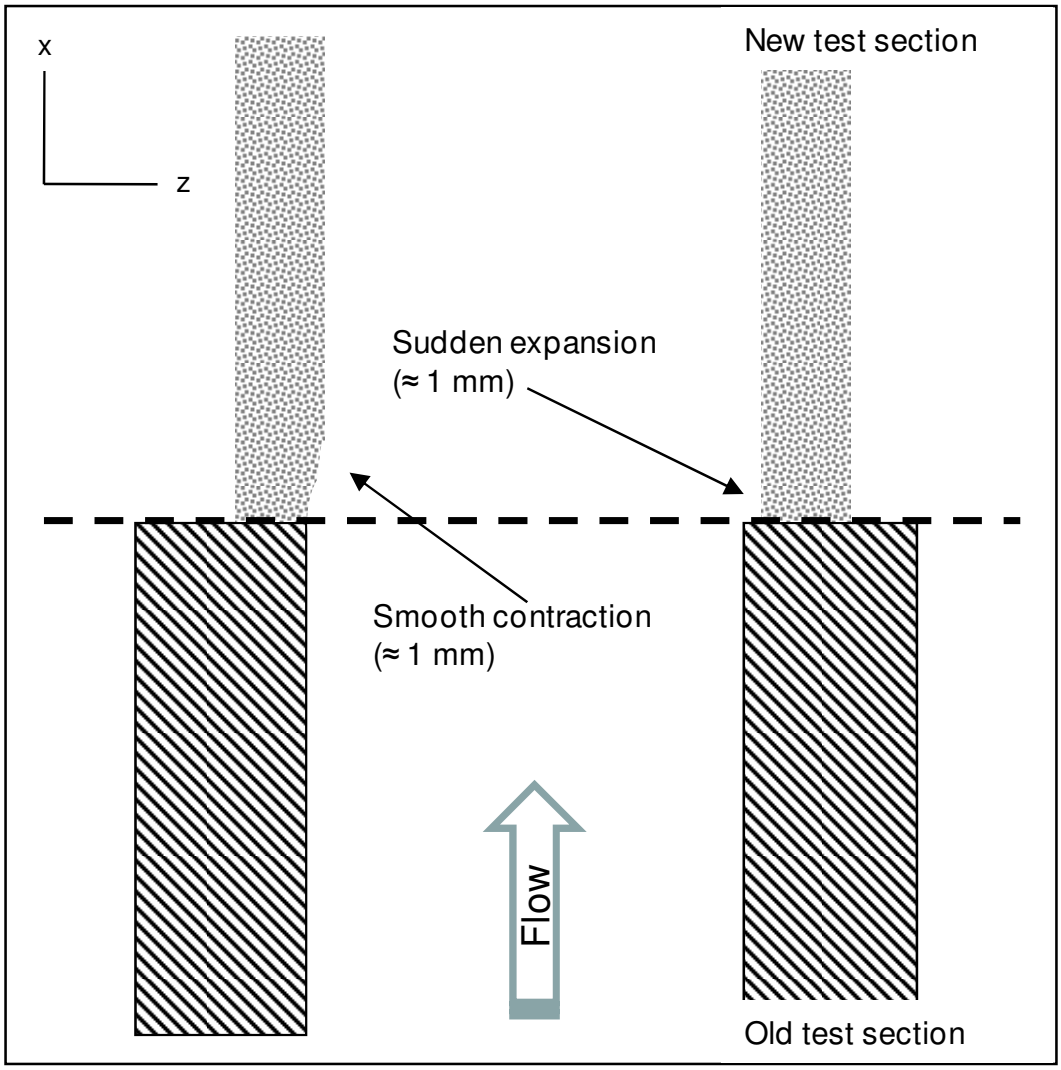

Figure 77. Representation of the new test section junction (not to scale)

A2. Wind Tunnel Procedures

Most wind tunnel operations were performed manually, to include operating individual data collection systems. Wind tunnel operation and monitoring were separate operations using separate equipment. The pressure scanner, signal analyzer, Schlieren/shadowgraph system, CO_2 seeding and PIV laser/camera operations all required independent actions on the part of the operator. Figure 78 shows the condensed operations checklist generated for wind tunnel operators. The expanded checklist items are explained below:

1. *Restart computer, if desired*

   The data acquisition computer would occasionally experience memory overflow issues if the data rate was set too high. For this study, the data rate was set to 20 Hz which eliminated hang-ups due to memory problems.

2. *Close tank supply valve, if required*

   The lab air supply lines cannot maintain pressure when the 800 ft^3 tank is emptied during a wind tunnel run. The loss of pressure will disrupt any other experiments in the lab that require a steady flow of pressurized air. In order to eliminate the risk of disrupting other experiments, the tank and wind tunnel can be separated from the compressor system by closing the tank supply valve once the tank is filled to the desired pressure. Alternatively, a back pressure regulator was installed around the tank supply valve that closes automatically when system pressure drops below approximately 790 kPa (100 psig). Filling the storage tank through the back pressure regulator requires more time due to valve cycling. Total filling time varies based on how much mass flow other users are drawing off the compressors. Whenever possible leave the supply valve open since the supply tank acts as an accumulator for the entire lab air system and minimizes surges or loss of pressure to other users due to compressor problems.

   Figure 79 shows the supply valve open and back-pressure regulator isolated. This position can be used for filling the tank and for tunnel operations when maintaining upstream system pressure is not required. The supply valve can be operated manually while recharging the storage

tank to maintain upstream pressure at a desired level by referencing the pressure gauge above the supply valve. If maintaining system pressure manually, cross check the system pressure frequently as it tends to drift at intermediate valve positions.

Figure 80 shows the supply valve closed and air flow through the back-pressure regulator. This position should be used anytime upstream pressure needs to be maintained. The regulator is set hold upstream system pressure above 790 kPa (100 psig) and will cycle while filling the storage tank until the tank exceeds 790 kPa (100 psig). Ensure electricity is supplied to the back-pressure regulator when used. If necessary, the back-pressure regulator set pressure can be changed. Consult with the laboratory technicians to change the set pressure on the back-pressure regulator.

3. *Check door closed and locked*

   Ensure the laboratory door is fully closed to minimize the chance of anyone entering without ear protection as the tunnel is started.

4. *Turn on laser warning light, if required*

   If the PIV system will be used, ensure the laser warning light is turned on to warn anyone entering the room that eye protection is necessary.

5. *Open main valve*

   When ready to start acquiring data ensure the main valve is open to provide supply air to the regulator valve to control stagnation tank pressure. The main valve is pictured in Figure 81.

6. *Open control pressure valve*

   The regulator is driven by an independent air source routed through an accumulator next to the regulator valve. Check that the control pressure valve is open to enable the regulator valve to operate. The control pressure valve is pictured in Figure 81.

7. *Set/check regulator set point pressure*

   The desired stagnation tank pressure can be set on the regulator control (Figure 82). However, because the supply pressure is constantly changing during a wind tunnel run, the regulator cannot maintain the pressure set in the regulator control. A calibration chart for the regulator was developed

and is shown in Figure 83 with the four test conditions used for this research highlighted. Vibration during data runs became excessive above a set pressure of 517 kPa / 75 psia (achieved pressure of approximately 386 kPa / 56 psia). It is possible to change controller gains in order to achieve higher pressure; however, the stability of the stagnation tank pressure becomes an issue. For instruction on operating the regulator control, consult with the laboratory technicians.

8. *Open software, as required*

   a. *Open pressure system*

      The pressure scanner software, independent of the LabView system used to monitor the tunnel, should be opened and set for use. Instructions for operating the pressure scanner and software can be found in the pressure scanner documentation.

   b. *Start Labview & enter datafile name*

      On the tunnel PC, start the monitoring program, or modified program, in LabView. The program can be set to save data to a file or run continuously to monitor ambient conditions. A typical screenshot of the current LabView program is shown in Figure 84. Enter the desired filename before starting the data run. The LabView program is easily modified, if desired.

9. *Check ear/eye protection on (whole room)*

   The wind tunnel noise can be excessive and dual hearing protection should be used, i.e., foam earplugs beneath full size hearing protectors. If PIV is in use, everyone should be using appropriate eye protection and be cleared to work around lasers. These safety precautions apply to anyone in the room. Consider darkening the room at this point if operating the PIV system.

10. *Start data capture*

    a. *Start pressure system*
    b. *Start Labview*

       Starting the pressure system data collection system before Labview was found from experience to be most efficient since they share the same PC.

11. *Start CO2, if required*

If operating the PIV system, start the CO_2 injection up to 30 seconds before operating the wind tunnel to allow sufficient time for the lines to pressurize and CO_2 particle generation to stabilize. As a check, experience indicates that when the stagnation tank temperature drops 20 °C or more and stays below that temperature, the system should be generating sufficient particles. This step may be accomplished before step 10 if it is taking a significant amount of time for the injectors to generate particles.

12. *START TUNNEL*

Start the tunnel run using the regulator control picture in Figure 82. Consult with the laboratory technicians on use of the regulator control. A typical run from start to finish typically requires less than 30 sec.

13. *Start PIV when stagnation tank pressure levels off, if required*

Trigger the PIV system at the desired stagnation tank pressure. If the run time is sufficiently long for a particular pressure setting wait for the stagnation tank pressure to level off. In general, however, the delay between triggering the PIV system and the laser firing is such that it was helpful to trigger the system approximately 70 kPa (10 psi) before the desired stagnation tank pressure was reached.

14. *Manually close regulator after data acquired*

Using the regulator control, manually drive the regulator valve closed after the desired data has been acquired. This action saves air in the storage tank and can significantly reduce the recharge time between runs. For instruction on operating the regulator control, consult with the laboratory technicians.

15. *Stop data capture*

a. *Stop Labview*
b. *Stop pressure system (run Binary-to-CSV routine, if required)*

The order of these actions is unimportant, although significant hard drive memory will be used if allowed to run for excessive periods of time. Labview will automatically write acquired data to the previously set

filename. The Binary-to-CSV subroutine in the pressure scanner control software must be run in order to generate a comma-delimited file that may be read by Excel, TecPlot, or other post-processing program. Consult the pressure scanner documentation for details.

16. *Save data files, as required*

    This step is a reminder to copy/move data files to a semi-permanent location for post-processing. This is especially important for the pressure scanner system since it will overwrite previous data runs.

17. *Close main valve, if desired*

    Closing the main valve removes pressure from the regulator valve. This step is not necessary in between multiple runs.

18. *Close control pressure valve*

    Closing the control pressure valve prevents the regulator valve from operating inadvertently. This step is not necessary in between multiple runs.

19. *Turn off laser warning light, if required*

    Turning off the laser warning light informs other lab users that it is safe to enter the room without eye protection.

20. *Open tank supply valve, if required (maintain 100+ psi if others using air)*

    If the tank supply valve was closed before the run in step 2, open the valve or check that the supply air is routed through the back-pressure regulator to charge the supply tank.

In the event of an emergency or tunnel malfunction:
Close main valve immediately
Turn off laser, if required

These actions remove air pressure from the system stopping flow through the wind tunnel and eliminate possible eye hazards from the laser system. When able, also shut down the CO_2 system, if used, close the regulator valve, and turn on the laboratory lights.

Tunnel Operation Checklist

1. Restart computer, if desired
2. Close tank supply valve, if required
3. Check door closed and locked
4. Turn on laser warning light, if required
5. Open main valve
6. Open control pressure valve
7. Set/check regulator set point pressure
8. Open software, as required
    a. Open pressure system
    b. Start Labview & enter datafile name
9. Check ear/eye protection on (whole room)

10. Start data capture
    a. Start pressure system
    b. Run Labview
11. Start CO2, if required

12. START TUNNEL

13. Start PIV when stagnation tank pressure levels off, if required
14. Manually close regulator after data acquired
15. Stop data capture
    a. Stop Labview
    b. Stop pressure system (run Binary-to-CSV routine, if reqd)

16. Save data files, as required
17. Close main valve, if desired
18. Close control pressure valve, if desired
19. Turn off laser warning light, if required
20. Open tank supply valve, if reqd (maintain 100+ psi if others using air)

In the event of an emergency or tunnel malfunction:

- **Close main valve immediately**
- **Turn off laser, if required**

Figure 78. Wind tunnel operations checklist

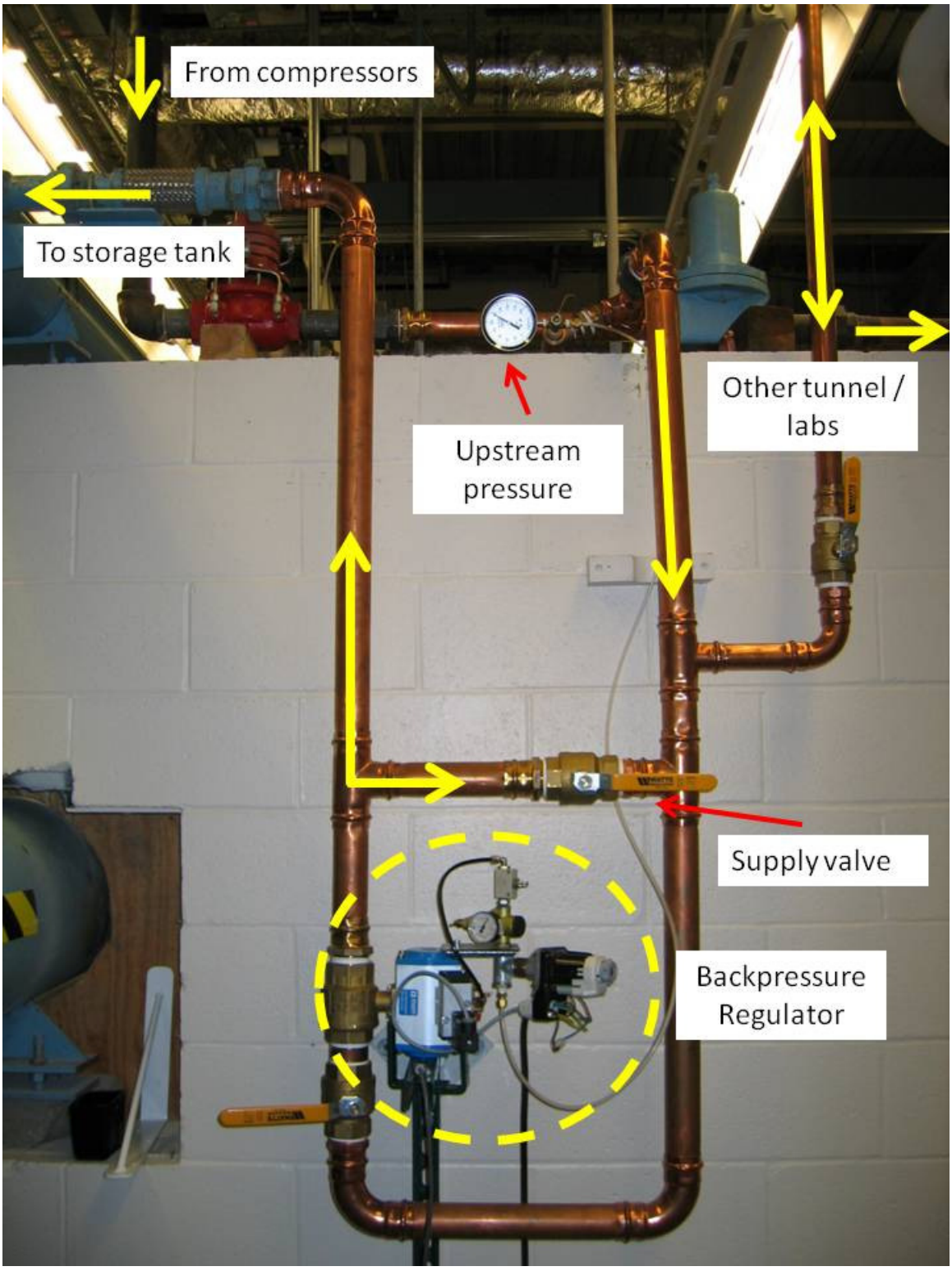

Figure 79. Supply valves configured for operation without the backpressure regulator

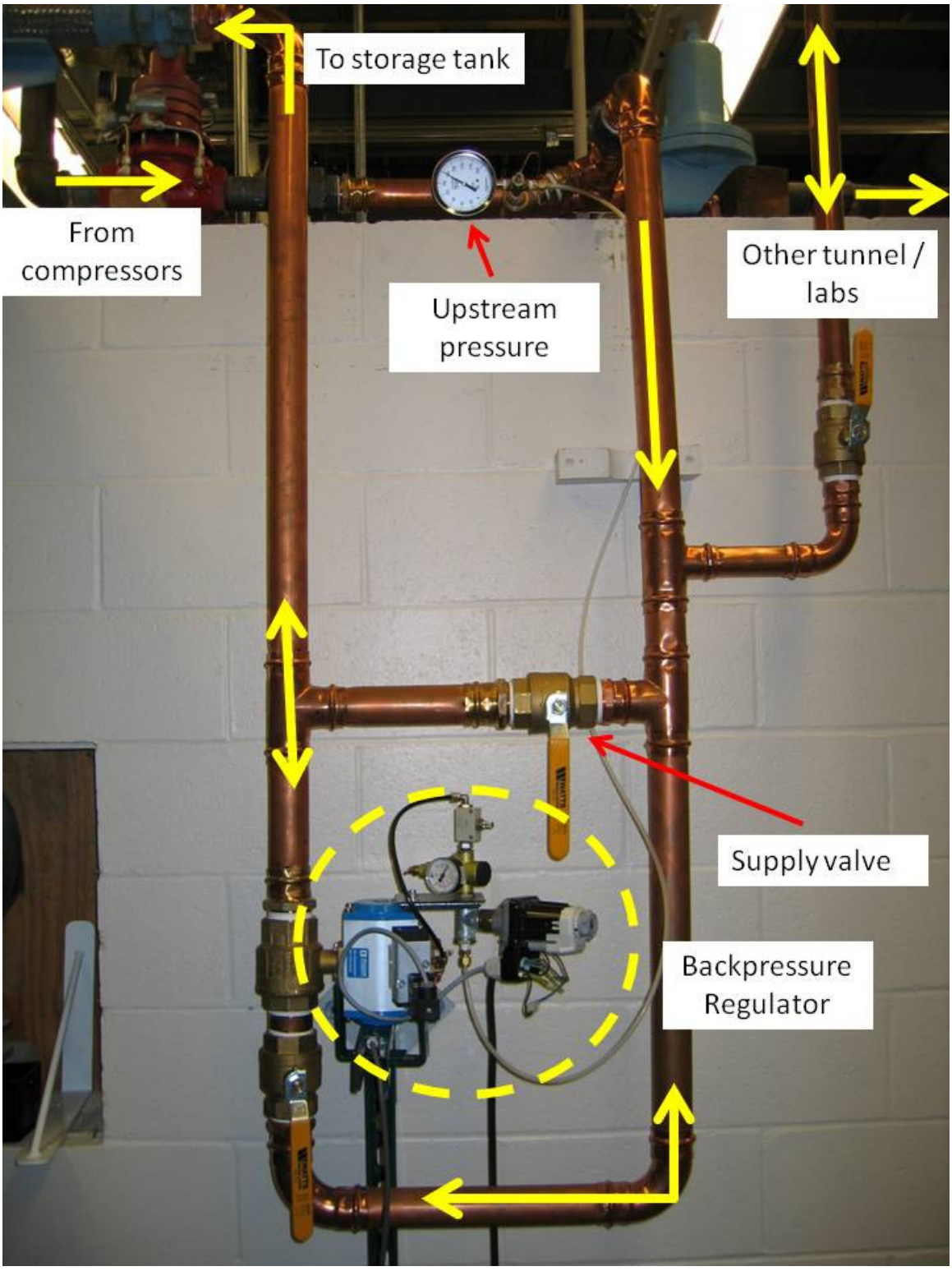

Figure 80. Supply valves configured for operation with the backpressure regulator

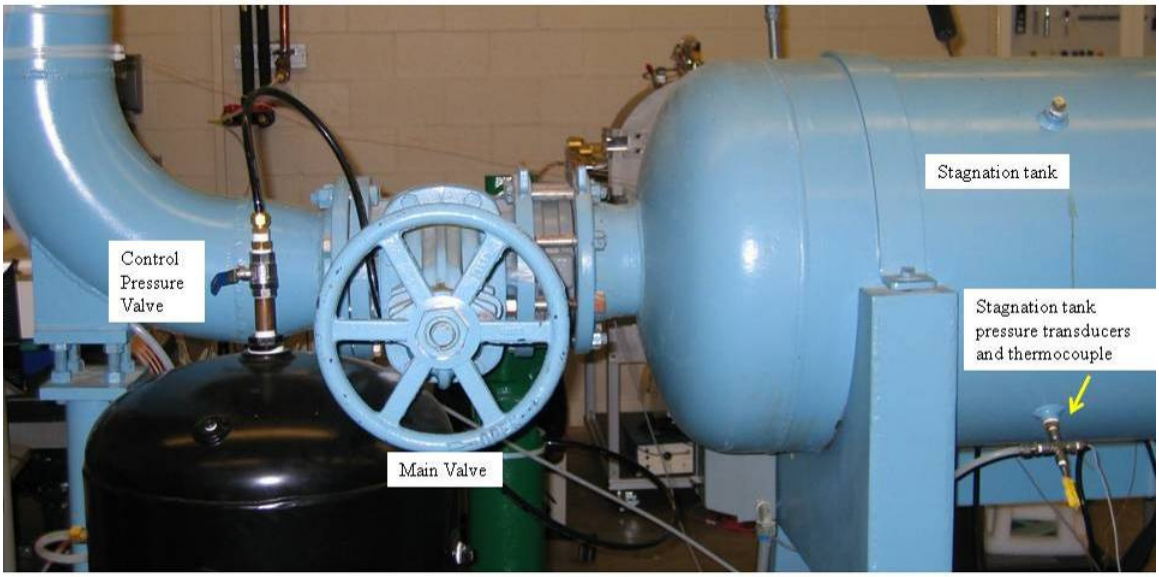

Figure 81. Main and pressure control valves

Figure 82. Regulator controller

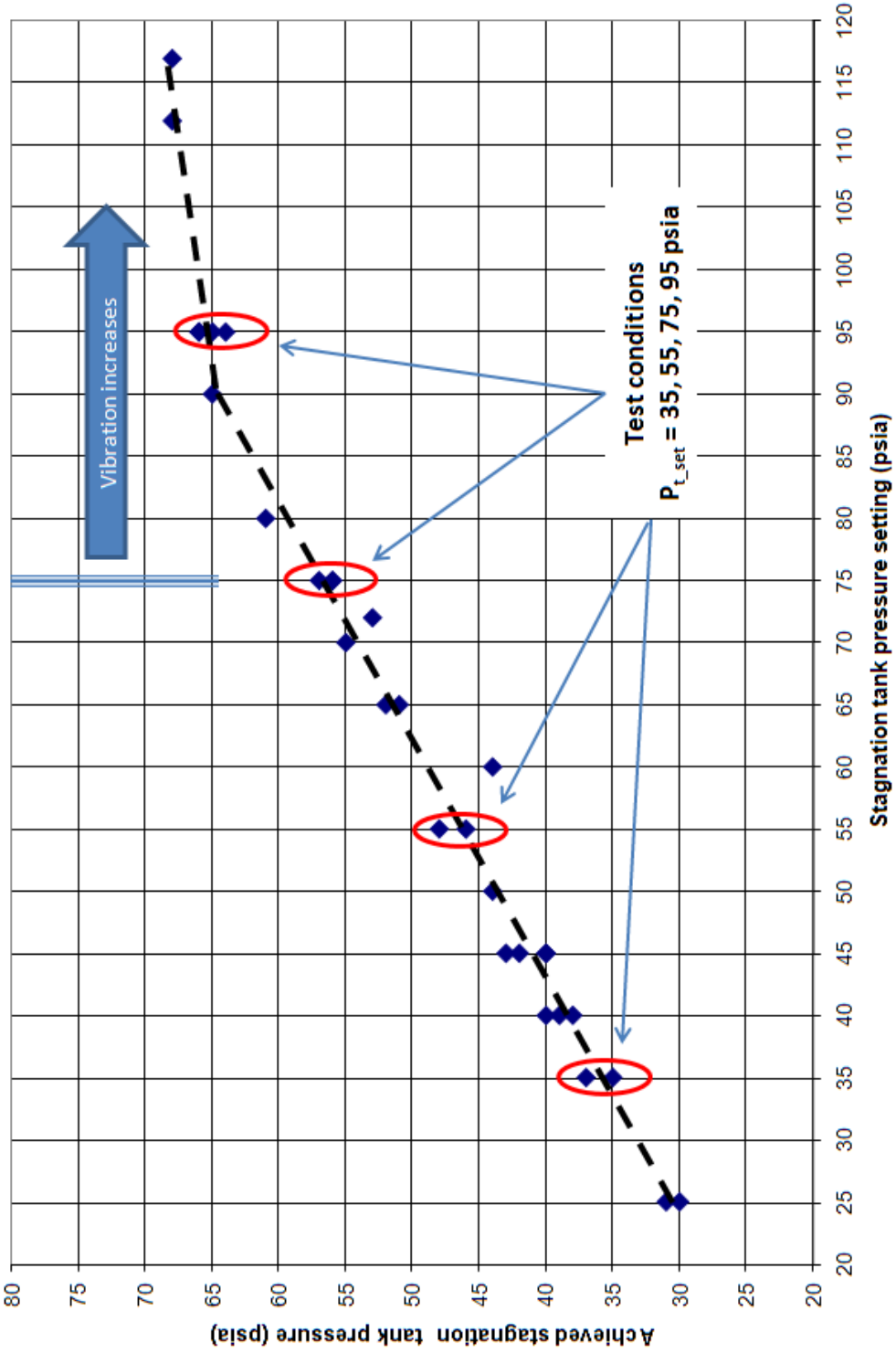

Figure 83. Wind tunnel stagnation tank pressure calibration chart and selected test condition settings

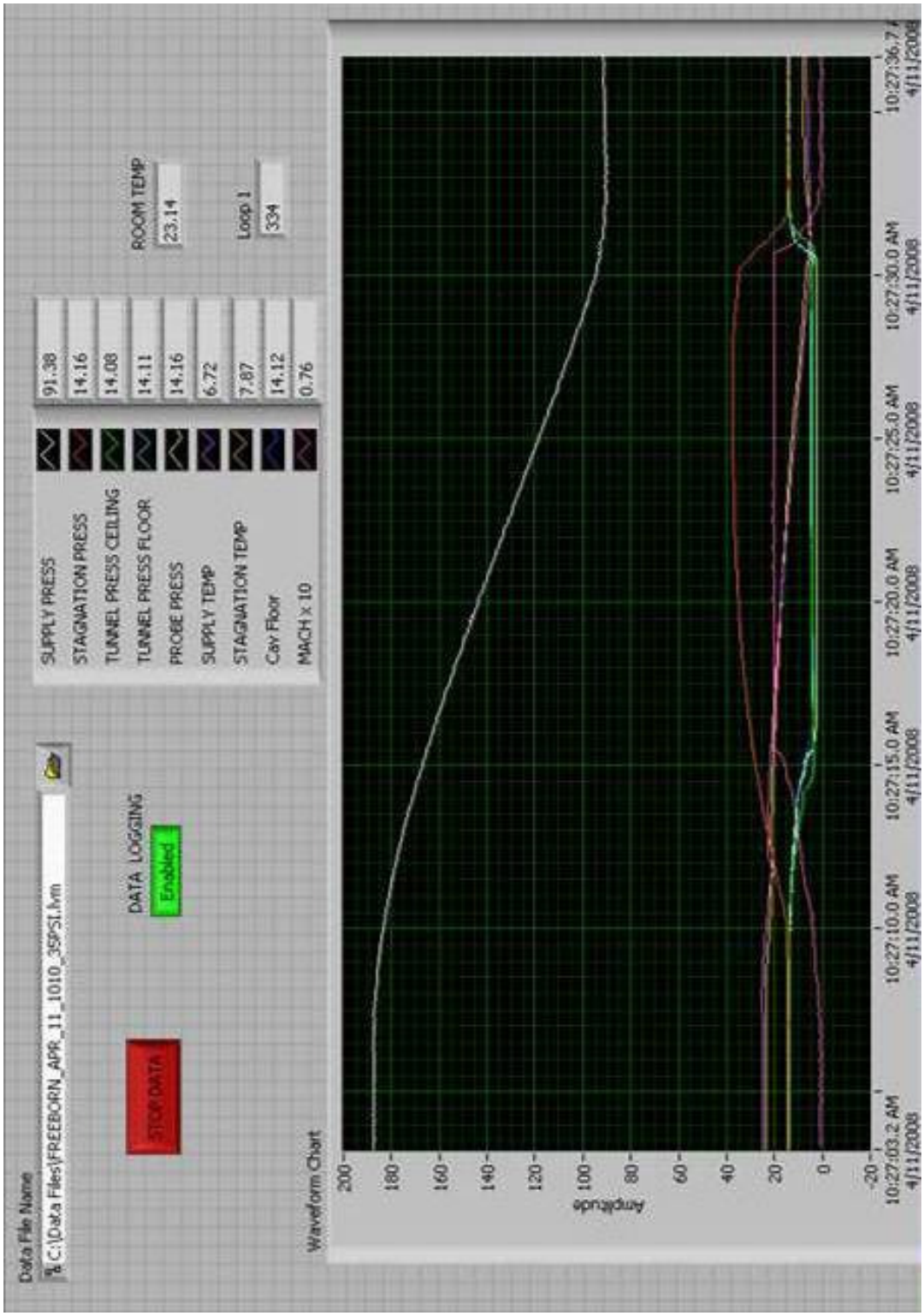

Figure 84. Screenshot of LabView monitoring program during a typical wind tunnel data run

A3. Data Collection and Reduction

A variety of data acquisition systems were used during this study. Flow visualization was accomplished using Schlieren and shadowgraph photography. Velocity profiles in selected locations were obtained using particle image velocimetry (PIV). Surface pressures at a variety of locations were measured using either a pressure scanner or individual pressure transducers. Pitot and static pressures were measured at discrete points in the flow as a check of the other techniques used in the study. The techniques for acquiring flow visualization and PIV data were discussed in section 3.2. More details for these methods and the CO_2/dry ice clean seeding for PIV may be found in Refs. [56-64]. A second CO_2 injector was added following the data collection in Ref. [64] in order to increase the seeding density. Despite having more than twice the CO_2 mass flow, seeding through the stagnation tank still provided sparse seeding at the laser sheet. When seeding the cavity directly through the cavity floor, there were ample seed particles, however the flow was severely disrupted, providing only qualitative data in the pylon wake. The *recipe* used for reducing the PIV data as well as a brief overview of the surface/probe pressure data reduction is provided below. In all cases, the raw data are averaged during the time the stagnation tank pressure is within 10% of peak, as described in Section III.

PIV Data Reduction

The PIV data were reduced in Dantec Dynamic Studio 2.0. Due to the sparse seeding, between 700-1100 image pairs were combined to obtain single velocity map. Typical images can be seen in Section A6. The interval between laser pulses was set to

0.5 μs, and the system captured image pairs at 7.5 Hz. The PIV computer had sufficient memory to capture 70 image pairs per run. The mathematics and further details of the steps behind the data reduction can be reviewed in Refs. [57; 60]. The following steps were used to reduce the collection of image pairs into a single velocity map and borrowed heavily from Refs. [60; 64]:

1. Adaptive correlation

   The interrogation region was set to be 32 pixels x 32 pixels. The scale of each interrogation area varied depending on the particular camera set-up. The size of the each pixel in the FlowSense 4M camera, the pixel pitch, was 7.4 μm. Due to the distance of the camera from the laser sheet, the scale factor for the velocity map seen in Figure 46 was 4.961, resulting in an interrogation region of approximately 1.2 mm x 1.2 mm (scale factor = 6.592 and 1.6 mm x 1.6 mm for Figure 43). A Gaussian window using default settings was employed to improve the signal-to-noise ratio. The regions were overlapped by 50% to avoid losing data on the boundaries of the interrogation region due to the Gaussian window. Peak validation was selected using default settings.

2. Range Validation

   Range validation was employed to discard spurious vectors. The limiting ranges were as follows:

Velocity magnitude (length):	$1 < \text{length} < 800$ m/s
Streamwise velocity (u):	$-400 < u < 600$ m/s
Vertical velocity (v):	$-350 < v < 350$ m/s

3. Vector Statistics

   The Vector Statistics function combines the series of vector maps into a single mean vector map of the flow. In addition to calculating velocities within the laser sheet, it also provides statistical quantities, such as standard deviation.

4. Vector Resampling

   Vector resampling was applied to refine the vector map. The default conditions were used: square grid, x = 2.0.

Test Section Mach Number

The average Mach number entering the test section was estimated from the stagnation tank pressure (P_t) and the pressure measured from a pressure tap on the tunnel floor (P_{floor}) approximately 0.5 cm ahead of the pylon.

$$M = \sqrt{\left(\frac{2}{\gamma - 1}\right)\left[\left(P_t / P_{floor}\right)^{\gamma - 1/\gamma} - 1\right]} \tag{13}$$

Static Temperature

The average static temperature entering the test section was estimated using the stagnation tank temperature (T_t) and the Mach number (M) calculated with equation (12).

$$T = T_t\left(1 + \frac{\gamma - 1}{2} M^2\right)^{-1} \tag{14}$$

Viscosity

The dynamic viscosity in the test section was estimated using Sutherland's Law with the static temperature (T) from equation (13).

$$\mu = \frac{C_1 T^{3/2}}{T + C_2} \tag{15}$$

where $C_1 = 1.46 \times 10^{-6}$ kg/m-s-K$^{1/2}$ and $C_2 = 111$ K.

Velocity

Mean velocity entering the test section is estimated using the static temperature (T) and Mach number (M) found from equations (12) and (13).

$$u = M\sqrt{\gamma RT} \tag{16}$$

Density

Density was estimated using the ideal gas law with pressure measured on the floor ahead of the pylon (P_{floor}) and temperature (T) determined using equation 13.

$$\rho = \frac{P_{floor}}{RT} \tag{17}$$

Unit Reynolds Number

The unit Reynolds number was determined using the velocity (u), density (ρ), and viscosity (μ) determined in equations (14), (15), and (16).

$$\mathrm{Re} = \frac{\rho u}{\mu} \ (\mathrm{m}^{-1}) \tag{18}$$

Dynamic Pressure

Dynamic pressure (q) was estimated using the pressure measured on the floor of the test section ahead of the pylon (P_{floor}) as well as Mach number (M) determined using equation (12).

$$q = \frac{1}{2}\gamma P_{floor} M^2 \tag{19}$$

Pressure Coefficient

Pressure coefficients were calculated using the floor pressure ahead of the pylon (P_{floor}) as a reference and the dynamic pressure (q) calculated from equation (18).

$$C_p = \frac{P - P_{floor}}{q} \tag{20}$$

Probe Mach Number

Probe measurements required two tunnel runs to derive flow variables. First a run using a pitot probe was accomplished (P_{pitot}), followed by a run with the same stagnation pressure setting using a 10 degree cone static probe (P_{cone}). The probe Mach number (M_{probe}) was then determined iteratively using the pitot equation for Mach number [69:4.4] and a curve fit for the pressure change behind the shock around a 10 degree cone derived from Ref. [70].

$$\frac{P_{pitot}}{P_{cone}} = f\left(M_{probe}\right)$$

(21)

$$f\left(M_{probe}\right) = \frac{\left(1.2M_{probe}^{2}\right)^{3.5}\left(\frac{6}{7M_{probe}^{2}-1}\right)^{2.5}}{0.0425M_{probe}^{2}+0.0405M_{probe}+1.0443}$$

Probe Static Pressure

Once the probe Mach number is known from equations (20) the probe static pressure may be determined.

$$P_{probe} = \frac{P_{cone}}{0.0425M_{probe}^{2}+0.0405M_{probe}+1.0443} \tag{22}$$

Probe Total Pressure

Probe total pressure is determined from probe Mach number (M_{probe}) and probe static pressure (P_{probe}) by rearranging equation (12).

$$P_{t_probe} = P_{probe}\left(1+\frac{\gamma-1}{2}M_{probe}^{2}\right)^{\gamma/\gamma-1} \tag{23}$$

Probe Static Temperature and Velocity

The probe static temperature and velocity were determined the same as mean test section values with equations (13) and (15).

Error Analysis

Error bars, when included, indicate the 95% confidence interval. Error analysis was accomplished in accordance with Ref. [71].

Temperature Corrections

When stated with results, velocity data was corrected for differing temperatures during the wind tunnel study. To accomplish this all results were standardized to the mean stagnation tank temperature of 280 K (see section A5). Mach number was assumed constant in all cases. The correction was based on equations (14) and (16).

$$u_{corrected} = u_{uncorrected} \sqrt{\frac{T_{t_standard}}{T_{t_uncorrected}}} \tag{24}$$

A4. Tunnel Nozzle Contours

No engineering drawings of the 6” x 6” Supersonic Wind Tunnel were available. However, the wind tunnel documentation [55] noted that the contours were derived from Ref. [54]. Reference [54] specified the contours of a supersonic wind tunnel with a sliding block nozzle allowing for operations over a significant range of Mach numbers. However, the contours provided were for a 4 in by 4 in test section. These contours were scaled up to the 6 in tunnel for use in computational studies of the wind tunnel flow and correspond to 1500 counts on the lower sliding block of the 6” x 6” wind tunnel. There was good agreement between the wind tunnel Mach number and the Mach number predicted at the tunnel nozzle exit using these M ≈ 2 contours which are provided on the following pages in Table 8. The coordinate system in Table 8 is centered 15 cm ahead of the end of the nozzle on the test section floor, therefore the contours begin at x = -15 cm and y = 0 cm. The derived contours are shown in Figure 85. Details on how these contours were used in modeling the tunnel nozzle may be found in Appendix B.

Figure 85. Derived wind tunnel nozzle contours ($M \approx 2$)

Table 8. 6” x 6” Supersonic Wind Tunnel nozzle contours ($M \approx 2$)

Upper Nozzle Surface			Lower Nozzle Surface	
x (cm)	y (cm)		x (cm)	y (cm)
-15	16.51		-15	0
-49.29	16.19758		-35.955	0
-50.2425	16.187674		-81.675	.52959
-51.195	16.176625		-82.6275	0.540639
-52.1475	16.164433		-83.58	0.550926
-53.1	16.151098		-84.5325	0.559689
-54.0525	16.13662		-85.485	0.566547
-55.005	16.120999		-86.4375	0.5715
-55.9575	16.104235		-87.39	0.574548
-56.91	16.086328		-88.3425	0.57531
-57.8625	16.066897		-89.295	0.573786
-58.815	16.046323		-90.2475	0.569976
-59.7675	16.024606		-91.2	0.56388
-60.72	16.001365		-92.1525	0.555117
-61.6725	15.976981		-93.105	0.544068
-62.625	15.951073		-94.0575	0.530352
-63.5775	15.923641		-95.01	0.513969
-64.53	15.894685		-95.9625	0.494919
-65.4825	15.864205		-96.915	0.473202
-66.435	15.832201		-97.8675	0.448818
-67.3875	15.798673		-98.82	0.421386
-68.34	15.763621		-99.7725	0.391287
-69.2925	15.727045		-100.725	0.35814
-70.245	15.688945		-101.6775	0.322326
-71.1975	15.649321		-102.63	0.283464
-72.15	15.607792		-103.5825	0.241935
-73.1025	15.564358		-104.535	0.197358
-74.055	15.519019		-105.4875	0.149733
-75.0075	15.471775		-106.44	0.09906
-75.96	15.422626		-107.3925	0.044958
-76.9125	15.371572		-108.345	-0.012192
-77.865	15.318613		-109.2975	-0.072771
-78.8175	15.263749		-110.25	-0.136779
-79.77	15.206599		-111.2025	-0.204216
-80.7225	15.147544		-112.155	-0.275082
-81.675	15.086203		-113.1075	-0.349758
-82.6275	15.022957		-114.06	-0.428244
-83.58	14.957425		-115.0125	-0.51054
-84.5325	14.889607		-115.965	-0.597027
-85.485	14.819503		-116.9175	-0.687705
-86.4375	14.747113		-117.87	-0.782574
-87.39	14.672056		-118.8225	-0.881634

-88.3425	14.594713		-119.775	-0.985266
-89.295	14.514703		-120.7275	-1.09347
-90.2475	14.432407		-121.68	-1.206246
-91.2	14.347444		-122.6325	-1.323594
-92.1525	14.259814		-123.585	-1.445514
-93.105	14.169517		-124.5375	-1.572006
-94.0575	14.076172		-125.49	-1.703451
-95.01	13.98016		-126.4425	-1.839849
-95.9625	13.8811		-127.395	-1.9812
-96.915	13.778992		-128.3475	-2.127504
-97.8675	13.673836		-129.3	-2.278761
-98.82	13.565251		-130.2525	-2.435352
-99.7725	13.453237		-131.205	-2.596896
-100.725	13.337794		-132.1575	-2.763774
-101.6775	13.218922		-133.11	-2.935986
-102.63	13.096621		-134.0625	-3.113532
-103.5825	12.970891		-135.015	-3.296412
-104.535	12.841732		-135.9675	-3.485007
-105.4875	12.709144		-136.92	-3.679317
-106.44	12.572746		-137.8725	-3.879342
-107.3925	12.432538		-138.825	-4.085463
-108.345	12.28852		-139.7775	-4.29768
-109.2975	12.140692		-140.73	-4.516374
-110.25	11.989054		-141.6825	-4.741926
-111.2025	11.833606		-142.635	-4.974717
-112.155	11.674348		-143.5875	-5.215128
-113.1075	11.51128		-144.54	-5.46354
-114.06	11.344402		-145.4925	-5.719953
-115.0125	11.173714		-146.445	-5.983605
-115.965	10.999216		-147.3975	-6.250686
-116.9175	10.820908		-148.35	-6.518148
-117.87	10.638409		-149.3025	-6.78561
-118.8225	10.4521		-150.255	-7.053072
-119.775	10.2616		-151.2075	-7.320534
-120.7275	10.06729		-152.16	-7.587996
-121.68	9.868789		-153.1125	-7.855458
-122.6325	9.666478		-154.065	-8.12292
-123.585	9.459976		-155.0175	-8.390763
-124.5375	9.249283		-155.97	-8.658987
-125.49	9.034399		-156.9225	-8.927973
-126.4425	8.815324		-157.875	-9.197721
-127.395	8.592058		-158.8275	-9.46404
-128.3475	8.364601		-159.78	-9.73074
-129.3	8.132953		-160.7325	-10.00125
-130.2525	7.896733		-161.685	-10.27938
-131.205	7.655941		-162.6375	-10.56513
-132.1575	7.410577		-163.59	-10.86231
-133.11	7.160641		-164.5425	-11.17092
-134.0625	6.906133		-165.495	-11.49477

-135.015	6.647053		-166.4475	-11.83767
-135.9675	6.383782		-167.4	-12.19581
-136.92	6.11632		-168.3525	-12.56919
-137.8725	5.845048		-169.305	-12.95781
-138.825	5.570728		-170.2575	-13.36167
-139.7775	5.294122		-171.21	-13.78077
-140.73	5.016754		-172.1625	-14.21511
-141.6825	4.739005		-173.115	-14.6685
-142.635	4.461256		-174.0675	-15.14475
-143.5875	4.183507		-175.02	-15.64005
-144.54	3.905758		-175.9725	-16.15821
-145.4925	3.628009		-176.925	-16.69542
-146.445	3.35026		-177.8775	-17.24787
-147.3975	3.072511		-178.83	-17.81556
-148.35	2.794762		-179.7825	-18.39468
-149.3025	2.517013		-180.735	-18.98904
-150.255	2.239645		-181.6875	-19.59102
-151.2075	1.962277		-182.64	-20.19681
-152.16	1.684909		-183.5925	-20.80641
-153.1125	1.407922		-184.545	-21.41982
-154.065	1.130935		-185.4975	-22.03323
-155.0175	0.853948		-186.45	-22.64664
-155.97	0.577342		-187.4025	-23.25624
-156.9225	0.300736		-188.355	-23.86584
-157.875	0.02413		-189.3075	-24.46782
-158.8275	-0.252095		-190.26	-25.05837
-159.78	-0.52832		-191.2125	-25.63368
-160.7325	-0.804545		-192.165	-26.19375
-161.685	-1.080389		-193.1175	-26.74239
-162.6375	-1.356233		-194.07	-27.27579
-163.59	-1.632077		-195.0225	-27.79014
-164.5425	-1.90754		-195.975	-28.28925
-165.495	-2.183003		-196.9275	-28.76931
-166.4475	-2.458085		-197.88	-29.22651
-167.4	-2.733167		-198.8325	-29.66085
-168.3525	-3.008249		-199.785	-30.07233
-169.305	-3.28295		-200.7375	-30.46476
-170.2575	-3.557651		-201.69	-30.83433
-171.21	-3.831971		-202.6425	-31.18485
-172.1625	-4.106291		-203.595	-31.51632
-173.115	-4.38023		-204.5475	-31.82493
-174.0675	-4.654169		-205.5	-32.11068
-175.02	-4.927727		-206.4525	-32.36976
-175.9725	-5.201285		-207.405	-32.60598
-176.925	-5.474462		-208.3575	-32.81934
-177.8775	-5.747639		-209.31	-33.00984
-178.83	-6.020435		-210.2625	-33.16986
-179.7825	-6.293231		-211.215	-33.29559
-180.735	-6.565646		-212.1675	-33.38322

-181.6875	-6.83768	-213.12	-33.42894
-182.64	-7.10819	-214.0725	-33.44418
-183.5925	-7.373747	-215.025	-33.44418
-184.545	-7.632065	-234.075	-33.44418
-185.4975	-7.879334	-239.79	-33.44418
-186.45	-8.11403		
-187.4025	-8.33501		
-188.355	-8.54075		
-189.3075	-8.72744		
-190.26	-8.89508		
-191.2125	-9.03986		
-192.165	-9.15797		
-193.1175	-9.24941		
-194.07	-9.31418		
-195.0225	-9.34847		
-195.975	-9.34847		
-196.9275	-9.31037		
-197.88	-9.23798		
-198.8325	-9.12368		
-199.785	-8.97128		
-200.7375	-8.77697		
-201.69	-8.54075		
-202.6425	-8.25881		
-203.595	-7.93115		
-204.5475	-7.55015		
-205.5	-7.112		
-206.4525	-6.62813		
-207.405	-6.10997		
-208.3575	-5.56514		
-209.31	-4.99745		
-210.2625	-4.41071		
-211.215	-3.80492		
-212.1675	-3.18389		
-213.12	-2.54762		
-214.0725	-1.89611		
-215.025	-1.23317		
-215.9775	-0.5588		
-216.93	0.127		
-217.8825	0.82042		
-218.835	1.52146		
-219.7875	2.22631		
-220.74	2.93116		
-221.6925	3.6322		
-222.645	4.32943		
-223.5975	5.01523		
-224.55	5.6896		
-225.5025	6.34873		
-226.455	6.98881		
-227.4075	7.60603		

-228.36	8.19277
-229.3125	8.74141
-230.265	9.24433
-231.2175	9.6901
-232.17	10.06729
-233.1225	10.36828
-234.075	10.59307
-235.0275	10.74928
-235.98	10.84834
-236.9325	10.90168
-237.885	10.92454
-238.8375	10.93216
-239.79	10.93597

A5. Detailed Wind Tunnel Test Conditions ($M \approx 2$)

Condition	Stagnation pressure setting (kPa / psia)	Mean stagnation pressure (kPa / psia)	Standard deviation of stagnation pressure (kPa / psia)	Mean stagnation temperature (K)	Standard deviation of stagnation temperature (K)	Mean static pressure (kPa / psia)[1]	Standard deviation of static pressure (kPa / psia)	Mean dynamic pressure (kPa / psia)	Standard deviation of dynamic pressure (kPa / psia)	Mean Reynolds number (m^{-1})	Standard deviation of Reynolds number (m^{-1})
1	241.3 / 35	248.2 / 36	6.1 / 0.89	280	3.1	30.3 / 4.4	0.5 / 0.07	89.6 / 13	1.5 / 0.22	3.2×10^7	1.2×10^6
2	379.2 / 55	324.1 / 47	9.0 / 1.30	280	2.6	37.9 / 5.5	0.17 / 0.17	110.3 / 16	3.4 / 0.5	4.2×10^7	1.3×10^6
3	517.1 / 75	372.3 / 54	5.9 / 0.85	280	3.2	44.8 / 6.5	0.5 / 0.07	131.0 / 19	1.6 / 0.23	4.9×10^7	1.5×10^6
4	655.0 / 95	427.5 / 62	7.6 / 1.10	280	4.4	50.3 / 7.3	1.7 / 0.24	144.8 / 21	4.7 / 0.68	5.5×10^7	2.5×10^6

[1] Static pressure measured on tunnel floor ahead of the pylon (x = -10.8 cm, y = 0 cm, z = 0cm)

A6. PIV Images

As discussed in Section III, the PIV images were very sparse necessitating 700-1100 image pairs to obtain usable data. Figure 86 through Figure 89 present several average and good quality PIV images. The bright region on the right side of Figure 89 is due to reflection off the pylon and cavity leading edge. The bright diffuse region at the bottom of the frame is due to the injector sitting immediately below the frame.

Figure 86. Average quality PIV wake image (pylon on center-right of frame, image plane at y = 3.7 cm)

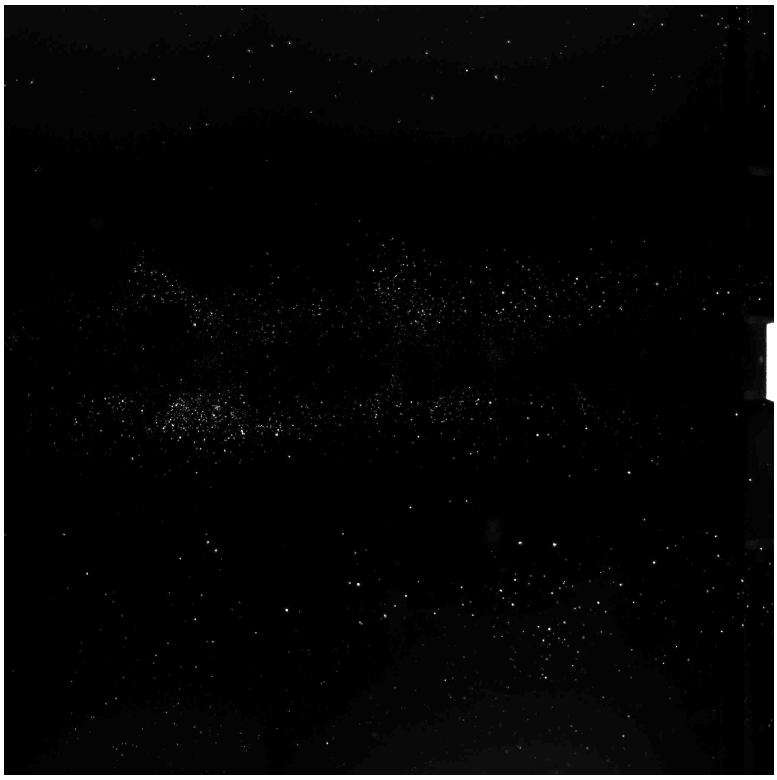

Figure 87. Good quality PIV wake image (pylon on center-right of frame, image plane at *y* = 3.7 cm)

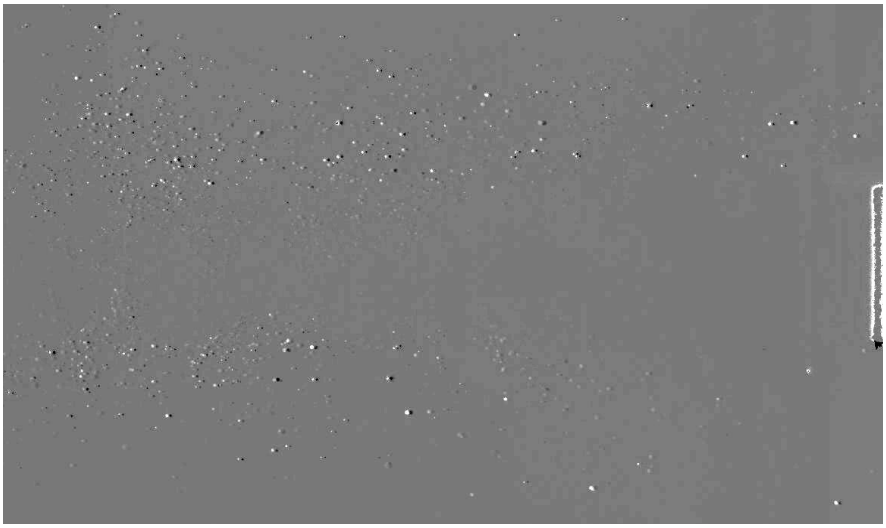

Figure 88. Comparison of good quality image pair (pylon on center-right of frame, image plane at *y* = 3.7 cm)

Figure 89. Average quality image of pylon wake on centerline (pylon on right edge of frame)

A7. Comparison of PIV and CFD Turbulence Intensity

Analysis of turbulence was not a specific goal of this study; however, both CFD and PIV provide the means of estimating the level of turbulence in the flow. The CFD turbulence results (Figure 90) were limited by the choice of using a large-scale two-equation turbulence model (SST model), i.e. no attempt was made at modeling the small scale eddies in the flow since the averaging process in two-equation models such as the SST turbulence model inherently prevents calculation of the turbulent structures themselves [74]. The CFD model assumes perfectly smooth surfaces and no vibration of the test section. In reality, the surfaces are not perfectly smooth, the tunnel vibrates significantly and the actual turbulence level leaving the stagnation chamber is unknown. The PIV turbulence results (Figure 91) were limited by the data available within the collected image pairs which was in turn severely limited by the sparse seeding of the flow, however it is not surprising the a higher overall level of turbulence was seen in the PIV data.

The highest intensity turbulence in the CFD results shown in Figure 90 are confined to the pylon wake, especially where the wake and expansion wave meet between approximately x = 1 cm and x = 3 cm. In the PIV results of Figure 91, this region had zero or close to zero image pairs available for data reduction (Figure 47), so a direct comparison is impossible. In contrast to the CFD results, the PIV results showed a high level of turbulence spanning the image as seen in Figure 92 along a line 8.8 cm behind the pylon and cavity leading edge.

Both sets of data present turbulent intensity and the comparison of the data requires the assumption of isotropic turbulence, i.e. the turbulent velocity fluctuations are the same in every direction [53:405], namely

$$u' = v' = w' \tag{25}$$

where *u'*, *v'*, and *w'* are the turbulent fluctuation in velocity in the *x*, *y*, and *z* directions respectively.

The CFD turbulent intensity (*I*) was determined as follows [73]:

$$I = \frac{\sqrt{\frac{2}{3}k}}{v_{ref}} \tag{26}$$

where turbulent kinetic energy (*k*) is solved specifically in the CFD turbulence model (see Appendix B) and the reference velocity is taken to be the mean velocity entering the test section (≈ 500 m/s). The turbulent kinetic energy is representative of the individual turbulent velocity fluctuation components [53:409; 74:233]:

$$k = \frac{1}{2}\left(\overline{u'u'} + \overline{v'v'} + \overline{w'w'}\right) \tag{27}$$

When isotropic turbulence is assumed for comparison purposes, the turbulent kinetic energy collapses to

$$k = \frac{3}{2}\overline{u'u'} \tag{28}$$

Applying this form of *k* to the turbulent intensity calculation used for CFD results in

$$I = \frac{u'}{v_{ref}} \tag{29}$$

which, when v_{ref} is assumed to equal the mean streamwise velocity through the test section (U), becomes the same form of turbulent intensity provided by the PIV data reduction software [72], namely

$$I = \frac{u'}{U} \tag{30}$$

thus supporting the comparison of CFD and PIV turbulence intensity results. While isotropic turbulence is not assumed in the SST turbulence model and the PIV data can produce fluctuation data in two axes, the assumption of isotropy for the comparison is required for two reasons. First, the PIV data lacks the vertical velocity fluctuation component (v') to make a direct comparison. Second, the spanwise turbulence data in the PIV data set was plagued with a high number of spurious data points making its use questionable. In any event, due to the sparse experimental data set, further investigation is required to draw any quantitative conclusion on the turbulence environment in the pylon-cavity flowfield.

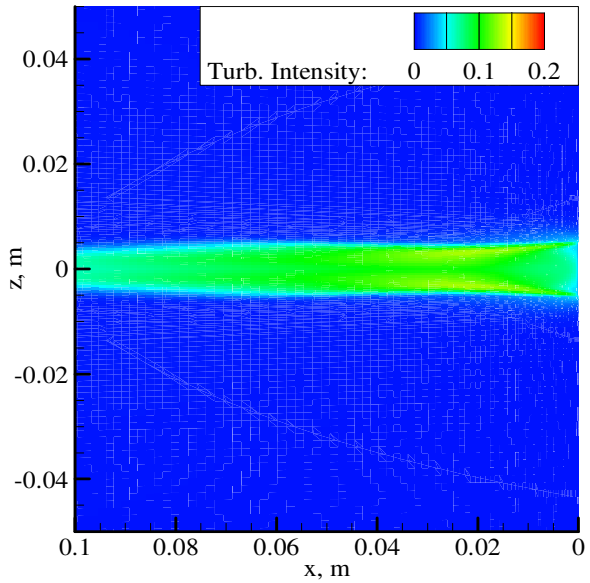

Figure 90. Turbulence intensity behind pylon 3.7 cm above the cavity (CFD; Re ≈ 32 x 10^6 m^{-1}; corresponds to Figure 46)

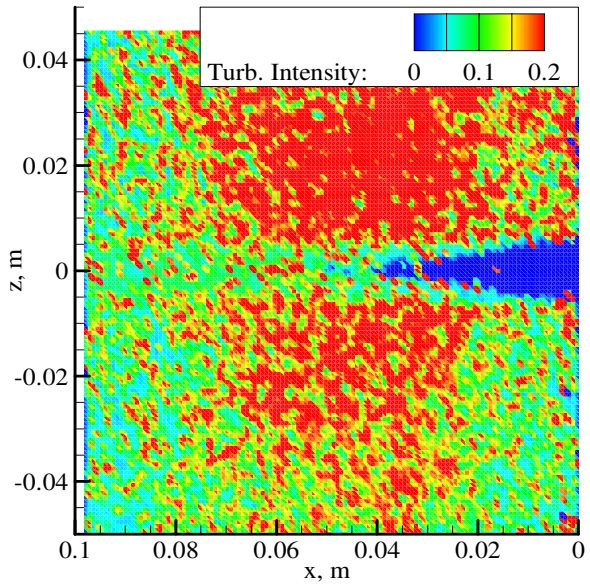

Figure 91. Turbulence intensity behind pylon 3.7 cm above the cavity (PIV; Re ≈ 32 x 10^6 m^{-1}; corresponds to Figure 46)

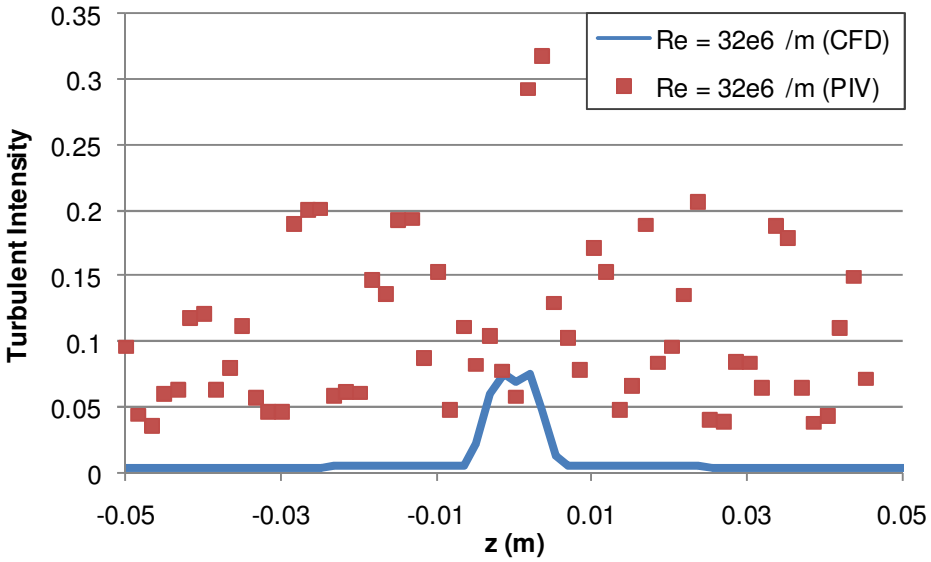

Figure 92. Turbulence intensity profile across test section (x = 8.8 cm, y = 3.7 cm)

Appendix B: CFD Details

This appendix presents a summary of the computational fluid dynamics (CFD) grid convergence study, software. The CFD was accomplished using a commercially available software package, Fluent. For more detailed information on the various inputs and underlying equations, consult the Fluent Users Guide [73].

B1. Grid Convergence

Initial grid convergence was accomplished using the baseline (no-pylon) mesh. The cavity-pylon model used the same mesh as the final baseline mesh, except for the cluster of cells around the pylon and pylon wake.

Grid convergence tests used the 241 kPa (35 psia) tunnel nozzle profile. Five baseline meshes were developed for grid convergence, with three being run out to flow convergence. The viscous spacing (y+) was reduced as layers of cells were added to model in order to better capture flow physics near the walls and especially in the shear layer. The three meshes were:

Low density: 2,725,478 cells
Med density: 3,281,698 cells
High density: 5,048,028 cells

Convergence was monitored using the mass flow error between the inlet and outlet, as well as the mean mass flow through the cavity and required less than 20,000 iterations. Both values tend to zero as the solution converges.

Three criteria were examined for the convergence study: pressure profile across the cavity ramp, pressure profile on test section centerline and average ramp pressure. Figure 93 through Figure 95 compare these data on the three different meshes. These

values were chosen for easy comparison with wind tunnel data. Except for cross ramp pressure, there was little difference between the medium and high density meshes. The high density mesh was chosen since it presented a slightly more uniform cross ramp pressure profile and had smaller y+ values along the model walls, yet stayed within a reasonable computational expense.

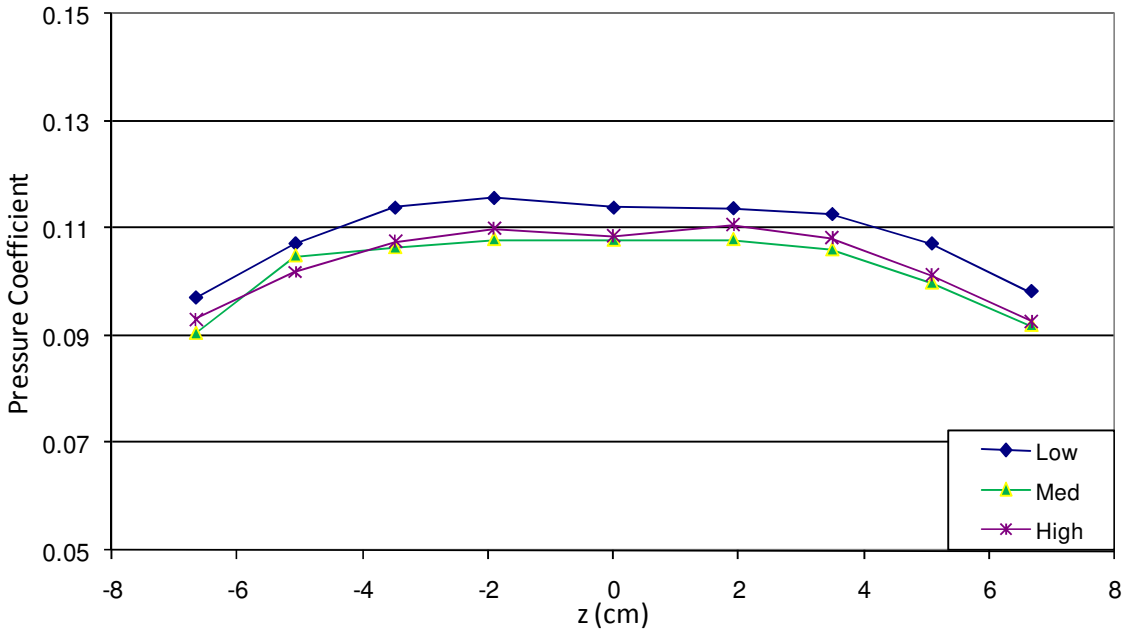

Figure 93. Grid convergence (cross ramp pressure coefficient)

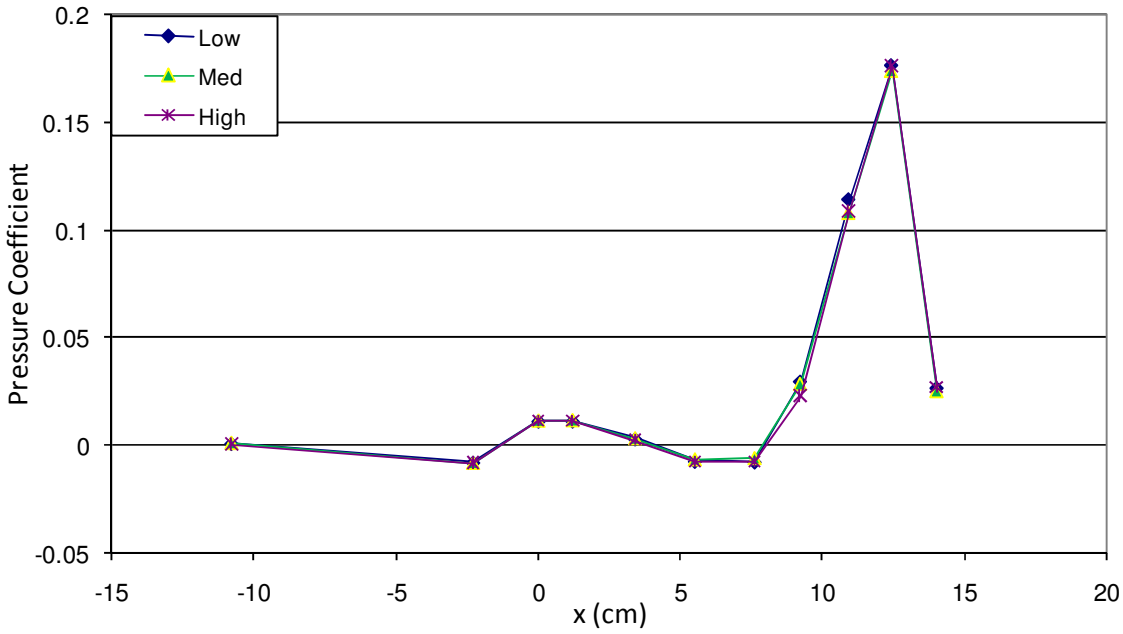

Figure 94. Grid convergence (centerline pressure coefficient)

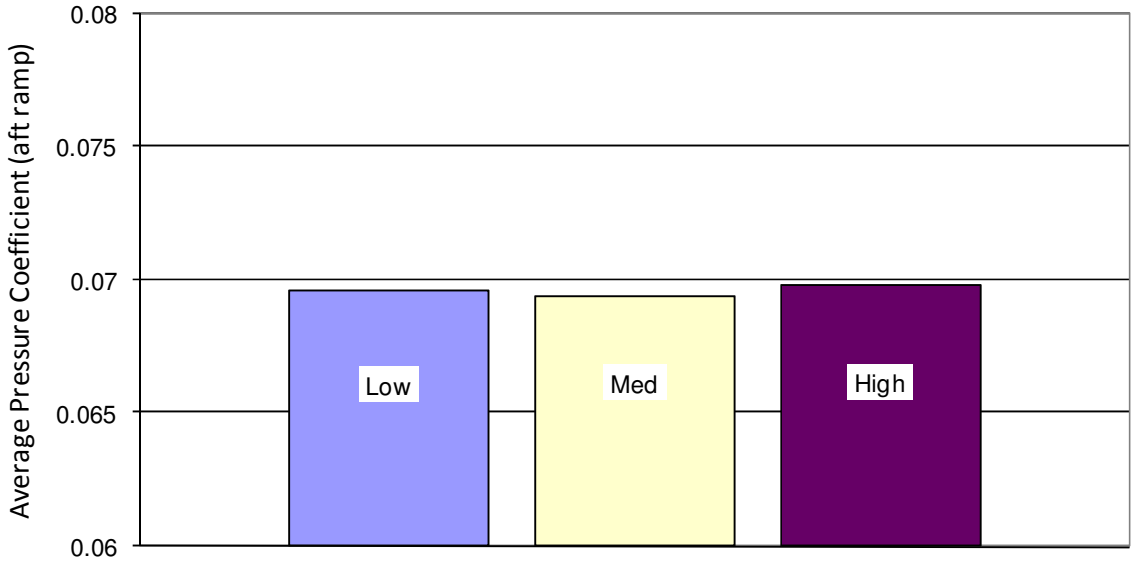

Figure 95. Grid convergence (average downstream ramp pressure coefficient)

B2. Computational Method

Fluent, as implemented for this study, uses a block Gauss-Seidel solver based on a finite volume approach [73: Ch 26]. A coupled, implicit, second-order accurate, upwind solution scheme was chosen to implement the governing equations. The basic equation set solved was

$$\frac{\partial}{\partial t}\int_V \vec{W}dV + \int_A \left|\vec{F} - \vec{G}\right| \cdot d\vec{A} = \int_V \vec{H}dV \tag{31}$$

$$\vec{W} = \begin{bmatrix} \rho \\ \rho u \\ \rho v \\ \rho w \\ \rho E \end{bmatrix}, \quad \vec{F} = \begin{bmatrix} \rho\vec{U} \\ \rho\vec{U}u + p\hat{i} \\ \rho\vec{U}v + p\hat{j} \\ \rho\vec{U}w + p\hat{k} \\ \rho\vec{U}E + p\vec{U} \end{bmatrix}, \quad \vec{G} = \begin{bmatrix} 0 \\ \tau_{xi} \\ \tau_{yi} \\ \tau_{zi} \\ \tau_{ij}U_j + \vec{q} \end{bmatrix}$$

The vector **H** is a source term and not required for this simulation. Turbulence effects are incorporated through the use of a turbulent viscosity model in the determination of the stress tensor $\boldsymbol{\tau}$ [73: Ch 26]. The turbulent viscosity is computed as

$$\mu_t = \alpha^* \frac{\rho k}{\omega}$$

where α* is a damping term that accounts for regions of low Reynold's number flow [73:Ch 11].

The k- ω shear stress transport (SST) turbulence model was chosen since it combines the advantages of the k- ω model near surfaces with the k-ε model which has good free-shear characteristics through the use of a blending function that accounts for

proximity to the wall [73:Ch11; 74; 75]. Default model coefficients were used. The k- ω SST governing equations are

$$\frac{\partial}{\partial t}(\rho k)+\frac{\partial}{\partial x_i}(\rho k u_i)=\frac{\partial}{\partial x_j}\left(\Gamma_k \frac{\partial k}{\partial x_j}\right)+\tilde{G}_k-Y_k+S_k \tag{32}$$

$$\frac{\partial}{\partial t}(\rho \omega)+\frac{\partial}{\partial x_i}(\rho \omega u_i)=\frac{\partial}{\partial x_j}\left(\Gamma_\omega \frac{\partial \omega}{\partial x_j}\right)+G_\omega-Y_\omega+D_\omega+S_\omega \tag{33}$$

The individual terms are as follows:

Γ_k = Effective diffusivity of turbulent kinetic energy (k)

Γ_ω = Effective diffusivity of specific dissipation rate (ω)

$\tilde{G}_k$ = Generation of turbulent kinetic energy (k)

G_ω = Generation of specific dissipation rate (ω)

Y_k = Dissipation of turbulent kinetic energy (k) due to turbulence

Y_ω = Dissipation of specific dissipation rate (ω) due to turbulence

S_k = Turbulent kinetic energy (k) source term (user-defined, not used)

S_ω = Specific dissipation rate (ω) source term (user-defined, not used)

D_ω = Cross-diffusion of specific dissipation rate (ω)

The cross-diffusion term is the result of transforming the k-ε model into the same form as the k-ω model in order to blend the two models. [66; 73:Ch 11]. The blending function between k-ω and k-ε is

$$\phi=F_1\phi_1+(1-F_1)\phi_2 \tag{34}$$

where ϕ_1 is any variable in the original k-ω model, ϕ_2 is the same variable in the transformed k-ε model and F_1 is a function of wall distance [66]. Since the mesh density along the surfaces was too coarse to fully resolve the turbulent boundary layer, the use of wall functions was required to calculate the boundary layer flow near solid boundaries. Further information on the specific wall functions used in Fluent can be found in Ref. [73:Ch 11].

The chosen solution scheme, while relatively efficient computationally, has difficulty in accurately resolving free-shear flows, such as in a pylon wake or cavity mixing layer. One of the underlying causes is the inability of the numerical solution to fully capture the relevant flow physics which is a trade-off for less computational expense. As research presented in Refs. [76; 77; 78] demonstrate, Reynolds (or Favre) Averaged Navier-Stokes (RANS) solutions tend to underpredict pressure and the length of the recirculation in base regions (such as behind a pylon). While the length of the recirculation is underpredicted the reverse flow velocity tends to be overpredicted. Even solutions with more complex methods require very high mesh densities to adequately model base flows. Additionally, base flow solutions are very sensitive to the incoming turbulence characteristics, so knowledge of the turbulent initial conditions in required to accurately capture these free shear flows.

The fluid model was air with density computed for an ideal gas and viscosity with the Sutherland model:

Density: $$\rho = \frac{P}{RT}$$

Viscosity: $$\mu = \frac{C_1 T^{3/2}}{T + C_2}$$

where P is the *static pressure*, R is the *gas constant* for air and T is the *static temperature*. The default constants C_1 and C_2 used in Fluent are: $C_1 = 1.458\text{x}10^{-6}$ kg/m-s-K$^{1/2}$ and C_2 = 110.4 K. Constant values of *specific heat*, *thermal conductivity* and *molecular weight* were used: Cp = 1006.43 J/kg-K, k = 0.0242 W/m-K, and MW = 28.966 kg/kmol.

Surface boundaries were modeled as no-slip, smooth, adiabatic surfaces. A pressure inlet boundary condition populated with values estimated from actual wind tunnel measurements and pressure far-field boundary conditions were used for the tunnel nozzle exit boundary. A pressure far-field boundary condition was used at the test section duct entry and exit and populated with the exit conditions of the tunnel nozzle solution. The method used to estimate the tunnel nozzle boundary conditions is presented below:

1) Inlet Mach number
Since the inlet and outlet areas are known and the outlet Mach number (M_{out} = 2) is based on geometry, it is possible to estimate the inlet Mach number using tables of A/A* [45]:

$$\left.\frac{A_{in}}{A^*}\right|_{M_{in}} = \left.\frac{A_{out}}{A^*}\right|_{M_{out}} \times \frac{A_{in}}{A_{out}} \tag{35}$$

A_{in} = 0.0676 m^2
A_{out} = 0.0232 m^2
$\left.A_{out}/A^*\right|_{M_{out}=2}$ = 1.687

Which results in $\left.A_{in}/A^*\right|_{M_{in}} = 4.8986$ and therefore $M_{in} = 0.12$.

2) Inlet total pressure
Averaged measured stagnation tank pressure from a wind tunnel run was used for modeling.

3) Inlet total temperature
This parameter is not controllable in the wind tunnel, but the average value from a wind tunnel run was used for modeling.

4) Inlet static conditions
Since the inlet Mach number and total conditions are known, the static conditions follow:

$$\left.P_t \middle/ P\right|_{M=0.12} = 1.01$$
$$\left.T_t \middle/ T\right|_{M=0.12} = 1.003$$

5) Outlet conditions
Assuming a negligible loss in total conditions through the nozzle, the boundary conditions at the nozzle outlet can be estimated using the test section Mach number (M = 2).

$$\left.P_t \middle/ P\right|_{M=2} = 7.824$$
$$\left.T_t \middle/ T\right|_{M=2} = 1.8$$

6) Turbulent boundary conditions
The initial values for turbulence were based on the hydraulic diameter and Reynold's number at the inlet and outlet. Turbulent intensity at the boundary was estimated using the empirical correlation [73:Ch 7]:

$$I \equiv \frac{u'}{u_{avg}} \equiv 0.16\left(\mathrm{Re}_{D_H}\right)^{-1/8} \tag{36}$$

D_H is the hydraulic diameter, 4A/P, which is 0.2268 m for the wind tunnel inlet and 0.1461 m for the outlet. The turbulent length scale is restricted by the duct dimensions and determined using the recommended empirical relation for duct flows from the Fluent user's manual [73:Ch 7]:

$$l = 0.7 D_H \tag{37}$$

For this model, l = 1.1cm. A better model would be to let the turbulent length scale be an empirical function of boundary layer thickness, however since the

actual flow through the distribution plate and turbulence screens in the stagnation tank is not known constant properties were assumed at the entry plane for simplicity. The turbulent conditions of the test section duct boundaries were obtained from the outlet solution of the wind tunnel nozzle.

B3. Detailed CFD Test Conditions ($M \approx 2$)

Condition	Mean stagnation pressure (kPa / psia)	Mean stagnation temperature (K)	Mean static pressure (kPa / psia)[1]	Mean dynamic pressure (kPa / psia)	CFD case Reynolds number (m^{-1})	Test condition Mean Reynolds number (m^{-1})
1	241317 / 35.0	273	29417 / 4.3	84857 \ 12.3	3.3×10^7	3.2×10^7
2	311436 / 45.2	271	37809 / 5.5	109065 / 15.8	4.3×10^7	4.2×10^7
3	394794 / 57.3	277	47776 / 6.9	137816 /20.0	5.3×10^7	4.9×10^7
4	426372 / 61.9	287	51573 / 7.5	148769 / 21.6	5.5×10^7	5.5×10^7

[1] Static pressure measured on tunnel floor ahead of the pylon (x = -10.8 cm, y = 0 cm, z = 0cm)

Appendix C: Additional Surface Pressure Data

Not all pressure data was used in analysis or presented in the main body of this study. For completeness, all available surface pressure data is presented in this appendix. The data correspond to the test conditions in Table 2 both with and without the pylon installed.

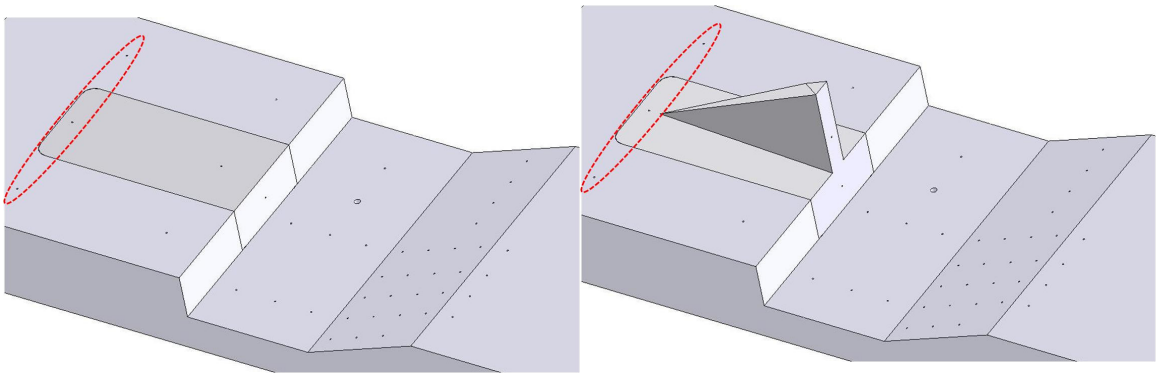

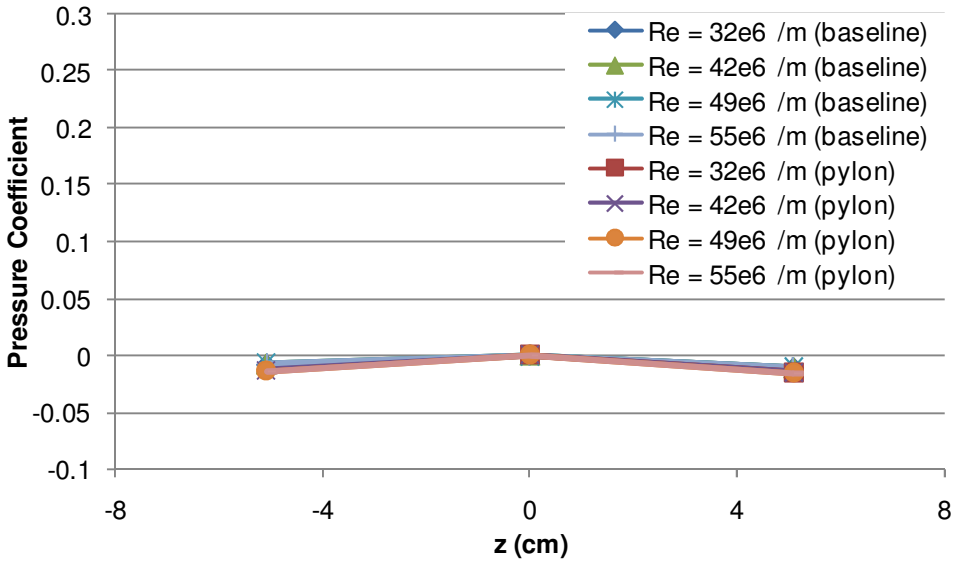

Figure 96. Surface pressure coefficients with and without a pylon installed (x = -10.8 cm)

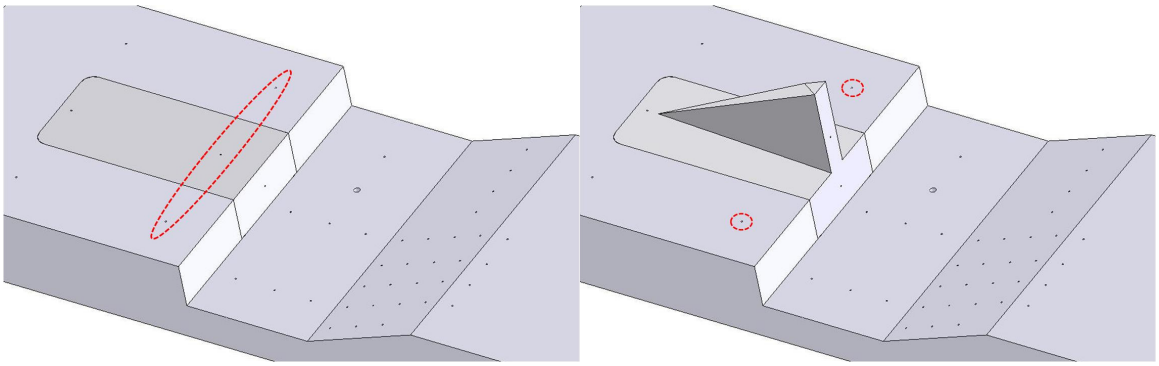

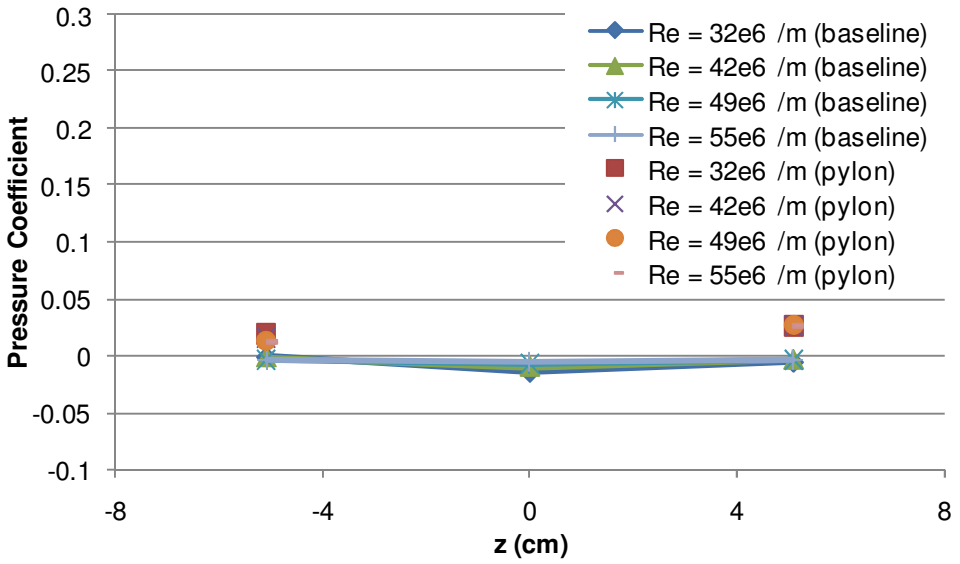

Figure 97. Surface pressure coefficients with and without a pylon installed (x = -2.3 cm, y = 0 cm)

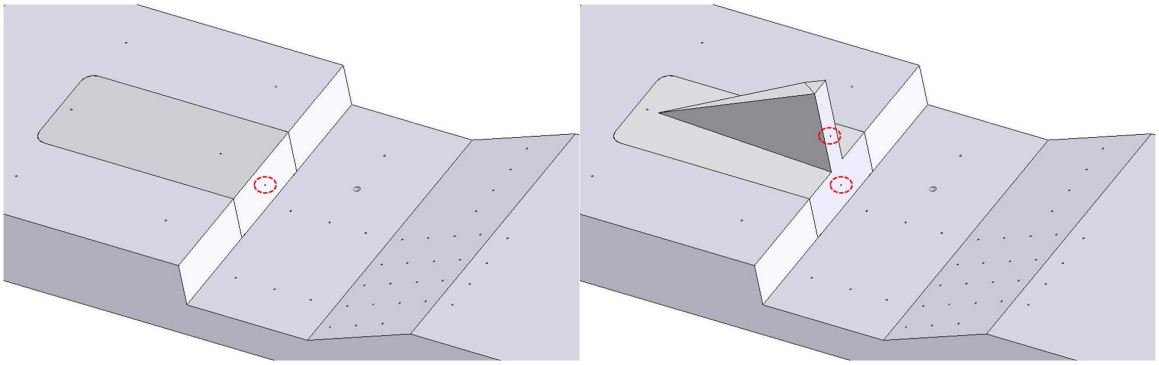

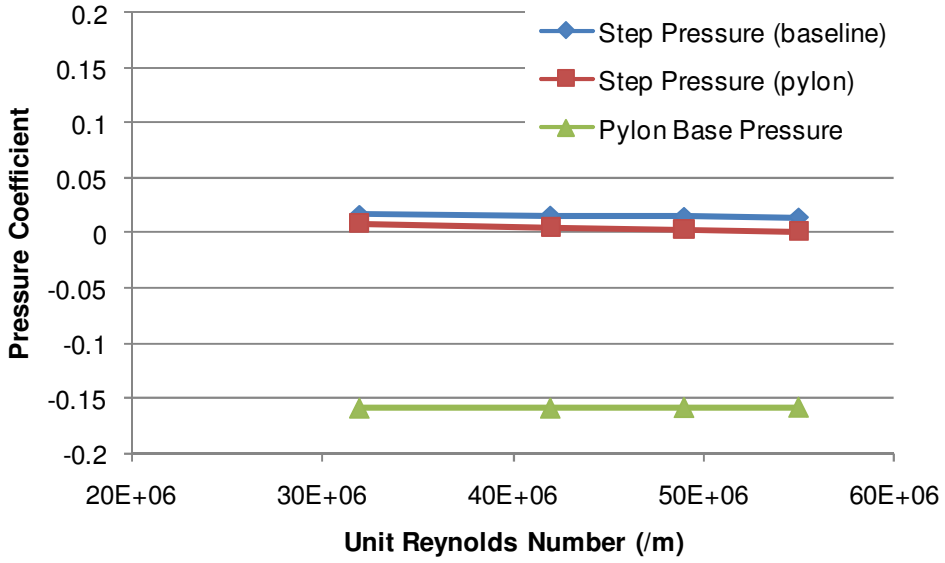

Figure 98. Cavity step pressure (with and without pylon installed) and pylon base pressure

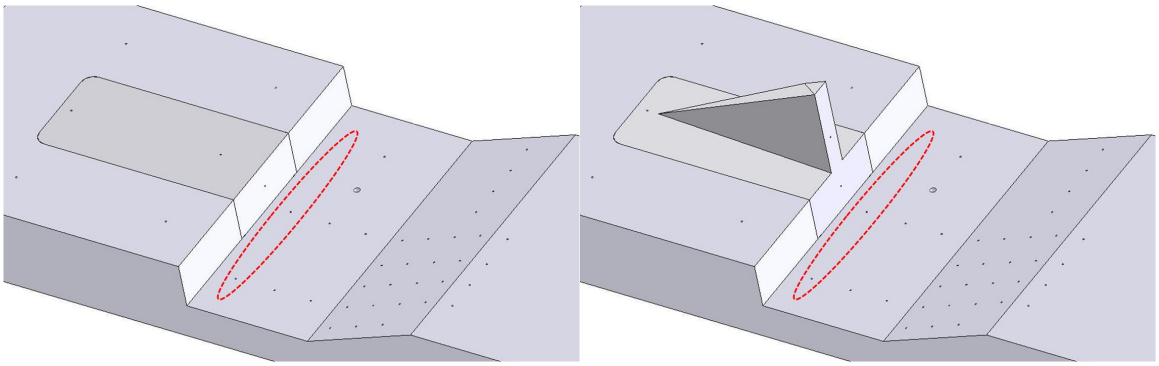

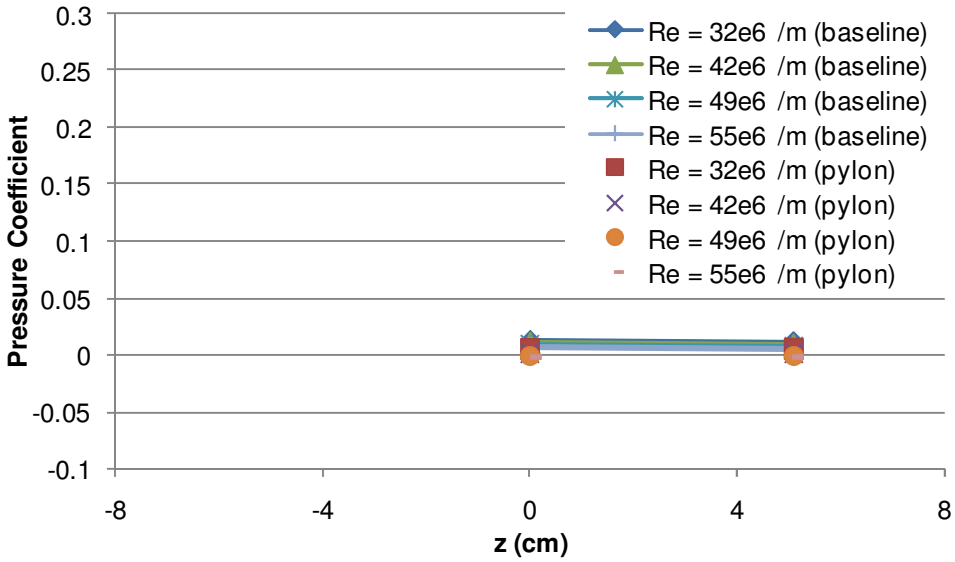

Figure 99. Surface pressure coefficients with and without a pylon installed (x = 1.2 cm, y = -2.54 cm)

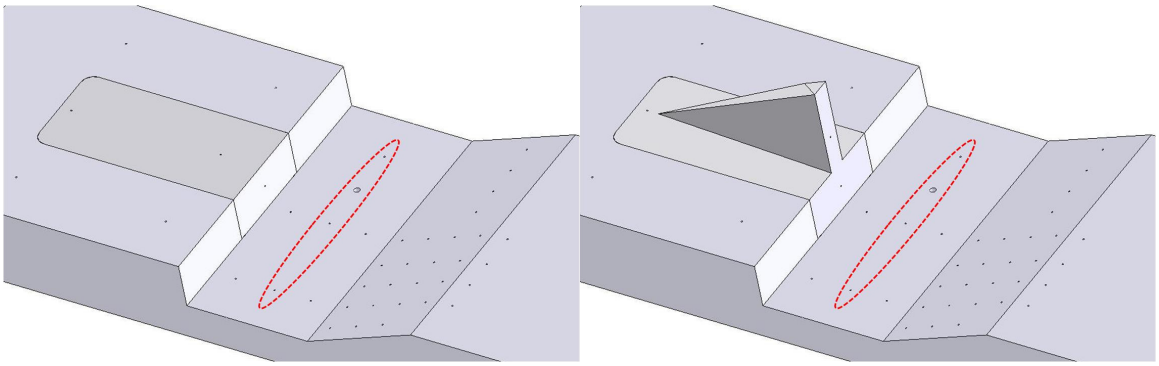

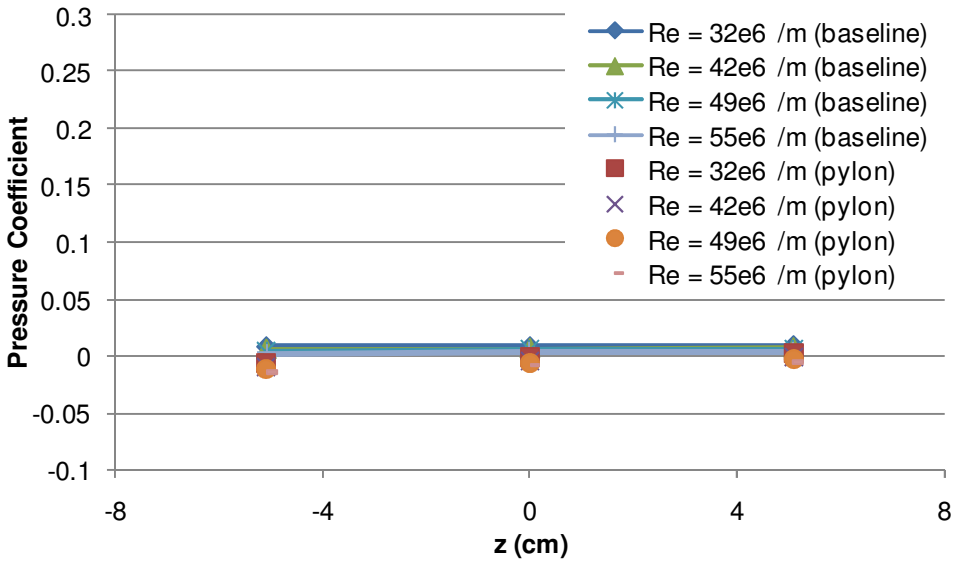

Figure 100. Surface pressure coefficients with and without a pylon installed (x = 3.4 cm, y = -2.54 cm)

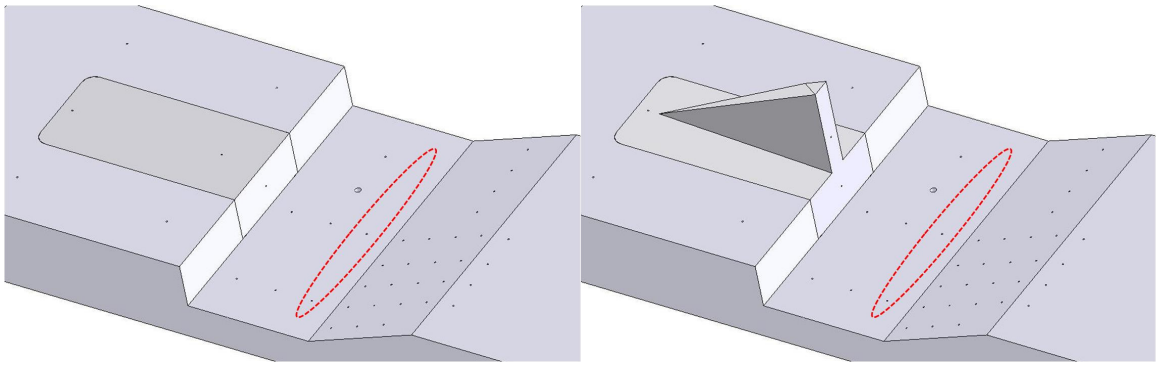

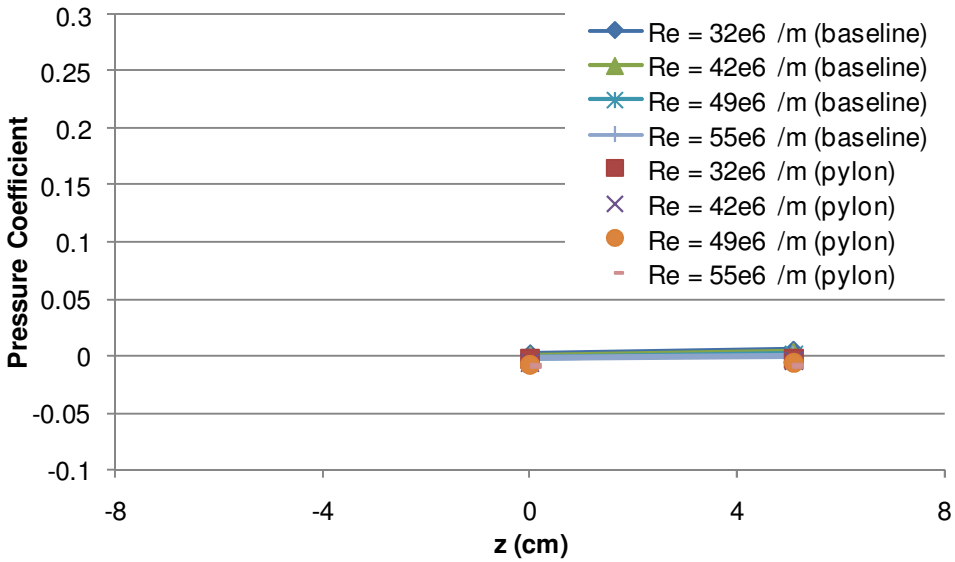

Figure 101. Surface pressure coefficients with and without a pylon installed (x = 5.5 cm, y = -2.54 cm)

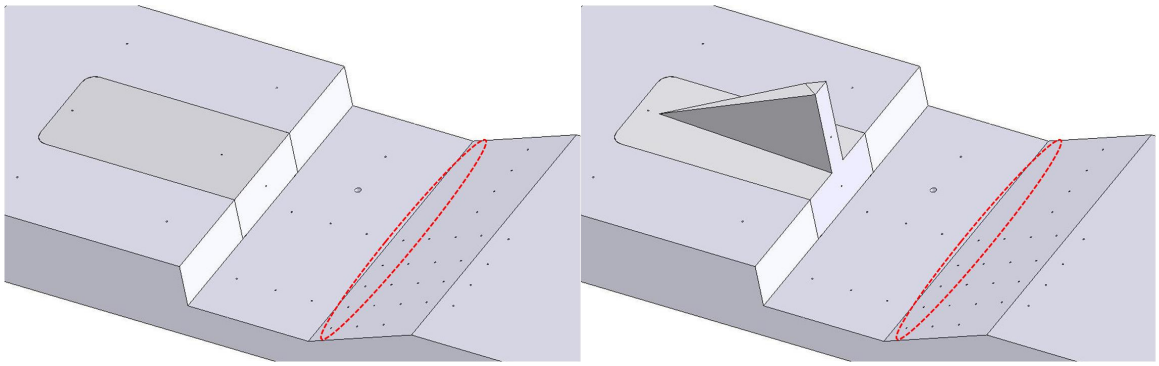

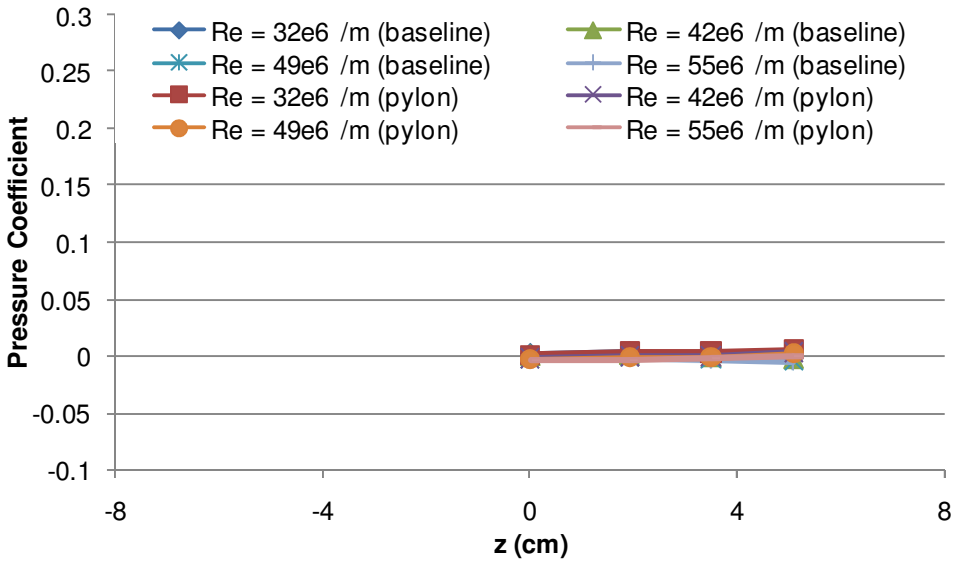

Figure 102. Surface pressure coefficients with and without a pylon installed (x = 7.6 cm, y = -2.2 cm)

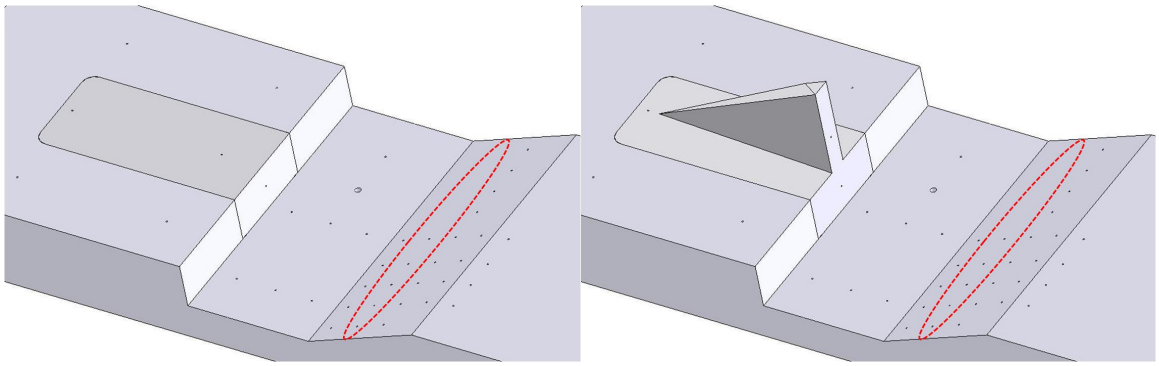

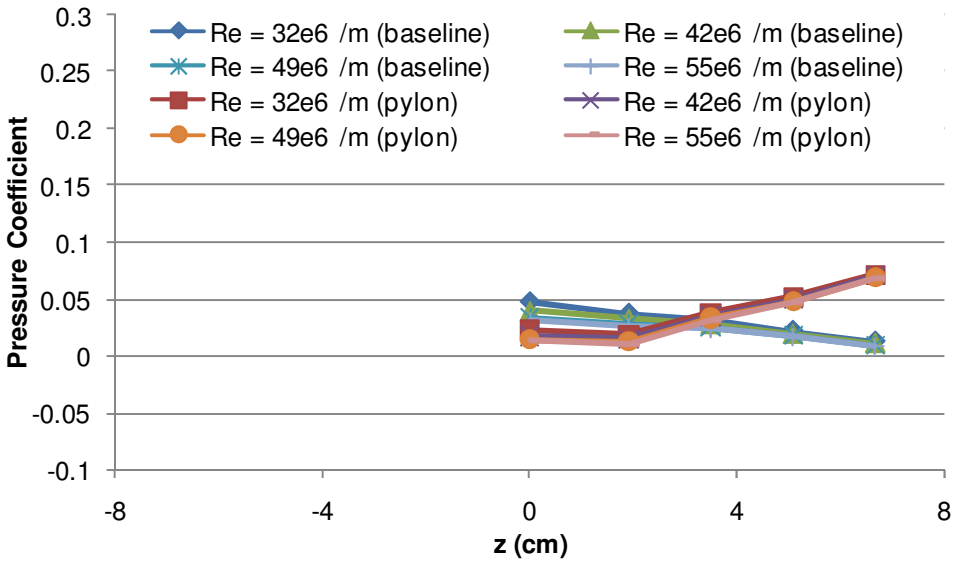

Figure 103. Surface pressure coefficients with and without a pylon installed (x = 9.2 cm, y = -1.6 cm)

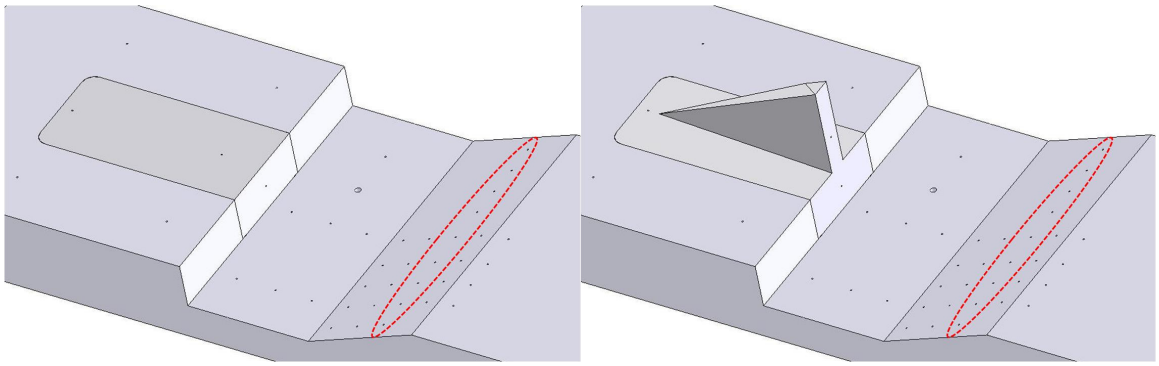

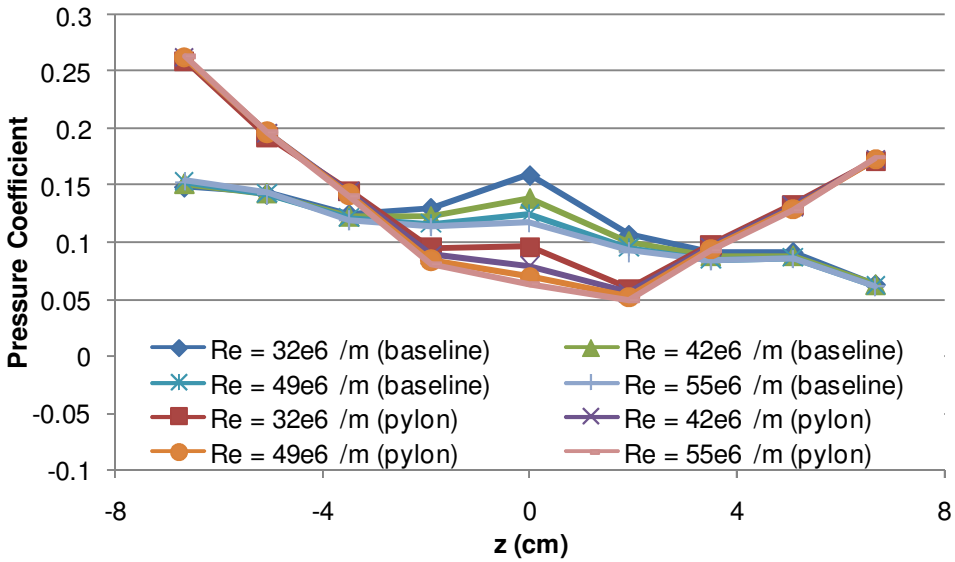

Figure 104. Surface pressure coefficients with and without a pylon installed (x = 10.9 cm, y = -0.95 cm)

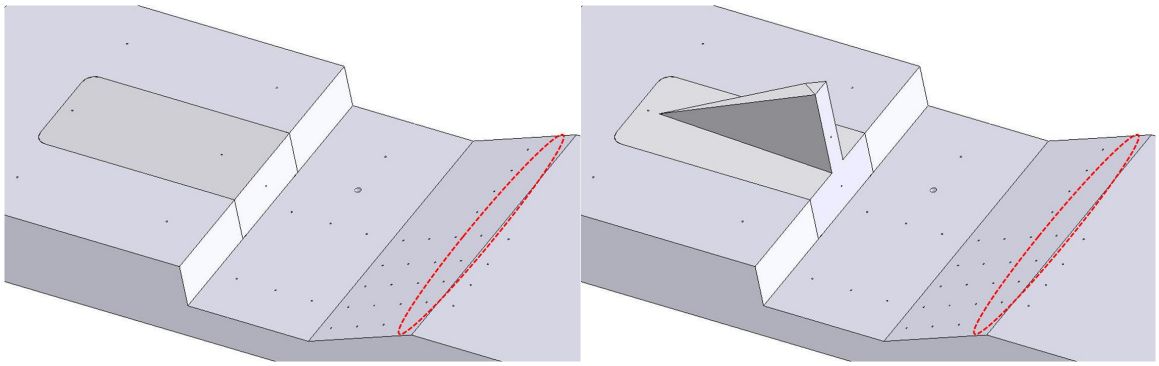

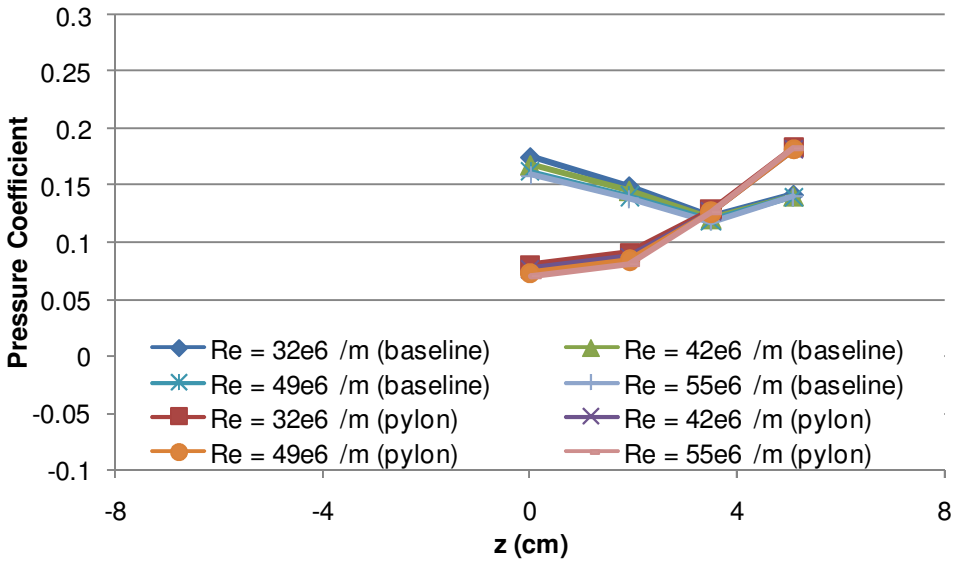

Figure 105. Surface pressure coefficients with and without a pylon installed (x = 12.4 cm, y = -0.32 cm)

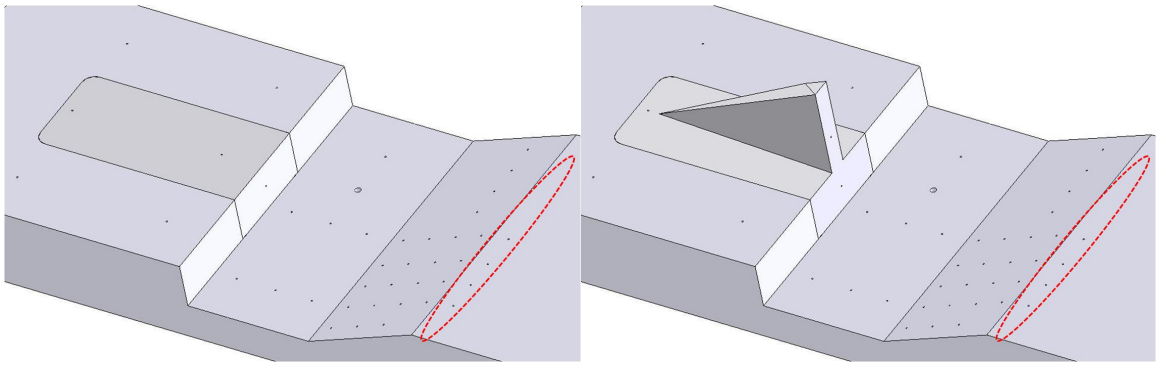

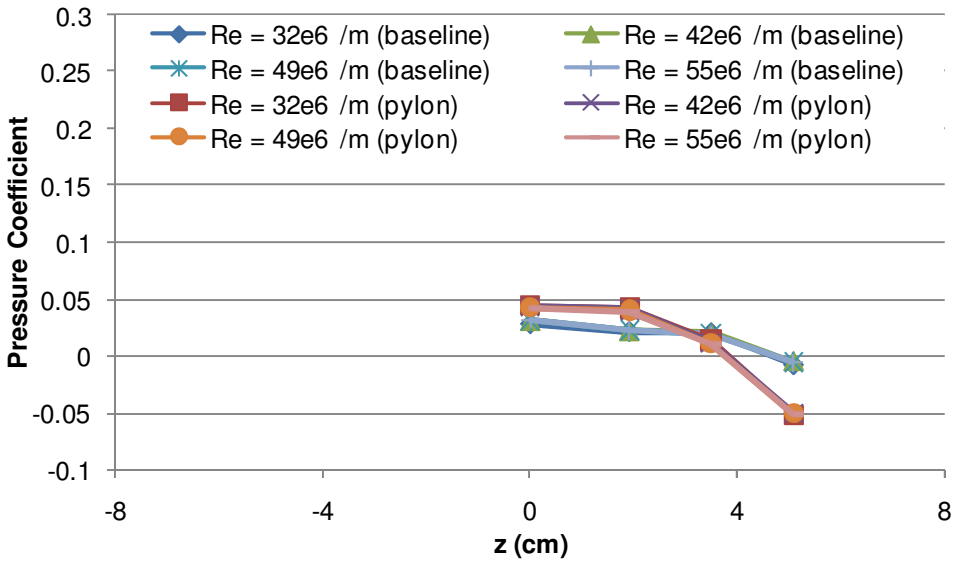

Figure 106. Surface pressure coefficients with and without a pylon installed (x = 14.0 cm, y = 0 cm)

Bibliography

1. Curran, E.T., "Scramjet Engines: The First Forty Years", *Journal of Propulsion and Power*, Vol. 17, No. 6, Nov-Dec 2001, pp. 1138-1148.

2. Heiser, W.H. and Pratt, D.T., *Hypersonic Airbreathing Propulsion*, AIAA, Washington, DC., 1994.

3. Maurice, L., Edwards T., and Griffiths J., "Liquid Hydrocarbon Fuels for Hypersonic Propulsion", *Scramjet Propulsion*, ed. By Curran, E.T. and Murthy, S.N.B., AIAA, Reston, 2000.

4. Canan, J.W., "Breathing New Hope Into Hypersonics", *Aerospace America*, Vol. 45, No. 11, Nov 2007.

5. Taverna M.A. and Barrie, D., "India Eyes Hyper-Cruise", *Aviation Week and Space Technology*, Vol. 167, No. 18, November 5, 2007.

6. Wilson, J.R., "High Hopes for HIFiRE Scramjet", *Aerospace America*, Vol. 45, No. 11, Nov 2007.

7. Norris, G., "All Fired Up", *Aviation Week and Space Technology*, Vol. 168, No. 18, May 5, 2008.

8. Butterworth-Hayes, P., "Europe Speeds Up Hypersonic Research", *Aerospace America*, Vol. 46, No. 6, June 2008.

9. Covault, C., "Going Hyper", *Aviation Week and Space Technology*, Vol. 166, No. 12, March 19/26, 2007, pp. 40-41.

10. Powell, O.A., Edwards, J.T., Norris, R.B., Numbers, K.E., and Pearce, J.A., "Development of Hydrocarbon-Fueled Scramjet Engines: The Hypersonic Technology (HyTech) Program", *Journal of Propulsion and Power*, Vol. 17, No. 6, Nov-Dec 2001, pp. 1170-1176.

11. Glassman, I., *Combustion*, 3rd ed., Academic Press, San Diego, 1996.

12. Arai, T., Sakaue, S., Morisaki, T., Kondo, A., Hiejima, T., and Nishioka, M., "Supersonic Streamwise Vortices Breakdown in Scramjet Combustor", AIAA Paper 2006-8025, 2006.

13. Gruber, M.R., Donbar, J.M., Carter, C.D. and Hsu, K., "Mixing and Combustion Studies Using Cavity-Based Flameholders in a Supersonic Flow", *Journal of Propulsion and Power*, Vol. 20, No. 5, Sep-Oct 2004, pp. 769-778.

14. Montes, D.R., King, P.I, Gruber, M.R., Carter, C.D., and Hsu, K., "Mixing Effects of Pylon-Aided Fuel Injection Located Upstream of a Flameholding Cavity in Supersonic Flow," AIAA Paper 2005-3913, July 2005.

15. Hsu, K., Carter, C.D., Gruber, M.R., and Barhosrt, T., "Experimental Study of Cavity-Strut Combustion in Supersonic Flow", AIAA Paper 2007-5394, July 2007.

16. Freeborn, A.B., King, P.I., and Gruber, M.R., "Characterization of Pylon Effects on a Scramjet Cavity Flameholder Flowfield", AIAA Paper 2008-0086, Jan 2008.

17. Freeborn, A.B., King, P.I., and Gruber, M.R., "Leading Edge Pylon Effects on a Scramjet Pylon-Cavity Flameholder Flowfield", AIAA Paper 2008-4709, Jul 2008.

18. Ben-Yakar, A. and Hanson, R.K., "Cavity Flame-Holders for Ignition and Flame Stabilization in Scramjets: An Overview", *Journal of Propulsion and Power*, Vol. 17, No. 4, Jul-Aug 2001, pp. 869-877.

19. Mattingly, J.D., Heiser, W.H., and Pratt, D.T., *Aircraft Engine Design*, 2nd ed., AIAA, Reston, 2002.

20. Lide, D.R., ed., *CRC Handbook of Chemistry and Physics*, 87th ed., CRC, Boca Raton, 2007.

21. Davis, D.L., *Numerical Analysis of Two and Three Dimensional Recessed Flame Holders For Scramjet Applications*. Air Force Institute of Technology (AU), Wright-Patterson AFB OH, 1996 (ADA324246).

22. Edwards, T., "Liquid Fuels and Propellants for Aerospace Propulsion: 1903-2003", *Journal of Propulsion and Power*, Vol. 19, No. 6, Nov-Dec 2003, pp. 1089-1107.

23. Hill, P.G. and Peterson, C.R., *Mechanics and Thermodynamics of Propulsion*, 2nd ed., Addison-Wesley, Reading, 1992.

24. Yu, K.H., Wilson, K.J., and Schadow, K.C., "Effect of Flame-Holding Cavities on Supersonic-Combustion Performance", *Journal of Propulsion and Power*, Vol. 17, No. 6, Nov-Dec 2001, pp. 1287-1295.

25. Tam, C.J., Orkwis, P.D., and Disimile, P.J., "Algebraic Turbulence Model Simulations of Supersonic Open-Cavity Flow Physics", *AIAA Journal*, Vol. 34, No. 11, Nov 1996.

26. Zhuang, N., Alvi, F.S., Alkislar, M.B., and Shih, C., "Supersonic Cavity Flows and Their Control", *AIAA Journal*, Vol. 44, No. 9, Sep 2006, pp.2118-2128.

27. Rizzetta, D.P., "Numerical Simulation of Supersonic Flow Over a Three-Dimensional Cavity", *AIAA Journal*, Vol. 26, No. 7, Jul 1988.

28. Rossiter, J.E., "Wind-Tunnel Experiments on the Flow over Rectangular Cavities at Subsonic and Transonic Speeds," Aeronautical Research Council Reports and Memoranda, No. 3438, Oct. 1964.

29. Murray, R.C. and Elliott, G.S., "Characteristics of the Compressible Shear Layer over a Cavity", *AIAA Journal*, Vol. 39, No. 5, May 2001, pp. 846-856.

30. Heller, H.H, Holmes, D.G., and Covert, E.E., "Flow-Induced Oscillations in Shallow Cavities", *Journal of Sound and Vibration*, Vol. 18, No. 4, 1971, pp. 545-553.

31. Zhang, X., "Compressible Cavity Flow Oscillation due to Shear Layer Instabilities and Pressure Feedback", *AIAA Journal*, Vol. 33, No. 8, Aug 1995, pp. 1404-1411.

32. Yu, K., Wilson, K.J., Smith, R.A., and Schadow, K.C., "Experimental Investigation on Dual-Purpose Cavity in Supersonic Reacting Flows", AIAA Paper 1998-0723, 1998.

33. Papamoschou, D. and Roshko, A., "The compressible turbulent shear layer: an experimental study", *Journal of Fluid Mechanics*, Vol. 197, 1988, pp. 453-477.

34. Dimotakis, P.E., "Turbulent Free Shear Layer Mixing and Combustion", *High-Speed Flight Propulsion Systems*, ed. By Murthy, S.N.B. and Curran, E.T., AIAA, Washington DC., 1991, pp. 265-340.

35. Jeong, E., O'Byrne, S., Jeung, I. and Houwing, A.F.P., "Cavity Flame-Holder Experiments in a Model Scramjet Engine", AIAA Paper 2006-7918, 2006.

36. Kim, C., Yu, S.J., and Zhang, Z., "Cavity Flow in Scramjet Engine by Space-Time Conservation and Solution Element Method", *AIAA Journal*, Vol. 42, No. 5, May 2004, pp. 912-919.

37. Rasmussen, C.C, Driscoll, J.F., Carter, C.D., and Hsu, K., "Characteristics of Cavity-Stabilized Flames in a Supersonic Flow", *Journal of Propulsion and Power*, Vol. 21, No. 4, Jul-Aug 2005, pp. 765-768.

38. Gruber, M.R., Baurle, R.A., Mathur, T., and Hsu, K., "Fundamental Studies of Cavity-Based Flameholder Concepts for Supersonic Combustors", *Journal of Propulsion and Power*, Vol. 17, No. 1, Jan-Feb 2001, pp. 146-153.

39. Baurle, R.A. and Gruber, M.R., "A Study of Recessed Cavity Flowfields for Supersonic Combustion Applications", AIAA Paper 98-0938, Jan 1998.

40. Allen, W.H., *Fuel-Air Injection Effects on Combustion in Cavity-Based Flameholders in a Supersonic Flow*, MS Thesis, AFIT/GAE/ENY/05-M02. School of Engineering and Management, Air Force Institute of Technology (AU), Wright-Patterson AFB OH, March 2005.

41. Owens, M., Tehranian, S., Segal, C., and Vinogradov, V., "Flame-Holding Configurations for Kerosene Combustion in a Mach 1.8 Airflow", *Journal of Propulsion and Power*, Vol. 14, No. 4, Jul-Aug 1998, pp. 456-461.

42. Edens, S.G., *Performance Measurements of Direct Air Injection in a Cavity-Based Flameholder for a Supersonic Combustor*, MS Thesis, AFIT/GAE/ENY/06-02. School of Engineering and Management, Air Force Institute of Technology (AU), Wright-Patterson AFB OH, December 2005.

43. Haubelt, L.C., *Supersonic Loss and Mixing Over A Cavity Flame Holder Located Downstream of Pylon-Aided Fuel Injection*, MS Thesis, AFIT/GAE/ENY/06-M13. School of Engineering and Management, Air Force Institute of Technology (AU), Wright-Patterson AFB OH, March 2006.

44. Bogdanoff, D.W., "Advanced Injection and Mixing Techniques for Scramjet Combustors", *Journal of Propulsion and Power*, Vol. 10, No. 2, Mar-Apr 1994, pp. 183-190.

45. Anderson, J.D., *Modern Compressible Flow with Historical Perspective*, 3rd ed., McGraw Hill, New York, 2003.

46. Seiner, J.M., Dash, S.M. and Kenzakowski, D.C., "Historical Survey on Enhanced Mixing in Scramjet Engines", *Journal of Propulsion and Power*, Vol. 17, No. 6, Nov-Dec 2001, pp. 1273-1286.

47. Fuller, R., Wu, P., Nejad, and A., Schetz, "Comparison of Physical and Aerodynamic Ramps as Fuel Injectors in Supersonic Flow", *Journal of Propulsion and Power,* Vol. 14, No. 2, Mar-Apr 1998, pp. 135-145.

48. Vinogradov, V., Shikhman, Y., and Segal, C., "A Review of Fuel Pre-injection in Supersonic, Chemically Reacting Flows", *Applied Mechanics Reviews*, Vol. 60, Jul 2007, pp. 139-148.

49. Vinogradov, V., Kobigsky, S., and Petrov, M., "Experimental Investigation of Kerosene Fuel Combustion in Supersonic Flow", *Journal of Propulsion and Power,* Vol. 11, No. 1, Jan-Feb 1995, pp. 130-134.

50. Vinogradov, V., Shikhman, Y. Albegov, R., and Vedeshkin, G., "Experimental Research of Pre-Injected Methane Combustion in High Speed Subsonic Airflow", AIAA Paper 2003-6940, 2003.

51. Ortwerth, P., Mathur, A., Vinogradov, V., Grin, V., Goldfeld, M., and Starov, A., "Experimental and Numerical Investigation of Hydrogen and Ethylene Combustion in a Mach 3-5 Channel with a Single Injector", AIAA Paper 96-3245, 1996.

52. Gu, H., Chen, L. and Chang, X., "Experimental Investigation of Cavity-based Scramjet Model", AIAA Paper 2006-7917, 2006.

53. White, F.M., *Viscous Fluid Flow*, 3rd ed., McGraw-Hill, New York, 2006.

54. Amick, J.L., Liepman, H.P., and Reynolds, T.H., "Development of a Variable Mach Number Sliding Block Nozzle and Evaluation in the Mach 1.3 to 4.0 Range", WADC Technical Report 55-88, Wright Air Development Center, March 1955.

55. "Operating Instructions for WPAFB 6" by 6" Supersonic Wind Tunnel", Aerolab, Mar 1996.

56. Holman, J.P., *Experimental Methods for Engineers*, 5th ed., McGraw-Hill, New York, 1989.

57. Raffel, M., Willert, C.E., and Kompenhans, J., *Particle Image Velocimetry: A Practical Guide*, Springer, Berlin, 1998.

58. Westerweel, J., "Fundamentals of Digital Particle Image Velocimetry", *Measurement Science and Technology*, Vol. 8, No. 12, 1997, pp. 1379-1392.

59. Melling, A., "Tracer Particles and Seeding for Particle Image Velocimetry", *Measurement Science and Technology*, Vol. 8, No. 12, 1997, pp. 1406-1416.

60. *2D PIV Reference Manual*, Dantec Dynamics A/S, Skovlunde, Denmark, 2006.

61. DeLapp, C.J., *Particle Image Velocimetry Using Novel, Non-Intrusive Particle Seeding*, MS Thesis, AFIT/GAE/ENY/06-J01. School of Engineering and Management, Air Force Institute of Technology (AU), Wright-Patterson AFB OH, June 2006.

62. McNiel, C.M., *Demonstration of Clean Particle Seeding For Particle Image Velocimetry in a Closed Circuit Supersonic Wind Tunnel,* MS Thesis, AFIT/GAE/ENY/07-M19. School of Engineering and Management, Air Force Institute of Technology (AU), Wright-Patterson AFB OH, March 2007.

63. Peltier, D.W. III, *Performing Particle Image Velocimetry in a Supersonic Wind Tunnel Using Carbon Dioxide as the Seed Material*, MS Thesis, AFIT/GAE/ENY/07-J17. School of Engineering and Management, Air Force Institute of Technology (AU), Wright-Patterson AFB OH, June 2007.

64. Greene, B.G., *Characterization and Control of Carbon Dioxide Seed Particles in Particle Image Velocimetry*, MS Thesis, AFIT/GAE/ENY/08-M12. School of Engineering and Management, Air Force Institute of Technology (AU), Wright-Patterson AFB OH, March 2008.

65. Greitzer, E.M., Tan, C.S., and Graf, M.B., *Internal Flow: Concepts and Applications*, Cambridge University Press, New York, 2004.

66. Menter, F.R., "Two-Equation Eddy-Viscosity Turbulence Models for Engineering Applications", *AIAA Journal*, Vol. 32, No. 8, Aug 1994, pp. 1598-1605.

67. *Piezoresistive Pressure Transducer: Endevco Model 8530C*. Product Data Sheet. San Juan Capistrano: Endevco Corporation, no date.

68. Settles, G.S., Williams, D.R., Baca, B.K., and Bogdonoff, S.M., "Reattachment of a Compressible Turbulent Free Shear Layer", *AIAA Journal*, Vol. 20, No. 1, Jan 1982, pp. 60-67.

69. *SFTE Reference Handbook*, Ed. Lee Gardner. Lancaster CA: Society of Flight Test Engineers, 2001.

70. Sims, J.L., *Tables for supersonic flow around right circular cones at zero angle of attack,* NASA-SP-3004, Washington DC., NASA, 1964.

71. Coleman, H.W. and Steele, W.G., *Experimentation and Uncertainty Analysis for Engineers*, John Wiley and Sons, New York, 1999.

72. Dynamic Studio, Version 2.0, CD-ROM. Computer software. Dantec Dynamics A/S, Skovlunde, Denmark, 2006.

73. *Fluent Users Guide*. Fluent, Inc., 2003.

74. Blazek, J., *Computational Fluid Dynamics: Principles and Applications*, Elsevier, Oxford, 2005, pp. 247-249.

75. Nichols, R.H., "Turbulence Models and Their Application to Complex Flows", Mississippi State University, ND.

76. Kawai, S. and Fujii, K., "Computational Study of Supersonic Base Flow Using Hybrid Turbulence Methodology", *AIAA Journal*, Vol. 43, No. 6, Jun 2005, pp. 60-67.

77. Simon, F., Deck, S., Guillen, P., and Sagaut, P., "Reynolds-Averaged Navier-Stokes/Large-Eddy Simulations of Supersonic Base Flow", AIAA *Journal*, Vol. 44, No. 11, Nov 2006, pp. 2578-2590.

78. Sandberg, R. and Fasel, H., "Investigation of Supersonic Wakes Using Conventional and Hybrid Turbulence Models", *AIAA Journal*, Vol. 44, No. 9, Sep 2006, pp. 2071-2083.

Vita

Lieutenant Colonel Andrew B. Freeborn graduated from Lower Lake High School in Lower Lake, CA in 1987. He began undergraduate study in engineering at the University of California, Davis before moving to the US Air Force Academy, graduating in 1992 with a Bachelor of Science degree in Astronautical Engineering, a minor in Russian language, and a commission as a Second Lieutenant. After a brief tour as an engineering intern for the Dept. of Energy, he attended Undergraduate Pilot Training at Laughlin AFB, TX and was assigned to the 909th Air Refueling Squadron, Kadena AB, Okinawa, Japan where he flew as a copilot, aircraft commander and instructor pilot.

In early 1999, he was assigned to KC-135 Combat Crew Training School, Altus AFB, OK as a school house instructor pilot. While at Altus AFB, he completed a Master of Aerospace Engineering degree through Auburn University. In 2000, he was accepted to the Air Force Test Pilot School, Edwards AFB, CA where he graduated in 2001. He then served as a KC-135 and KC-10 test pilot, Tanker Test Flight Commander, Chief of Standardization/Evaluation, and Assistant Director of Operations for the 418th and then 445th Flight Test Squadrons. His test background included avionics and wheels/brakes upgrades to the tanker fleets as well as extensive air refueling qualification testing for a variety of aircraft. He has logged over 3000 hours in more than 30 different aircraft.

In 2005 he was assigned to the Air Force Institute of Technology at Wright-Patterson AFB, OH. Upon graduation he will be assigned back to the Air Force Test Pilot School as an instructor.

REPORT DOCUMENTATION PAGE

Form Approved
OMB No. 074-0188

The public reporting burden for this collection of information is estimated to average 1 hour per response, including the time for reviewing instructions, searching existing data sources, gathering and maintaining the data needed, and completing and reviewing the collection of information. Send comments regarding this burden estimate or any other aspect of the collection of information, including suggestions for reducing this burden to Department of Defense, Washington Headquarters Services, Directorate for Information Operations and Reports (0704-0188), 1215 Jefferson Davis Highway, Suite 1204, Arlington, VA 22202-4302. Respondents should be aware that notwithstanding any other provision of law, no person shall be subject to an penalty for failing to comply with a collection of information if it does not display a currently valid OMB control number.
PLEASE DO NOT RETURN YOUR FORM TO THE ABOVE ADDRESS.

1. REPORT DATE *(DD-MM-YYYY)*	2. REPORT TYPE	3. DATES COVERED *(From – To)*
September 2008	**Doctoral Dissertation**	June 2005 – September 2008

4. TITLE AND SUBTITLE

Pylon Effects on a Scramjet Cavity Flameholder Flowfield

5a. CONTRACT NUMBER

5b. GRANT NUMBER

5c. PROGRAM ELEMENT NUMBER

6. AUTHOR(S)

Freeborn, Andrew B., Lt Col, USAF

5d. PROJECT NUMBER

5e. TASK NUMBER

5f. WORK UNIT NUMBER

7. PERFORMING ORGANIZATION NAMES(S) AND ADDRESS(S)
Air Force Institute of Technology
Graduate School of Engineering and Management (AFIT/EN)
2950 Hobson Way
WPAFB OH 45433-7765

8. PERFORMING ORGANIZATION REPORT NUMBER

AFIT/DS/ENY/08-04

9. SPONSORING/MONITORING AGENCY NAME(S) AND ADDRESS(ES)
AFRL/RZAS
Attn: Dr. Mark Gruber
1950 5th Street
WPAFB OH 45433 DSN: 785-7350

10. SPONSOR/MONITOR'S ACRONYM(S)

11. SPONSOR/MONITOR'S REPORT NUMBER(S)

12. DISTRIBUTION/AVAILABILITY STATEMENT
APPROVED FOR PUBLIC RELEASE; DISTRIBUTION UNLIMITED.

13. SUPPLEMENTARY NOTES

14. ABSTRACT

Cavity flameholders in supersonic combustion ramjet (scramjet) combustors, while effective, fail to take advantage of the full combustor volume. Adding a pylon to the leading edge of a cavity flameholder generates a flowfield increasing mass exchange between the cavity and main combustor flow, increasing the mixing interface between flameholder products and main combustor flow, and exhibiting minimal Reynolds number effects. To demonstrate this modified flowfield driven by supersonic expansion behind the pylon, pylon-cavity flameholder flowfield data were obtained through a combination of wind tunnel experimentation and steady-state computational fluid dynamics. Flowfield effects of the pylon-cavity were examined at a Mach number of two and Reynolds numbers from approximately 33 million m^{-1} to 55 million m^{-1}. Addition of the pylon resulted in approximately three times the mass exchange between the cavity and overlying flow. Reynolds number effects were weak. A strong upward flow behind the pylon, from the cavity to the top of the pylon wake, significantly increased exposure and exchange of cavity fluid with the main combustor flow. Assuming a suitably reacting fuel-air mixture, the addition of a pylon offers the scramjet designer an attractive option to take advantage of a greater proportion of combustor volume and improve combustor performance.

15. SUBJECT TERMS
CAVITIES, VORTICES, FLOW FIELDS, SUPERSONIC COMBUSTION, FLOW VISUALIZATION, STRUTS, COMBUSTORS, PROPULSION SYSTEM COMPONENTS, REYNOLDS NUMBER, COMPUTATIONAL FLUID DYNAMICS

16. SECURITY CLASSIFICATION OF:			17. LIMITATION OF ABSTRACT	18. NUMBER OF PAGES	19a. NAME OF RESPONSIBLE PERSON
REPORT	ABSTRACT	c. THIS PAGE			King, Paul. I., CIV (ENY)
U	U	U	UU	205	19b. TELEPHONE NUMBER *(Include area code)* (937) 255-6565, ext 4628; e-mail: paul.king@afit.edu